A Study of Viscous Flow Past Axisymmetric and Two-dimensional Bodies

Thesis by

Sung Phill Kang

In Partial Fulfillment of the Requirements

for the Degree of

Doctor of Philosophy

California Institute of Technology

Pasadena, California

1999

(Submitted November 4, 1998)

Acknowledgements

I would like to thank my advisor Dr. Meiron for his invaluable encouragement, guidance, and support. I also would like to thank my colleagues including Muruhan Rathinam, David Hill, and Peter Park for their friendship and for many useful discussions. The entire department of applied mathematics was tremendous in providing an excellent environment for research and study. Last but not least, I would also like to thank my parents for their patience.

Abstract

In this thesis, we study the behavior of viscous flow past bodies of different shapes. In Chapter 2, we construct a boundary-fitted, numerical grid around a rigid spheroid of various aspect ratios and solve numerically the Navier-Stokes equations in steady, axisymmetric form at various Reynolds numbers. In addition, we use these steady solutions as a base flow and perform a linear stability analysis to determine the critical Reynolds numbers above which the base flow becomes unstable. We are able to confirm the results of Natarajan and Acrivos [26] and extend them to more generalized body shapes.

In Chapter 3, we solve the Navier-Stokes equations to investigate flows past an oblate ellipsoidal bubble of fixed shape, which is characterized by a free-slip boundary condition. We then compare our results with previous results by Dandy and Leal [6] and Blanco and Magnaudet [4] and use the computed steady solutions as the base flow to perform a linear stability analysis. We show that even with a free-slip boundary condition, if the body is sufficiently oblate, the flow can become unstable in a manner similar to that of flows past rigid bodies.

In Chapter 4, we develop an alternative numerical method to compute steady flows past a deforming, axisymmetric bubble. A newly developed conformal grid generation method is applied. We show that our results are in good agreement with those of Ryskin and Leal [34], [35] and then extend some of their results to higher Reynolds number.

In Chapter 5, we modify the method developed in Chapter 4 to compute steady flows past a symmetric, two-dimensional bubble. We show that the bubble deforms to an elliptical shape and that a wake can develop if the deformation of the bubble is sufficiently large.

Contents

List of Figures

List of Tables

Chapter 1 Introduction

In the case of uniform external flow past bodies of axisymmetric and two-dimensional shape, a standing eddy develops behind the body at a certain Reynolds number, a parameter that relates the geometry of the body and the properties of the outer flow. As the Reynolds number increases, the eddy increases in size, and the flow eventually loses symmetry and becomes unstable. Clift, Grace, and Weber [5] give a good summary of various investigations carried out in this field.

There exist many papers [23], [42], [45], [50], [31] & [49] that study the flow past a solid sphere experimentally. Each of those papers observed transition in the flow at some critical Reynolds numbers. Achenbach [1] studied experimentally vortex shedding of flow past a solid sphere for the Reynolds numbers higher than 400. According to the numerical investigations in which the Navier-Stokes equations are solved to approximate fluid flow, there are two conflicting results in terms of the critical Reynolds number at which the flow becomes unstable. Kim and Pearlstein [17] used a linear stability analysis to determine that the critical Reynolds number is around 175.1 and concluded that the transition in the flow occurs as the axisymmetric, steady flow becomes oscillatory. On the other hand, Natarajan and Acrivos [26] determined the critical Reynolds number to be around 210 and concluded that the transition in the flow occurs as the axisymmetric, steady flow becomes nonaxisymmetric, but still steady. Full simulation of the flow past a solid sphere by Tomboulides, Orszag, and Karniadakis [44] and the linear stability analysis of the flow past a sphere in a pipe of finite width by Tavener [43] support the results by Natarajan and Acrivos [26].

One of the more interesting areas in the study of uniform flow past axisymmetric bodies is that of a rising gas bubble. Saffman [36] studied rising air bubbles in distilled water and observed that under certain conditions, the bubbles oscillate and sometimes spiral as they rise. Several papers including [14], [46], [9], & [3] also investigated flow past bubbles experimentally and noticed that the bubbles deform to an

oblate ellipsoidal shape. Using this fact, Moore [24] used boundary layer perturbation analysis to study distorted gas bubbles of oblate ellipsoidal shape rising in a fluid of small viscosity. Dandy and Leal [6] and later Blanco and Magnaudet [4] investigated this further by solving the Navier-Stokes equations numerically. They assumed the bubble to be an oblate ellipsoid with a free-slip boundary condition on the interface and numerically computed the flow field around it for various values of the Reynolds numbers. They both observed that with the aspect ratio of the ellipsoidal bubble fixed, a wake develops behind the bubble, grows to a maximal shape, shrinks back, and eventually disappears as the Reynolds number increases. However, they differed greatly in terms of the specific numerical results.

Of course, in order to study the full bubble problem numerically, the method has to account for the deformation of the bubble to satisfy the balance of the pressure, the viscous forces, and the surface tension of the bubble. Ryskin and Leal [34] & [35] used a boundary-fitted, curvilinear, orthogonal grid generation method to numerically compute the steady flow past a rising, deforming bubble for various values of the Reynolds number and the Weber number, a dimensionless measure of surface tension. Expanding on this, Takagi, Matsumoto, and Huang [40] used a similar approach to investigate the unsteady, axisymmetric flow past a deforming bubble. In terms of stability results, Meiron [22] performed a linear stability analysis of an inviscid, irrotational flow past a deforming axisymmetric bubble and showed that it is stable.

There exist also numerous papers [48], [21], & [32] that deal with two-dimensional bubbles experimentally. This is done using the Hele-Shaw cell set up which is basically a flattened gas bubble rising through a thin layer of fluid trapped between a pair of plates. More recently, Kelley and Wu [16] performed experiments in which they studied rising gas bubbles in such a set up and observed nearly circular bubbles zigzagging as they moved upward. Shankar [38] analytically studied two-dimensional bubbles in an inviscid flow and showed that the bubble deforms to an oblate elliptical shape. Nie and Tanveer [28] expanded on this and performed a linear stability analysis on an inviscid flow past a two-dimensional bubble to show that the flow is stable.

In this thesis, we attempt to expand on some the above investigations. In Chapter

2, we use the boundary-fitted, curvilinear, numerical grid generation method developed by Ryskin and Leal [33] to compute the steady flow past oblate and prolate spheroids. We also perform a linear stability analysis on the flow to determine the critical Reynolds numbers above which the axisymmetric flow past spheroids become unstable. In the case of the solid sphere, our results agree well with Natarajan and Acrivos' result [26]. We are then able to expand the result to a more general body shape of oblate and prolate spheroids and observe a relation between the critical Reynolds numbers and the aspect ratios of the body.

In Chapter 3, we try to reconcile the differences in the results of Dandy and Leal [6] and Blanco and Magnaudet [4] in the computation of steady flow past an ellipsoidal bubble of fixed shape by using basically the same numerical method used by Dandy and Leal [6]. The results that we obtain differ substantially from Dandy and Leal [6] and agrees reasonably well with that of Blanco and Magnaudet [4]. However, it is not a perfect agreement in that our numerical results tend to have smaller wakes over a shorter range of Reynolds numbers. Blanco and Magnaudet [4] suggest at the end of their paper that it would be interesting to carry out a linear stability analysis similar to [26] and [17] to study the dynamics of bubbles, even though the fixed shape of the bubble makes the problem very simplified compared to the actual bubble problem. We carry out this linear stability analysis and show that the dynamics of the ellipsoidal bubble of fixed shape is similar to that of the rigid, oblate spheroids determined in Chapter 2.

In Chapter 4, we develop an alternative method in computing steady flows past an axisymmetric, deforming bubble. While Ryskin and Leal [34] used a grid generation method that involves iteration, we use Symm's method [39] to generate a conformal map which allows the grid around the bubble to be computed directly without iteration. In addition, we develop a bubble shape prediction step which uses minimization, and this also differs from the Ryskin and Leal [34] approach. The steady flows past an axisymmetric bubble that are computed using our method agree well with Ryskin and Leal's results.

In Chapter 5, we modify the method discussed in Chapter 4 to compute steady,

viscous flow past a symmetric, two-dimensional bubble. We show that the two-dimensional bubble deforms to an oblate, elliptical shape and that a standing wake can develop if the deformation of the bubble is sufficiently large.

Chapter 2 The Behavior of Viscous Flow Past Axisymmetric Spheroids

2.1 Introduction

Fluid flow past solid bodies has been studied extensively for many years. Generally, it is observed that if the flow is moving slowly, then it is attached to the body and is steady. As the velocity of the flow increases, a separation of the fluid occurs on the surface of the body; and a standing wake forms on the rear of the body. When the velocity of the flow is large enough, the flow becomes unstable and eventually turbulent [5].

In studying flows past solid bodies, a parameter called the Reynolds number is usually used to relate the geometry of the body and the properties of the outer flow. In our studies, it is defined as

$$R_d = \frac{2d\rho U}{\mu}$$

where d is the characteristic length of the body, ρ is the density of the fluid, U is the velocity of the free stream flow, and μ is the viscosity of the fluid.

There exist numerous papers that investigate fluid flow past a solid sphere experimentally. Möller [23] vertically towed spheres with dye ports through water and observed low-frequency oscillatory motion in the wake behind the sphere occurring somewhere between a Reynolds number of 170 and 200. Taneda [42] suspended a sphere using a piano wire and horizontally dragged it through water and reported observing unsteadiness when the Reynolds number was around 130. Toulcova and Podzimek [45] and Zikmundova [50] dropped aluminum spheres through a mixture of water and glycerol and reported transition in the flow to unsteadiness around a Reynolds number of between 130 and 150. A somewhat different result is reported

by Goldburg and Florsheim [13]. They observed that around a Reynolds number of 210, the wake behind a falling solid sphere became nonaxisymmetric and eventually unsteady around Reynolds number 270. Also, Roos and Willmarth [31] reported that when they towed a sphere in water, they observed side forces around a Reynolds number of between 215 and 290. More recently, Wu and Faeth [49] towed spheres in a tank full of water and glycerin mixture and reported that for a Reynolds number lower than 200, the wake behind the sphere was steady, became nonaxisymmetric and steady up to Reynolds number 280, and then became unsteady for Reynolds number higher than 280. Achenbach [1] carried out experiments for flow past a sphere at Reynolds numbers as high as $5\text{x}10^6$ and studied vortex shedding in the flow. These differing results in experiments indicate the importance of the experimental set up.

There is also an extensive series of papers that seeks to study fluid flow past solid bodies using numerical computation. In these investigations, an attempt is made to solve the Navier-Stokes equations numerically to simulate the fluid flow past a solid sphere. More recently, Fornberg [12] calculated steady, axisymmetric flows past a sphere for Reynolds numbers as large as 5000. Magnaudet, Rivero, and Fabre [19] computed steady, axisymmetric flows past a sphere and accelerated flow past a sphere using a finite volume method. Kim and Pearlstein [17] were the first to use a linear stability analysis to compute the critical Reynolds number at which the steady, axisymmetric flow past a solid sphere becomes unstable. A spectral method was used in all directions to solve for the steady, axisymmetric flow. The computed steady, axisymmetric flow was then used as the base flow about which the unknowns of the full Navier-Stokes equations were perturbed, and the resulting equations were linearized to derive a set of perturbation equations. The perturbations are further simplified by expanding them as a Fourier series in the azimuthal direction of the sphere. Because the equations are linear, the perturbations can be expressed as a linear combination of the eigenfunctions associated with the system so that, with $\tilde{u}$ defined as a perturbation variable and t indicating time,

$$\tilde{u} \sim C_1 e^{\alpha_1 t}\tilde{v}_1 + C_2 e^{\alpha_2 t}\tilde{v}_2 + C_2 e^{\alpha_3 t}\tilde{v}_3 + ...$$

where $\alpha_1, \alpha_2, ...$ are the eigenvalues, and $\tilde{v}_1, \tilde{v}_2, ...$ are the corresponding eigenfunctions. The eigenvalues are defined so that

$$\mathrm{Re}(\alpha_1) \geq \mathrm{Re}(\alpha_2) \geq ....$$

Clearly, as $\mathrm{Re}(\alpha_1)$ goes from negative to positive, the perturbation becomes unstable. They computed these eigenvalues as a function of the Reynolds number and attempted to determine the critical value of the Reynolds number at which the real part of the leading eigenvalue becomes positive. They reported this critical Reynolds number to be 175.1 and determined that this transition occurs as the real part of the leading eigenvalue α_1, which is complex, of the $n = 1$ Fourier mode of the perturbation becomes positive. This result appears to agree with some of the experiments. However, several years later, Natarajan and Acrivos [26], using conformal mapping and the finite-element method, also computed the critical Reynolds numbers for instability for flows past a solid sphere and a flat disk and came up with a result that contradicted the results of Kim and Pearlstein [17]. They reported that while it is the $n = 1$ Fourier mode of the perturbation that becomes unstable, the critical Reynolds number is 210. Furthermore, in the work of Natarajan and Acrivos [26] the leading eigenvalue of the perturbation is purely real. They also indicated that around a Reynolds number of 277.5, time dependent, oscillatory transition occurs as the real part of the secondary eigenvalue α_2 becomes positive. Tomboulides, Orszag, and Karniadakis [44], using the spectral element-Fourier method, performed a full numerical simulation of viscous flow past a solid sphere; they reported that the flow goes from axisymmetric and steady to nonaxisymmetric and steady at a Reynolds number of 212. They also observed the appearance of time-periodic flow between a Reynolds number of 270 and 285. Further bolstering the results of Natarajan and Acrivos [26], Tavener [43] performed a linear stability analysis of viscous flow past a solid sphere in a pipe of finite width and determined that the initial instability occurs as the $n = 1$ Fourier mode of the perturbation becomes unstable and that the leading eigenvalue of the perturbation is also purely real.

In the case of more general body shapes, the results are not as numerous. Masliyah and Epstein [20] numerically calculated flows past oblate and prolate spheroids of various aspect ratios in steady and axisymmetric form for Reynolds numbers up to 100. In terms of stability analysis, there appears to be no published results. While the behavior should be similar to that of the solid sphere, it is not clear how the aspect ratio of the spheroids can influence the instability of the flow.

In this chapter, the viscous flow past solid bodies is studied numerically using a numerical grid generation and a linear stability analysis. We use the numerical grid generation method developed by Ryskin and Leal [33] who used this method to numerically solve for steady axisymmetric flow past a rising, deformable air bubble. We use their numerical grid generation method to solve for steady, axisymmetric flow past oblate and prolate spheroids of various aspect ratios and Reynolds numbers and then apply a numerical, linear stability analysis to determine the critical Reynolds numbers around which the flows become unstable.

2.2 Numerical Grid Generation

2.2.1 Equations for orthogonal grid system

In order to solve the fluid equations for flow past spheroids, the numerical grid generation method developed by Ryskin and Leal [33] is used to construct an orthogonal, curvilinear, boundary fitted coordinate system.

Figure 2.1 shows the setup of the physical problem being studied. Since the body is axisymmetric, the physical space can be denoted by

$$\begin{aligned} x &= x(\xi,\eta), \\ y &= \sigma(\xi,\eta)\cos(\phi), \\ z &= \sigma(\xi,\eta)\sin(\phi), \end{aligned}$$

where ϕ is the azimuthal angle ranging from 0 to 2π. ξ and η are the coordinates in

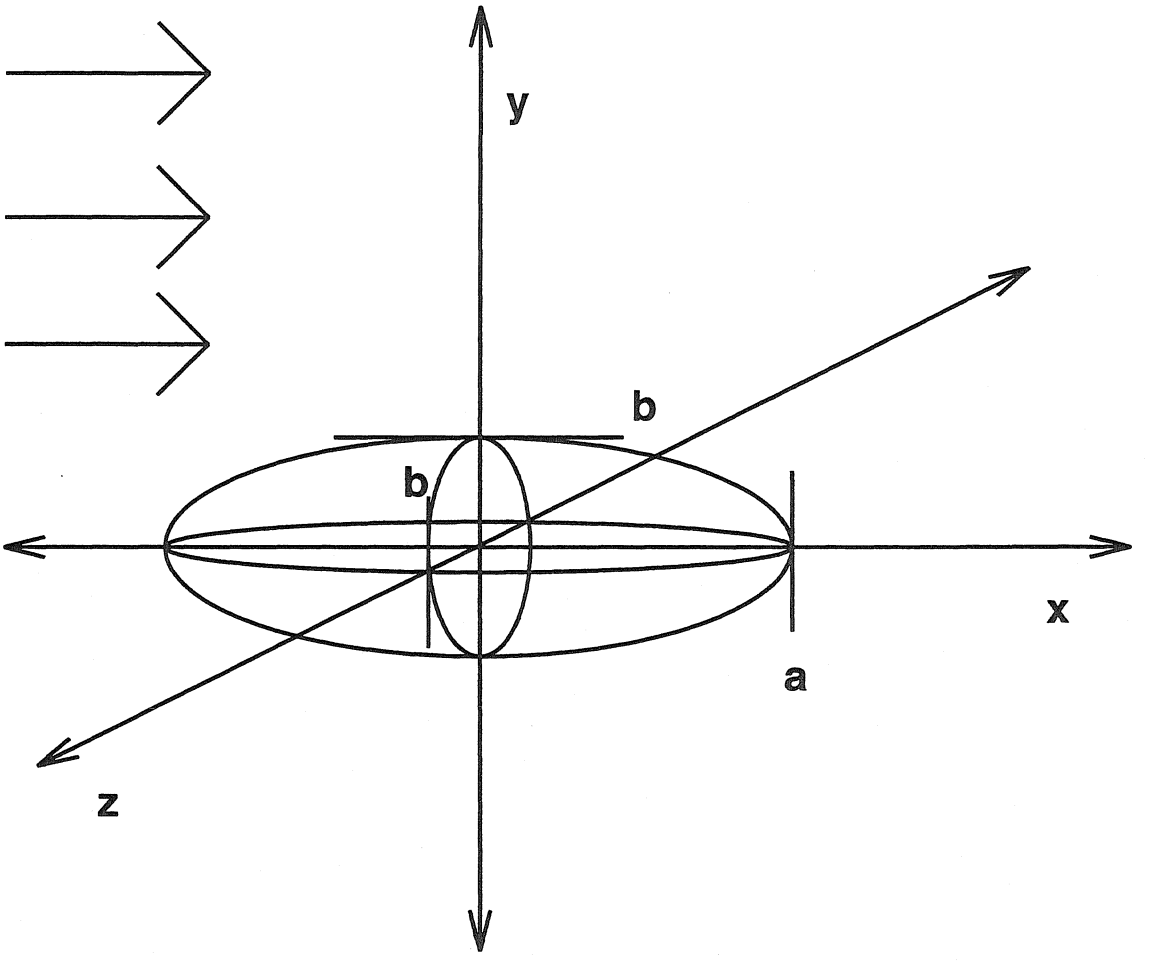

Figure 2.1: Model of flow past an axisymmetric spheroid.

the orthogonal space to which x and σ are mapped. The problem essentially becomes two-dimensional as seen in Figure 2.2. The region D exterior to the curve $r(\theta)$ is to be mapped to the unit square as seen in Figure 2.4.

Since D extends out to infinity, an inversion map is used so that x and σ are first mapped to an auxiliary space whose coordinates are x^* and σ^* as seen in Figure 2.3. That is,

$$x^* = \frac{x}{(x)^2 + (\sigma)^2}, \tag{2.1}$$

$$\sigma^* = \frac{\sigma}{(x)^2 + (\sigma)^2}. \tag{2.2}$$

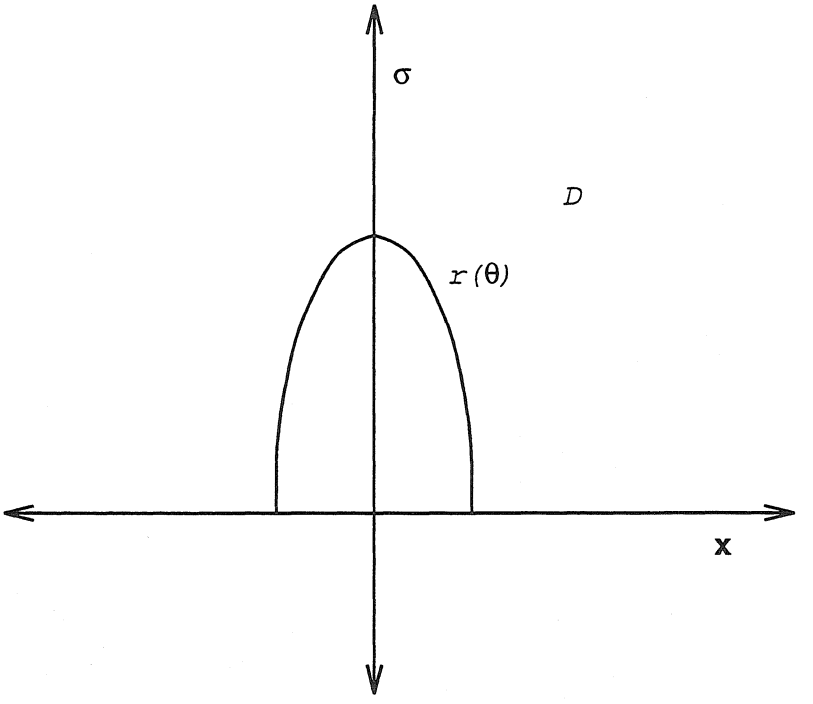

Figure 2.2: Physical space $(x(\xi,\eta), \sigma(\xi,\eta))$.

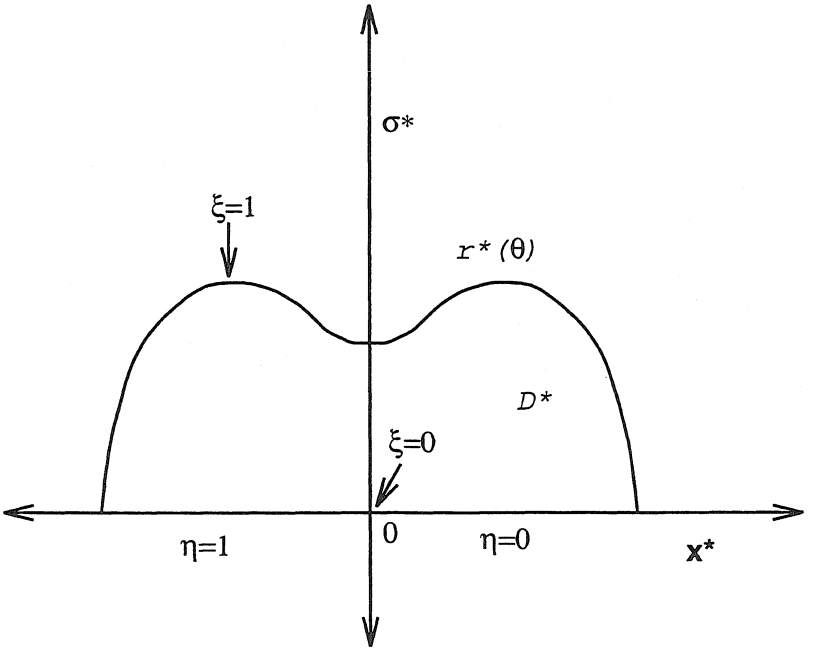

Figure 2.3: Auxiliary space $(x^*(\xi,\eta), \sigma^*(\xi,\eta))$.

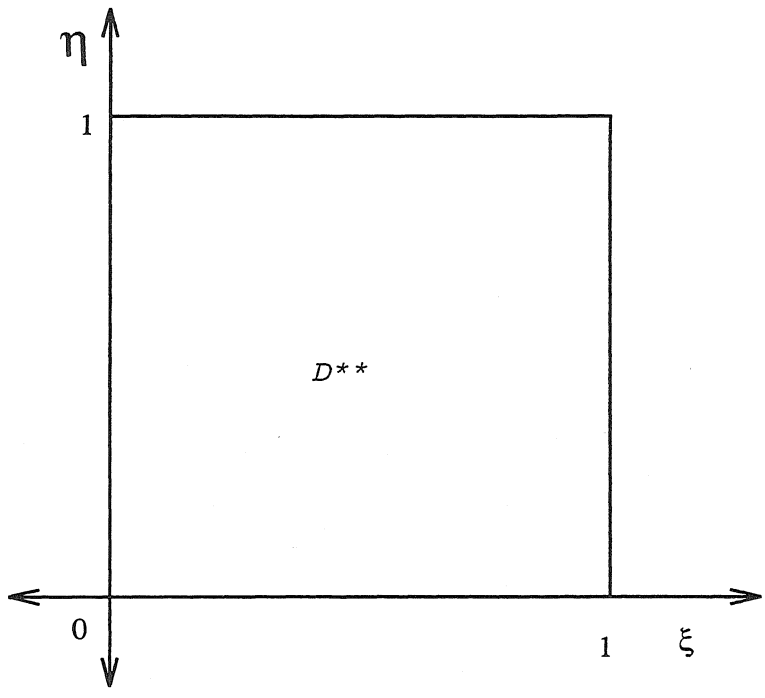

Figure 2.4: Orthogonal, curvilinear space (ξ, η).

Let D^* be the image of D, and $r^*(\theta)$ be the image of $r(\theta)$ under this mapping. It is clear from Figure 2.3 that this mapping changes the problem to finding a mapping from an interior of a curve to a unit square.

The functions x^* and σ^* are orthogonal maps and therefore satisfy the covariant Laplace equations:

$$\begin{aligned} \frac{\partial}{\partial \xi}\left(f(\xi,\eta)\frac{\partial x^*}{\partial \xi}\right)+\frac{\partial}{\partial \eta}\left(\frac{1}{f(\xi,\eta)}\frac{\partial x^*}{\partial \eta}\right) &= 0, \\ \frac{\partial}{\partial \xi}\left(f(\xi,\eta)\frac{\partial \sigma^*}{\partial \xi}\right)+\frac{\partial}{\partial \eta}\left(\frac{1}{f(\xi,\eta)}\frac{\partial \sigma^*}{\partial \eta}\right) &= 0. \end{aligned} \tag{2.3}$$

These equations are derived from curvilinear, orthogonal mapping as discussed by Morse and Feshbach [25]. The existence of these types of mappings is fully discussed by Duraiswami and Prosperetti [10]. The coordinates ξ and η are such that they range from zero to one. The point $(\xi, \eta) = (0, 0)$ corresponds to the origin of the auxiliary space. The curves $\eta = 0$ and $\eta = 1$ correspond to the axis of symmetry,

and the curve $\xi = 1$ corresponds to the curve r^*. The function $f(\xi, \eta)$ is called the distortion function and controls how equally spaced (ξ, η) points are mapped to the auxiliary space. It is defined as $f(\xi, \eta) = \frac{h_\eta^*}{h_\xi^*}$, where

$$\begin{aligned} h_\xi^* &= \sqrt{\left(\frac{\partial x^*}{\partial \xi}\right) + \left(\frac{\partial \sigma^*}{\partial \xi}\right)^2}, \\ h_\eta^* &= \sqrt{\left(\frac{\partial x^*}{\partial \eta}\right) + \left(\frac{\partial \sigma^*}{\partial \eta}\right)^2}. \end{aligned} \tag{2.4}$$

Ryskin and Leal's strong constraint method, where $f(\xi, \eta)$ is prescribed to solve for the numerical grid, is used in this case. Letting $f(\xi, \eta) = \pi\xi$ gives an evenly spaced polar coordinate system. In practice, Ryskin and Leal [34] used

$$\begin{aligned} f(\xi, \eta) &= \pi\xi\left[1 - \alpha\cos(\pi\eta)\right], \\ \alpha &= 0.5 \end{aligned}$$

in their computation of steady flow past deforming bubbles. The grid system associated with this distortion function is such that the mesh is more dense on the right side of the σ-axis. Setting α close to zero results in grids that are more evenly spaced, and setting α close to one results in grids that are more dense to the right of the σ-axis. Figures 2.5 and 2.6 show the grids computed with different values of α.

We next address the boundary conditions. From inspection of the mapping and the symmetry conditions, it is clear that

$$\begin{aligned} x^*(0, \eta) &= 0, \\ \frac{\partial}{\partial \eta} x^*(\xi, 0) &= 0, \\ \frac{\partial}{\partial \eta} x^*(\xi, 1) &= 0, \end{aligned} \tag{2.5}$$

and

$$\frac{\partial}{\partial \xi} x^*(1, \eta) = \frac{\tilde{h}_\xi^*}{h_\eta^*} \frac{\partial}{\partial \eta} \sigma^*(1, \eta). \tag{2.6}$$

Similarly for σ^*,

$$\begin{aligned} \sigma^*(0,\eta) &= 0, \\ \sigma^*(\xi,0) &= 0, \\ \sigma^*(\xi,1) &= 0, \end{aligned} \tag{2.7}$$

and

$$\frac{\partial}{\partial\xi}\sigma^*(1,\eta) = -\frac{\tilde{h}^*_\xi}{h^*_\eta}\frac{\partial}{\partial\eta}x^*(1,\eta). \tag{2.8}$$

The term $\tilde{h}^*_\xi$ has to be determined iteratively so that $\xi = 1$ gets mapped orthogonally to r^*. The boundary conditions (2.6) and (2.8) come from having the orthogonality condition imposed on the mapping $(x^*(\xi,\eta), \sigma^*(\xi,\eta))$, which is

$$\frac{\partial x^*}{\partial\xi}\frac{\partial x^*}{\partial\eta} + \frac{\partial\sigma^*}{\partial\xi}\frac{\partial\sigma^*}{\partial\eta} = 0,$$

and the definition of the scale factors h^*_ξ and h^*_η as defined in (2.4).

2.2.2 Numerical formulation

With the appropriate equations and the boundary conditions, $x^*(\xi,\eta)$ and $\sigma^*(\xi,\eta)$ can be determined numerically. We use the ADI method of Peaceman and Rachford to solve the grid equations (2.3). The ADI method involves adding artificial time to the equations (2.3) and splitting them so that the derivatives in the spatial directions are alternatively treated implicitly at one half-step time and explicitly at the next half-step [30].

Letting $\Delta x = \frac{1}{m+1}$ allows us to set $\xi = i\Delta x$, and $\eta = j\Delta x$ for $i, j = 0, ..., m+1$. The auxiliary coordinates then can be denoted by

$$\begin{aligned} x^*(\xi,\eta) &= x^*(i\Delta x, j\Delta x) = {x^*}_{i,j}, \\ \sigma^*(\xi,\eta) &= \sigma^*(i\Delta x, j\Delta x) = {\sigma^*}_{i,j}. \end{aligned}$$

Applying second order, finite differencing to the covariant Laplace equations and applying the ADI splitting produce

$$\begin{aligned}\frac{x_{i,j}^{*N+\frac{1}{2}}-x_{i,j}^{*N}}{\frac{1}{2}\Delta t} &= f(\xi,\eta)\left(\frac{x_{i+1,j}^{*N+\frac{1}{2}}-2x_{i,j}^{*N+\frac{1}{2}}+x_{i-1,j}^{*N+\frac{1}{2}}}{\Delta x^2}\right) \\ &+\frac{1}{f(\xi,\eta)}\left(\frac{x_{i,j+1}^{*N}-2x_{i,j}^{*N}+x_{i,j-1}^{*N}}{\Delta x^2}\right) \\ &+\frac{\partial}{\partial\xi}f(\xi,\eta)\left(\frac{x_{i+1,j}^{*N+\frac{1}{2}}-x_{i-1,j}^{*N+\frac{1}{2}}}{2\Delta x}\right) \\ &+\frac{-1}{[f(\xi,\eta)]^2}\frac{\partial}{\partial\eta}f(\xi,\eta)\left(\frac{x_{i,j+1}^{*N}-x_{i,j-1}^{*N}}{2\Delta x}\right),\end{aligned} \tag{2.9}$$

and

$$\begin{aligned}\frac{x_{i,j}^{*N+1}-x_{i,j}^{*N+\frac{1}{2}}}{\frac{1}{2}\Delta t} &= f(\xi,\eta)\left(\frac{x_{i+1,j}^{*N+\frac{1}{2}}-2x_{i,j}^{*N+\frac{1}{2}}+x_{i-1,j}^{*N+\frac{1}{2}}}{\Delta x^2}\right) \\ &+\frac{1}{f(\xi,\eta)}\left(\frac{x_{i,j+1}^{*N+1}-2x_{i,j}^{*N+1}+x_{i,j-1}^{*N+1}}{\Delta x^2}\right) \\ &+\frac{\partial}{\partial\xi}f(\xi,\eta)\left(\frac{x_{i+1,j}^{*N+\frac{1}{2}}-x_{i-1,j}^{*N+\frac{1}{2}}}{2\Delta x}\right) \\ &+\frac{-1}{[f(\xi,\eta)]^2}\frac{\partial}{\partial\eta}f(\xi,\eta)\left(\frac{x_{i,j+1}^{*N+1}-x_{i,j-1}^{*N+1}}{2\Delta x}\right).\end{aligned} \tag{2.10}$$

The equations for σ^* can be found by replacing x^* in the above equations (2.9) and (2.10) with σ^*. Δt is some small parameter that can be used to control convergence, and N is the iteration index denoting the artificial time used in the ADI method. The derivatives of the distortion $f(\xi,\eta)$ are easily calculated from differentiating $f(\xi,\eta)=\pi\xi\left[1-\alpha\cos\left(\pi\eta\right)\right]$ analytically.

The boundary conditions (2.5) and (2.7) are rewritten in discretized notation to give

$$x_{0,j}^{*} = 0, \tag{2.11}$$

$$\begin{aligned}
\sigma^*_{0,j} &= 0, \\
x^*_{i,-1} &= x^*_{i,1}, \\
x^*_{i,m+2} &= x^*_{i,m}, \\
\sigma^*_{i,0} &= 0, \\
\sigma^*_{i,m+1} &= 0.
\end{aligned}$$

These are to be satisfied at time levels $N+\frac{1}{2}$ and $N+1$.

Now, at $i = m+1$ where $\xi = 1$ the boundary conditions (2.6) and (2.8) are discretized to give

$$\begin{aligned}
x^{*N+\frac{1}{2}}_{m+2,j} - x^{*N+\frac{1}{2}}_{m,j} &= \left(\frac{\tilde{h}^{*N+\frac{1}{2}}_{\xi}}{h^{*N}_{\eta}}\right)\left(\sigma^{*N}_{m+1,j+1} - \sigma^{*N}_{m+1,j-1}\right), \qquad (2.12) \\
\sigma^{*N+\frac{1}{2}}_{m+2,j} - \sigma^{*N+\frac{1}{2}}_{m,j} &= -\left(\frac{\tilde{h}^{*N+\frac{1}{2}}_{\xi}}{h^{*N}_{\eta}}\right)\left(x^{*N}_{m+1,j+1} - x^{*N}_{m+1,j-1}\right).
\end{aligned}$$

Here is the summary of the steps involved in solving the above discretized equations using the ADI method.

1. At time N, $x^{*N}_{i,j}$ and $\sigma^{*N}_{i,j}$ are known. The radial boundary shape at time N is then

   $$r^{*N}_j(\theta^N_j) = \sqrt{\left(x^{*N}_{m+1,j}\right)^2 + \left(\sigma^{*N}_{m+1,j}\right)^2}$$

   where

   $$\theta^N_j = \tan^{-1}\left(\frac{\sigma^{*N}_{m+1,j}}{x^{*N}_{m+1,j}}\right).$$

   Now, $r^*_j \equiv r^*(\theta^N_j)$ is the desired physical shape at θ^N_j. In the case of an ellipse of aspect ratio $\lambda = a/b$,

   $$r^*_j = \frac{\sqrt{b^2\cos^2\theta^N_j + a^2\sin^2\theta^N_j}}{ab}.$$

   The term $\tilde{h}^{*N+\frac{1}{2}}_{\xi}$ has to be modified so that r^{*N}_j gets closer to r^*_j. So, the normal

scale factor at $\xi = 1$ is, in a sense, stretched or shrunk by letting

$$\tilde{h}_{\xi}^{*N+\frac{1}{2}} = \tilde{h}_{\xi}^{*N} + \beta\left(r_j^* - r^{*N}\left(\theta_j^N\right)\right).$$

β is a small parameter that can be used to control convergence, and its typical value is 0.01. This completes the boundary conditions (2.12), and they can be placed in equations (2.9) at $i = m + 1$.

2. First, the discretized equation (2.9) is rearranged to give

$$\begin{aligned} & C_{i,j}^0 x_{i-1,j}^{*N+\frac{1}{2}} + C_{i,j}^1 x_{i,j}^{*N+\frac{1}{2}} + C_{i,j}^2 x_{i+1,j}^{*N+\frac{1}{2}} \\ = & -\left(C_{i,j}^3 x_{i,j-1}^{*N} + C_{i,j}^4 x_{i,j}^{*N} + C_{i,j}^5 x_{i,j+1}^{*N}\right), \end{aligned} \tag{2.13}$$

and

$$\begin{aligned} & C_{i,j}^0 \sigma_{i-1,j}^{*N+\frac{1}{2}} + C_{i,j}^1 \sigma_{i,j}^{*N+\frac{1}{2}} + C_{i,j}^2 \sigma_{i+1,j}^{*N+\frac{1}{2}} \\ = & -\left(C_{i,j}^3 \sigma_{i,j-1}^{*N} + C_{i,j}^4 \sigma_{i,j}^{*N} + C_{i,j}^5 \sigma_{i,j+1}^{*N}\right) \end{aligned}$$

where

$$\begin{aligned} C_{i,j}^0 &= -\frac{f}{(\Delta x)^2} + \frac{1}{2\Delta x}\frac{\partial f}{\partial \xi}, \\ C_{i,j}^1 &= \frac{2}{\Delta t} + \frac{2f}{(\Delta x)^2}, \\ C_{i,j}^2 &= -\frac{f}{(\Delta x)^2} - \frac{1}{2\Delta x}\frac{\partial f}{\partial \xi}, \\ C_{i,j}^3 &= -\frac{1}{(\Delta x)^2 f} - \frac{1}{2\Delta x f^2}\frac{\partial f}{\partial \eta}, \\ C_{i,j}^4 &= -\frac{2}{\Delta t} + \frac{2}{(\Delta x)^2 f}, \\ C_{i,j}^5 &= -\frac{1}{(\Delta x)^2 f} + \frac{1}{2\Delta x f^2}\frac{\partial f}{\partial \eta}. \end{aligned}$$

The equations (2.13) for $i = 1, ..., m + 1$ are then rearranged as a vector, and

the boundary conditions (2.11) and (2.12) are applied to get

$$\mathbf{M}_{\frac{1}{2}}\mathbf{s}_{\frac{1}{2}} = \mathbf{v}_{\frac{1}{2}}$$

where

$$\mathbf{M}_{\frac{1}{2}} = \begin{bmatrix} C^1_{1,j} & C^2_{1,j} & 0 & 0 & 0 & 0 & 0 \\ C^0_{2,j} & C^1_{2,j} & C^2_{2,j} & 0 & 0 & 0 & 0 \\ 0 & . & . & . & 0 & 0 & 0 \\ 0 & 0 & C^0_{i,j} & C^1_{i,j} & C^2_{i,j} & 0 & 0 \\ 0 & 0 & 0 & . & . & . & 0 \\ 0 & 0 & 0 & 0 & C^0_{m,j} & C^1_{m,j} & C^2_{m,j} \\ 0 & 0 & 0 & 0 & 0 & C^0_{m+1,j} + C^2_{m+1,j} & C^1_{m+1,j} \end{bmatrix},$$

$$\mathbf{s}_{\frac{1}{2}} = \begin{bmatrix} x^{*N+\frac{1}{2}}_{1,j} \\ : \\ x^{*N+\frac{1}{2}}_{i-1,j} \\ x^{*N+\frac{1}{2}}_{i,j} \\ x^{*N+\frac{1}{2}}_{i+1,j} \\ : \\ x^{*N+\frac{1}{2}}_{m+1,j} \end{bmatrix},$$

$$\mathbf{v}_{\frac{1}{2}} = \begin{bmatrix} -\left(C^4_{1,j}x^{*N}_{1,j} + C^5_{1,j}x^{*N}_{1,j+1}\right) \\ -\left(C^3_{2,j}x^{*N}_{2,j-1} + C^4_{2,j}x^{*N}_{2,j} + C^5_{2,j}x^{*N}_{2,j+1}\right) \\ . \\ . \\ -\left(C^3_{i,j}x^{*N}_{i,j-1} + C^4_{i,j}x^{*N}_{i,j} + C^5_{i,j}x^{*N}_{i+1,j+1}\right) \\ . \\ . \\ -\left(C^3_{m+1,j}x^{*N}_{m+1,j-1} + C^4_{m+1,j}x^{*N}_{m+1,j} - C^5_{m+1,j}x^{*N}_{i+1,j+1}\right) \\ -\left(\frac{\tilde{h}^{*N+\frac{1}{2}}_{\xi}}{h^{*N}_{\eta}}\right) C^2_{m+1,j}\left(\sigma^{*N}_{m+1,j+1} - \sigma^{*N}_{m+1,j-1}\right) \end{bmatrix}.$$

A similar linear system is solved for $\sigma^{*N+\frac{1}{2}}$ as well. Since the linear systems involve tridiagonal matrices, they can be solved easily using a standard tridiagonal LU solver.

3. Now that x^* and σ^* at time $N+\frac{1}{2}$ are known, they can be used to solve the equation (2.10) which is rearranged to get

$$\begin{aligned} & C^3_{i,j}x^{*N+1}_{i,j-1} + \left(C^4_{i,j} + \frac{4}{\Delta t}\right)x^{*N+1}_{i,j} + C^5_{i,j}x^{*N+1}_{i,j+1} \\ = & -\left(C^0_{i,j}x^{*N+\frac{1}{2}}_{i-1,j} + \left(C^1_{i,j} - \frac{4}{\Delta t}\right)x^{*N+\frac{1}{2}}_{i,j} + C^2_{i,j}x^{*N+\frac{1}{2}}_{i+1,j}\right) \end{aligned} \tag{2.14}$$

and

$$\begin{aligned} & C^3_{i,j}\sigma^{*N+1}_{i,j-1} + \left(C^4_{i,j} + \frac{4}{\Delta t}\right)\sigma^{*N+1}_{i,j} + C^5_{i,j}\sigma^{*N+1}_{i,j+1} \\ = & -\left(C^0_{i,j}\sigma^{*N+\frac{1}{2}}_{i-1,j} + \left(C^1_{i,j} - \frac{4}{\Delta t}\right)\sigma^{*N+\frac{1}{2}}_{i,j} + C^2_{i,j}\sigma^{*N+\frac{1}{2}}_{i+1,j}\right) . \end{aligned}$$

The equations (2.14) for $j = 0, ..., m+1$ are then rearranged as a vector, and the appropriate boundary conditions at $j = 0$ and $j = m+1$ are applied to get a linear system

$$\mathbf{M_1 s_1} = \mathbf{v_1}$$

where

$$\mathbf{M_1} = \begin{bmatrix} C^4_{i,0} + \frac{4}{\Delta t} & C^5_{i,0} + C^3_{i,0} & 0 & 0 & 0 & 0 \\ . & . & . & 0 & 0 & 0 \\ 0 & C^3_{i,j} & C^4_{i,j} + \frac{4}{\Delta t} & C^5_{i,j} & 0 & 0 \\ 0 & 0 & . & . & . & 0 \\ 0 & 0 & 0 & C^3_{i,m} & C^4_{i,m} + \frac{4}{\Delta t} & C^5_{i,m} \\ 0 & 0 & 0 & 0 & C^3_{i,m+1} + C^5_{i,m+1} & C^4_{i,m+1} + \frac{4}{\Delta t} \end{bmatrix},$$

$$\mathbf{s}_1 = \begin{bmatrix} x_{i,0}^{*N+1} \\ . \\ x_{i,j-1}^{*N+1} \\ x_{i,j}^{*N+1} \\ x_{i,j+1}^{*N+1} \\ . \\ x_{i,m+1}^{*N+1} \end{bmatrix},$$

$$\mathbf{v}_1 = \begin{bmatrix} -\left(C_{i,0}^0 x_{i-1,0}^{*N+\frac{1}{2}} + \left(C_{i,0}^1 - \frac{4}{\Delta t}\right) x_{i,0}^{*N+\frac{1}{2}} + C_{i,0}^2 x_{i+1,0}^{*N+\frac{1}{2}}\right) \\ -\left(C_{i,1}^0 x_{i-1,1}^{*N+\frac{1}{2}} + \left(C_{i,1}^1 - \frac{4}{\Delta t}\right) x_{i,1}^{*N+\frac{1}{2}} + C_{i,1}^2 x_{i+1,1}^{*N+\frac{1}{2}} \right) \\ . \\ . \\ -\left(C_{i,j}^0 x_{i-1,j}^{*N+\frac{1}{2}} + \left(C_{i,j}^1 - \frac{4}{\Delta t}\right) x_{i,j}^{*N+\frac{1}{2}} + C_{i,j}^2 x_{i+1,j}^{*N+\frac{1}{2}}\right) \\ . \\ . \\ -\left(C_{i,m+1}^0 x_{i-1,m+1}^{*N+\frac{1}{2}} + \left(C_{i,m+1}^1 - \frac{4}{\Delta t}\right) x_{i,m+1}^{*N+\frac{1}{2}} + C_{i,m+1}^2 x_{i+1,m+1}^{*N+\frac{1}{2}}\right) \end{bmatrix}.$$

Again, a similar linear system of equations for σ^{*N+1} is generated. These are solved using a standard tridiagonal LU solver.

4. Steps 1), 2), and 3) are repeated until $\max_{j=0..m+1} \left(r_j^* - r^{*N}\left(\theta^N\right)\right) < 10^{-6}$.

In practice, it takes about 4000 ADI iterations to achieve a reasonable 80x80 grid. The functions x^* and σ^* are then inverted to get the physical grid $(x(\xi,\eta), \sigma(\xi,\eta))$.

2.2.3 Numerical grids generated

Shown below are some of the grids that are generated using the Ryskin and Leal grid generation method in the case of a sphere, where $r(\theta) = 1$. Different types of distortion functions are used here to determine their influence on grid density. Figures 2.5 a), b) and Figures 2.6 a), b) show the numerical grids fitted around a sphere of radius one generated using different distortion functions.

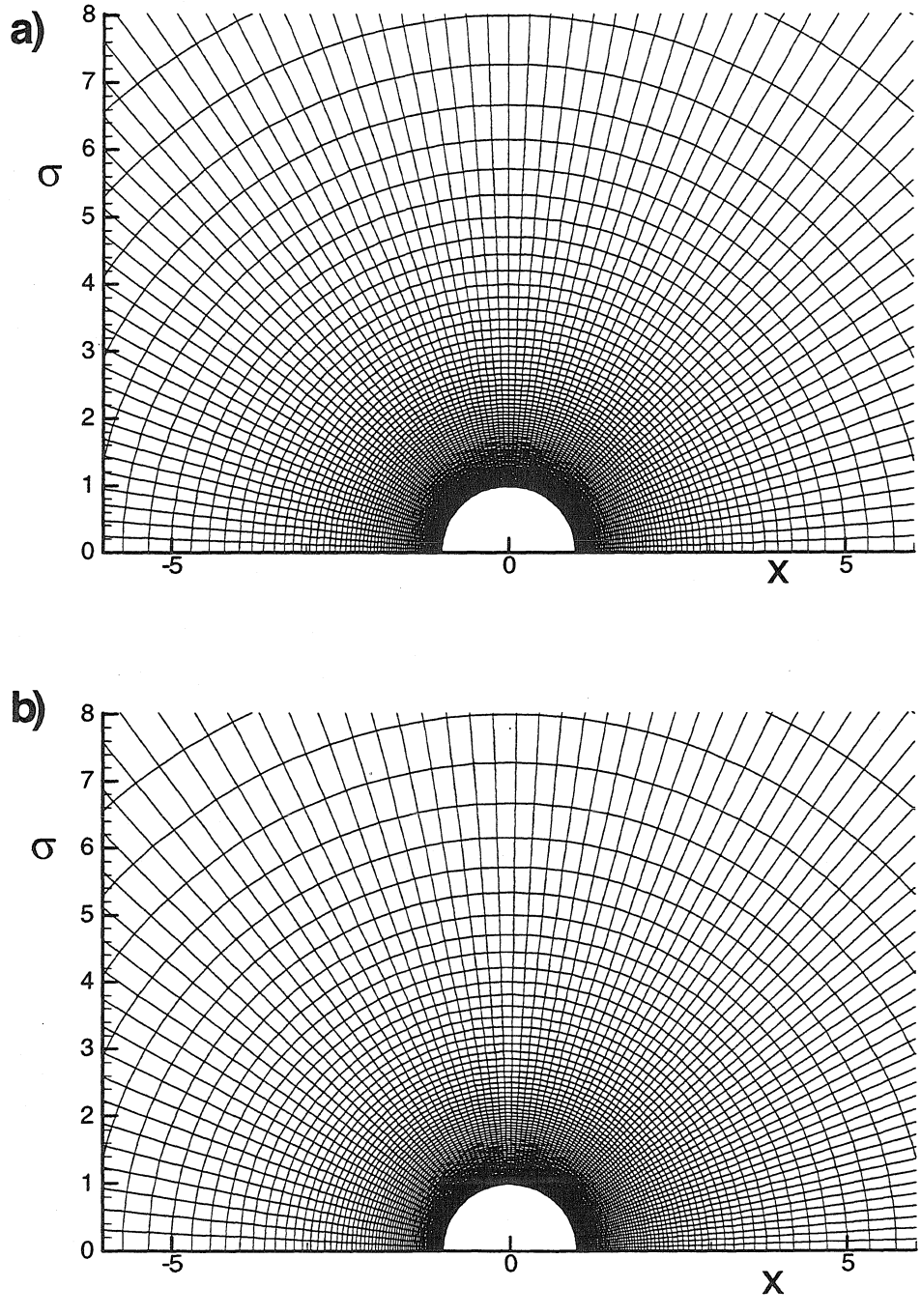

Figure 2.5: a)$f = \pi\xi$, b)$f = \pi\xi\,[1 - 0.3\cos(\pi\eta)]$.

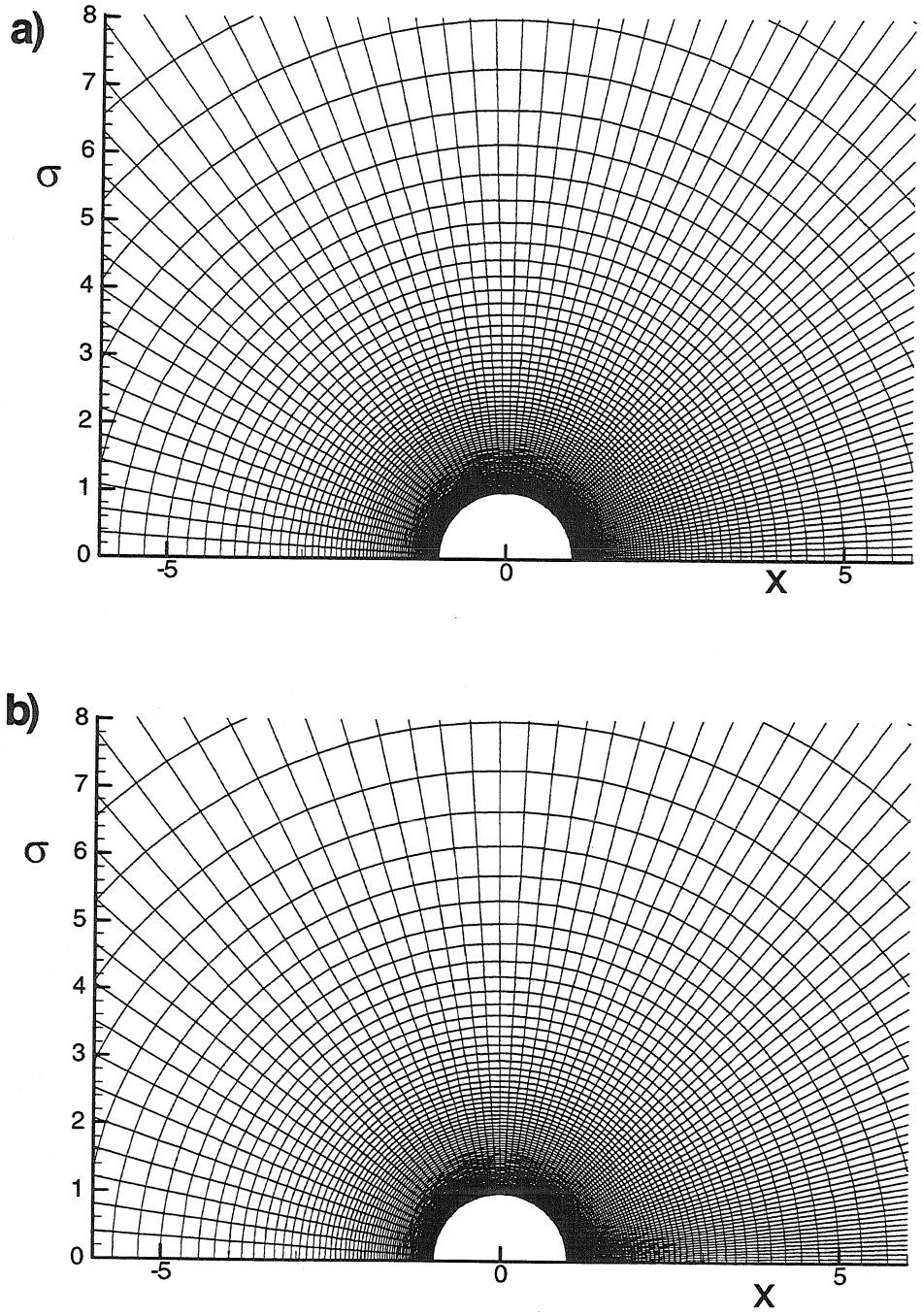

Figure 2.6: a) $f = \pi\xi\,[1 - 0.5\cos(\pi\eta)]$, b) $f = \pi\xi\,[1 - 0.7\cos(\pi\eta)]$.

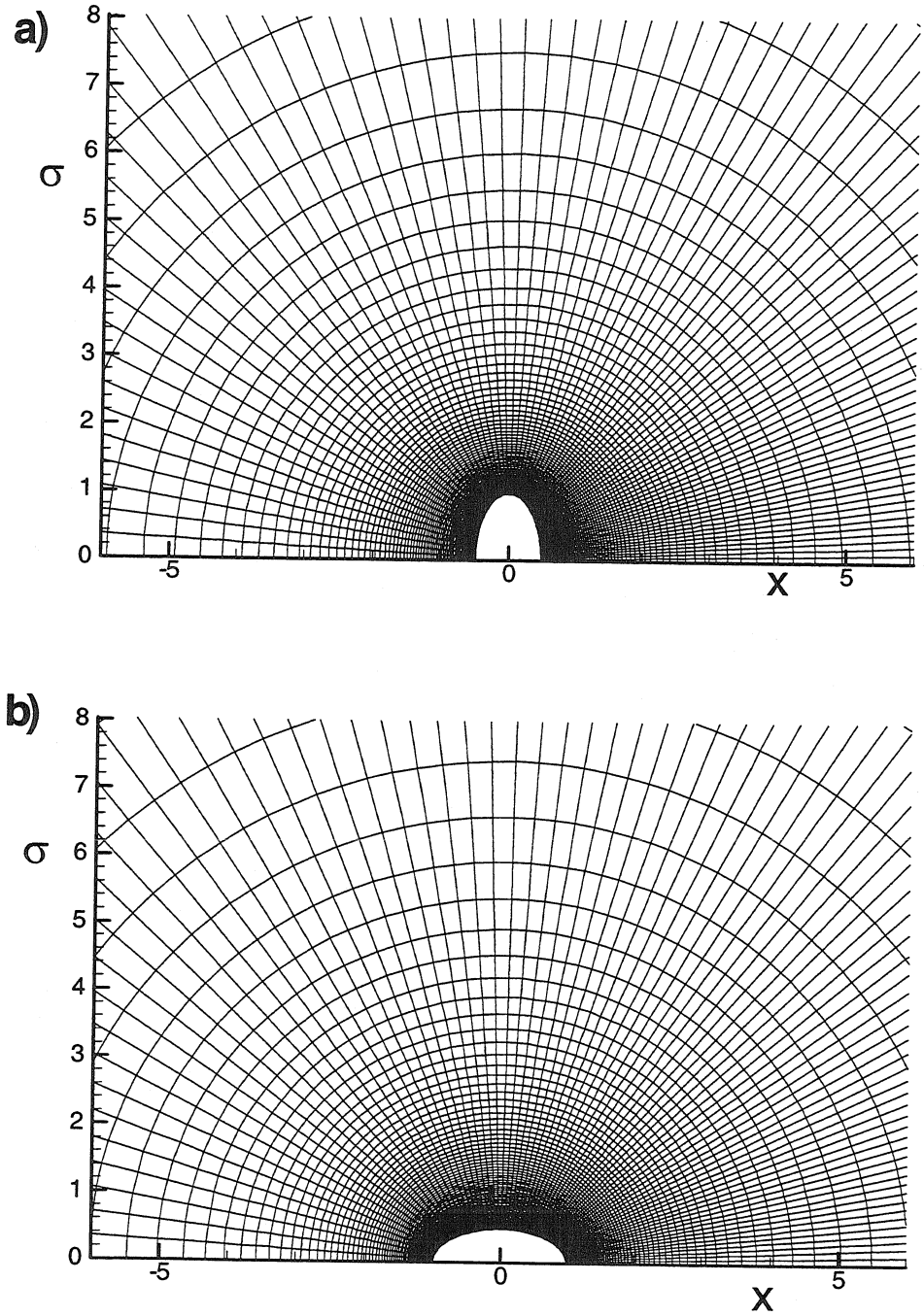

Figure 2.7: a) $f = \pi\xi\left[1 - 0.5\cos\left(\pi\eta\right)\right]$, $a = 0.5, b = 1$; b)$f = \pi\xi\left[1 - 0.5\cos\left(\pi\eta\right)\right]$, $a = 1, b = 0.5$.

It is clear from the figures that using different values for the distortion coefficient α of $f = \pi\xi\,[1 - \alpha\cos(\pi\eta)]$ shifts mesh points to the right of the body. This is important in that when the fluid equations are solved, the wake that can occur on the back of the body needs to be well resolved. In each case, the number of points used to generate the grids is 80x80.

Figures 2.7 a) and b) are generated with the distortion function set to $f = \pi\xi\,[1 - 0.5\cos(\pi\eta)]$. They show grids that fit around an ellipse with aspect ratio denoted by $\lambda = a/b$. Given a and b, the boundary shape $r(\theta)$ can be determined by

$$r(\theta) = \frac{ab}{\sqrt{b^2\cos^2\theta + a^2\sin^2\theta}}.$$

Figure 2.7 a) shows a grid fitted around an oblate spheroid, and Figure 2.7 b) shows a grid fitted around a prolate spheroid. Again, the number of points used to generate the grids is 80x80.

2.3 Steady Flow Past Spheroids

2.3.1 Flow equations in axisymmetric form

Given an orthogonal, boundary-fitted, curvilinear, numerical grid system around an ellipse, the Navier-Stokes equations can now be solved numerically to study viscous flows past spheroids of various aspect ratios at various Reynolds numbers. The Navier-Stokes equations in a nondimensionalized form are

$$\begin{aligned} \mathbf{u}_t + (\mathbf{u}\cdot\nabla)\mathbf{u} &= -\frac{1}{2}\nabla p + \frac{2}{R_d}\nabla^2\mathbf{u}, \\ \nabla\cdot\mathbf{u} &= 0. \end{aligned} \tag{2.15}$$

$\mathbf{u} = \hat{\boldsymbol{\xi}}u_\xi + \hat{\boldsymbol{\eta}}u_\eta + \hat{\boldsymbol{\phi}}u_\phi$ is the velocity vector, and p is the pressure. Here, d is the characteristic length of the body, and U is velocity of outer flow in the x -axis direction.

R_d is the Reynolds number defined by

$$R_d = \frac{2\rho dU}{\mu}.$$

The base flow which is axisymmetric and steady around the body needs to be calculated. To do this, the Navier-Stokes equations need to be written in the curvilinear (ξ, η, ϕ) space. Such equations can be found in several books including those by Morse and Feshbach [25] and by Batchelor [2]. Since the flow is axisymmetric and steady, $u_\phi = 0$. Furthermore, in curvilinear coordinates, the two remaining velocity components are

$$\begin{aligned} u_\xi &= -\frac{1}{\sigma h_\eta}\frac{\partial \psi}{\partial \eta}, \\ u_\eta &= \frac{1}{\sigma h_\xi}\frac{\partial \psi}{\partial \xi}, \end{aligned} \tag{2.16}$$

as determined by the divergence free condition. The vorticity is defined by setting

$$\omega = \frac{-1}{h_\xi h_\eta}\left[\frac{\partial}{\partial \xi}(h_\eta u_\eta) - \frac{\partial}{\partial \eta}(h_\xi u_\xi)\right].$$

This gives the Navier-Stokes equations in axisymmetric, steady, stream function-vorticity form:

$$\begin{aligned} &\frac{1}{h_\xi h_\eta}\left[\frac{\partial \psi}{\partial \xi}\frac{\partial}{\partial \eta}\left(\frac{\omega}{\sigma}\right) - \frac{\partial \psi}{\partial \eta}\frac{\partial}{\partial \xi}\left(\frac{\omega}{\sigma}\right)\right] \\ &-\frac{2}{R_d}\frac{1}{h_\xi h_\eta}\left\{\frac{\partial}{\partial \xi}\left[\frac{h_\eta}{h_\xi \sigma}\frac{\partial}{\partial \xi}(\omega\sigma)\right] + \frac{\partial}{\partial \eta}\left[\frac{h_\xi}{h_\eta \sigma}\frac{\partial}{\partial \eta}(\omega\sigma)\right]\right\} = 0, \end{aligned} \tag{2.17}$$

$$\frac{-1}{h_\xi h_\eta}\left[\frac{\partial}{\partial \xi}\left(\frac{h_\eta}{h_\xi \sigma}\frac{\partial \psi}{\partial \xi}\right) + \frac{\partial}{\partial \eta}\left(\frac{h_\xi}{h_\eta \sigma}\frac{\partial \psi}{\partial \eta}\right)\right] = \omega. \tag{2.18}$$

To solve the above equations, we need the proper boundary conditions for $\psi(\xi, \eta)$ and $\omega(\xi, \eta)$ along $\xi = 0, 1$ and $\eta = 0, 1$. Since we have a solid rigid body, both u_ξ

and u_η on the body are zero. So,

$$\psi(1,\eta) = 0,$$

and

$$\frac{\partial}{\partial \xi}\psi(1,\eta) = 0.$$

As $\xi \to 0$, the flow becomes further away from the body. The stream function can, therefore, be approximated by a free stream flow:

$$\psi = \tilde{\psi} + \frac{1}{2}\sigma^2(1-\xi^3). \tag{2.19}$$

This allows $\tilde{\psi}$ to have a homogeneous boundary condition for all sides of our curvilinear grid. This also sets

$$\omega(0,\eta) = 0.$$

By examining Oseen type solutions as discussed in Ryskin and Leal [34], it is clear that $\tilde{\psi}$ is bounded at infinity, and $\xi = 0$ is a regular singular point of equations (2.17) and (2.18).

The boundary conditions imposed on $\tilde{\psi}(\xi,\eta)$ and $\omega(\xi,\eta)$ by enforcing the flow to be axisymmetric along $\eta = 0$ and 1 are

$$\begin{aligned}
\tilde{\psi}(\xi,0) &= 0,\\
\tilde{\psi}(\xi,1) &= 0,\\
\omega(\xi,0) &= 0,\\
\omega(\xi,1) &= 0.
\end{aligned}$$

Rewriting the no-slip condition in terms of $\tilde{\psi}$ gives

$$\frac{\partial}{\partial \xi}\tilde{\psi}(1,\eta) - \frac{3}{2}\sigma^2 = 0 \tag{2.20}$$

2.3.2 Numerical formulation

The flow equations (2.17) and (2.18) must be solved numerically, and the formulation suggested by Dandy and Leal [8] is used. They used second-order finite differencing to discretize the flow equations, rearranged them as a vector of difference equations, and solved them using Newton's method. Newton's method requires the computation of an LU decomposition of a large sparse matrix. In our case, it is used to solve for fluid flow past a body of a fixed shape.

Rewriting the equations (2.17) and (2.18) in a more manageable form gives

$$q_{\omega 1}\frac{\partial^2\omega}{\partial\xi^2} + q_{\omega 2}\frac{\partial^2\omega}{\partial\eta^2} + q_{\omega 3}\frac{\partial\omega}{\partial\xi} + q_{\omega 4}\frac{\partial\omega}{\partial\eta} + q_{\omega 5}\omega = 0 \tag{2.21}$$

where

$$\begin{aligned}
q_{\omega 1} &= -\frac{2}{R_d}\frac{1}{h_\xi^2}, \\
q_{\omega 2} &= -\frac{2}{R_d}\frac{1}{h_\eta^2}, \\
q_{\omega 3} &= \frac{2}{R_d}\left(\frac{1}{h_\xi^3}\frac{\partial h_\xi}{\partial\xi} - \frac{1}{\sigma h_\xi^2}\frac{\partial\sigma}{\partial\xi} - \frac{1}{h_\xi^2 h_\eta}\frac{\partial h_\eta}{\partial\xi}\right) + \frac{\partial\sigma}{\partial\eta}\left(\frac{\xi^3}{h_\eta h_\xi} - \frac{1}{h_\eta h_\xi}\right) - \frac{1}{h_\eta h_\xi\sigma}\frac{\partial\tilde{\psi}}{\partial\eta} \\
q_{\omega 4} &= \frac{2}{R_d}\left(\frac{-1}{h_\xi h_\eta^2}\frac{\partial h_\xi}{\partial\eta} - \frac{1}{\sigma h_\eta^2}\frac{\partial\sigma}{\partial\eta} + \frac{1}{h_\eta^3}\frac{\partial h_\eta}{\partial\eta}\right) \\
&\quad + \frac{\partial\sigma}{\partial\xi}\left(\frac{1}{h_\eta h_\xi} - \frac{\xi^3}{h_\eta h_\xi}\right) - \frac{3}{2}\frac{\sigma\xi^2}{h_\xi h_\eta} + \frac{1}{h_\eta h_\xi\sigma}\frac{\partial\tilde{\psi}}{\partial\xi}, \\
q_{\omega 5} &= \frac{2}{R_d}\left[\left(\frac{\partial\sigma}{\partial\xi}\frac{1}{h_\xi\sigma}\right)^2 + \frac{\partial\sigma}{\partial\xi}\left(-\frac{1}{h_\eta h_\xi^2\sigma}\frac{\partial h_\eta}{\partial\xi} + \frac{1}{h_\xi^3\sigma}\frac{\partial h_\xi}{\partial\xi}\right) + \left(\frac{\partial\sigma}{\partial\eta}\frac{1}{h_\eta\sigma}\right)^2\right] \\
&\quad + \frac{2}{R_d}\left[\frac{\partial\sigma}{\partial\eta}\left(\frac{1}{h_\eta^3\sigma}\frac{\partial h_\eta}{\partial\eta} - \frac{1}{h_\xi h_\eta^2\sigma}\frac{\partial h_\xi}{\partial\eta}\right) - \frac{\partial^2\sigma}{\partial\eta^2}\frac{1}{h_\eta^2\sigma} - \frac{\partial^2\sigma}{\partial\xi^2}\frac{1}{h_\xi^2\sigma}\right] + \frac{3}{2}\frac{\xi^2}{h_\xi h_\eta}\frac{\partial\sigma}{\partial\eta} \\
&\quad + \frac{1}{h_\eta h_\xi\sigma^2}\frac{\partial\sigma}{\partial\xi}\frac{\partial\tilde{\psi}}{\partial\eta} - \frac{1}{h_\eta h_\xi\sigma^2}\frac{\partial\sigma}{\partial\eta}\frac{\partial\tilde{\psi}}{\partial\xi};
\end{aligned}$$

and

$$q_{\psi 1}\frac{\partial^2\tilde{\psi}}{\partial\xi^2} + q_{\psi 2}\frac{\partial^2\tilde{\psi}}{\partial\eta^2} + q_{\psi 3}\frac{\partial\tilde{\psi}}{\partial\xi} + q_{\psi 4}\frac{\partial\tilde{\psi}}{\partial\eta} + \omega + q_{\psi 5} = 0 \tag{2.22}$$

where

$$\begin{aligned}
q_{\psi 1} &= \frac{1}{h_\xi^2 \sigma}, \\
q_{\psi 2} &= \frac{1}{h_\eta^2 \sigma}, \\
q_{\psi 3} &= -\frac{1}{h_\xi^3 \sigma}\frac{\partial h_\xi}{\partial \xi} + \frac{1}{\sigma h_\xi^2 h_\eta}\frac{\partial h_\eta}{\partial \xi} - \frac{1}{h_\xi^2 \sigma^2}\frac{\partial \sigma}{\partial \xi}, \\
q_{\psi 4} &= \frac{1}{h_\xi h_\eta^2 \sigma}\frac{\partial h_\xi}{\partial \eta} - \frac{1}{\sigma h_\eta^3}\frac{\partial h_\eta}{\partial \eta} - \frac{1}{h_\eta^2 \sigma^2}\frac{\partial \sigma}{\partial \eta}, \\
q_{\psi 5} &= \frac{3}{2}\frac{\sigma \xi^2}{h_\xi^3}\frac{\partial h_\xi}{\partial \xi} - \frac{9}{2}\frac{\xi^2}{h_\xi^2}\frac{\partial \sigma}{\partial \xi} - \frac{3}{2}\frac{\sigma \xi^2}{h_\xi^2 h_\eta}\frac{\partial h_\eta}{\partial \xi} - \frac{3\sigma \xi}{h_\xi^2}.
\end{aligned}$$

Let $\Delta x = \frac{1}{m+1}$ to get $\xi = i\Delta x, \eta = j\Delta x$ for $i, j = 0, ..., m+1$. This allows us to set

$$\omega(\xi, \eta) = \omega(i\Delta x, j\Delta x) = \omega_{i,j}$$

and

$$\tilde{\psi}(\xi, \eta) = \tilde{\psi}(i\Delta x, j\Delta x) = \tilde{\psi}_{i,j}.$$

Using second-order finite differencing to approximate equations (2.21) and (2.22) gives

$$H_{0_{i,j}} = A^0_{i,j}\omega_{i-1,j} + A^1_{i,j}\omega_{i,j-1} + A^2_{i,j}\omega_{i,j} + A^3_{i,j}\omega_{i,j+1} + A^4_{i,j}\omega_{i+1,j}$$

where

$$\begin{aligned}
A^0_{i,j} &= \frac{-1}{2}\frac{q_{\omega 3}}{\Delta x} + \frac{q_{\omega 1}}{(\Delta x)^2}, \\
A^1_{i,j} &= \frac{q_{\omega 2}}{(\Delta x)^2} - \frac{1}{2}\frac{q_{\omega 4}}{\Delta x}, \\
A^2_{i,j} &= -2\frac{q_{\omega 2}}{(\Delta x)^2} - 2\frac{q_{\omega 1}}{(\Delta x)^2} + q_{\omega 5}, \\
A^3_{i,j} &= \frac{q_{\omega 2}}{(\Delta x)^2} + \frac{1}{2}\frac{q_{\omega 4}}{\Delta x}, \\
A^4_{i,j} &= \frac{1}{2}\frac{q_{\omega 3}}{\Delta x} + \frac{q_{\omega 1}}{(\Delta x)^2};
\end{aligned}$$

and

$$H_{1_{i,j}} = B^0_{i,j}\tilde{\psi}_{i-1,j} + B^1_{i,j}\tilde{\psi}_{i,j-1} + B^2_{i,j}\tilde{\psi}_{i,j} + B^3_{i,j}\tilde{\psi}_{i,j+1} + B^4_{i,j}\tilde{\psi}_{i+1,j} + B^5_{i,j}\omega_{i,j} + B^6_{i,j},$$

where

$$\begin{aligned}
B^0_{i,j} &= \frac{-1}{2}\frac{q_{\psi 3}}{\Delta x} + \frac{q_{\psi 1}}{(\Delta x)^2}, \\
B^1_{i,j} &= \frac{q_{\psi 2}}{(\Delta x)^2} - \frac{1}{2}\frac{q_{\psi 4}}{\Delta x}, \\
B^2_{i,j} &= -2\frac{q_{\psi 2}}{(\Delta x)^2} - 2\frac{q_{\psi 1}}{(\Delta x)^2}, \\
B^3_{i,j} &= \frac{q_{\psi 2}}{(\Delta x)^2} + \frac{1}{2}\frac{q_{\psi 4}}{\Delta x}, \\
B^4_{i,j} &= \frac{1}{2}\frac{q_{\psi 3}}{\Delta x} + \frac{q_{\psi 1}}{(\Delta x)^2}, \\
B^5_{i,j} &= 1, \\
B^6_{i,j} &= q_{\psi 5}.
\end{aligned}$$

So, for each (i,j), a pair of unknowns $\omega_{i,j}$ and $\tilde{\psi}_{i,j}$ is associated with a pair of difference equations $H_{0_{i,j}}$ and $H_{1_{i,j}}$. The vorticity $\omega_{i,j}$ is also unknown along $\xi = 1$ and can be accounted for by the no-slip boundary condition (2.20). Properly discretizing it using second-order, one-sided finite differencing gives

$$H_{B_j} = D^0_j\tilde{\psi}_{m-1,j} + D^1_j\tilde{\psi}_{m,j} + D^2_j,$$

where

$$\begin{aligned}
D^0_j &= \frac{1}{2\Delta x}, \\
D^1_j &= -\frac{2}{\Delta x}, \\
D^2_j &= -\frac{3}{2}\sigma^2.
\end{aligned}$$

Now, it is possible to organize the difference equations in i and j. However, in order to minimize computation time, it is a good idea to organize the equations in

such a way that the band of the diagonal of the sparse matrix generated is as narrow as possible. So, the organization scheme suggested by Dandy and Leal [8] is used to set up the equations this way.

Let $\mathbf{G}$ be the vector that is formed by rearranging the difference equations, and let $\mathbf{G}_k$ be its components. First, set $\mathbf{G}_1 = H_{0_{1,1}}$; with $i = 1$ fixed, increment j until $\mathbf{G}_m = H_{0_{1,m}}$. Then, set $\mathbf{G}_{m+1} = H_{1_{1,1}}$ and increment j until $\mathbf{G}_{m+m} = H_{1_{1,m}}$. Now, increment i by one and repeat the whole process until $i = m$. Then, set $\mathbf{G}_{2m^2+j} = H_{B_j}$ for $j = 1, ..., m$.

Now, let $\mathbf{U}$ be the vector of unknowns and let $\mathbf{U}_k$ be its components. First, set $\mathbf{U}_1 = \tilde{\psi}_{1,1}$; with $i = 1$ fixed, increment j until $\mathbf{U}_m = \tilde{\psi}_{1,m}$. Then, set $\mathbf{U}_{m+1} = \omega_{1,1}$ and increment j until $\mathbf{U}_{m+m} = \omega_{1,m}$. Now, increment i by one and repeat the whole process until $i = m$. Then, set $\mathbf{U}_{2m^2+j} = \omega_{m+1,j}$ for $j = 1, ..., m$.

In other words, the components of $\mathbf{G}$ and $\mathbf{U}$ are such that

$$\begin{aligned} \mathbf{G}_{2m(i-1)+em+j} &= \left\{ H_{e_{i,j}} \qquad e = 0, 1 \right\};\ i = 1, ..., m, j = 1, ..., m, \\ \mathbf{G}_{2m^2+j} &= H_{B_j};\ j = 1, ..., m; \end{aligned}$$

and

$$\begin{aligned} \mathbf{U}_{2m(i-1)+em+j} &= \left\{ \begin{array}{ll} \tilde{\psi}_{i,j} & e = 0 \\ \omega_{i,j} & e = 1 \end{array} \right\};\ i = 1, ..., m, j = 1, ..., m, \\ \mathbf{U}_{2m^2+j} &= \omega_{m+1,j};\ j = 1, ..., m. \end{aligned}$$

Now, we need to solve for $\mathbf{U}$ such that $\mathbf{G}(\mathbf{U}) \approx 0$, and Newton's method is used to achieve this. In order to use Newton's method, we need to calculate the Jacobian matrix

$$\frac{\delta \mathbf{G}}{\delta \mathbf{U}}$$

associated with $\mathbf{G}$ by differentiating each component of $\mathbf{G}$ with respect to each component of $\mathbf{U}$. Suppose some initial vector $\mathbf{U}^N$ is given. After we compute the Jacobian

matrix $\frac{\delta \mathbf{G}}{\delta \mathbf{U}}$, we iterate for $\mathbf{U}^{N+1}$ by solving

$$\mathbf{U}^{N+1} = \mathbf{U}^N + \left(\frac{\delta \mathbf{G}(\mathbf{U}^N)}{\delta \mathbf{U}}\right)^{-1} \mathbf{G}(\mathbf{U}^N),$$

or

$$\frac{\delta \mathbf{G}(\mathbf{U}^N)}{\delta \mathbf{U}} \left(\mathbf{U}^{N+1} - \mathbf{U}^N\right) = \mathbf{G}(\mathbf{U}^N). \tag{2.23}$$

The whole process is repeated until $\mathbf{G}(\mathbf{U}) \approx 0$. The difficulty comes from solving the linear system (2.23) in that it involves computing the LU decomposition of a large sparse matrix $\frac{\delta \mathbf{G}}{\delta \mathbf{U}}$. So, a sparse matrix solver developed by Kundert and Sangiovanni-Vincentelli [18] is used in computing the LU decomposition of the matrix. Figure 2.8 shows the structure of the sparse matrix $\frac{\delta \mathbf{G}}{\delta \mathbf{U}}$ used. Their solver allows the user to enter the nonzero elements of the sparse matrix and uses partial pivoting to compute the LU decomposition. In practice, one LU decomposition in the beginning of the iteration is sufficient; a new LU is not needed at every iteration. So, a secant method is generally used.

2.3.3 Numerical results of steady flow past a solid sphere

Here, we present the results of our computations of steady, axisymmetric flows past a solid sphere. As mentioned previously, there are several numerical results for flows past a sphere, and we compare our results with previous work. The nondimensionalization is such that $d = a = b$, and we define the Reynolds number as $R = R_d$. The grid shown in Figure 2.6 a) is used as the numerical grid in order to compute the steady solutions for various values of R.

The drag coefficient C_D of the flow is computed by numerically integrating

$$\begin{aligned} C_D &= 2\int_0^1 \left[u_\eta^2 \sigma \frac{\partial \sigma}{\partial \eta} - \frac{2}{R_d}\frac{h_\eta \sigma}{h_\xi}\frac{\partial}{\partial \xi}(\sigma\omega) + \frac{8}{R_d} e_{\xi\xi}\sigma \frac{\partial \sigma}{\partial \eta}\right]_{\xi=1} d\eta \\ &\quad +2\int_0^1 \left(\frac{8}{R_d} e_{\xi\eta}\sigma \frac{\partial x}{\partial \eta}\right)_{\xi=1} d\eta \end{aligned} \tag{2.24}$$

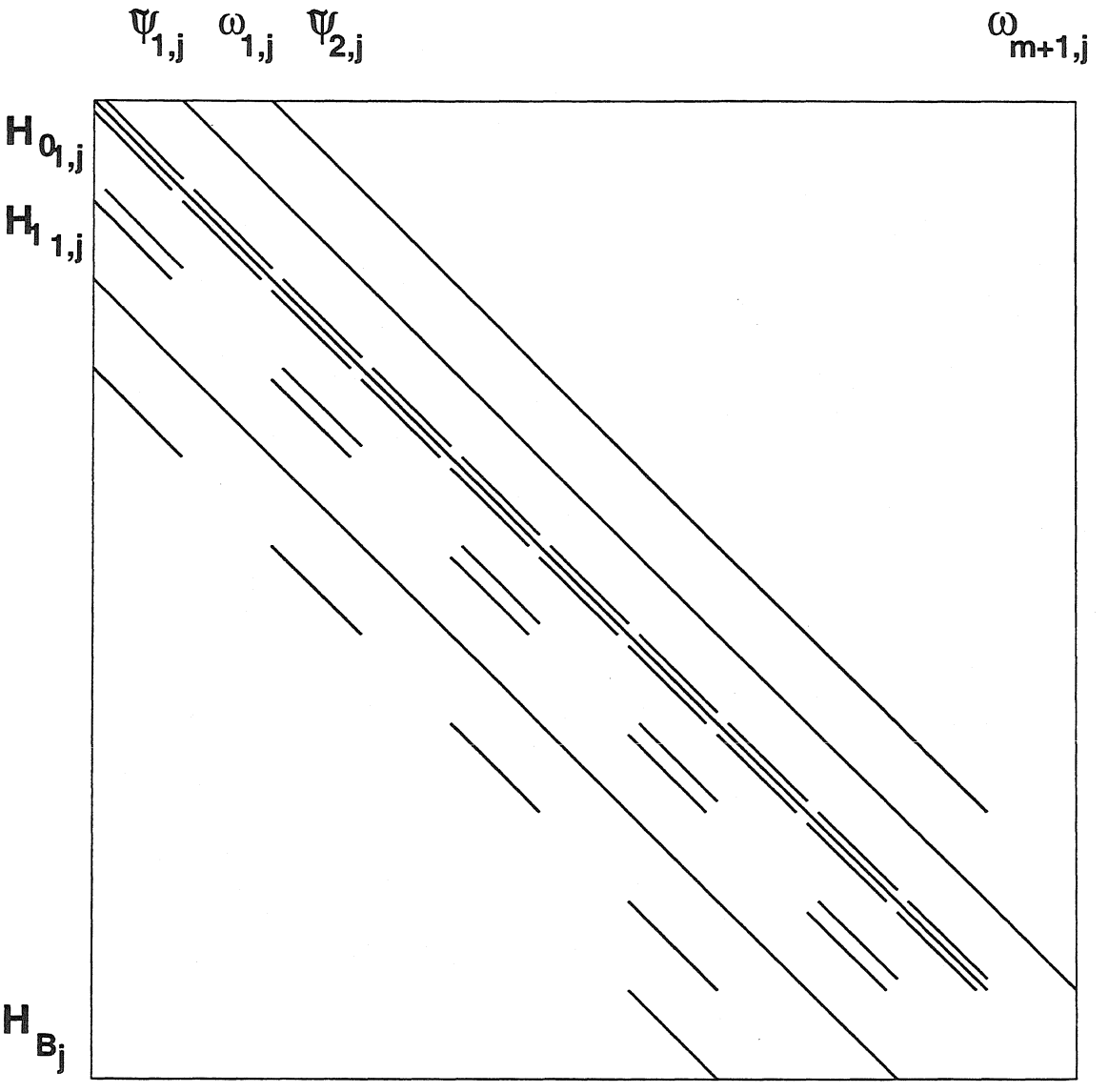

Figure 2.8: The banded structure of the sparse matrix used in the outer flow solver of flow past spheroids with the no-slip boundary condition.

Sphere	$R =$	100	$R =$	200
	C_D	Wake length	C_D	Wake length
60x60	1.078	2.77	0.755	4.01
70x70	1.081	2.76	0.760	3.97
80x80	1.082	2.76	0.760	3.95

Table 2.1: Convergence study for steady, axisymmetric flow past a solid sphere. The wake length is measured from the center of the sphere.

R	0.01	0.1	1	5	10
Oseen's	2404.4	244.1	27.6	15.5	28.6
This work, 80x80 grid	2420.9	245.4	27.4	7.14	4.30

Table 2.2: Drag coefficients of flow past a solid sphere at low Reynolds numbers using grid of resolution 80x80 compared with Oseen's results.

where

$$
\begin{aligned}
e_{\xi\xi} &= \frac{1}{h_\xi}\frac{\partial u_\xi}{\partial \xi} + \frac{u_\eta}{h_\xi h_\eta}\frac{\partial h_\xi}{\partial \eta}, \\
e_{\xi\eta} &= -\frac{h_\eta}{2h_\xi}\frac{\partial}{\partial \xi}\left(\frac{u_\eta}{h_\eta}\right) - \frac{h_\xi}{2h_\eta}\frac{\partial}{\partial \eta}\left(\frac{u_\xi}{h_\xi}\right).
\end{aligned}
$$

This equation is also used to calculate the drag coefficients for spheroids as well. According to asymptotic results by Oseen and others as reported in Masliyah Epstein [20], for R_d small,

$$
C_D \sim \frac{24}{R_d}K\left[1 + \frac{3KR_d}{16} + \frac{9K^2}{160}R_d^2 \ln\left(\frac{R_d}{2}\right)\right].
$$

The values of K are tabulated in Happel and Brenner [15]. This equation is also valid for spheroids as well.

Table 2.1 shows the drag coefficients and wake lengths of steady solutions computed at Reynolds numbers of 100 and 200 under different resolutions. The results are in good agreement for all three mesh sizes, and this indicates that our results are convergent. Table 2.2 compares the drag coefficients at low Reynolds numbers with Oseen's asymptotic results. They also appear to agree well for $R = 1$ and lower.

Table 2.3 compares our results with some of the previous results of others who

Sphere	$R =$	100	$R =$	200
	C_D	Wake length	C_D	Wake length
Fornberg [12]	1.085	2.74	0.768	3.867
Natarajan and Acrivos [26]	1.092		0.79	3.86
Magnaudet, Rivero, and Fabre [19]			0.765	
This work, 80x80 grid	1.082	2.76	0.760	3.95

Table 2.3: Comparison of the drag coefficients and the wake lengths of flow past a solid sphere as determined by others. The wake length is measured from the center of the sphere.

R	50	100	200	300	400	500	550
C_D	1.571	1.081	0.760	0.616	0.528	0.465	0.442

Table 2.4: Drag coefficients of flow past a solid sphere at various Reynolds numbers using grid of resolution 80x80.

used different types of numerical methods. Fornberg [12] used conformal mapping to compute steady, axisymmetric flow past a rigid sphere for Reynolds number up to 5000, and Natarajan and Acrivos [26] also computed some steady solutions in their perturbation analysis. In addition, Magnaudet, Rivero, and Fabre [19] used a finite volume method to extensively study steady and accelerated flows. The results all appear to agree reasonably well with one another.

Figures 2.10 and 2.11 show the contour lines of vorticity and stream function computed for $R = 1$, 50, 100, 200, 300, 400, 500, and 550. A standing wake begins to form around $R = 20$ and becomes quite large around $R = 200$. Figure 2.9 shows the length and the separation angle of the wake behind a sphere as a function of the Reynolds number. It appears that the wake increases in size as the Reynolds number increases.

2.3.4 Numerical results of steady flow past an oblate spheroid

In this section, we present the computations of steady flow past an oblate spheroid of aspect ratio $\lambda = a/b$. The nondimensionalization is such that $d = b$ so that the

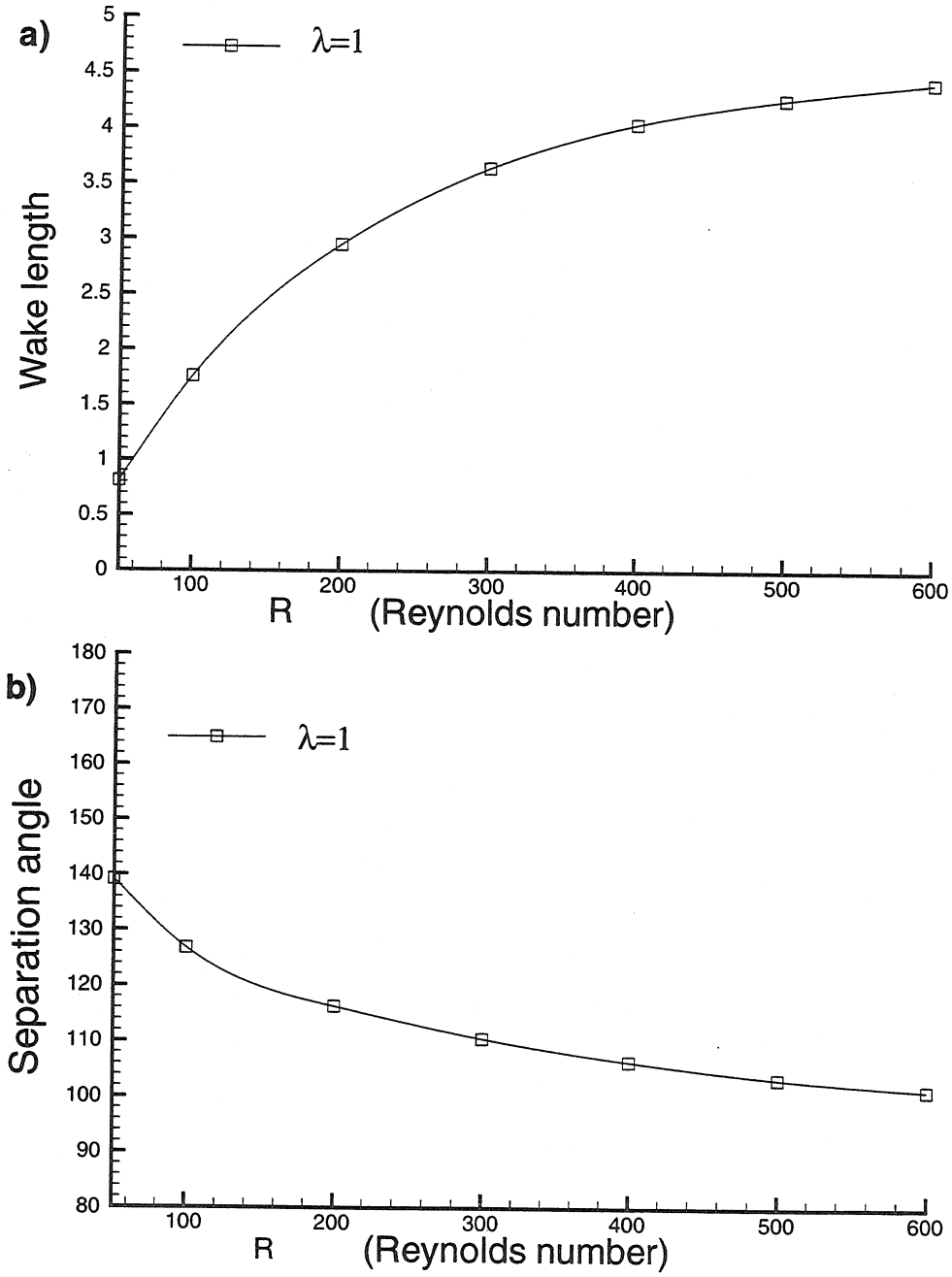

Figure 2.9: a) Length of the wake as measured from the back of a sphere using a grid of resolution 80x80 and $\alpha = 0.5$. b) Separation angle of the wake as measured from the front of a sphere using a grid of resolution 80x80 and $\alpha = 0.5$.

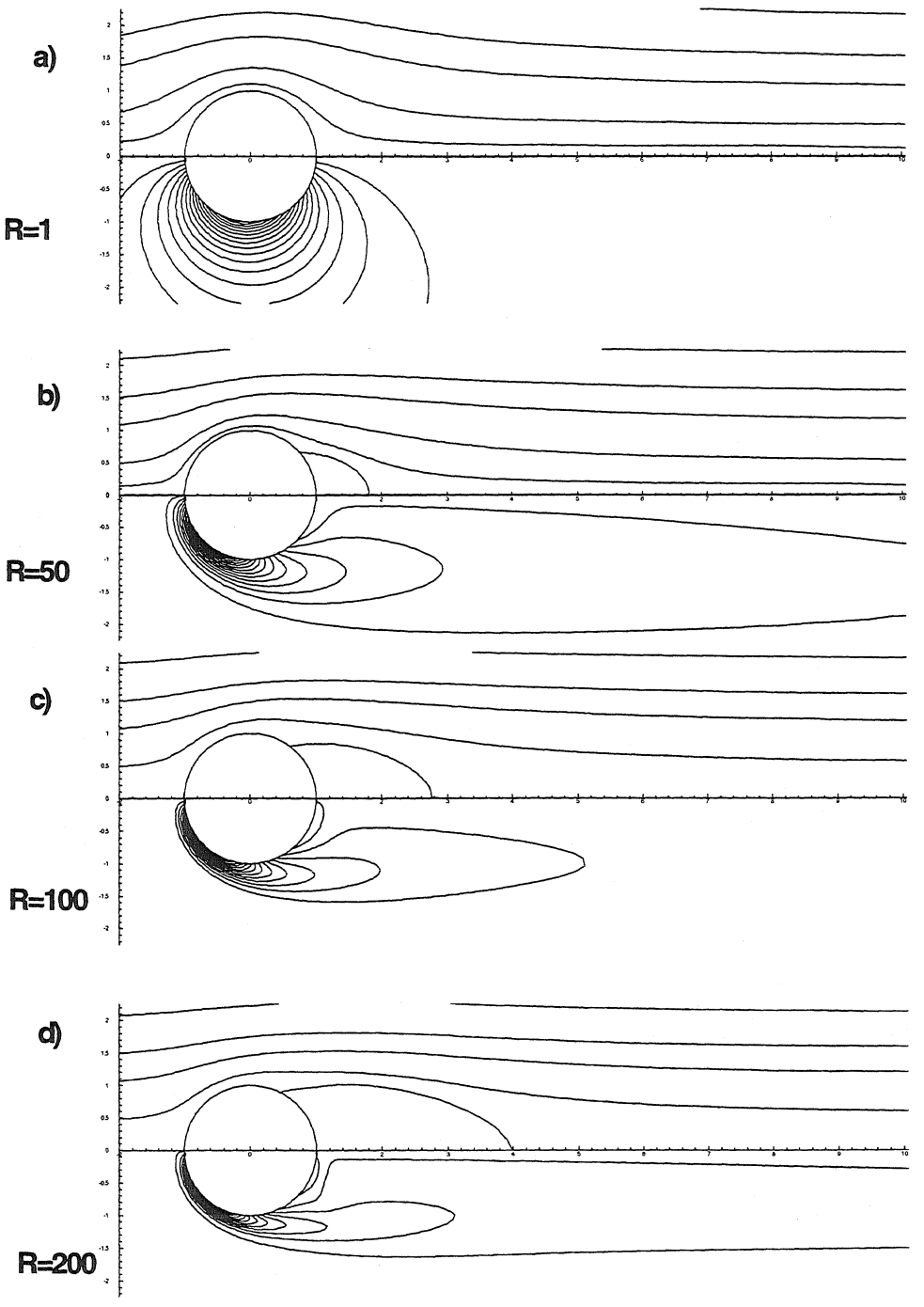

Figure 2.10: Steady solutions of flow past a sphere are shown for $R = 1$, 50, 100, and 200. In each case top is the stream function, and the bottom is the vorticity.

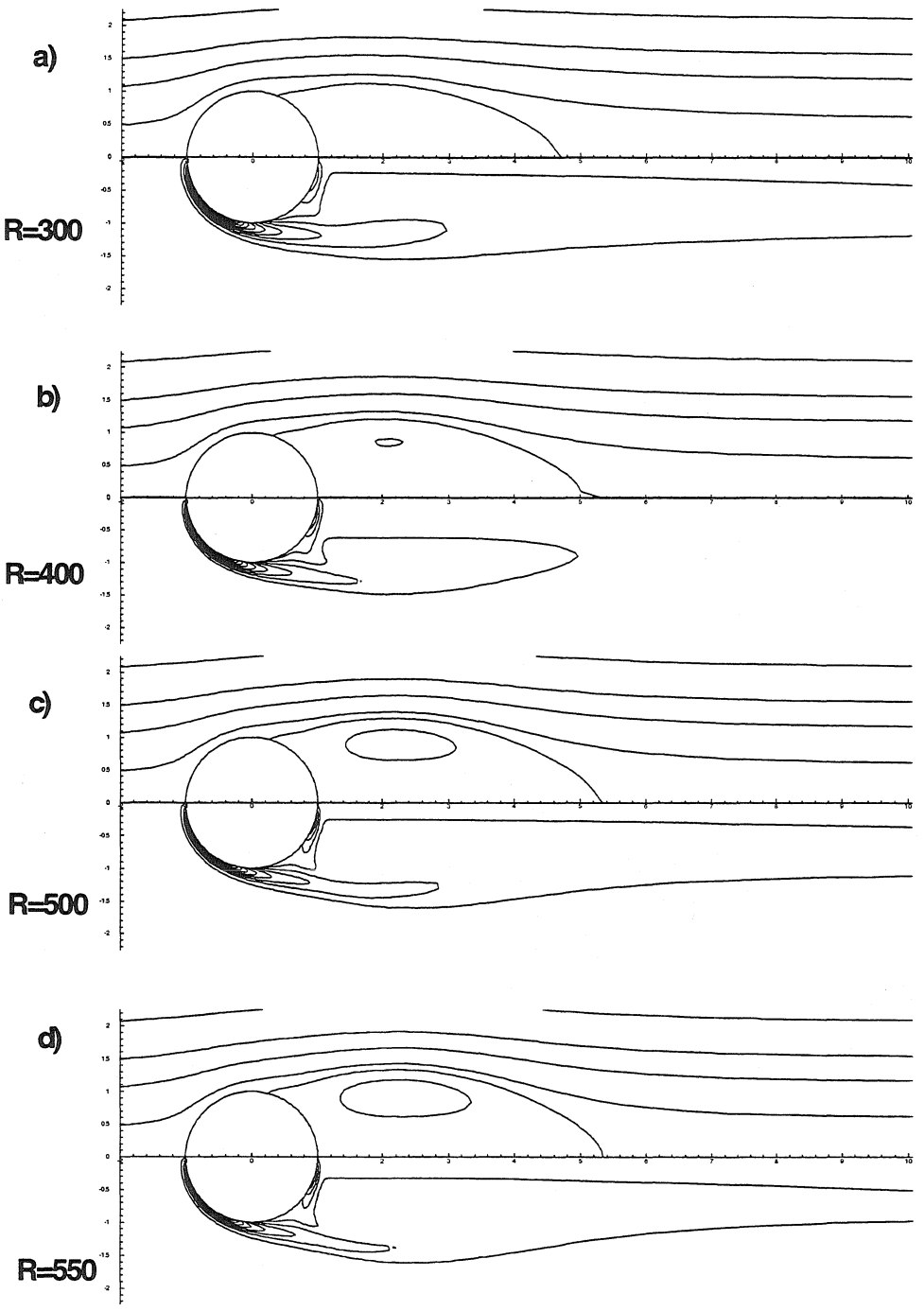

Figure 2.11: Steady solutions of flow past a sphere are shown for $R = 300$, 400, 500, and 550. In each case the top is the stream function, and the bottom is the vorticity.

Oblate spheroid	Oseen's	This work 70x70	This work 80x80
	$R_b = 0.1$	$R_b = 0.1$	$R_b = 0.1$
$\lambda = 0.3$	212.9	217.1	216.4
0.4	216.6	218.9	218.5
0.5	220.7	222.2	222.0
0.6	225.0	226.2	226.1
0.7	229.6	230.8	230.6
0.8	234.3	235.6	235.4
0.9	239.2	240.5	240.3

Table 2.5: Drag coefficients of flow past an oblate spheroid at low Reynolds number.

Oblate spheroid	This work 70x70		This work 80x80	
	$R_b = 100$	$R_b = 200$	$R_b = 100$	$R_b = 200$
$\lambda = 0.3$	1.191	0.896	1.187	0.888
0.4	1.151	0.855	1.150	0.851
0.5	1.124	0.826	1.124	0.824
0.6	1.105	0.804	1.106	0.804
0.7	1.092	0.786	1.094	0.788
0.8	1.084	0.773	1.086	0.776
0.9	1.080	0.764	1.082	0.766

Table 2.6: Drag coefficients of flow past an oblate spheroid using grids of resolution of 70x70 and 80x80.

Reynolds number is defined by

$$R_b = R_d = \frac{2\rho bU}{\mu}.$$

Grids similar to Figure 2.7 a) are used to compute the steady solutions for various values of R_b, given $\lambda = 0.3$, 0.4, 0.5, 0.6, 0.7, 0.8, and 0.9. Results for λ smaller than 0.3 were not calculated due to the limitations of our method; the numerical grids computed for such values of λ were too distorted for our steady solution solver to obtain a converged solution.

Table 2.5 shows the comparison of the drag coefficient for flows past an oblate spheroid at low Reynolds number. Our results seem to agree well with the asymptotic results under different resolutions.

Table 2.6 shows our results for moderate Reynolds numbers $R_b = 100$ and 200. They appear to agree well under different resolutions.

Oblate spheroid	R_b 50	100	200	300	400	500
$\lambda = 0.3$	1.592	1.187	0.888	0.746	0.661	0.603
0.4	1.565	1.150	0.851	0.709	0.622	0.564
0.5	1.551	1.124	0.824	0.682	0.594	0.535
0.6	1.545	1.106	0.804	0.661	0.573	0.513
0.7	1.545	1.094	0.788	0.646	0.557	0.497
0.8	1.550	1.086	0.776	0.633	0.545	0.483
0.9	1.560	1.082	0.766	0.624	0.535	0.473

Table 2.7: Drag coefficients of flow past an oblate spheroid. 80x80 grid.

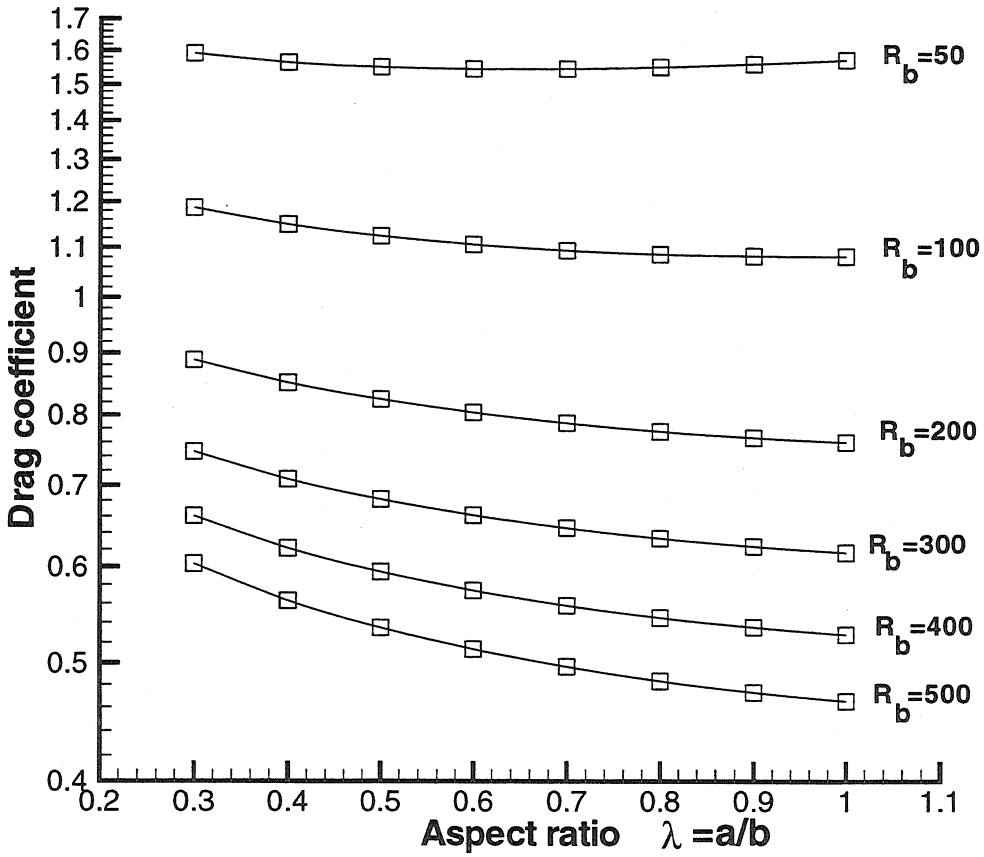

Figure 2.12: Drag coefficients of flow past an oblate spheroid for various values of R_b.

Prolate spheroid	Oseen's	Our results 70x70	Our results 80x80
	$R_a = 0.1$	$R_a = 0.1$	$R_a = 0.1$
$\lambda = 1.1$	226.2	227.5	227.3
1.2	211.3	212.5	212.3
1.3	198.8	199.9	199.7
1.4	187.9	189.1	188.9
1.5	178.8	179.7	179.5
1.6	170.6	171.5	171.3
1.7	163.4	164.2	164.0

Table 2.8: Drag coefficients of flow past a prolate spheroid at low Reynolds number.

Figures 2.14 and 2.15 show the steady solutions that we computed using the 80x80 grid for $\lambda = 0.3$ at various values of R_b. Figures 2.16 and 2.17 show the steady solutions that we computed using the 80x80 grid for $\lambda = 0.7$ at various values of R_b.

Figure 2.12 and Table 2.7 show the drag coefficients of steady flow past an oblate spheroid of various aspect ratios at various values of R_b. It appears that the drag coefficient becomes smaller as the body becomes more spherical if R_b is large. Figure 2.13 shows the wake length and the separation angle of the wake behind an oblate spheroid of various aspect ratios. It appears that for a very oblate spheroid, as the Reynolds number increases, the wake shrinks back a little.

2.3.5 Numerical results of steady flow past a prolate spheroid

In this section, we present the computations of steady flows past a prolate spheroid of aspect ratio $\lambda = a/b$. The nondimensionalization is such that $d = a$, and the Reynolds number is defined by

$$R_a = R_d = \frac{2\rho U a}{\mu}.$$

Numerical grids similar to Figure 2.7 b) are used for our computations. Steady solutions are computed for $\lambda = 1.1$, 1.2, 1.3, 1.4, 1.5, 1.6, and 1.7.

Table 2.8 shows the comparison of the drag coefficient results obtained for creeping flows. Our results appear to agree well with Oseen's asymptotic results.

Table 2.10 compares our results computed using two different grid resolutions for

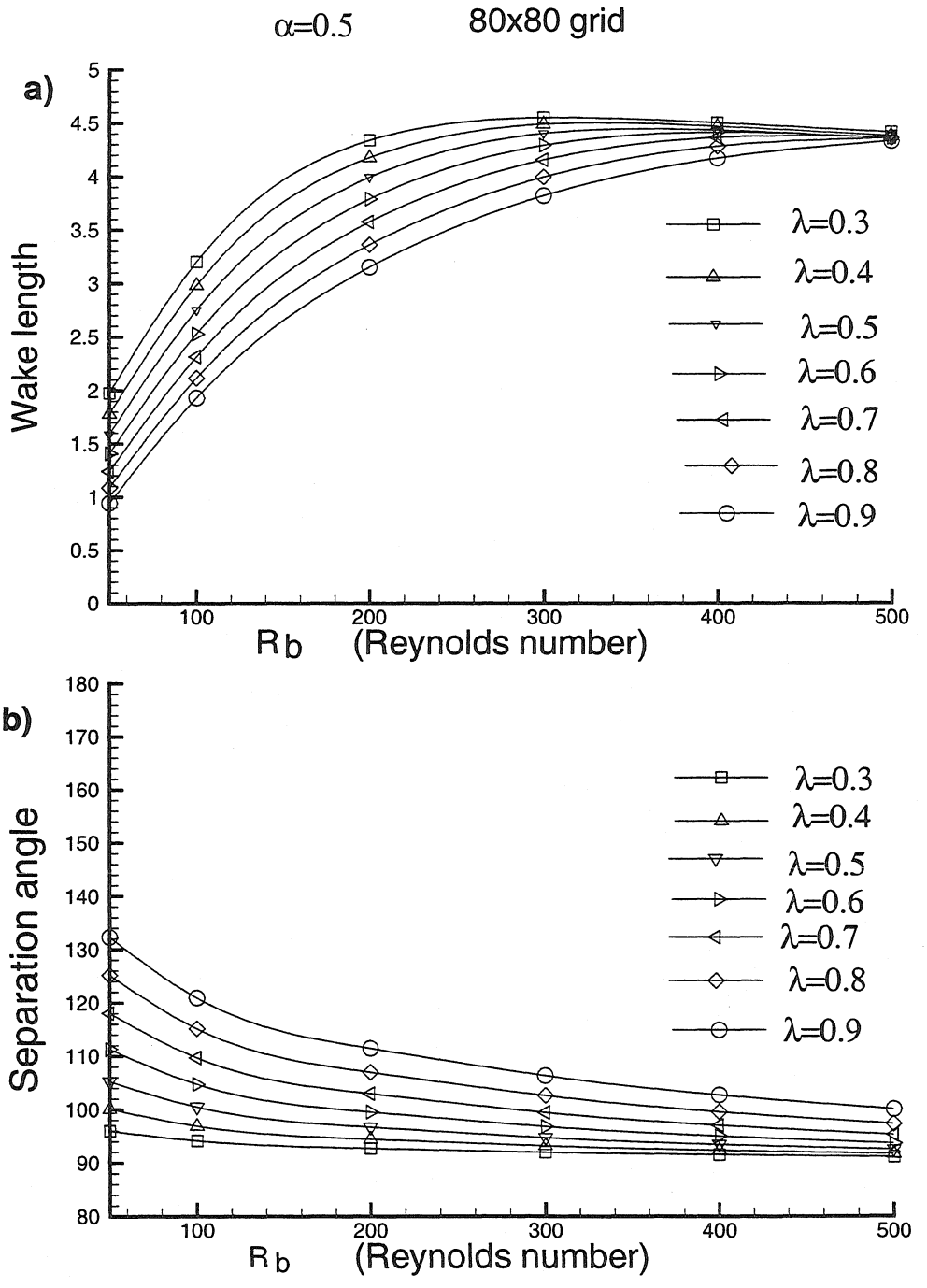

Figure 2.13: a) Length of the wake as measured from the back of an oblate spheroid using a grid of 80x80 resolution with $\alpha = 0.5$. b) Separation angle of the wake as measured from the front of an oblate spheroid using a grid of 80x80 resolution with $\alpha = 0.5$.

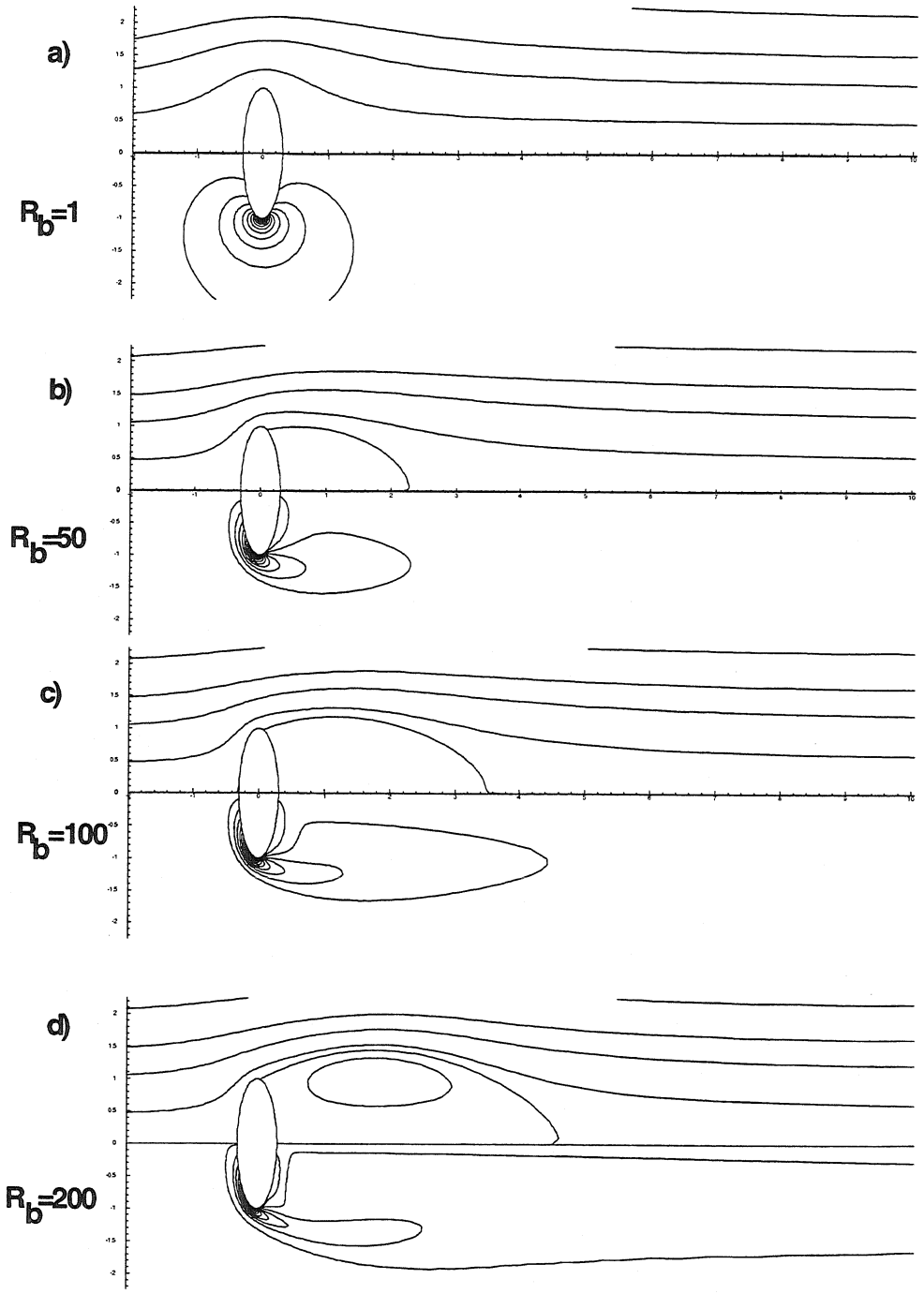

Figure 2.14: Steady solutions of flow past an oblate spheroid with $\lambda = 0.3$ are shown for $R_b = 1$, 50, 100, and 200. In each case the top is the stream function, and the bottom is the vorticity.

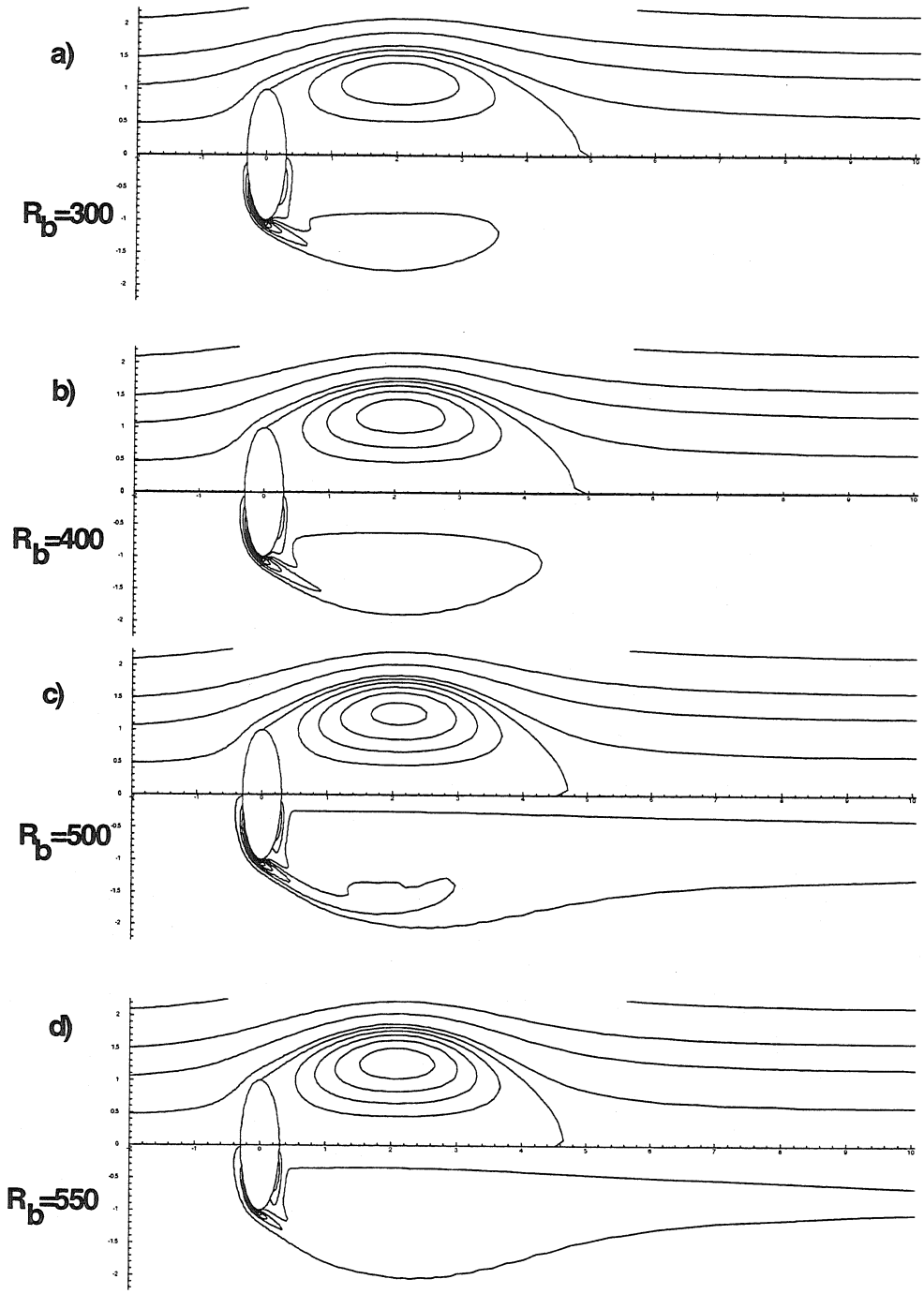

Figure 2.15: Steady solutions of flow past an oblate spheroid with $\lambda = 0.3$ are shown for $R_b = 300$, 400, 500, and 550. In each case the top is the stream function, and the bottom is the vorticity.

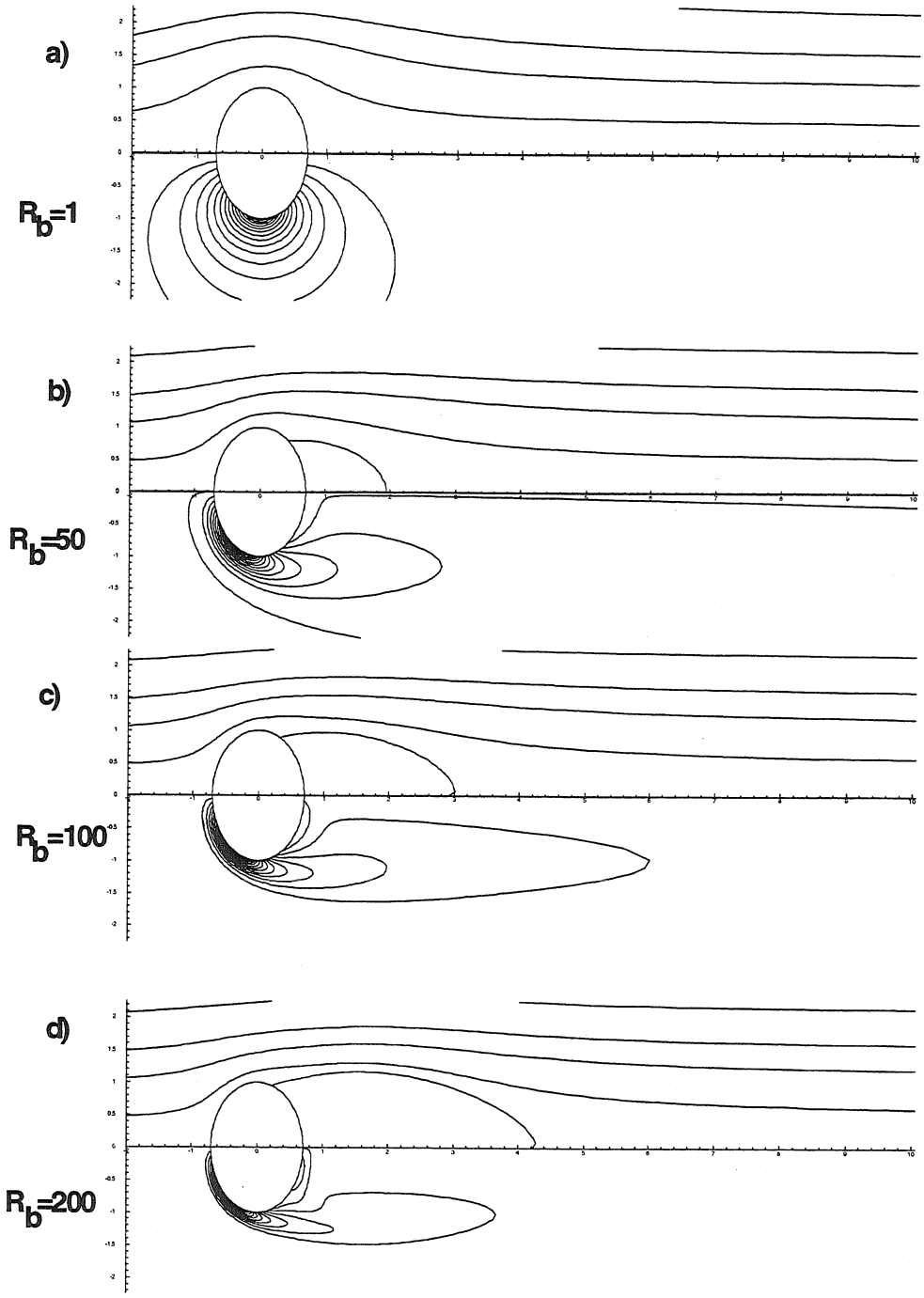

Figure 2.16: Steady solutions of flow past an oblate spheroid with $\lambda = 0.7$ for $R_b = 1$, 50, 100, and 200. In each case the top is the stream function, and the bottom is the vorticity.

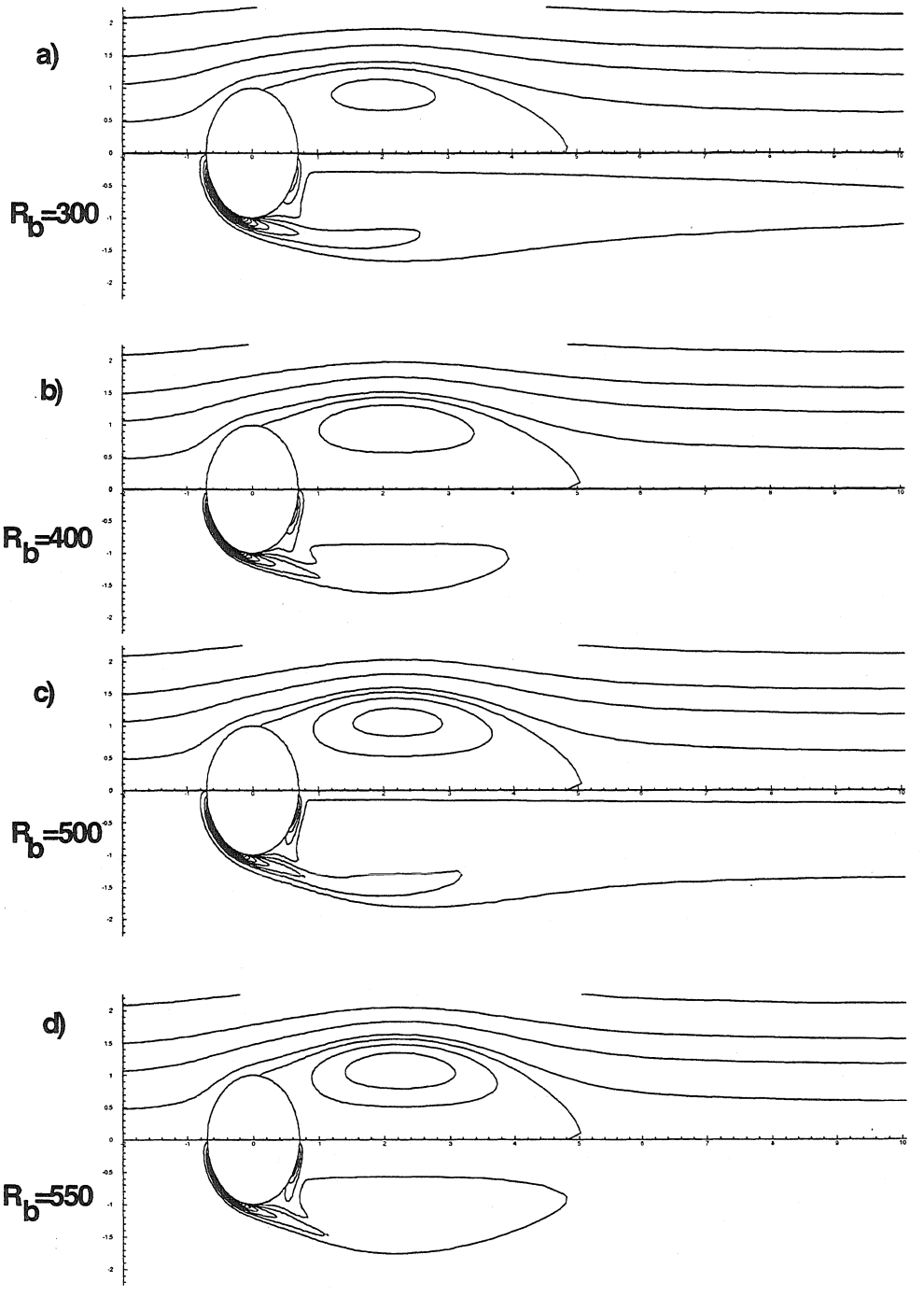

Figure 2.17: Steady solutions of flow past an oblate spheroid with $\lambda = 0.7$ are shown for $R_b = 300$, 400, 500, and 550. In each case the top is the stream function, and the bottom is the vorticity.

Prolate spheroid	R_a	50	100	200	300	400	500	600
$\lambda = 1.1$		1.384	0.942	0.656	0.531	0.455	0.401	0.344
1.2		1.238	0.834	0.576	0.465	0.398	0.351	0.320
1.3		1.120	0.749	0.512	0.413	0.353	0.312	0.282
1.4		1.024	0.679	0.462	0.371	0.317	0.280	0.252
1.5		0.945	0.622	0.420	0.336	0.287	0.253	0.228
1.6		0.877	0.574	0.385	0.307	0.262	0.231	0.208
1.7		0.820	0.534	0.356	0.283	0.241	0.213	0.191

Table 2.9: Drag coefficients of flow past a prolate spheroid. 80x80 grid.

Prolate spheroid	Our results 70x70		Our results 80x80	
	$R_a = 100$	$R_a = 200$	$R_a = 100$	$R_a = 200$
$\lambda = 1.1$	0.941	0.654	0.942	0.656
1.2	0.833	0.574	0.834	0.576
1.3	0.748	0.511	0.749	0.512
1.4	0.679	0.461	0.679	0.462
1.5	0.622	0.419	0.622	0.420
1.6	0.574	0.385	0.574	0.385
1.7	0.533	0.356	0.533	0.356

Table 2.10: Drag coefficients of flow past a prolate spheroid computed using 70x70 grid and 80x80 grid.

moderate Reynolds numbers $R_a = 100$ and 200. They appear to agree well indicating that our results are convergent.

Figures 2.20 and 2.21 show the steady solutions computed using the 80x80 grid for $\lambda = 1.3$ at various values of R_a. Figures 2.22 and 2.23 show the steady solutions computed using the 80x80 grid for $\lambda = 1.7$ at various values of R_a. Figure 2.19 and Table 2.9 show the drag coefficients for steady flow past a prolate spheroid of various aspect ratios at various values of R_a. It appears that the drag coefficient becomes smaller as the body becomes more prolate. Figure 2.18 compares the wake length and the separation angle of the wake behind a prolate spheroid of various aspect ratios. It appears that as the Reynolds number increases, the wake increases in size as well.

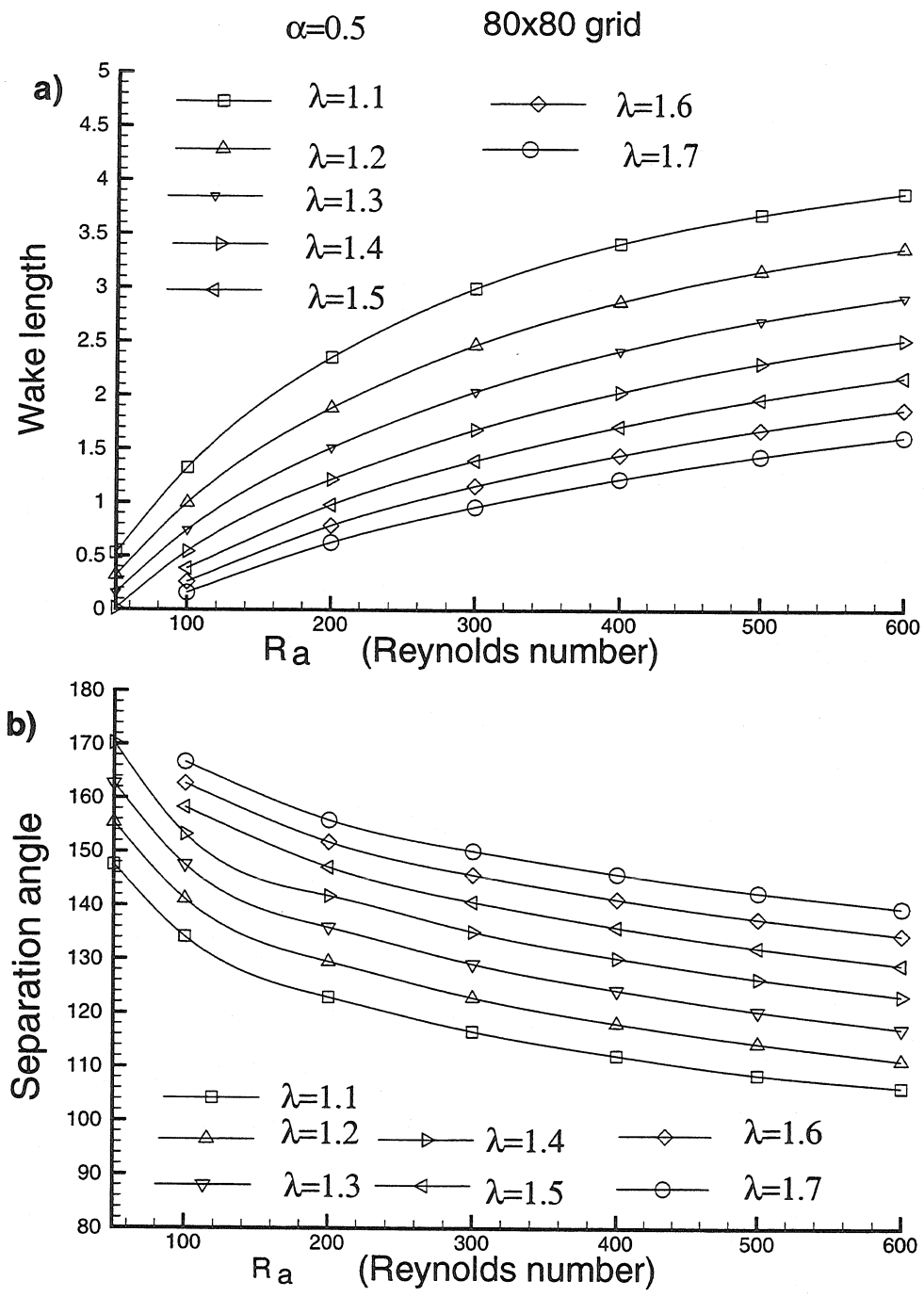

Figure 2.18: a) Length of the wake as measured from the back of a prolate spheroid using a grid of 80x80 resolution with $\alpha = 0.5$. b) Separation angle of the wake as measured from the front of a prolate spheroid using a grid of 80x80 resolution with $\alpha = 0.5$.

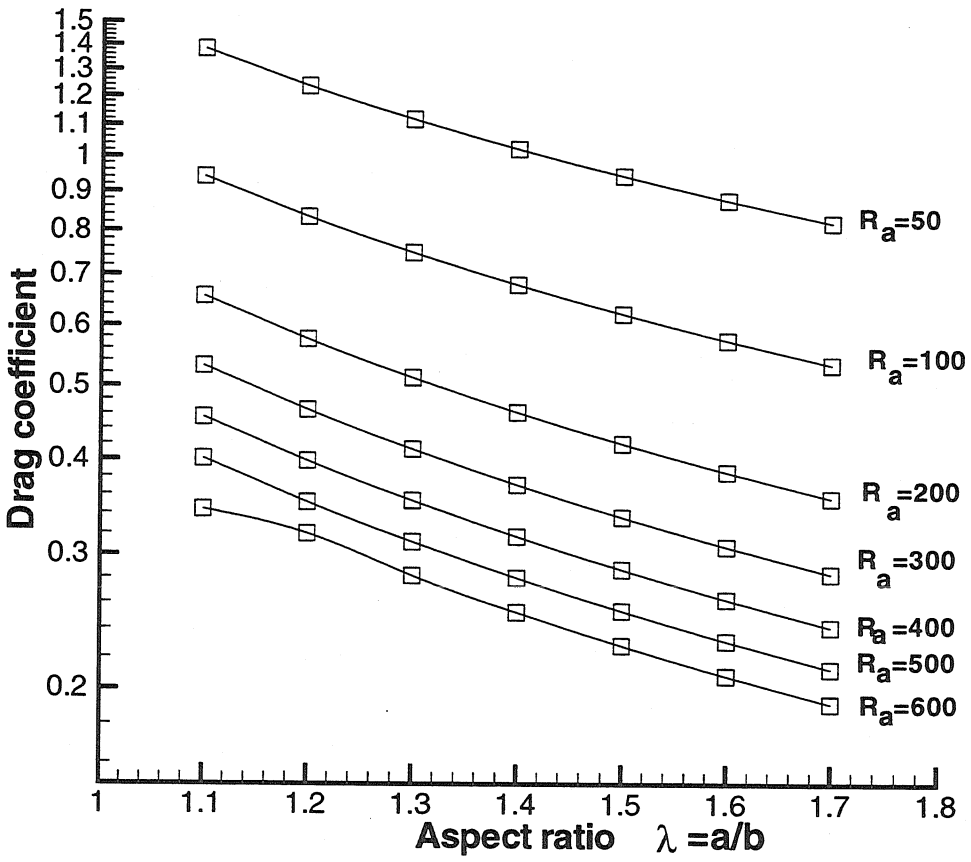

Figure 2.19: Drag coefficients of flow past a prolate spheroid for various values of R_a.

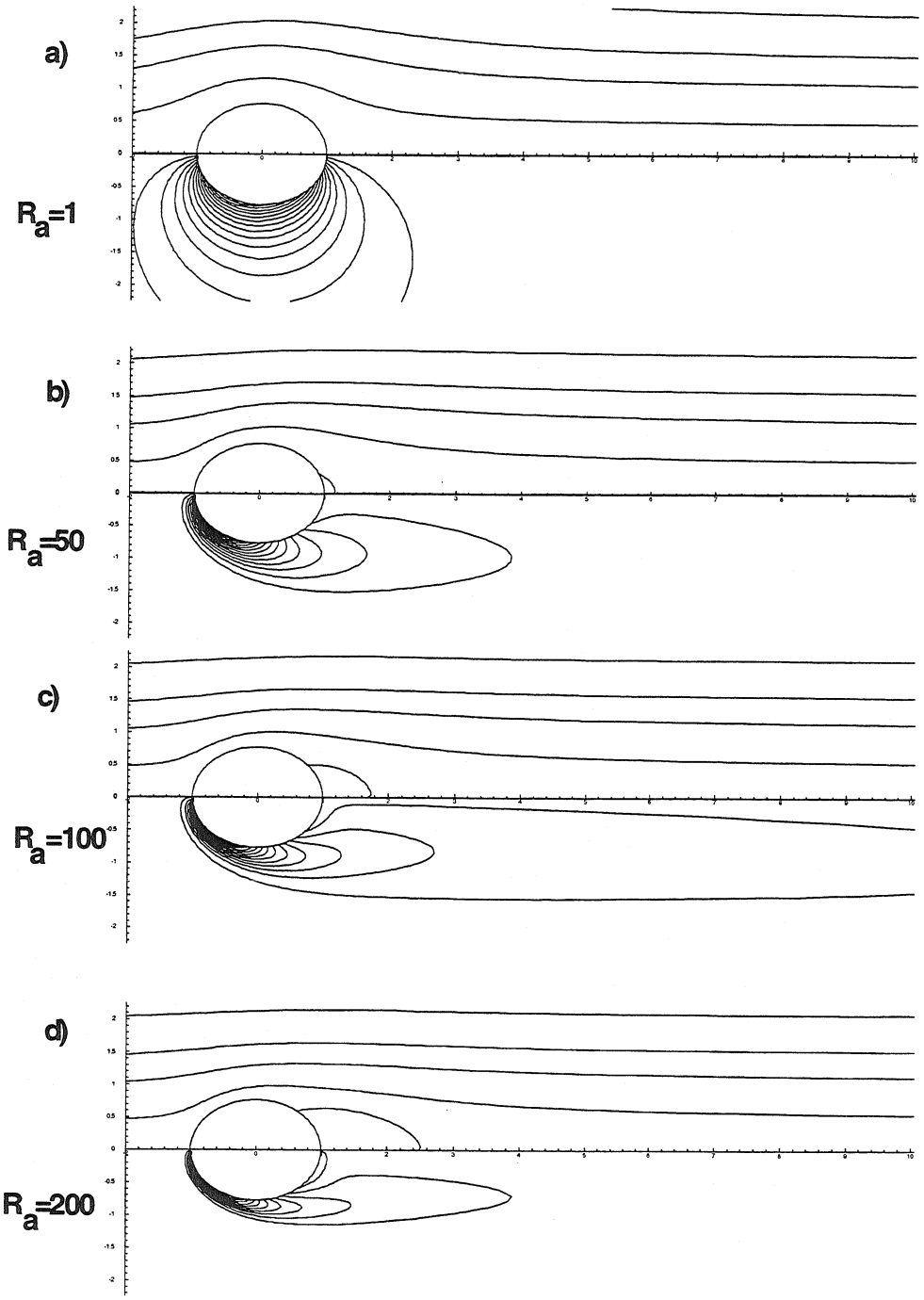

Figure 2.20: Steady solutions of flow past a prolate spheroid with $\lambda = 1.3$ are shown for $R_a = 1$, 50, 100, and 200. In each case the top is the stream function, and the bottom is the vorticity.

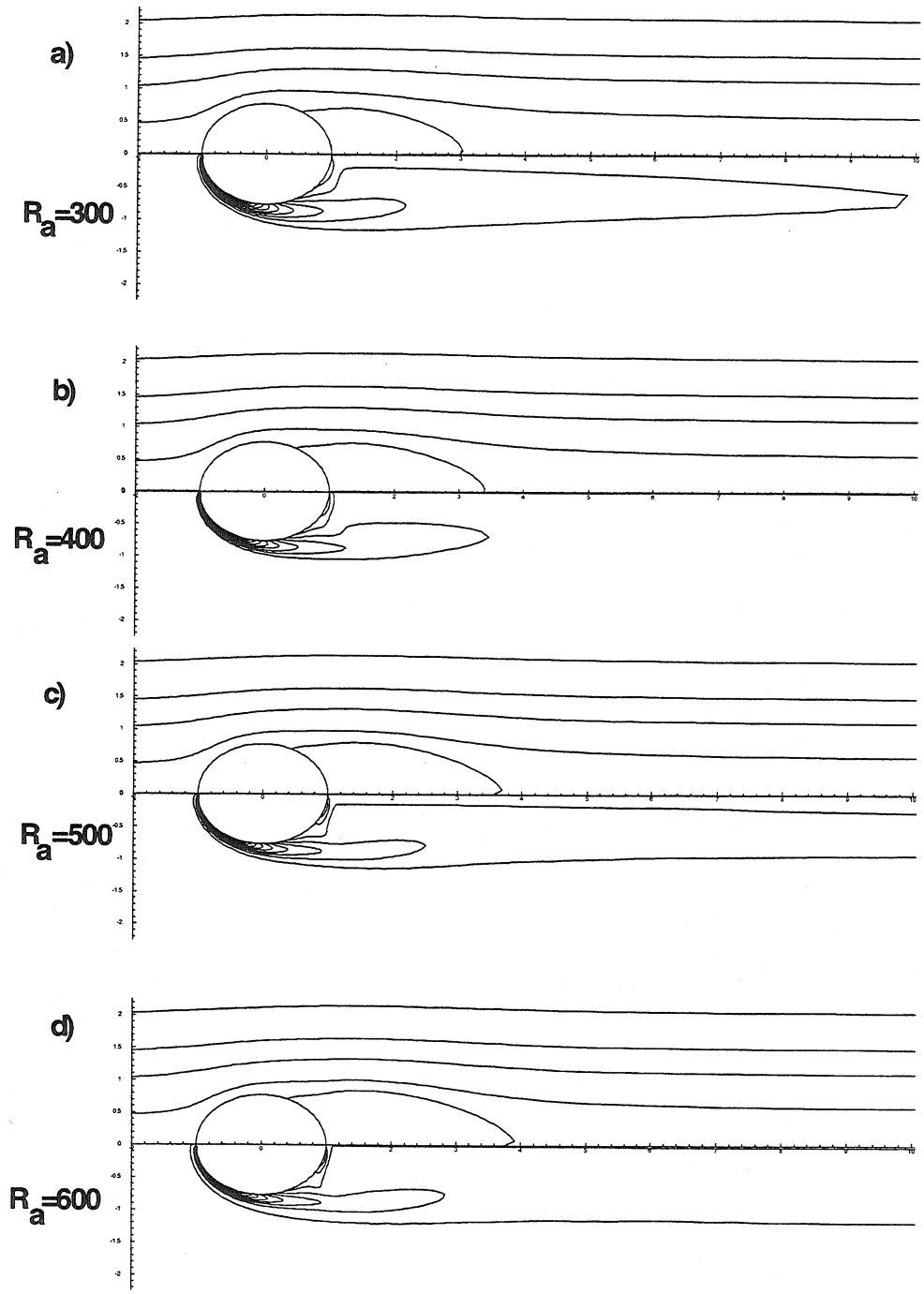

Figure 2.21: Steady solutions of flow past a prolate spheroid with $\lambda = 1.3$ are shown for $R_a = 300$, 400, 500, and 600. In each case the top is the stream function, and the bottom is the vorticity.

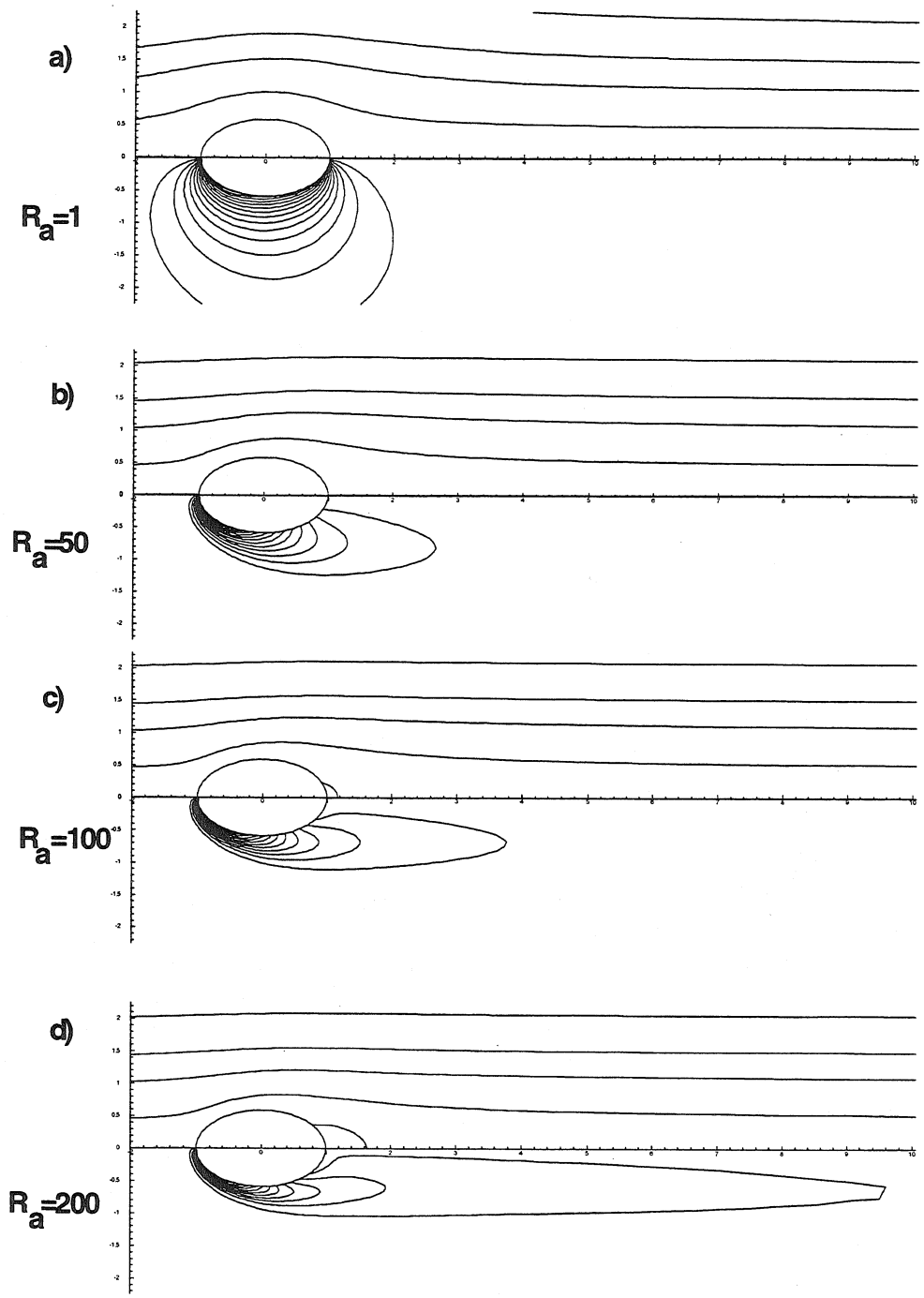

Figure 2.22: Steady solutions of flow past a prolate spheroid with $\lambda = 1.7$ are shown for $R_a = 1,\ 50,\ 100,$ and 200. In each case the top is the stream function, and the bottom is the vorticity.

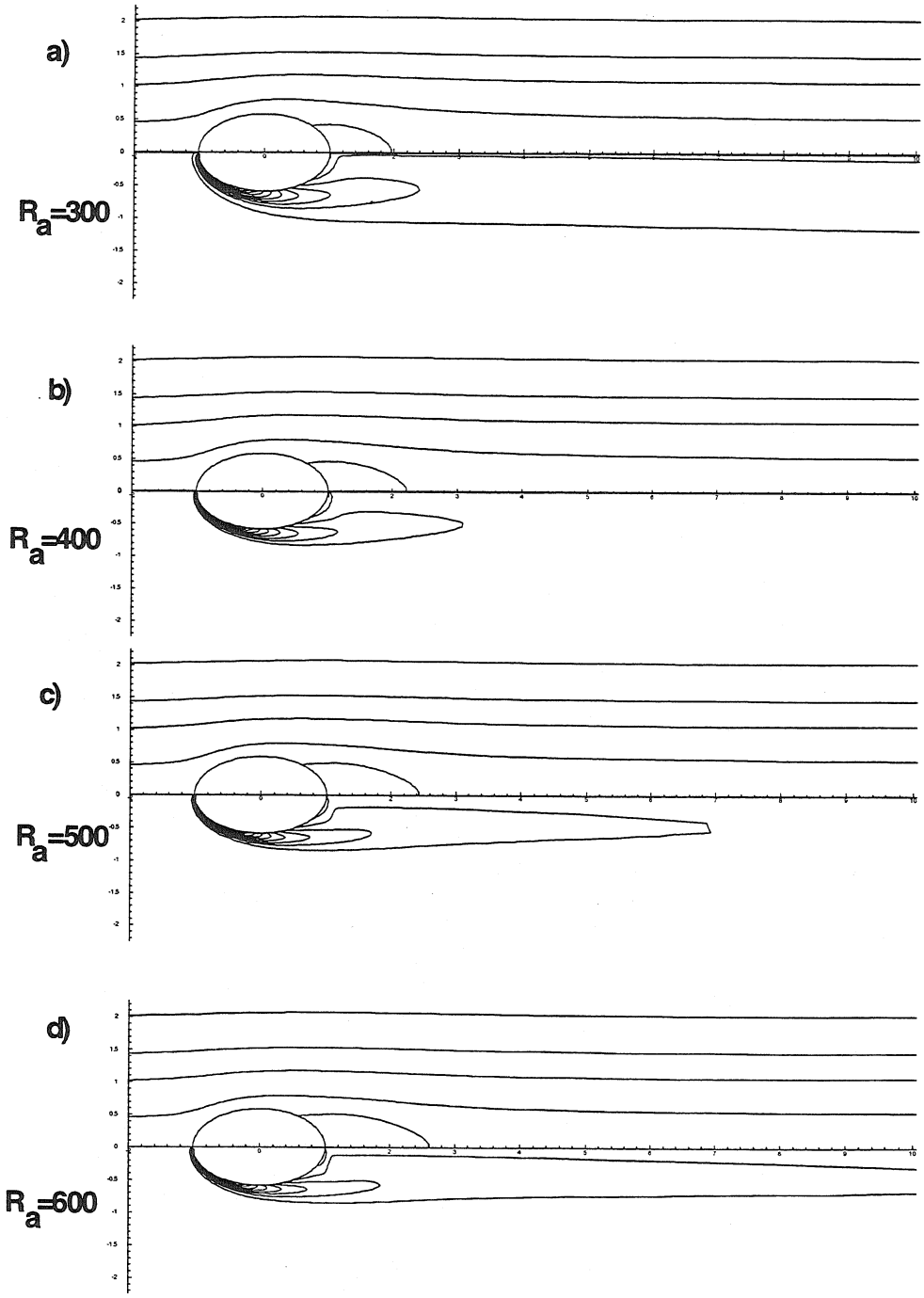

Figure 2.23: Steady solutions of flow past a prolate spheroid with $\lambda = 1.7$ are shown for $R_a = 300$, 400, 500, and 600. In each case the top is the stream function, and the bottom is the vorticity.

2.4 Linear Stability Analysis

2.4.1 Perturbation equations

With the steady, axisymmetric solutions determined for a reasonable range of aspect ratios and Reynolds numbers, a linear stability analysis is performed to investigate perturbations that may deviate from the steady, axisymmetric base flow. The main focus of this linear stability analysis is to determine the critical Reynolds numbers at which the flow may become unstable. It is of interest to determine also the nature of the instability. First, the perturbations to the pressure p and the three velocity components are expanded as a Fourier series in the azimuthal ϕ direction:

$$\begin{aligned} u_\xi &= U_{\xi_S}(\xi,\eta) + \varepsilon \sum_{n=-\infty}^{\infty} e^{\iota n\phi}\tilde{u}_{\xi n}(\xi,\eta,t), \\ u_\eta &= U_{\eta_S}(\xi,\eta) + \varepsilon \sum_{n=-\infty}^{\infty} e^{\iota n\phi}\tilde{u}_{\eta n}(\xi,\eta,t), \\ u_\phi &= \varepsilon \sum_{n=-\infty}^{\infty} e^{\iota n\phi}\tilde{u}_{\phi n}(\xi,\eta,t), \\ p &= P_S(\xi,\eta) + \varepsilon \sum_{n=-\infty}^{\infty} e^{\iota n\phi}\tilde{p}_{n}(\xi,\eta,t). \end{aligned} \tag{2.25}$$

U_{ξ_S} and U_{η_S} are the radial and polar components of the steady, axisymmetric base flow velocity vector and are calculated using (2.16). The variable ε is a small parameter of perturbation, and ι is the imaginary number $\sqrt{-1}$. Expanding the perturbation in the azimuthal direction as a Fourier series reduces the problem to our original, two-dimensional grid. The perturbed variables are physical quantities and are expected to be real. So, $\tilde{u}_n = \tilde{u}^*_{-n}$. This allows us to restrict our computations to $n \geq 0$.

The equations (2.25) are plugged into the Navier Stokes equations (2.15), and a set of $O(\varepsilon)$ perturbation equations is derived:

$$q_0^0 \frac{\partial}{\partial \xi}\tilde{u}_{\xi n} + q_1^0 \frac{\partial}{\partial \eta}\tilde{u}_{\eta n} + q_2^0\tilde{u}_{\xi n} + q_3^0\tilde{u}_{\eta n} + \iota q_4^0\tilde{u}_{\phi n} = 0$$

where

$$
\begin{aligned}
q_0^0 &= \frac{1}{h_\xi}, \\
q_1^0 &= \frac{1}{h_\eta}, \\
q_2^0 &= \frac{1}{h_\xi h_\eta}\frac{\partial h_\eta}{\partial \xi} + \frac{1}{h_\xi \sigma}\frac{\partial \sigma}{\partial \xi}, \\
q_3^0 &= \frac{1}{h_\xi h_\eta}\frac{\partial h_\xi}{\partial \eta} + \frac{1}{h_\eta \sigma}\frac{\partial \sigma}{\partial \eta}, \\
q_4^0 &= \frac{n}{\sigma};
\end{aligned}
$$

$$
\begin{aligned}
&\frac{\partial}{\partial t}\tilde{u}_{\xi n} + q_9^1\frac{\partial}{\partial \xi}\tilde{p}_n + q_0^1\frac{\partial^2}{\partial \xi^2}\tilde{u}_{\xi n} + q_1^1\frac{\partial^2}{\partial \eta^2}\tilde{u}_{\xi n} + q_2^1\frac{\partial}{\partial \xi}\tilde{u}_{\xi n} \\
&+q_3^1\frac{\partial}{\partial \eta}\tilde{u}_{\xi n} + q_4^1\frac{\partial}{\partial \xi}\tilde{u}_{\eta n} + q_5^1\frac{\partial}{\partial \eta}\tilde{u}_{\eta n} + q_6^1\tilde{u}_{\xi n} + q_7^1\tilde{u}_{\eta n} + \iota q_8^1\tilde{u}_{\phi n} = 0
\end{aligned}
$$

where

$$
\begin{aligned}
q_0^1 &= -\frac{2}{R_d}\frac{1}{h_\xi^2}, \\
q_1^1 &= -\frac{2}{R_d}\frac{1}{h_\eta^2}, \\
q_2^1 &= \frac{U_{\xi s}}{h_\xi} + \frac{2}{R_d}\left(-\frac{1}{h_\xi^2\sigma}\frac{\partial \sigma}{\partial \xi} - \frac{1}{h_\xi^2 h_\eta}\frac{\partial h_\eta}{\partial \xi} + \frac{1}{h_\xi^3}\frac{\partial h_\xi}{\partial \xi}\right), \\
q_3^1 &= \frac{U_{\eta s}}{h_\eta} + \frac{2}{R_d}\left(-\frac{1}{h_\eta^2\sigma}\frac{\partial \sigma}{\partial \eta} - \frac{1}{h_\xi h_\eta^2}\frac{\partial h_\xi}{\partial \eta} + \frac{1}{h_\eta^3}\frac{\partial h_\eta}{\partial \eta}\right), \\
q_4^1 &= -\frac{4}{R_d}\frac{1}{h_\xi^2 h_\eta}\frac{\partial h_\xi}{\partial \eta}, \\
q_5^1 &= \frac{4}{R_d}\frac{1}{h_\xi h_\eta^2}\frac{\partial h_\eta}{\partial \xi}, \\
q_6^1 &= \frac{2}{R_d}\frac{n^2}{\sigma^2} + \frac{U_{\eta s}}{h_\xi h_\eta}\frac{\partial h_\xi}{\partial \eta} + \frac{1}{h_\xi}\frac{\partial}{\partial \xi}U_{\xi s} \\
&\quad +\frac{2}{R_d}\left[\frac{1}{h_\xi^3\sigma}\frac{\partial h_\xi}{\partial \xi}\frac{\partial \sigma}{\partial \xi} - \frac{1}{h_\xi^2\sigma}\frac{\partial^2 \sigma}{\partial \xi^2} + \left(\frac{1}{h_\xi \sigma}\frac{\partial \sigma}{\partial \xi}\right)^2 + \left(\frac{1}{h_\xi h_\eta}\frac{\partial h_\xi}{\partial \eta}\right)^2\right] \\
&\quad +\frac{2}{R_d}\left[-\frac{1}{h_\xi h_\eta^2}\frac{\partial^2 h_\xi}{\partial \eta^2} + \frac{1}{h_\xi^3 h_\eta}\frac{\partial h_\xi}{\partial \xi}\frac{\partial h_\eta}{\partial \xi} + \left(\frac{1}{h_\xi h_\eta}\frac{\partial h_\eta}{\partial \xi}\right)^2 - \frac{1}{h_\xi^2 h_\eta}\frac{\partial^2 h_\eta}{\partial \xi^2}\right]
\end{aligned}
$$

$$
\begin{aligned}
&+\frac{2}{R_d}\left(\frac{1}{h_\xi h_\eta^3}\frac{\partial h_\eta}{\partial \eta}\frac{\partial h_\xi}{\partial \eta}-\frac{1}{h_\xi h_\eta^2\sigma}\frac{\partial \sigma}{\partial \eta}\frac{\partial h_\xi}{\partial \eta}\right),\\
q_7^1 &= \frac{U_{\xi s}}{h_\xi h_\eta}\frac{\partial h_\xi}{\partial \eta}-\frac{2U_{\eta s}}{h_\xi h_\eta}\frac{\partial h_\eta}{\partial \xi}+\frac{1}{h_\eta}\frac{\partial}{\partial \eta}U_{\xi s}\\
&+\frac{2}{R_d}\left(-\frac{1}{h_\xi^2 h_\eta}\frac{\partial^2 h_\xi}{\partial \xi\partial \eta}-\frac{1}{h_\xi h_\eta\sigma}\frac{\partial^2\sigma}{\partial\xi\partial\eta}+\frac{1}{h_\xi h_\eta\sigma^2}\frac{\partial\sigma}{\partial\xi}\frac{\partial\sigma}{\partial\eta}+\frac{1}{h_\xi h_\eta^2}\frac{\partial^2 h_\eta}{\partial\xi\partial\eta}\right)\\
&+\frac{2}{R_d}\left(-\frac{1}{h_\xi h_\eta^3}\frac{\partial h_\eta}{\partial\eta}\frac{\partial h_\eta}{\partial\xi}+\frac{2}{h_\xi h_\eta^2\sigma}\frac{\partial\sigma}{\partial\eta}\frac{\partial h_\eta}{\partial\xi}+\frac{1}{h_\xi^3 h_\eta}\frac{\partial h_\xi}{\partial\eta}\frac{\partial h_\xi}{\partial\xi}\right),\\
q_8^1 &= \frac{4}{R_d}\frac{n}{h_\xi\sigma^2}\frac{\partial\sigma}{\partial\xi},\\
q_9^1 &= \frac{1}{2h_\xi}\ ;
\end{aligned}
$$

$$
\begin{aligned}
&\frac{\partial}{\partial t}\tilde{u}_{\eta n}+q_9^2\frac{\partial}{\partial\eta}\tilde{p}_n\ +q_0^2\frac{\partial^2}{\partial\xi^2}\tilde{u}_{\eta n}+q_1^2\frac{\partial^2}{\partial\eta^2}\tilde{u}_{\eta n}+q_2^2\frac{\partial}{\partial\xi}\tilde{u}_{\xi n}\\
&+q_3^2\frac{\partial}{\partial\eta}\tilde{u}_{\xi n}+q_4^2\frac{\partial}{\partial\xi}\tilde{u}_{\eta n}+q_5^2\frac{\partial}{\partial\eta}\tilde{u}_{\eta n}+q_6^2\tilde{u}_{\xi n}+q_7^2\tilde{u}_{\eta n}+\iota q_8^2\tilde{u}_{\phi n}\ =0
\end{aligned}
$$

where

$$
\begin{aligned}
q_0^2 &= -\frac{2}{R_d}\frac{1}{h_\xi^2},\\
q_1^2 &= -\frac{2}{R_d}\frac{1}{h_\eta^2},\\
q_2^2 &= \frac{4}{R_d}\frac{1}{h_\xi^2 h_\eta}\frac{\partial h_\xi}{\partial\eta},\\
q_3^2 &= -\frac{4}{R_d}\frac{1}{h_\xi h_\eta^2}\frac{\partial h_\eta}{\partial\xi},\\
q_4^2 &= \frac{U_{\xi s}}{h_\xi}+\frac{2}{R_d}\left(-\frac{1}{h_\xi^2\sigma}\frac{\partial\sigma}{\partial\xi}-\frac{1}{h_\xi^2 h_\eta}\frac{\partial h_\eta}{\partial\xi}+\frac{1}{h_\xi^3}\frac{\partial h_\xi}{\partial\xi}\right),\\
q_5^2 &= \frac{U_{\eta s}}{h_\eta}+\frac{2}{R_d}\left(-\frac{1}{h_\eta^2\sigma}\frac{\partial\sigma}{\partial\eta}-\frac{1}{h_\xi h_\eta^2}\frac{\partial h_\xi}{\partial\eta}+\frac{1}{h_\eta^3}\frac{\partial h_\eta}{\partial\eta}\right),\\
q_6^2 &= \frac{-2U_{\xi s}}{h_\xi h_\eta}\frac{\partial h_\xi}{\partial\eta}+\frac{U_{\eta s}}{h_\xi h_\eta}\frac{\partial h_\eta}{\partial\xi}+\frac{1}{h_\xi}\frac{\partial}{\partial\xi}U_{\eta s}\\
&+\frac{2}{R_d}\left(-\frac{1}{h_\xi h_\eta\sigma}\frac{\partial^2\sigma}{\partial\xi\partial\eta}+\frac{2}{h_\xi^2 h_\eta\sigma}\frac{\partial h_\xi}{\partial\eta}\frac{\partial\sigma}{\partial\xi}-\frac{1}{h_\xi h_\eta^2}\frac{\partial^2 h_\eta}{\partial\xi\partial\eta}+\frac{1}{h_\xi^2 h_\eta}\frac{\partial^2 h_\xi}{\partial\xi\partial\eta}\right)
\end{aligned}
$$

$$
\begin{aligned}
&+\frac{2}{R_d}\left(-\frac{1}{h_\xi^3 h_\eta}\frac{\partial h_\xi}{\partial \xi}\frac{\partial h_\xi}{\partial \eta}+\frac{1}{h_\xi h_\eta \sigma^2}\frac{\partial \sigma}{\partial \xi}\frac{\partial \sigma}{\partial \eta}+\frac{1}{h_\xi h_\eta^3}\frac{\partial h_\eta}{\partial \eta}\frac{\partial h_\eta}{\partial \xi}\right),\\
q_7^2 &= \frac{2}{R_d}\frac{n^2}{\sigma^2}+\frac{U_{\xi s}}{h_\xi h_\eta}\frac{\partial h_\eta}{\partial \xi}+\frac{1}{h_\eta}\frac{\partial}{\partial \eta}U_{\eta s}\\
&+\frac{2}{R_d}\left[\left(\frac{1}{h_\eta \sigma}\frac{\partial \sigma}{\partial \eta}\right)^2-\frac{1}{h_\eta^2 \sigma}\frac{\partial^2 \sigma}{\partial \eta^2}+\left(\frac{1}{h_\xi h_\eta}\frac{\partial h_\eta}{\partial \xi}\right)^2-\frac{1}{h_\xi^2 h_\eta}\frac{\partial^2 h_\eta}{\partial \xi^2}\right]\\
&+\frac{2}{R_d}\left(-\frac{1}{h_\xi^2 h_\eta \sigma}\frac{\partial \sigma}{\partial \xi}\frac{\partial h_\eta}{\partial \xi}+\frac{1}{h_\xi h_\eta^3}\frac{\partial h_\eta}{\partial \eta}\frac{\partial h_\xi}{\partial \eta}+\frac{1}{h_\eta^3 \sigma}\frac{\partial \sigma}{\partial \eta}\frac{\partial h_\eta}{\partial \eta}-\frac{1}{h_\xi h_\eta^2}\frac{\partial^2 h_\xi}{\partial \eta^2}\right)\\
&+\frac{2}{R_d}\left[\frac{1}{h_\xi^3 h_\eta}\frac{\partial h_\xi}{\partial \xi}\frac{\partial h_\eta}{\partial \xi}+\left(\frac{1}{h_\xi h_\eta}\frac{\partial h_\xi}{\partial \eta}\right)^2\right],\\
q_8^2 &= \frac{4}{R_d}\frac{n}{h_\eta \sigma^2}\frac{\partial \sigma}{\partial \eta},\\
q_9^2 &= \frac{1}{2h_\eta}\ ;
\end{aligned}
$$

and

$$
\begin{aligned}
&\frac{\partial}{\partial t}\tilde{u}_{\phi n}+\iota q_7^3\ \tilde{p}_n+q_0^3\frac{\partial^2}{\partial \xi^2}\tilde{u}_{\phi n}+q_1^3\frac{\partial^2}{\partial \eta^2}\tilde{u}_{\phi n}+q_2^3\frac{\partial}{\partial \xi}\tilde{u}_{\phi n}\\
&+q_3^3\frac{\partial}{\partial \eta}\tilde{u}_{\phi n}+\iota q_4^3\tilde{u}_{\xi n}+\iota q_5^3\tilde{u}_{\eta n}\ +q_6^3\tilde{u}_{\phi n}\ =0
\end{aligned}
$$

where

$$
\begin{aligned}
q_0^3 &= -\frac{2}{R_d}\frac{1}{h_\xi^2},\\
q_1^3 &= -\frac{2}{R_d}\frac{1}{h_\eta^2},\\
q_2^3 &= \frac{U_{\xi s}}{h_\xi}+\frac{2}{R_d}\left(\frac{1}{h_\xi^3}\frac{\partial h_\xi}{\partial \xi}-\frac{1}{h_\xi^2 \sigma}\frac{\partial \sigma}{\partial \xi}-\frac{1}{h_\xi^2 h_\eta}\frac{\partial h_\eta}{\partial \xi}\right),\\
q_3^3 &= \frac{U_{\eta s}}{h_\eta}+\frac{2}{R_d}\left(-\frac{1}{h_\xi h_\eta^2}\frac{\partial h_\xi}{\partial \eta}+\frac{1}{h_\eta^3}\frac{\partial h_\eta}{\partial \eta}-\frac{1}{h_\eta^2 \sigma}\frac{\partial \sigma}{\partial \eta}\right),\\
q_4^3 &= -\frac{4}{R_d}\frac{n}{h_\xi \sigma^2}\frac{\partial \sigma}{\partial \xi},\\
q_5^3 &= -\frac{4}{R_d}\frac{n}{h_\eta \sigma^2}\frac{\partial \sigma}{\partial \eta},
\end{aligned}
$$

$$q_6^3 = \frac{2}{R_d}\frac{n^2}{\sigma^2} + \frac{U_{\xi s}}{h_\xi \sigma}\frac{\partial \sigma}{\partial \xi} + \frac{U_{\eta s}}{h_\eta \sigma}\frac{\partial \sigma}{\partial \eta} + \frac{2}{R_d}\left[\left(\frac{1}{h_\xi \sigma}\frac{\partial \sigma}{\partial \xi}\right)^2 + \left(\frac{1}{h_\eta \sigma}\frac{\partial \sigma}{\partial \eta}\right)^2\right],$$

$$q_7^3 = \frac{n}{2\sigma}.$$

Next, we address the boundary conditions that need to be imposed on the perturbations to solve the above perturbation equations. Clearly for $\xi = 0$, which corresponds to the point at infinity, we set

$$\begin{aligned} \tilde{p}_n(0,\eta,t) &= 0, \\ \tilde{u}_{\xi n}(0,\eta,t) &= 0, \\ \tilde{u}_{\eta n}(0,\eta,t) &= 0, \\ \tilde{u}_{\phi n}(0,\eta,t) &= 0. \end{aligned}$$

Since we impose the no-slip boundary condition at $\xi = 1$, we have

$$\begin{aligned} \tilde{u}_{\xi n}(1,\eta,t) &= 0, \\ \tilde{u}_{\eta n}(1,\eta,t) &= 0, \\ \tilde{u}_{\phi n}(1,\eta,t) &= 0. \end{aligned}$$

For $\tilde{p}_n$, the perturbed divergence condition is imposed at $\xi = 1$ to give

$$\frac{\partial}{\partial \xi}\tilde{u}_{\xi n} = 0.$$

The difficulty comes from imposing boundary conditions along the axis of symmetry at $\eta = 0$ and $\eta = 1$. Because of the $\frac{1}{\sigma}$ terms, care must be taken in the limit $\sigma \to 0$. Quarterpelle and Verri [29] encounter similar problems in their discussions of solving the Navier-Stokes equations in primitive variables in spherical and cylindrical coordinate system using spectral methods. They deal with such coordinate singularity problems occurring in their equations by imposing differentiability of vectors and scalars at the origin by employing L'Hôpital's rule. They show that for each Fourier

mode, the boundary conditions are determined to be

$$\begin{aligned}
\frac{\partial}{\partial\eta}\tilde{p}_0(\xi,0,t) &= 0,\\
\frac{\partial}{\partial\eta}\tilde{p}_0(\xi,1,t) &= 0,\\
\frac{\partial}{\partial\eta}\tilde{u}_{\xi 0}(\xi,0,t) &= 0,\\
\frac{\partial}{\partial\eta}\tilde{u}_{\xi 0}(\xi,1,t) &= 0,\\
\tilde{u}_{\eta 0}(\eta,0,t) &= 0,\\
\tilde{u}_{\eta 0}(\eta,1,t) &= 0,\\
\tilde{u}_{\phi 0}(\eta,0,t) &= 0,\\
\tilde{u}_{\phi 0}(\eta,1,t) &= 0,
\end{aligned}$$

for $n = 0$;

$$\begin{aligned}
\tilde{p}_1(\xi,0,t) &= 0,\\
\tilde{p}_1(\xi,1,t) &= 0,\\
\tilde{u}_{\xi 1}(\eta,0,t) &= 0,\\
\tilde{u}_{\xi 1}(\eta,1,t) &= 0,\\
\tilde{u}_{\eta 1}(\eta,0,t) + \iota\tilde{u}_{\phi 1}(\eta,0,t) &= 0,\\
\tilde{u}_{\eta 1}(\eta,1,t) - \iota\tilde{u}_{\phi 1}(\eta,1,t) &= 0,\\
\frac{\partial}{\partial\eta}\tilde{u}_{\eta 1}(\eta,0,t) - \iota\frac{\partial}{\partial\eta}\tilde{u}_{\phi 1}(\eta,0,t) &= 0,\\
\frac{\partial}{\partial\eta}\tilde{u}_{\eta 1}(\eta,1,t) + \iota\frac{\partial}{\partial\eta}\tilde{u}_{\phi 1}(\eta,1,t) &= 0,
\end{aligned}$$

for $n = 1$; and

$$\begin{aligned}
\tilde{p}_n(\xi,0,t) &= 0,\\
\tilde{p}_n(\xi,1,t) &= 0,\\
\tilde{u}_{\xi n}(\eta,0,t) &= 0,
\end{aligned}$$

$$\begin{aligned}
\tilde{u}_{\xi n}(\eta, 1, t) &= 0, \\
\tilde{u}_{\eta n}(\eta, 0, t) &= 0, \\
\tilde{u}_{\eta n}(\eta, 1, t) &= 0, \\
\tilde{u}_{\phi n}(\eta, 0, t) &= 0, \\
\tilde{u}_{\phi n}(\eta, 1, t) &= 0
\end{aligned}$$

for $n \geq 2$.

The perturbation equations along with the boundary conditions can be solved for each Fourier mode in several ways. One way is by letting $\tilde{u} = e^{\alpha t}\tilde{v}$ and solving them as a generalized eigenvalue problem. Let $\alpha_1, \alpha_2, \ldots$ be the eigenvalues, and $\tilde{v}_1, \tilde{v}_2, \tilde{v}_3, \ldots$ be the eigenfunctions associated with them. Rearrange the eigenvalues so that $\mathrm{Re}(\alpha_1) \geq \mathrm{Re}(\alpha_2) \geq \mathrm{Re}(\alpha_3) \ldots$ Since the equations are linear,

$$\tilde{u} \sim c_1 e^{\alpha_1 t}\tilde{v}_1 + c_2 e^{\alpha_2 t}\tilde{v}_2 + c_3 e^{\alpha_2 t}\tilde{v}_3 + \ldots$$

If $\mathrm{Re}(\alpha_1)$ is negative, $\tilde{u}$ decays exponentially, and the base flow is stable. On the other hand, if $\mathrm{Re}(\alpha_1)$ is positive, $\tilde{u}$ blows up exponentially and denotes instability. By tracking the leading eigenvalues generated for each R_d, the critical Reynolds number for which $\mathrm{Re}(\alpha_1)$ is zero can be determined.

In our case, instead of solving the system of equations as a generalized eigenvalue problem, we evolve the perturbations in time. When t is large, the term $e^{\alpha_1 t}\tilde{v}_1$ dominates $\tilde{u}$. Taking the logarithm of $\tilde{u}$ as t becomes large should result in a linear growth curve whose slope, i.e., the growth rate, is equal to the real part of α_1. If α_1 is complex, the logarithmic growth curve is such that the peaks of the oscillations line up linearly. The real and the imaginary part of α_1 can then be determined from taking the slope of the peaks and measuring the distance between them.

It is also of interest to determine the secondary eigenvalue α_2 as well. The results of Natarajan and Acrivos [26] and Tomboulides, Orszag, and Karniadakis [44] indicate that when $\mathrm{Re}(\alpha_2)$ goes from negative to positive, the flow may become oscillatory. It is, therefore, important to determine the critical Reynolds number around which

this secondary transition may occur. Even though our method does not employ the generalized eigenvalue method, it is still possible to determine α_2 . When t is large, $\tilde{u} \approx C\tilde{v}_1$ where C is some constant. Since the eigenfunction $\tilde{v}_1$ is now known, a Gram-Schmidt orthogonalization method can be used to determine α_2 and $\tilde{v}_2$.

To further simplify the computation, we write the perturbations as

$$\tilde{u} = \mathrm{Re}(\tilde{u}) + \iota\,\mathrm{Im}(\tilde{u}).$$

Rearranging the perturbation equations gives

$$\mathbf{\Theta}\left(\mathrm{Re}(\tilde{p}_n), \mathrm{Re}(\tilde{u}_{\xi n}), \mathrm{Re}(\tilde{u}_{\eta n}), -\mathrm{Im}(\tilde{u}_{\phi n})\right) + \iota\mathbf{\Theta}\left(\mathrm{Im}(\tilde{p}_n), \mathrm{Im}(\tilde{u}_{\xi n}), \mathrm{Im}(\tilde{u}_{\eta n}), \mathrm{Re}(\tilde{u}_{\phi n})\right) = 0$$

where $\mathbf{\Theta}$ is a vector of functions with components Θ_k, $k = 0, 1, 2, 3$ defined this way. Let

$$\begin{aligned} l_n^0 &= \mathrm{Re}(\tilde{p}_n) = \mathrm{Im}(\tilde{p}_n), \\ l_n^1 &= \mathrm{Re}(\tilde{u}_{\xi n}) = \mathrm{Im}(\tilde{u}_{\xi n}), \\ l_n^2 &= \mathrm{Re}(\tilde{u}_{\eta n}) = \mathrm{Im}(\tilde{u}_{\eta n}), \\ l_n^3 &= -\mathrm{Im}(\tilde{u}_{\phi n}) = \mathrm{Re}(\tilde{u}_{\phi n}). \end{aligned}$$

These quantities satisfy the following equations:

$$\Theta_0 = q_0^0 \frac{\partial}{\partial \xi} l_n^1 + q_1^0 \frac{\partial}{\partial \eta} l_n^2 + q_2^0 l_n^1 + q_3^0 l_n^2 + q_4^0 l_n^3; \tag{2.26}$$

$$\Theta_1 = \frac{\partial}{\partial t} l_n^1 + q_9^1 \frac{\partial}{\partial \xi} l_n^0 + F_1(\xi, \eta, t), \tag{2.27}$$

where

$$\begin{aligned} F_1(\xi, \eta, t) &= q_0^1 \frac{\partial^2}{\partial \xi^2} l_n^1 + q_1^1 \frac{\partial^2}{\partial \eta^2} l_n^1 + q_2^1 \frac{\partial}{\partial \xi} l_n^1 + q_3^1 \frac{\partial}{\partial \eta} l_n^1 \\ &\quad + q_4^1 \frac{\partial}{\partial \xi} l_n^2 + q_5^1 \frac{\partial}{\partial \eta} l_n^2 + q_6^1 l_n^1 + q_7^1 l_n^2 + q_8^1 l_n^3; \end{aligned}$$

$$\Theta_2 = \frac{\partial}{\partial t} l_n^2 + q_9^1 \frac{\partial}{\partial \eta} l_n^0 + F_2(\xi, \eta, t), \tag{2.28}$$

where

$$\begin{aligned} F_2(\xi,\eta,t) &= q_0^2 \frac{\partial^2}{\partial \xi^2} l_n^2 + q_1^2 \frac{\partial^2}{\partial \eta^2} l_n^2 + q_2^2 \frac{\partial}{\partial \xi} l_n^1 + q_3^2 \frac{\partial}{\partial \eta} l_n^1 \\ &\quad + q_4^2 \frac{\partial}{\partial \xi} l_n^2 + q_5^2 \frac{\partial}{\partial \eta} l_n^2 + q_6^2 l_n^1 + q_7^2 l_n^2 + q_8^2 l_n^3; \end{aligned}$$

and

$$\Theta_3 = \frac{\partial}{\partial t} l_n^3 - q_7^3 l_n^0 + F_3(\xi, \eta, t), \tag{2.29}$$

where

$$\begin{aligned} F_3(\xi,\eta,t) &= q_0^3 \frac{\partial^2}{\partial \xi^2} l_n^3 + q_1^3 \frac{\partial^2}{\partial \eta^2} l_n^3 + q_2^3 \frac{\partial}{\partial \xi} l_n^3 + q_3^3 \frac{\partial}{\partial \eta} l_n^3 \\ &\quad - q_4^3 l_n^1 - q_5^3 l_n^2 + q_6^3 l_n^3. \end{aligned}$$

The boundary conditions become

$$\begin{aligned} \frac{\partial}{\partial \eta} l_0^0(\xi, 0, t) &= 0, \\ \frac{\partial}{\partial \eta} l_0^0(\xi, 1, t) &= 0, \\ \frac{\partial}{\partial \eta} l_0^1(\xi, 0, t) &= 0, \\ \frac{\partial}{\partial \eta} l_0^1(\xi, 1, t) &= 0, \\ l_0^2(\eta, 0, t) &= 0, \\ l_0^2(\eta, 1, t) &= 0, \\ l_0^3(\eta, 0, t) &= 0, \\ l_0^3(\eta, 1, t) &= 0, \end{aligned} \tag{2.30}$$

for $n = 0$;

$$l_1^0(\xi, 0, t) = 0, \tag{2.31}$$

$$
\begin{aligned}
l_1^0(\xi,1,t) &= 0,\\
l_1^1(\eta,0,t) &= 0,\\
l_1^1(\eta,1,t) &= 0,\\
l_1^2(\eta,0,t)+l_1^3(\eta,0,t) &= 0,\\
l_1^2(\eta,1,t)-l_1^3(\eta,1,t) &= 0,\\
\frac{\partial}{\partial\eta}l_1^2(\eta,0,t)-\frac{\partial}{\partial\eta}l_1^3(\eta,0,t) &= 0,\\
\frac{\partial}{\partial\eta}l_1^2(\eta,1,t)+\frac{\partial}{\partial\eta}l_1^3(\eta,1,t) &= 0,
\end{aligned}
$$

for $n = 1$; and

$$
\begin{aligned}
l_n^0(\xi,0,t) &= 0,\\
l_n^0(\xi,1,t) &= 0,\\
l_n^1(\eta,0,t) &= 0,\\
l_n^1(\eta,1,t) &= 0,\\
l_n^2(\eta,0,t) &= 0,\\
l_n^2(\eta,1,t) &= 0,\\
l_n^3(\eta,0,t) &= 0,\\
l_n^3(\eta,1,t) &= 0
\end{aligned}
\tag{2.32}
$$

for $n \geq 2$.

This tells us that determining the behavior of $(l_n^0, l_n^1, l_n^2, l_n^3)$ in time gives the behavior of both the real and the imaginary part of the perturbations.

2.4.2 Numerical formulation

The perturbation equations are solved numerically using the Crank-Nicolson method in time and second order finite differencing in space. Let $t = N\Delta t$, and denote, for now,

$$l_n^k(\xi,\eta,t) = l_n^k(\xi,\eta,N\Delta t) = l_n^{k,N}.$$

Applying the Crank-Nicolson integration in time gives

$$\begin{aligned}
q_0^0\frac{\partial}{\partial\xi}l_n^{1,N+1}+q_1^0\frac{\partial}{\partial\eta}l_n^{2,N+1}+\ q_2^0l_n^{1,N+1}+q_3^0l_n^{2,N+1}+q_4^0l_n^{3,N+1} &= 0,\\
\frac{\left(l_n^{1,N+1}-l_n^{1,N}\right)}{\Delta t}+q_9^1\frac{\partial}{\partial\xi}l_n^{0,N+1}+\frac{F_1(\xi,\eta,(N+1)\Delta t)+F_1(\xi,\eta,N\Delta t)}{2} &= 0,\\
\frac{\left(l_n^{2,N+1}-l_n^{2,N}\right)}{\Delta t}+q_9^2\frac{\partial}{\partial\eta}l_n^{0,N+1}+\frac{F_2(\xi,\eta,(N+1)\Delta t)+F_2(\xi,\eta,N\Delta t)}{2} &= 0,\\
\frac{\left(l_n^{3,N+1}-l_n^{3,N}\right)}{\Delta t}-q_7^3l_n^{0,N+1}+\frac{F_3(\xi,\eta,(N+1)\Delta t)+F_3(\xi,\eta,N\Delta t)}{2} &= 0.
\end{aligned}$$

At each (i,j), there are four equations coupled with four unknowns.

Let $\Delta x=\frac{1}{m+1}$, and let $\xi=i\Delta x$, $\eta=j\Delta x$, $i,j=0,...,m+1$. The perturbations can be discretized such that for $k=0,1,2$, and 3,

$$l_n^k(\xi,\eta,t)=l_n^k(i\Delta x,j\Delta x,N\Delta t)=l_{n_{i,j}}^{k,N}.$$

Discretizing the perturbation equations (2.26),(2.27),(2.28), and (2.29) gives

$$\begin{aligned}
\Gamma_{0_{i,j}} &= C_{0_{i,j}}^0\,l_{n_{i-1,j}}^{1,N+1}+C_{1_{i,j}}^0l_{n_{i,j-1}}^{2,N+1}+C_{2_{i,j}}^0l_{n_{i,j}}^{1,N+1}+C_{3_{i,j}}^0l_{n_{i,j}}^{2,N+1}\\
&\quad +C_{4_{i,j}}^0l_{n_{i,j}}^{3,N+1}+C_{5_{i,j}}^0l_{n_{i,j+1}}^{2,N+1}+C_{6_{i,j}}^0l_{n_{i+1,j}}^{1,N+1},
\end{aligned}\tag{2.33}$$

where

$$\begin{aligned}
C_{0_{i,j}}^0 &= -\frac{q_0^0}{2\Delta x},\\
C_{1_{i,j}}^0 &= -\frac{q_1^0}{2\Delta x},\\
C_{2_{i,j}}^0 &= q_2^0,\\
C_{3_{i,j}}^0 &= q_3^0,\\
C_{4_{i,j}}^0 &= q_4^0,\\
C_{5_{i,j}}^0 &= \frac{q_1^0}{2\Delta x},\\
C_{6_{i,j}}^0 &= \frac{q_0^0}{2\Delta x};
\end{aligned}$$

$$\begin{aligned}\Gamma_{1_{i,j}} &= C^1_{0_{i,j}} l^{0,N+1}_{n_{i-1,j}} + C^1_{1_{i,j}} l^{1,N+1}_{n_{i-1,j}} + C^1_{2_{i,j}} l^{2,N+1}_{n_{i-1,j}} + C^1_{3_{i,j}} l^{1,N+1}_{n_{i,j-1}} \\ &+C^1_{4_{i,j}} l^{2,N+1}_{n_{i,j-1}} + C^1_{5_{i,j}} l^{1,N+1}_{n_{i,j}} + C^1_{6_{i,j}} l^{2,N+1}_{n_{i,j}} + C^1_{7_{i,j}} l^{3,N+1}_{n_{i,j}} \\ &+C^1_{8_{i,j}} l^{1,N+1}_{n_{i,j+1}} + C^1_{9_{i,j}} l^{2,N+1}_{n_{i,j+1}} + C^1_{10_{i,j}} l^{0,N+1}_{n_{i+1,j}} + C^1_{11_{i,j}} l^{1,N+1}_{n_{i+1,j}} \\ &+C^1_{12_{i,j}} l^{2,N+1}_{n_{i+1,j}} + g^N_{1_{i,j}},\end{aligned} \tag{2.34}$$

where

$$\begin{aligned}g^N_{1_{i,j}} &= C^1_{0_{i,j}} l^{0,N}_{n_{i-1,j}} + C^1_{1_{i,j}} l^{1,N}_{n_{i-1,j}} + C^1_{2_{i,j}} l^{2,N}_{n_{i-1,j}} + C^1_{3_{i,j}} l^{1,N}_{n_{i,j-1}} \\ &+C^1_{4_{i,j}} l^{2,N}_{n_{i,j-1}} + \left(C^1_{5_{i,j}} - \frac{2}{\Delta t}\right) l^{1,N}_{n_{i,j}} + C^1_{6_{i,j}} l^{2,N}_{n_{i,j}} + C^1_{7_{i,j}} l^{3,N}_{n_{i,j}} \\ &+C^1_{8_{i,j}} l^{1,N}_{n_{i,j+1}} + C^1_{9_{i,j}} l^{2,N}_{n_{i,j+1}} + C^1_{10_{i,j}} l^{0,N}_{n_{i+1,j}} + C^1_{11_{i,j}} l^{1,N}_{n_{i+1,j}} \\ &+C^1_{12_{i,j}} l^{2,N}_{n_{i+1,j}},\end{aligned}$$

$$C^1_{0_{i,j}} = -\frac{q^1_9}{2\Delta x},$$

$$C^1_{1_{i,j}} = \frac{q^1_0}{2\Delta x^2} - \frac{q^1_2}{4\Delta x},$$

$$C^1_{2_{i,j}} = -\frac{q^1_4}{4\Delta x},$$

$$C^1_{3_{i,j}} = \frac{q^1_1}{2\Delta x^2} - \frac{q^1_3}{4\Delta x},$$

$$C^1_{4_{i,j}} = -\frac{q^1_5}{4\Delta x},$$

$$C^1_{5_{i,j}} = \frac{q^1_6}{2} + \frac{1}{\Delta t} - \frac{q^1_0}{\Delta x^2} - \frac{q^1_1}{\Delta x^2},$$

$$C^1_{6_{i,j}} = \frac{q^1_7}{2},$$

$$C^1_{7_{i,j}} = \frac{q^1_8}{2},$$

$$C^1_{8_{i,j}} = \frac{q^1_1}{2\Delta x^2} + \frac{q^1_3}{4\Delta x},$$

$$C^1_{9_{i,j}} = \frac{q^1_5}{4\Delta x},$$

$$C^1_{10_{i,j}} = \frac{q^1_9}{2\Delta x},$$

$$C^1_{11_{i,j}} = \frac{q^1_0}{2\Delta x^2} + \frac{q^1_2}{4\Delta x},$$

$$C^1_{12_{i,j}} = \frac{q^1_4}{4\Delta x};$$

$$\begin{aligned}\Gamma_{2_{i,j}} &= C^2_{0_{i,j}} l^{1,N+1}_{n_{i-1,j}} + C^2_{1_{i,j}} l^{2,N+1}_{n_{i-1,j}} + C^2_{2_{i,j}} l^{0,N+1}_{n_{i,j-1}} + C^2_{3_{i,j}} l^{1,N+1}_{n_{i,j-1}} \\ &+C^2_{4_{i,j}} l^{2,N+1}_{n_{i,j-1}} + C^2_{5_{i,j}} l^{1,N+1}_{n_{i,j}} + C^2_{6_{i,j}} l^{2,N+1}_{n_{i,j}} + C^2_{7_{i,j}} l^{3,N+1}_{n_{i,j}} \\ &+C^2_{8_{i,j}} l^{0,N+1}_{n_{i,j+1}} + C^2_{9_{i,j}} l^{1,N+1}_{n_{i,j+1}} + C^2_{10_{i,j}} l^{2,N+1}_{n_{i,j+1}} + C^2_{11_{i,j}} l^{1,N+1}_{n_{i+1,j}} \\ &+C^2_{12_{i,j}} l^{2,N+1}_{n_{i+1,j}} + g^N_{2_{i,j}},\end{aligned} \tag{2.35}$$

where

$$\begin{aligned}g^N_{2_{i,j}} &= C^2_{0_{i,j}} l^{1,N}_{n_{i-1,j}} + C^2_{1_{i,j}} l^{2,N}_{n_{i-1,j}} + C^2_{2_{i,j}} l^{0,N}_{n_{i,j-1}} + C^2_{3_{i,j}} l^{1,N}_{n_{i,j-1}} \\ &+C^2_{4_{i,j}} l^{2,N}_{n_{i,j-1}} + C^2_{5_{i,j}} l^{1,N}_{n_{i,j}} + \left(C^2_{6_{i,j}} - \frac{2}{\Delta t}\right) l^{2,N}_{n_{i,j}} + C^2_{7_{i,j}} l^{3,N}_{n_{i,j}} \\ &+C^2_{8_{i,j}} l^{0,N}_{n_{i,j+1}} + C^2_{9_{i,j}} l^{1,N}_{n_{i,j+1}} + C^2_{10_{i,j}} l^{2,N}_{n_{i,j+1}} + C^2_{11_{i,j}} l^{1,N}_{n_{i+1,j}} + C^2_{12_{i,j}} l^{2,N}_{n_{i+1,j}},\end{aligned}$$

$$C^2_{0_{i,j}} = -\frac{q_2^2}{4\Delta x},$$

$$C^2_{1_{i,j}} = \frac{q_0^2}{2\Delta x^2} - \frac{q_4^2}{4\Delta x},$$

$$C^2_{2,j} = -\frac{q_9^2}{2\Delta x},$$

$$C^2_{3_{i,j}} = -\frac{q_3^2}{4\Delta x},$$

$$C^2_{4_{i,j}} = \frac{q_1^2}{2\Delta x^2} - \frac{q_5^2}{4\Delta x},$$

$$C^2_{5_{i,j}} = \frac{q_6^2}{2},$$

$$C^2_{6_{i,j}} = \frac{q_7^2}{2} + \frac{1}{\Delta t} - \frac{q_0^2}{\Delta x^2} - \frac{q_1^2}{\Delta x^2},$$

$$C^2_{7_{i,j}} = \frac{q_8^2}{2},$$

$$C^2_{8_{i,j}} = \frac{q_9^2}{2\Delta x},$$

$$C^2_{9_{i,j}} = \frac{q_3^2}{4\Delta x},$$

$$C^2_{10_{i,j}} = \frac{q_1^2}{2\Delta x^2} + \frac{q_5^2}{4\Delta x},$$

$$C^2_{11_{i,j}} = \frac{q_2^2}{4\Delta x},$$

$$C^2_{12_{i,j}} = \frac{q_0^2}{2\Delta x^2} + \frac{q_4^2}{4\Delta x};$$

and

$$\begin{aligned}\Gamma_{3_{i,j}} &= C^3_{0_{i,j}} l^{3,N+1}_{n_{i-1,j}} + C^3_{1_{i,j}} l^{3,N+1}_{n_{i,j-1}} + C^3_{2_{i,j}} l^{0,N+1}_{n_{i,j}} + C^3_{3_{i,j}} l^{1,N+1}_{n_{i,j}} \\ &\quad + C^3_{4_{i,j}} l^{2,N+1}_{n_{i,j}} + C^3_{5_{i,j}} l^{3,N+1}_{n_{i,j}} + C^3_{6_{i,j}} l^{3,N+1}_{n_{i,j+1}} \\ &\quad + C^3_{7_{i,j}} l^{3,N+1}_{n_{i+1,j}} + g^N_{3_{i,j}},\end{aligned} \tag{2.36}$$

where

$$\begin{aligned}g^N_{3_{i,j}} &= C^3_{0_{i,j}} l^{3,N}_{n_{i-1,j}} + C^3_{1_{i,j}} l^{3,N}_{n_{i,j-1}} + C^3_{2_{i,j}} l^{0,N}_{n_{i,j}} + C^3_{3_{i,j}} l^{1,N}_{n_{i,j}} \\ &\quad + C^3_{4_{i,j}} l^{2,N}_{n_{i,j}} + \left(C^3_{5_{i,j}} - \frac{2}{\Delta t} \right) l^{3,N}_{n_{i,j}} + C^3_{6_{i,j}} l^{3,N}_{n_{i,j+1}} \\ &\quad + C^3_{7_{i,j}} l^{3,N}_{n_{i+1,j}}, \\ C^3_{0_{i,j}} &= \frac{q^3_0}{2\Delta x^2} - \frac{q^3_2}{4\Delta x}, \\ C^3_{1_{i,j}} &= \frac{q^3_1}{2\Delta x^2} - \frac{q^3_3}{4\Delta x}, \\ C^3_{2_{i,j}} &= -q^3_7, \\ C^3_{3_{i,j}} &= -\frac{q^3_4}{2}, \\ C^3_{4_{i,j}} &= -\frac{q^3_5}{2}, \\ C^3_{5_{i,j}} &= \frac{q^3_6}{2} + \frac{1}{\Delta t} - \frac{q^3_0}{\Delta x^2} - \frac{q^3_1}{\Delta x^2}, \\ C^3_{6_{i,j}} &= \frac{q^3_1}{2\Delta x^2} + \frac{q^3_3}{4\Delta x}, \\ C^3_{7_{i,j}} &= \frac{q^3_0}{2\Delta x^2} + \frac{q^3_2}{4\Delta x}.\end{aligned}$$

We next discretize the boundary conditions. As stated before, at $\xi = 1$, the perturbed velocities are set to zero due to the no-slip condition on the body. For the perturbed pressure at $\xi = 1$, a one-sided derivative is used on the perturbed divergence free condition. This gives

$$\Gamma_{Bj} = C^0_{0_{m+1,j}} l^{1,N+1}_{n_{m-1,j}} + C^0_{1_{m+1,j}} l^{1,N+1}_{n_{m,j}}$$

where

$$\begin{aligned} C^0_{0_{m+1,j}} &= \frac{1}{2\Delta x}, \\ C^0_{1_{m+1,j}} &= -\frac{2}{\Delta x}. \end{aligned}$$

Along the axis of symmetry where $j = 0$ and $j = m + 1$, different boundary conditions are needed for each Fourier mode. It is clear from the boundary conditions (2.32) that, for modes $n \geq 2$, all the unknowns are set to zero at $j = 0$ and $j = m+1$. For $n = 0$, which corresponds to a symmetric perturbation, a one-sided second-order finite differencing can be used on the equations (2.30) to give

$$\begin{aligned} l^0_{0_{i,0}} &= \frac{4}{3}l^0_{0_{i,1}} - \frac{1}{3}l^0_{0_{i,2}}, \\ l^0_{0_{i,m+1}} &= \frac{4}{3}l^0_{0_{i,m}} - \frac{1}{3}l^0_{0_{i,m-1}}, \\ l^1_{0_{i,0}} &= \frac{4}{3}l^1_{0_{i,1}} - \frac{1}{3}l^1_{0_{i,2}}, \\ l^1_{0_{i,m+1}} &= \frac{4}{3}l^1_{0_{i,m}} - \frac{1}{3}l^1_{0_{i,m-1}}. \end{aligned}$$

The other unknowns can be set to zero.

For the $n = 1$ mode, the boundary conditions as indicated by (2.31) along $j = 0$ and $j = m + 1$ are somewhat tricky to implement. Clearly,

$$\begin{aligned} l^0_{1_{i,0}} &= 0, \\ l^0_{1_{i,m+1}} &= 0, \\ l^1_{1_{i,0}} &= 0, \\ l^1_{1_{i,m+1}} &= 0. \end{aligned}$$

For $l^2_{1_{i,j}}$ and $l^3_{1_{i,j}}$, one-sided second order finite differencing and some reshuffling give

$$\begin{aligned} l^2_{1_{i,0}} &= \frac{2}{3}l^2_{1_{i,1}} - \frac{1}{6}l^2_{1_{i,2}} - \frac{2}{3}l^3_{1_{i,1}} + \frac{1}{6}l^3_{1_{i,2}}, \\ l^3_{1_{i,0}} &= \frac{2}{3}l^3_{1_{i,1}} - \frac{1}{6}l^3_{1_{i,2}} - \frac{2}{3}l^2_{1_{i,1}} + \frac{1}{6}l^2_{1_{i,2}}, \end{aligned}$$

and

$$
\begin{aligned}
l^2_{1_{i,m+1}} &= \frac{2}{3}l^2_{1_{i,m}} - \frac{1}{6}l^2_{1_{i,m-1}} + \frac{2}{3}l^3_{1_{i,m}} - \frac{1}{6}l^3_{1_{i,m-1}}, \\
l^3_{1_{i,m+1}} &= \frac{2}{3}l^3_{1_{i,m}} - \frac{1}{6}l^3_{1_{i,m-1}} + \frac{2}{3}l^2_{1_{i,m}} - \frac{1}{6}l^2_{1_{i,m-1}}.
\end{aligned}
$$

Now, the difference equations (2.33), (2.34), (2.35), and (2.36) are linear and can be represented as a product of a matrix and a vector. Let $\mathbf{U}^N$ be the vector that is formed by rearranging the unknowns $\left(l^{0,N}_{n_{i,j}}, l^{1,N}_{n_{i,j}}, l^{2,N}_{n_{i,j}}, l^{3,N}_{n_{i,j}}\right)$, and let $\mathbf{U}^N_k$ be its components. First, set $\mathbf{U}^N_1 = l^{0,N}_{n_{1,1}}$, and increment j with $i = 1$ fixed until $\mathbf{U}^N_m = l^{0,N}_{n_{1,m}}$. Then, let $\mathbf{U}^N_{m+1} = l^{1,N}_{n_{1,1}}$ and increment j until $\mathbf{U}^N_{m+m} = l^{1,N}_{n_{1,m}}$. Then, let $\mathbf{U}^N_{2m+1} = l^{2,N}_{n_{1,1}}$ and increment j until $\mathbf{U}^N_{2m+m} = l^{2,N}_{n_{1,m}}$. Then, put $\mathbf{U}^N_{3m+1} = l^{3,N}_{n_{1,1}}$ and increment j until $\mathbf{U}^N_{3m+m} = l^{3,N}_{n_{1,m}}$. Now, increment i by one and repeat the whole process until $i = m$. Then, let $\mathbf{U}^N_{4m^2+j} = l^{0,N}_{n_{m+1,j}}$ for $j = 1, ..., m$. This makes $\mathbf{U}^N$ a vector of length $4m^2 + m$.

Now, let $\mathbf{G}$ be the vector that is formed by ordering the difference equations $\left(\Gamma_{0_{i,j}}, \Gamma_{1_{i,j}}, \Gamma_{2_{i,j}}, \Gamma_{3_{i,j}}\right)$, and let $\mathbf{G}_k$ be its components. First, set $\mathbf{G}_1 = \Gamma_{0_{1,1}}$, and increment j,with $i = 1$ fixed, until $\mathbf{G}_m = \Gamma_{0_{1,m}}$. Then, let $\mathbf{G}_{m+1} = \Gamma_{1_{1,1}}$ and increment j until $\mathbf{G}_{m+m} = \Gamma_{1_{1,m}}$. Then, let $\mathbf{G}_{2m+1} = \Gamma_{2_{1,1}}$ and increment j until $\mathbf{G}_{2m+m} = \Gamma_{2_{1,m}}$. Then, let $\mathbf{G}_{3m+1} = \Gamma_{3_{1,1}}$ and increment j until $\mathbf{G}_{3m+m} = \Gamma_{3_{1,m}}$. Now, increment i by one and repeat the whole process until $i = m$. Then, let $\mathbf{G}_{4m^2+j} = \Gamma_{B_j}$ for $j = 1$, ..., m. This makes $\mathbf{G}$ a vector of length $4m^2 + m$.

In other words, the components of $\mathbf{G}$ and $\mathbf{U}$ are such that

$$
\begin{aligned}
\mathbf{G}_{4m(i-1)+em+j} &= \left\{\Gamma_{e_{i,j}} \qquad e = 0, 1, 2, 3\right\}; i = 1, ..., m, j = 1, ..., m, \\
\mathbf{G}_{4m^2+j} &= \Gamma_{B_j}; j = 1, ..., m;
\end{aligned}
$$

and

$$\mathbf{U}_{4m(i-1)+em+j} = \left\{ \begin{array}{ll} l^{0,N+1}_{n_{i,j}} & e=0 \\ l^{1,N+1}_{n_{i,j}} & e=1 \\ l^{2,N+1}_{n_{i,j}} & e=2 \\ l^{3,N+1}_{n_{i,j}} & e=3 \end{array} \right\}; i=1,...,m, j=1,...,m,$$

$$\mathbf{U}^{N+1}_{4m^2+j} = l^{0,N+1}_{n_{m+1,j}}; j=1,...,m.$$

$\mathbf{G}$ can now be written as a product of a matrix $\mathbf{M}$ and the vector $\mathbf{U}^{N+1}$ with a forcing vector $\mathbf{F}^N$. That is

$$\mathbf{M}\mathbf{U}^{N+1} = \mathbf{F}^N \tag{2.37}$$

where

$$\mathbf{U}^{N+1} = \begin{bmatrix} l^{0,N+1}_{n_{1,1}} \\ : \\ l^{0,N+1}_{n_{1,m}} \\ l^{1,N+1}_{n_{1,1}} \\ : \\ l^{1,N+1}_{n_{1,m}} \\ : \\ l^{0,N+1}_{n_{m+1,m-1}} \\ l^{0,N+1}_{n_{m+1,m}} \end{bmatrix}, \mathbf{F}^N = \begin{bmatrix} 0 \\ : \\ 0 \\ g^N_{1_{1,1}} \\ : \\ g^N_{1_{1,m}} \\ : \\ 0 \\ 0 \end{bmatrix}.$$

$\mathbf{M}$ is a sparse matrix in that its elements are mostly zero except for a few bands that are composed of the coefficients $C^k_{c_{i,j}}$. Figure 2.24 shows the banded structure of the sparse matrix $\mathbf{M}$. The sparse matrix solver used in the steady solution calculation is used here as well. Since the elements of $\mathbf{M}$ do not depend on time, the LU decomposition needs to be done only once in the beginning of our computation. Still, it is a very large matrix; and for a typical run for $m = 80$, it takes about two hours to obtain an LU decomposition of $\mathbf{M}$ on a Sun Ultra workstation.

Here is the summary of the steps in solving the perturbation equations.

1. A guess for initial perturbed values $\mathbf{U}^0$ is given. The steady velocity values are

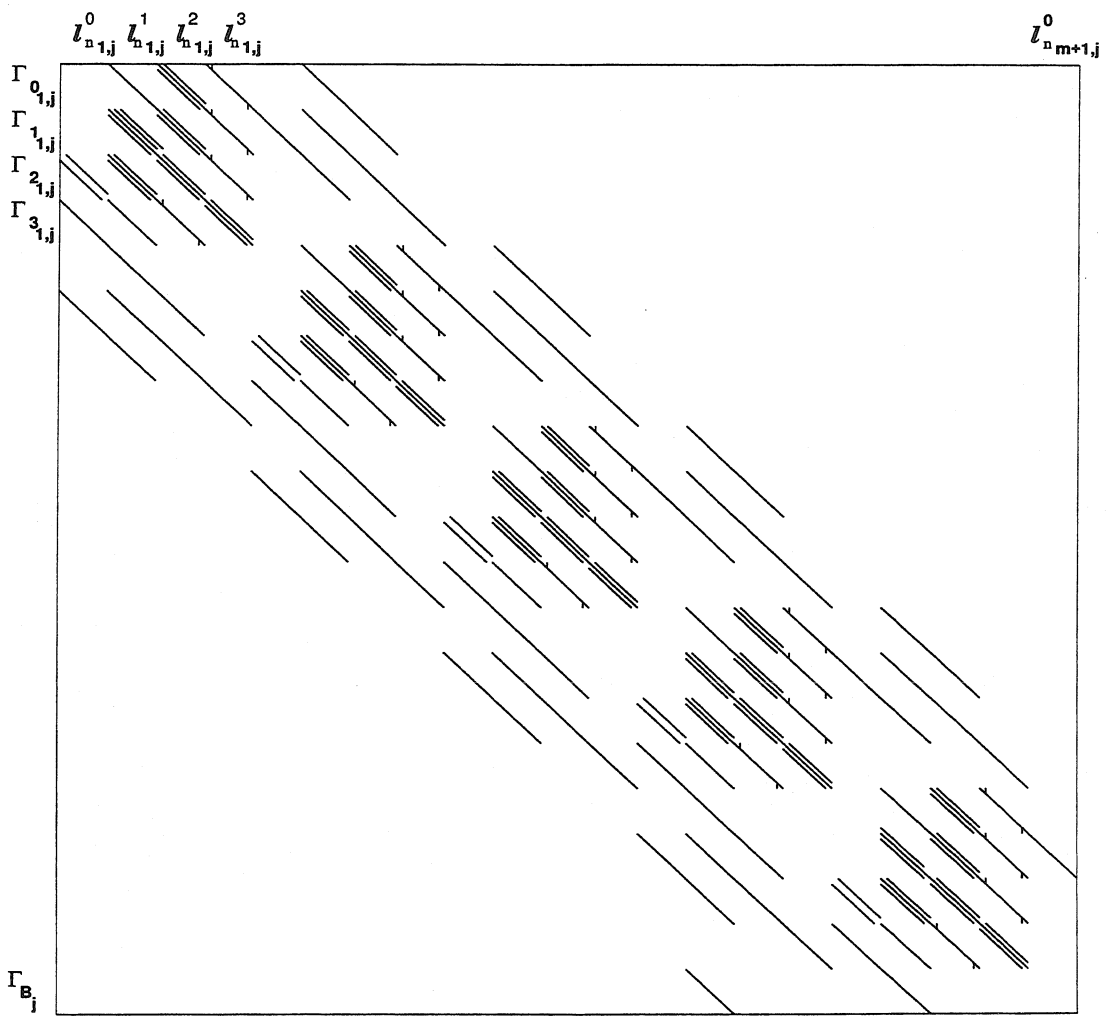

Figure 2.24: The banded structure of the sparse matrix used in the perturbation analysis of flow past spheroids with the no-slip boundary condition.

calculated from ψ and ω previously obtained, and $\mathbf{M}$ and $\mathbf{F}^0$ are determined. We use $\Delta t \approx 0.1$.

2. After LU decomposition on the sparse matrix is performed, the linear system (2.37) is solved to calculate $\mathbf{U}^1$. $\mathbf{F}^1$ then can be calculated and used as the forcing vector to solve for $\mathbf{U}^2$. Since $\mathbf{M}$ is constant in time, only backsolving needs to be performed to get $\mathbf{U}^2$.

3. The whole process is then repeated until $N = N_L$ where $N_L = 2500$. The resulting $\mathbf{U}^{N_L}$ gives the eigenfunctions corresponding to the leading eigenvalue α_1, and the slope and the distance between the peaks of the growth curve should give the eigenvalue α_1.

4. To obtain the secondary eigenvalue α_2, $\mathbf{U}^{N_L}$ is set to be the leading eigenfunction $\mathbf{E}^L$. Then, the computation is repeated from the beginning except this time the data to be collected is

$$\mathbf{V}^{N+1} = \mathbf{U}^{N+1} - \frac{< \mathbf{U}^{N+1}, \mathbf{E}^L >}{< \mathbf{E}^L, \mathbf{E}^L >} \mathbf{E}^L.$$

5. As N becomes large, $\mathbf{V}^N$ is dominated by the secondary eigenfunction. So, the log growth curve of $\mathbf{V}^N$ gives the value of the secondary eigenvalue α_2, and $\mathbf{V}^N$ becomes proportional to the corresponding eigenfunction $\mathbf{E}^S$. In this case, the iteration is done until $N = N_s$ where $N_s \approx 1300$.

2.4.3 Numerical results of the linear stability analysis of flow past a solid sphere

In this section, we present the linear stability analysis results for flow past a solid sphere using the grid of resolution of 80x80 with distortion coefficient $\alpha = 0.5$. The nondimensionalization is such that $d = a = b$, and the Reynolds number is defined as

$$R = \frac{2a\rho U}{\mu}.$$

Previous results indicate that the $n = 1$ Fourier mode of the perturbation is the one that becomes unstable, and this is indeed the case in our calculations as well.

Figure 2.25 shows how $\log\left(\| \mathbf{U}^N \|\right)$ of the $n = 1$ Fourier mode of the perturbation grows in time at various values of R. It is clear that the curves grow linearly and that the slope of each curve varies with respect to R. This shows that the leading eigenvalue α_1 is purely real. If the slope is negative, the flow is stable. If the slope is positive, the flow is unstable. The slope is calculated using a least squares fit to determine the growth rate, i.e., the leading eigenvalue, and is plotted with respect to the corresponding Reynolds number R in Figure 2.26.

Figure 2.26 shows that the leading eigenvalue increases as R increases. It also shows that convergence test using a 60x60 grid and 80x80 grid give similar results. Linear interpolation is performed on the curve of the leading eigenvalues to determine the value of the critical Reynolds number R^L corresponding to a zero eigenvalue, and the critical Reynolds number turns out to be $R^L = 212.8$. This agrees well with Natarajan and Acrivos's result [26] of 210 and Tomboulidis, Orszag, and Karniadakis's result [44] of 212. We also compare the leading eigenvalues that we computed with Natarajan and Acrivos's results in Figure 2.27. Our curve is slightly lower than Natarajan's. This may be due to the different types of numerical methods used. In addition, the growth rates computed by Tomboulides, Orszag, and Karniadakis [44] in their direct, full, numerical simulation of flow past a solid sphere are also slightly below the values computed by Natarajan and Acrivos [26] indicating that our linear stability results are quite reasonable. Since our results appear to be convergent, the differences in the results may not be due to convergence. Figure 2.28 shows $\mathbf{U}^{N_L}$ at the critical Reynolds number of 212.8. They are basically the eigenfunctions corresponding to the leading eigenvalue such that the leading eigenvalue is zero. They agree well with those in Natarajan and Acrivos [26].

Figure 2.29 shows how $\log\left(\| \mathbf{V}^N \|\right)$ of the $n = 1$ Fourier mode of the perturbation of flow past a solid sphere grows in time at various values of R. The curves grow as a series of peaks, and the peaks grow linearly. This indicates that the secondary eigenvalue α_2 is complex. Once again, a least squares fit is used on the peaks to

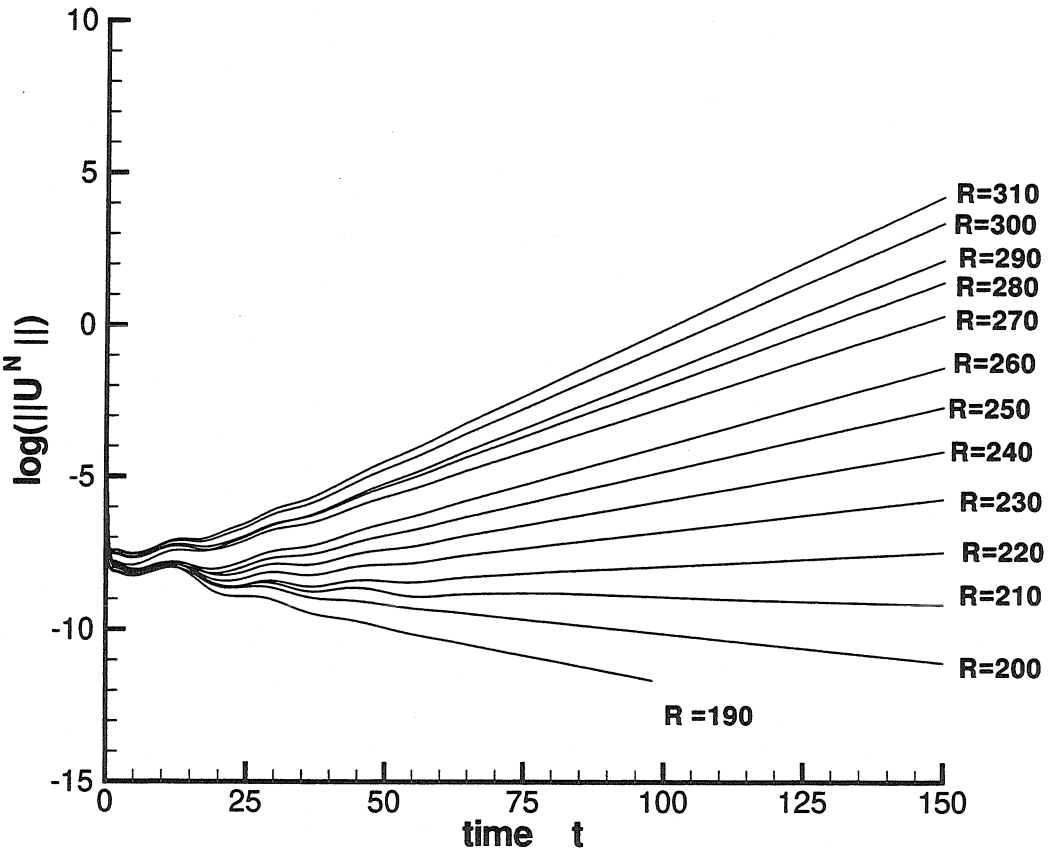

Figure 2.25: *Log* $(\| \mathbf{U}^N \|)$ of the $n = 1$ Fourier mode of the perturbation of flow past a solid sphere versus time t at various Reynolds numbers.

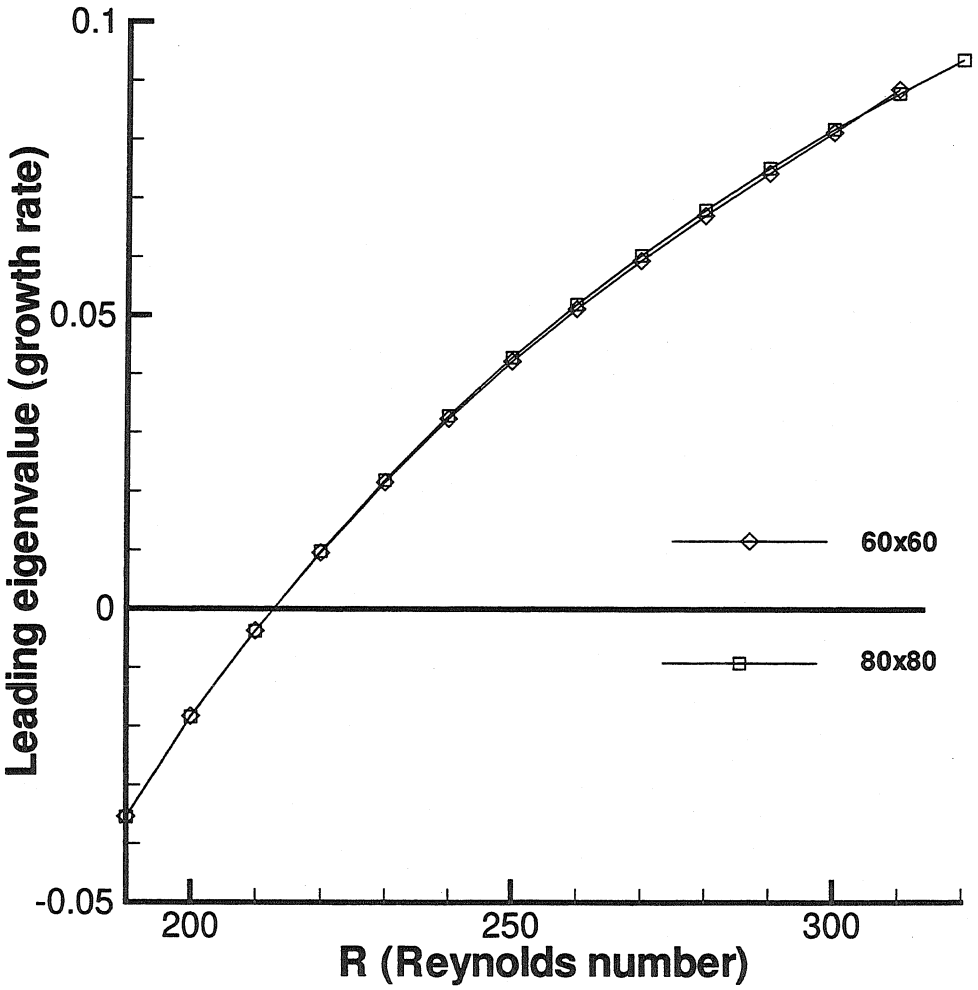

Figure 2.26: Leading eigenvalues α_1, i.e., the growth rates, of the $n = 1$ Fourier mode of the perturbation of flow past a solid sphere versus R using 60x60 grid and 80x80 grid.

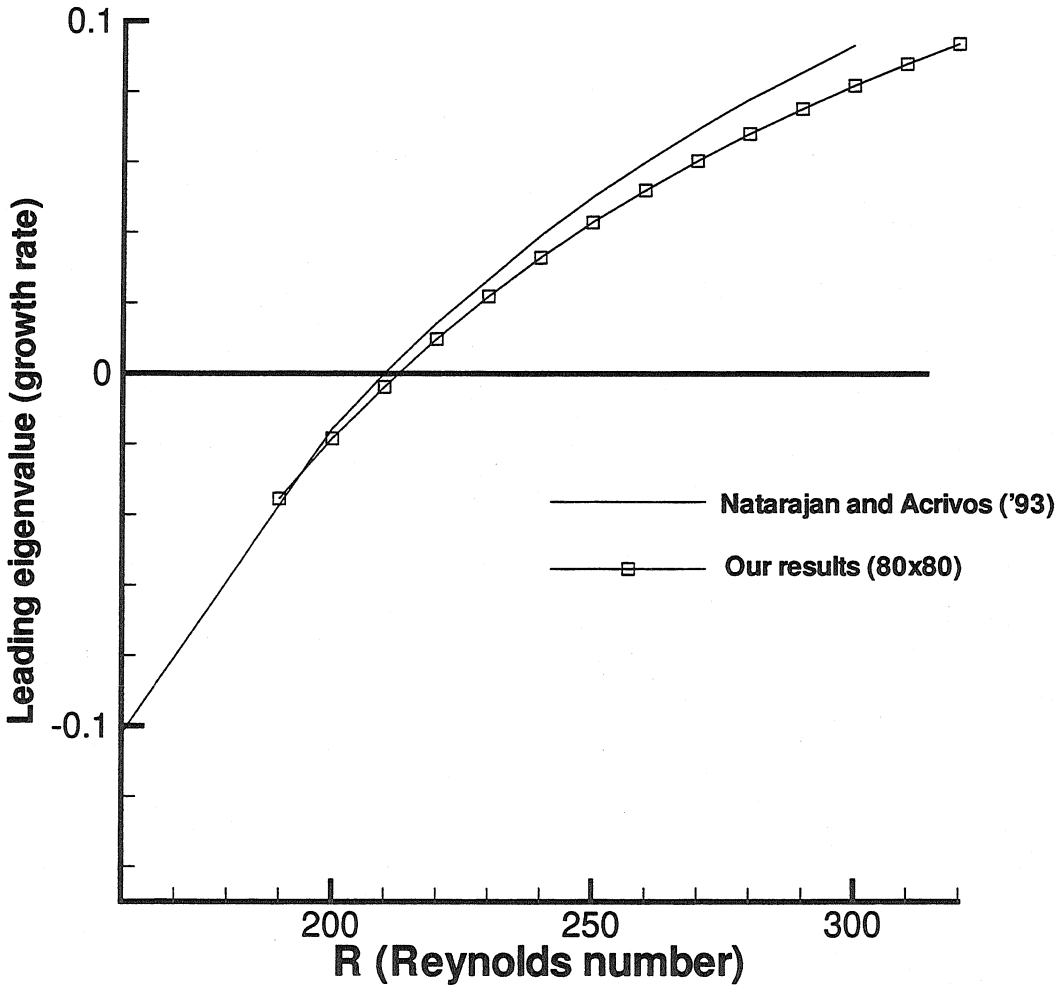

Figure 2.27: Comparison of the leading eigenvalues of the $n = 1$ Fourier mode of the perturbation of flow past a solid sphere between this work and Natarajan and Acrivos [26].

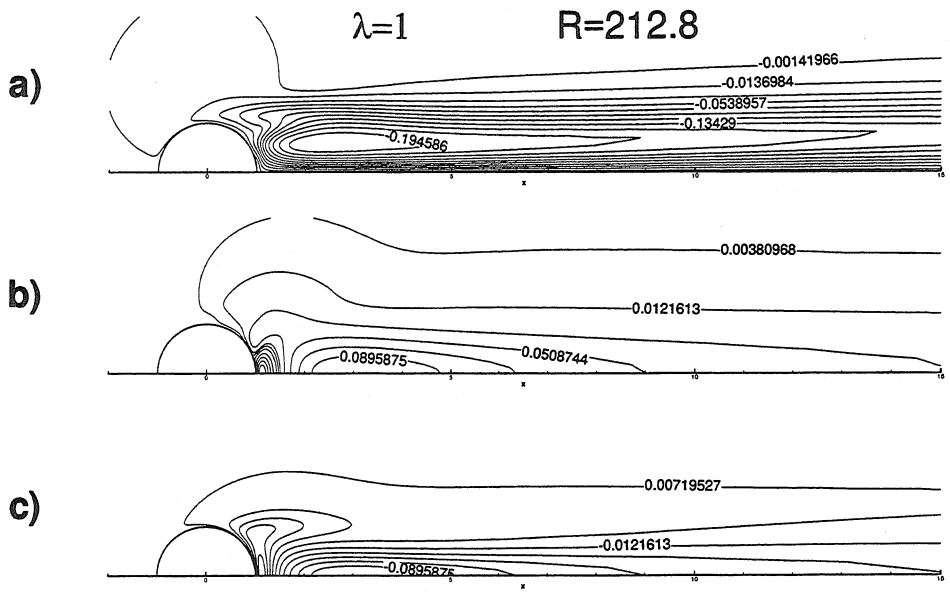

Figure 2.28: Eigenfunctions corresponding to the leading eigenvalue α_1 of the $n = 1$ Fourier mode of the perturbation of flow past a solid sphere at $R^L = 212.8$. a) $\mathrm{Re}\,(\tilde{u}_{x_1})$, b) $\mathrm{Re}\,(\tilde{u}_{\sigma_1})$, c) $\mathrm{Im}\,(\tilde{u}_{\phi_1})$.

determine the real part of α_2, and the distance between the peaks is measured to determine the imaginary part of α_2.

Figure 2.30 shows the secondary eigenvalues plotted with respect to R. Good agreement under different resolutions indicates convergence. Once again, linear interpolation is used to determine the critical Reynolds number R^S corresponding to zero growth; and it turns out to be $R^S = 281.4$. In terms of periodicity, at the critical Reynolds number, the imaginary part of the secondary eigenvalue α_2 in our case is determined to be 0.342. This agrees reasonably well with Natarajan and Acrivos's result [26] of 277.5 and 0.355. The slight differences in the results may come from the numerical methods used and the uncertainty of the Gram-Schmidt orthogonalization method. Tomboulidis, Orszag, and Karniadakis's result [44] indicates the importance of this critical Reynolds number, as their full numerical simulation showed time dependent, periodic oscillation beginning to be induced around $R = 270$ and 285. Our result falls well within their range. The pictures of eigenfunctions shown in Figure

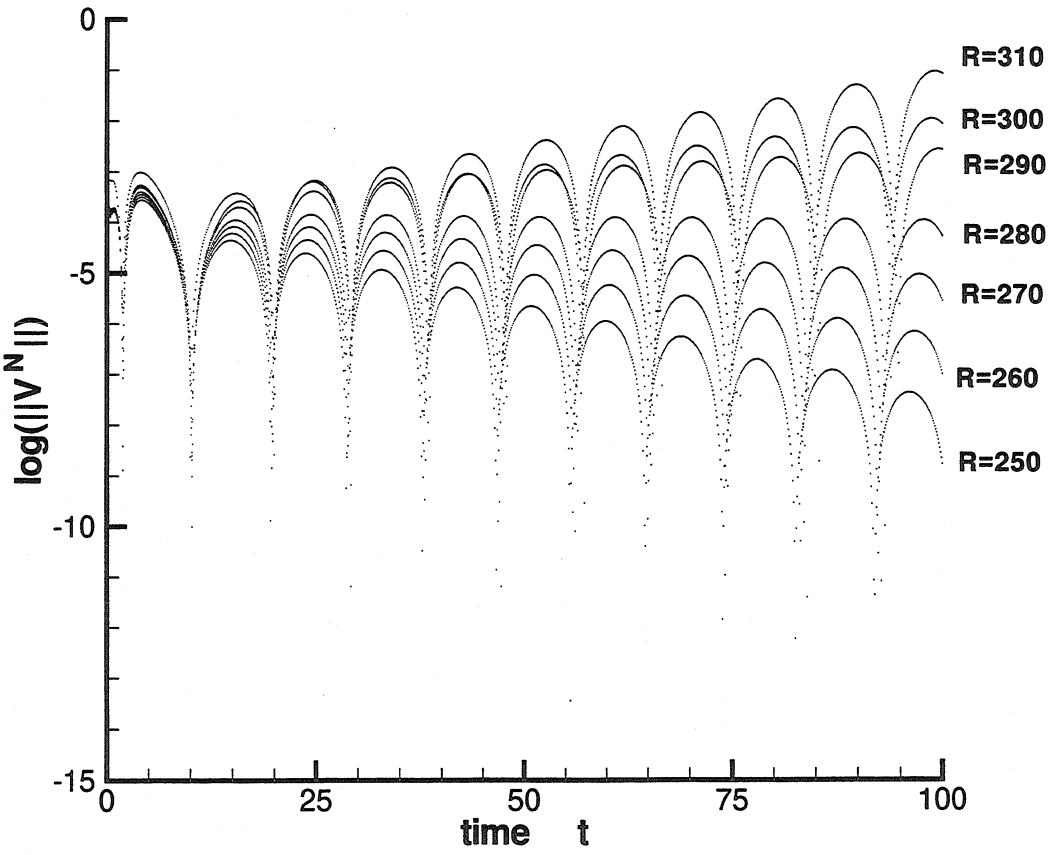

Figure 2.29: *Log* $(\| \mathbf{V}^N \|)$ of the $n = 1$ Fourier mode of the perturbation of flow past a solid sphere versus time t at various Reynolds numbers.

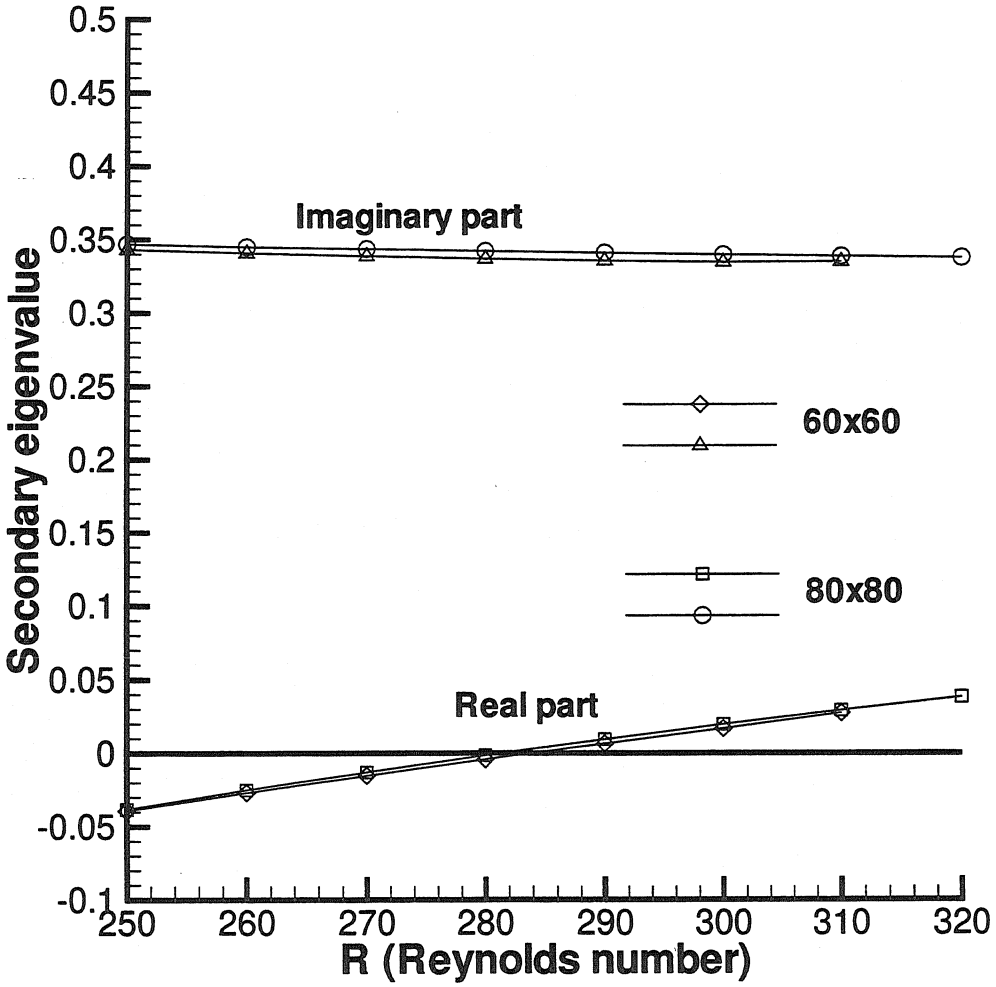

Figure 2.30: Secondary eigenvalues α_2 of the $n = 1$ Fourier mode of the perturbation of flow past a solid sphere versus R using 60x60 grid and 80x80 grid.

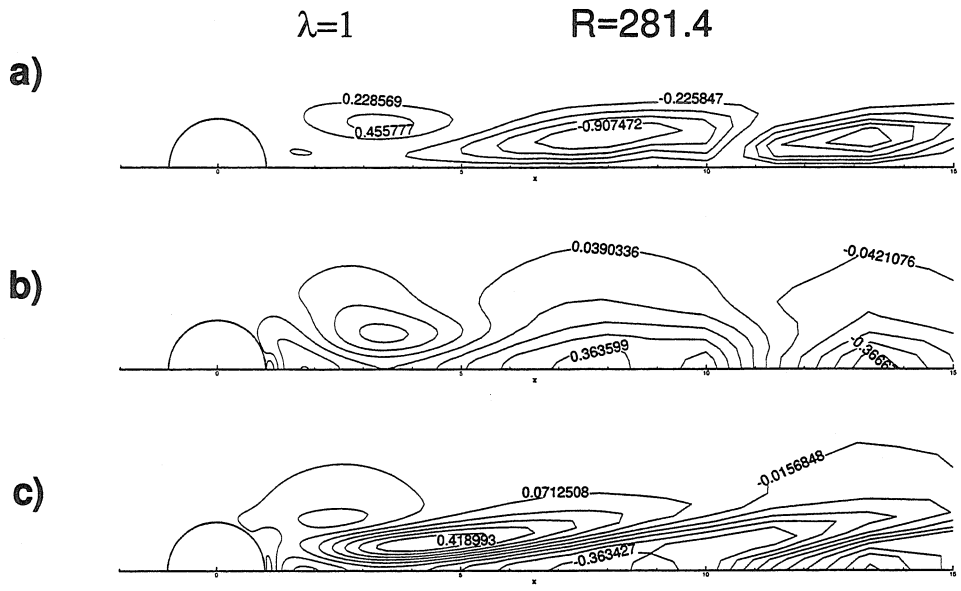

Figure 2.31: Eigenfunctions corresponding to the secondary eigenvalue α_2 of the $n = 1$ Fourier mode of the perturbation of flow past a solid sphere at $R^S = 281.4$. a) $\mathrm{Re}(\tilde{u}_{x_1})$, b) $\mathrm{Re}(\tilde{u}_{\sigma_1})$, c) $\mathrm{Im}(\tilde{u}_{\phi_1})$.

2.31 also agree well with those of Natarajan and Acrivos [26]. The figures show that the value of eigenfunctions is large near the body where the wake is located and decays to zero quickly away from the body.

In conclusion, our numerical results of the critical Reynolds numbers of 212.8 and 281.4 agree well with Natarajan and Acrivos [26] and with Tomboulides, Orszag, and Karniadakis [44] and disagrees with Kim and Pearlstein [17]. This indicates that our numerical method works well in determining flow instability.

Figure 2.32 shows the Fourier modes $n = 0$, $n = 2$, and $n = 3$ of the perturbations evolving in time at $R = 280$. It is clear that they are all stable even when the flow is beyond the critical Reynolds number at which the $n = 1$ Fourier mode is already unstable. This indicates that the $n = 1$ Fourier mode is the dominant mode of the instability of the perturbation for the range of the Reynolds numbers that we studied.

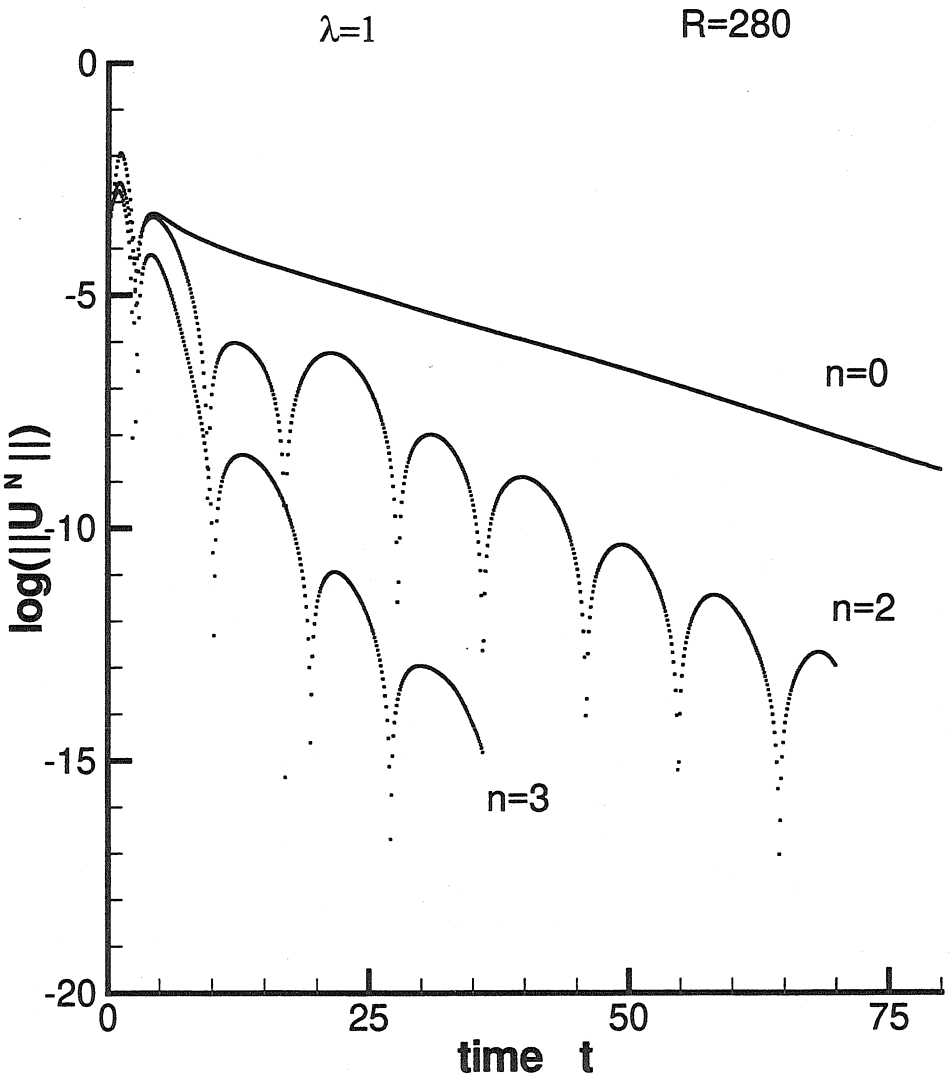

Figure 2.32: *Log* $(||\mathbf{U}^N||)$ of the $n = 0$, $n = 2$, and $n = 3$ Fourier modes of the perturbation of flow past a solid sphere versus time t at $R = 280$.

2.4.4 Numerical results of the linear stability analysis of flow past an oblate spheroid

We discuss here the linear stability analysis results obtained for flow past an oblate spheroid with $\lambda = 0.3, ..., 0.9$ using grids of resolution of 80x80 with distortion coefficient $\alpha = 0.5$. For λ small, the spheroid is flat along the axis of symmetry; and for λ near one, the spheroid is nearly spherical. The nondimensionalization is such that $d = b$, and the Reynolds number is defined as

$$R_b = \frac{2b\rho U}{\mu}.$$

Again, the $n = 1$ Fourier mode of the perturbation turns out to be the mode that becomes unstable.

Figure 2.33 shows the leading eigenvalues for the $n = 1$ Fourier mode of the perturbation determined for $\lambda = 0.5$ under different resolutions. The two curves more or less lie on top of each other, and this indicates that the results are convergent. Our method is therefore consistent when computing the stability for flow past an oblate spheroid. Figure 2.34 shows the leading eigenvalues α_1 associated with the $n = 1$ Fourier mode of the perturbation of flow past an oblate spheroid for $\lambda = 0.3, ..., 0.9$. As the body becomes more oblate, the critical Reynolds numbers become smaller. Similar to the case of sphere, the leading eigenvalues are purely real. Figure 2.35 shows the secondary eigenvalues obtained for $\lambda = 0.3, ..., 0.9$. Similar to the case of sphere, they are complex.

Figure 2.36 shows the critical Reynolds numbers R_b^L at which the leading eigenvalue α_1 of the $n = 1$ Fourier mode of the perturbation is zero and the critical Reynolds numbers R_b^S at which the real part of the secondary eigenvalue α_2 is zero versus the aspect ratio λ. The two curves converge as λ gets smaller. This indicates that the more oblate the body is, the lower the critical Reynolds number above which the flow may become unstable.

Figure 2.37 shows a relation between the imaginary part of the secondary eigenval-

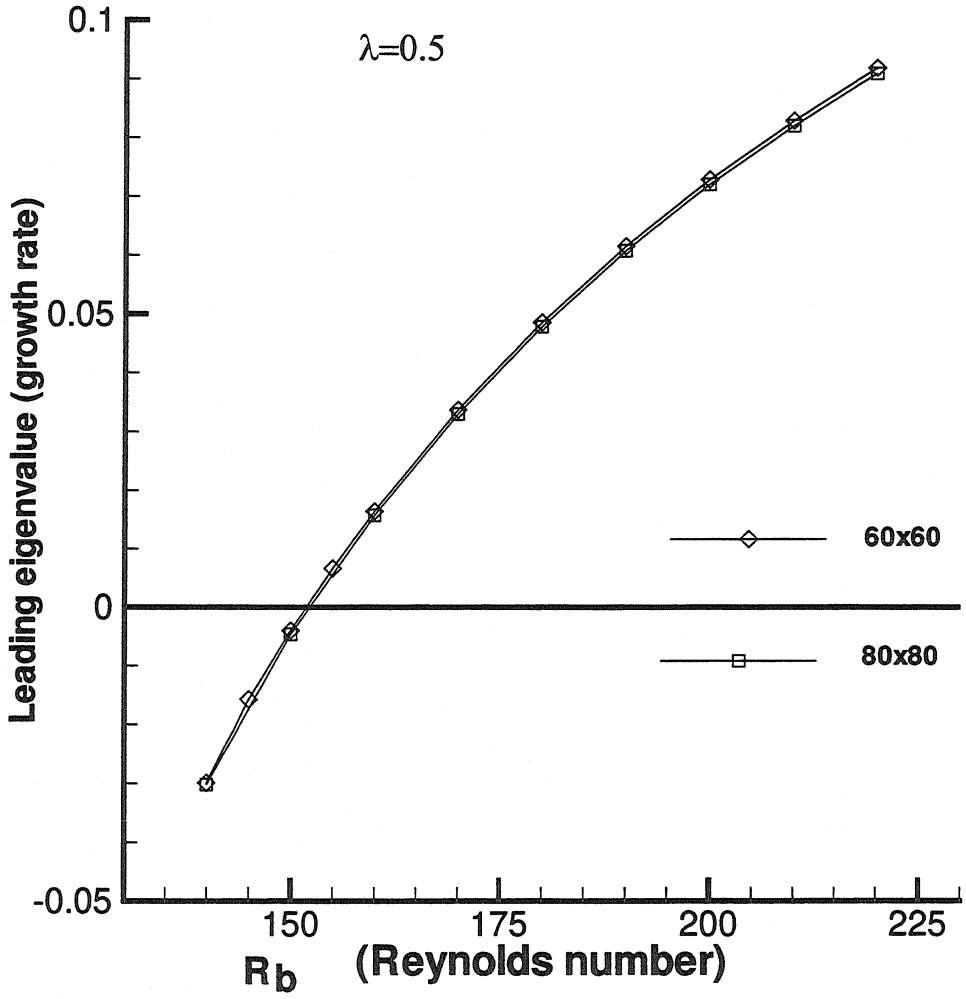

Figure 2.33: Comparison of the leading eigenvalues α_1, i.e., the growth rates, for the $n = 1$ Fourier mode of the perturbation of flow past an oblate spheroid with $\lambda = 0.5$ versus R_b using 60x60 grid and 80x80 grid.

	$\lambda = 0.3$	0.4	0.5	0.6	0.7	0.8	0.9	1.0
R_b^L	134.2	143.1	152.3	162.4	173.5	185.6	198.7	212.8

Table 2.11: Critical Reynolds numbers at which the leading eigenvalues of the $n = 1$ Fourier mode of the perturbation of flow past an oblate spheroid are zero.

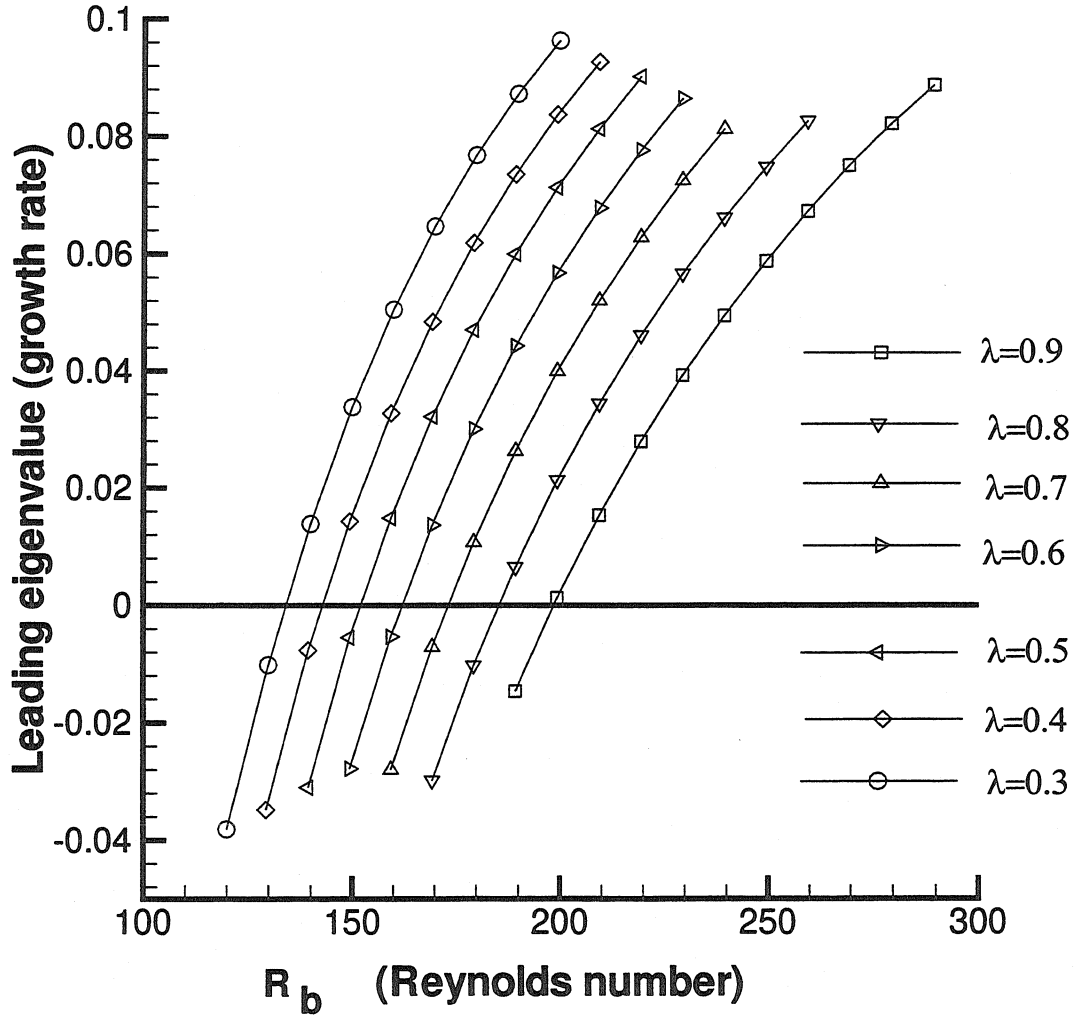

Figure 2.34: Leading eigenvalues α_1 of the $n = 1$ Fourier mode of the perturbation of flow past an oblate spheroid of various aspect ratios versus R_b.

	$\lambda = 0.3$	0.4	0.5	0.6	0.7	0.8	0.9	1.0
R_b^S	151.3	162.2	175.7	191.6	210.2	231.5	255.5	281.4
α_2 at R_b^S	0.388ι	0.381ι	0.375ι	0.369ι	0.363ι	0.356ι	0.349ι	0.342ι

Table 2.12: Critical Reynolds numbers and the secondary eigenvalues of the $n = 1$ Fourier mode of the perturbation of flow past an oblate spheroid.

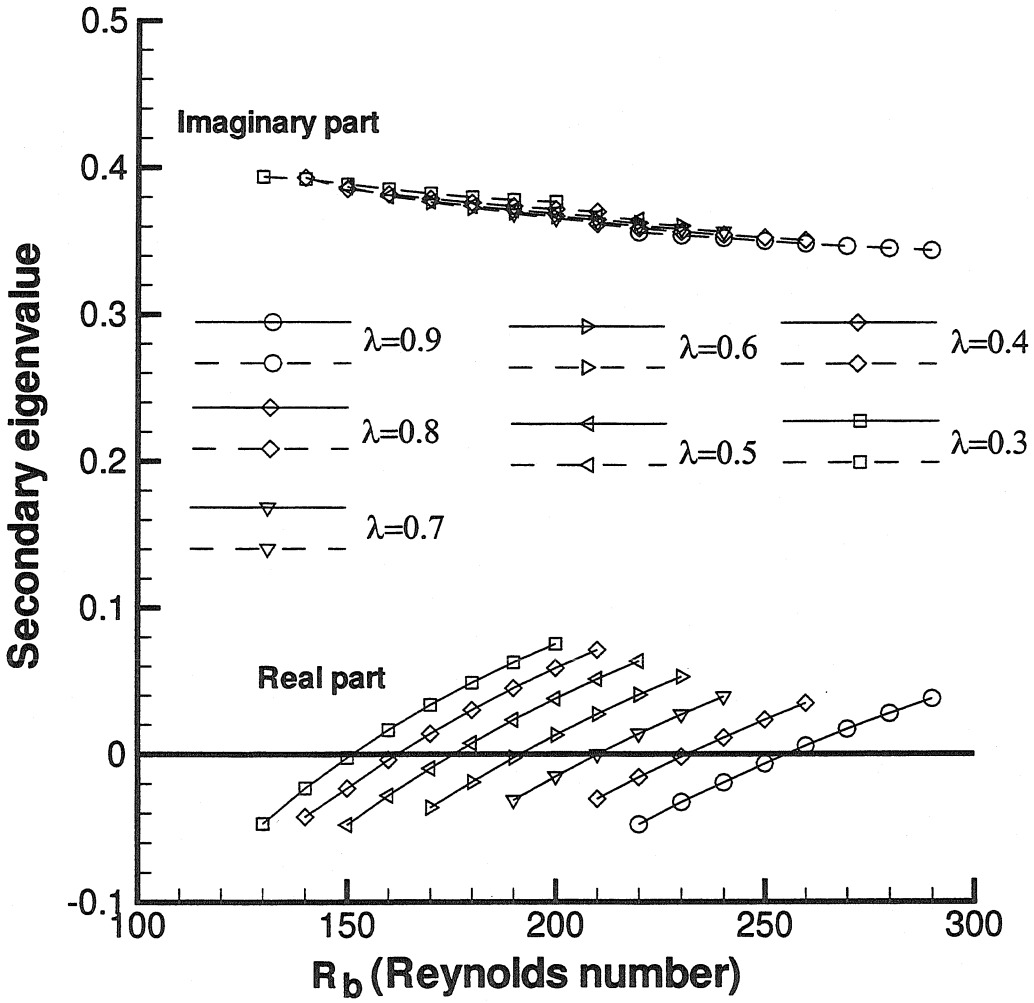

Figure 2.35: Secondary eigenvalues α_2 of the $n = 1$ Fourier mode of the perturbation of flow past an oblate spheroid of various aspect ratios versus R_b.

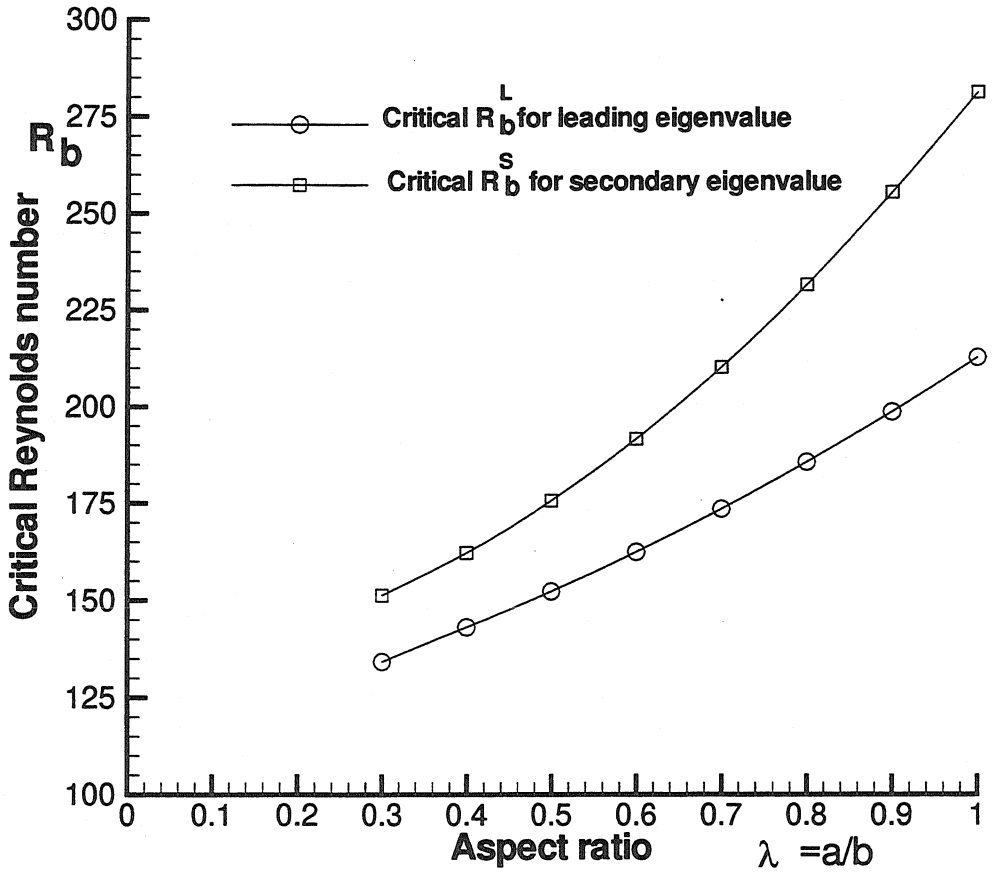

Figure 2.36: Critical Reynolds numbers R_b^L and R_b^S versus aspect ratio λ for the $n = 1$ Fourier mode of the perturbation of flow past an oblate spheroid.

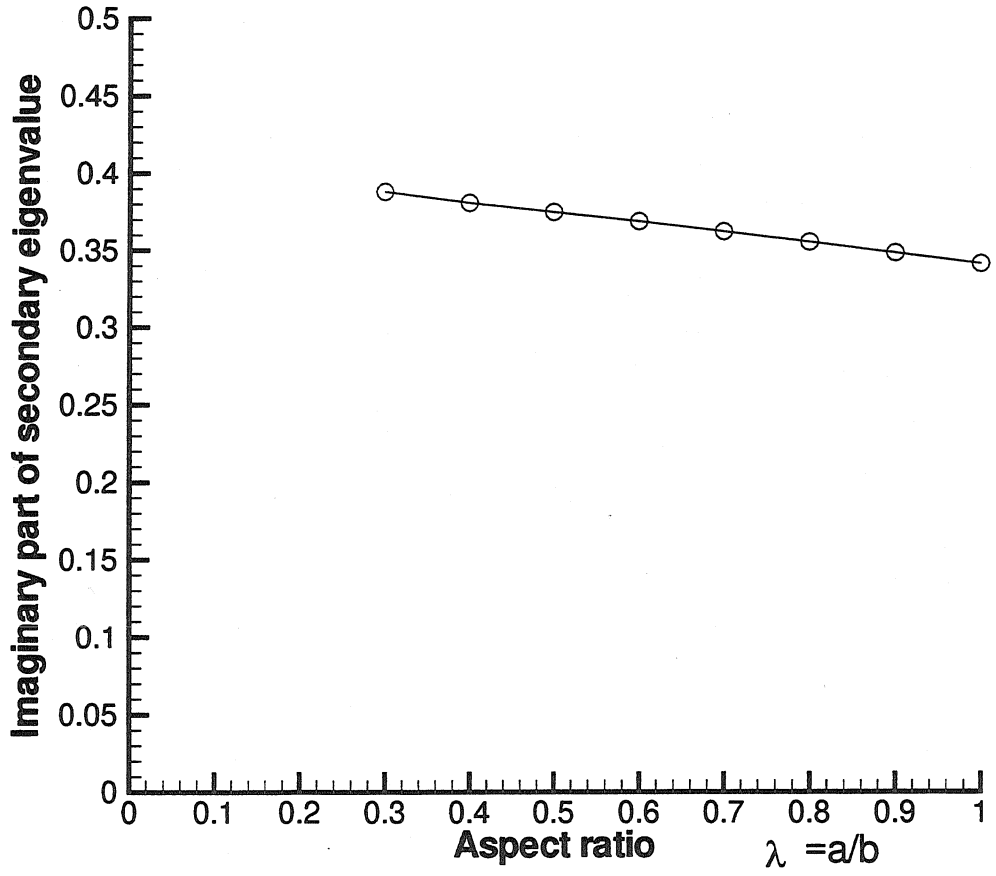

Figure 2.37: Secondary eigenvalues α_2 at the critical Reynolds numbers R_b^S versus aspect ratio λ for the $n = 1$ Fourier mode of the perturbation of flow past an oblate spheroid.

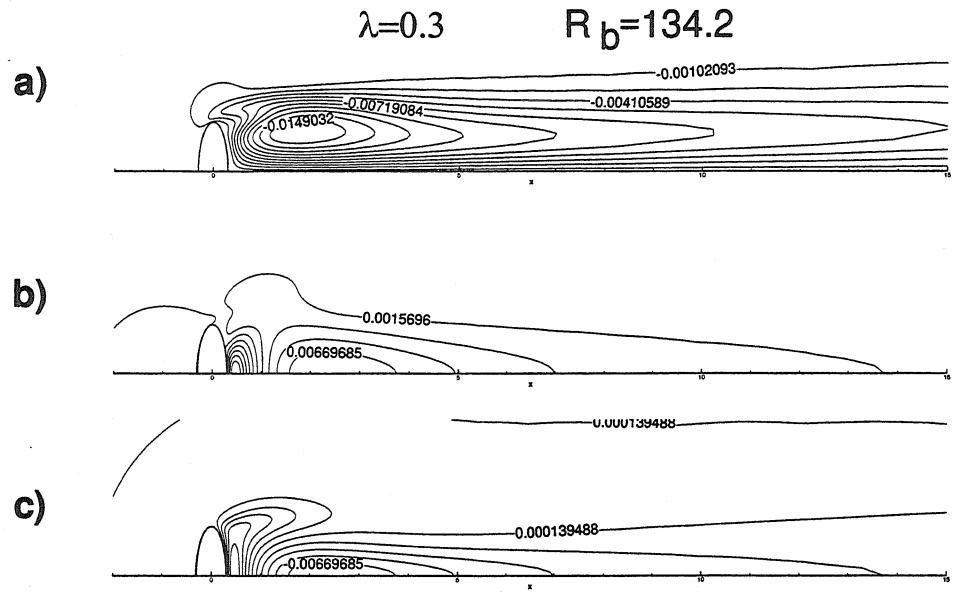

Figure 2.38: Eigenfunctions corresponding to the leading eigenvalue α_1 of the $n = 1$ Fourier mode of the perturbation of flow past an oblate spheroid with $\lambda = 0.3$ at $R_b^L = 134.2$. a) $\mathrm{Re}(\tilde{u}_{x_1})$, b) $\mathrm{Re}(\tilde{u}_{\sigma_1})$, c) $\mathrm{Im}(\tilde{u}_{\phi_1})$.

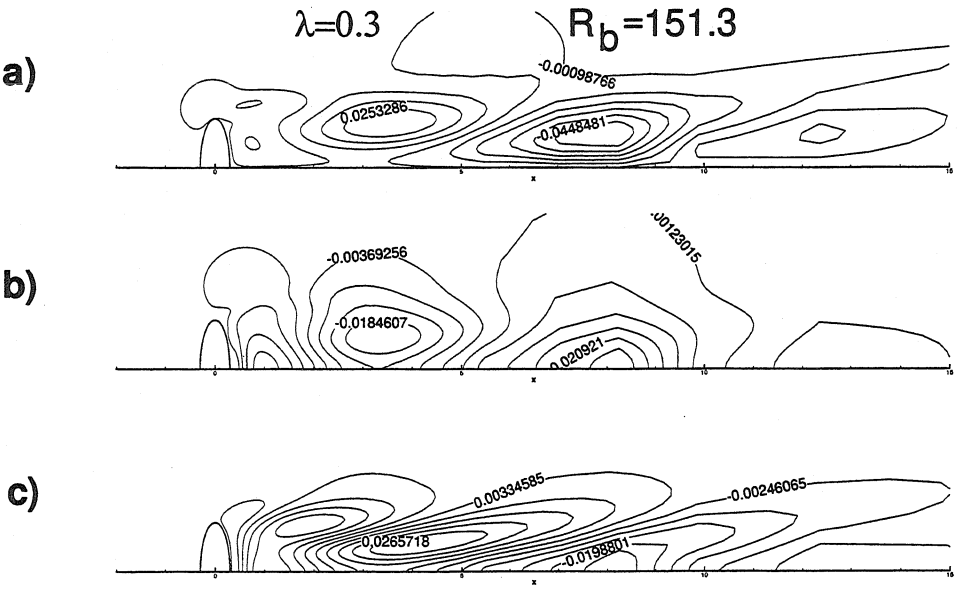

Figure 2.39: Eigenfunctions corresponding to the secondary eigenvalue α_2 of the $n = 1$ Fourier mode of the perturbation of flow past an oblate spheroid with $\lambda = 0.3$ at $R_b^S = 151.3$. a) $\mathrm{Re}(\tilde{u}_{x_1})$, b) $\mathrm{Re}(\tilde{u}_{\sigma_1})$, c) $\mathrm{Im}(\tilde{u}_{\phi_1})$.

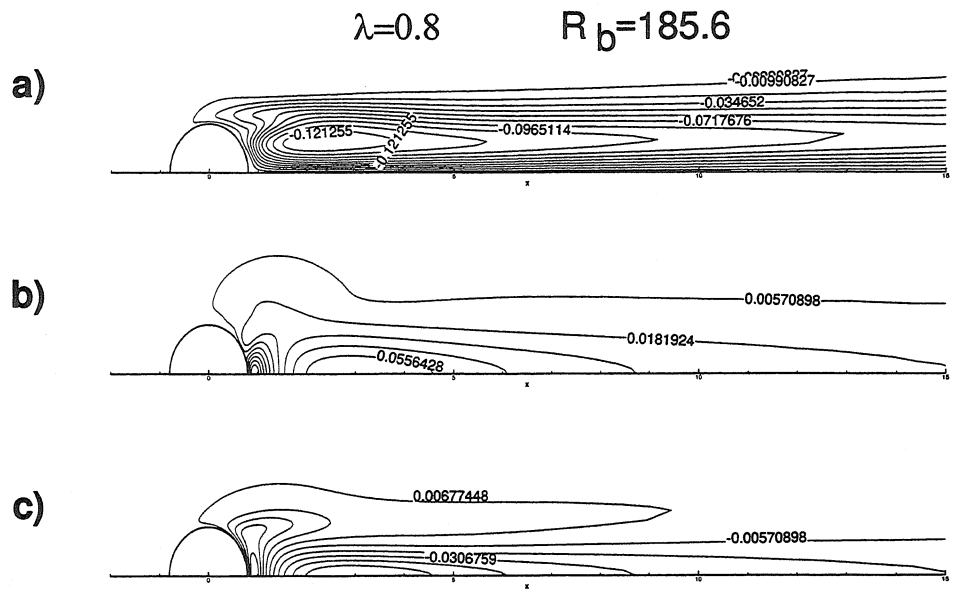

Figure 2.40: Eigenfunctions corresponding to the leading eigenvalue α_1 of the $n = 1$ Fourier mode of the perturbation of flow past an oblate spheroid with $\lambda = 0.8$ at $R_b^L = 185.6$. a) Re $(\tilde{u}_{x_1})$, b) Re $(\tilde{u}_{\sigma_1})$, c) Im $(\tilde{u}_{\phi_1})$.

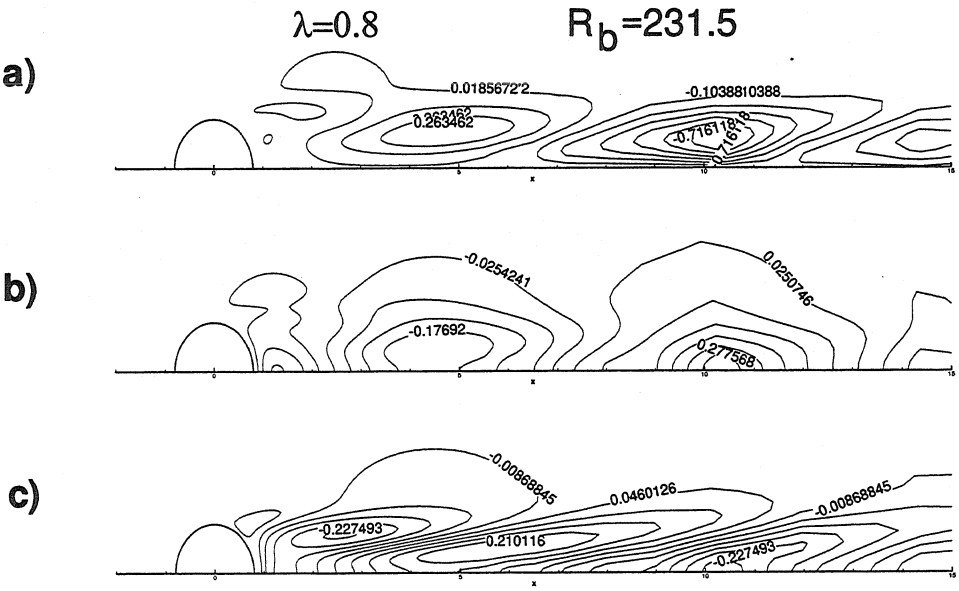

Figure 2.41: Eigenfunctions corresponding to the secondary eigenvalue α_2 of the $n = 1$ Fourier mode of the perturbation of flow past an oblate spheroid with $\lambda = 0.8$ at $R_b^S = 231.5$. a) Re $(\tilde{u}_{x_1})$, b) Re $(\tilde{u}_{\sigma_1})$, c) Im $(\tilde{u}_{\phi_1})$.

ues at the critical Reynolds number R_b^S and the aspect ratio of the oblate spheroids. The curve appears to be linear and increasing as λ gets smaller.

The Figures 2.38 and 2.40 show the eigenfunctions corresponding to the leading eigenvalue for $\lambda = 0.3$ and 0.8. They appear to be similar to each other and are similar to the eigenfunctions corresponding to the leading eigenvalue for the sphere.

Figures 2.39 and 2.41 show the eigenfunctions corresponding to the secondary eigenvalue for $\lambda = 0.3$ and 0.8. They also appear to be similar to each other and are similar to the eigenfunctions corresponding to the secondary eigenvalue for the sphere. In addition, the figures show that the value of eigenfunctions is large near the body where the wake is located and decays to zero quickly away from the body.

Figure 2.42 shows the Fourier modes $n = 0$, $n = 2$, and $n = 3$ of the perturbations of flow past an oblate spheroid with $\lambda = 0.5$ evolving in time at $R_b = 200$. It is clear that they are all stable even when the flow is beyond the critical Reynolds number at which the $n = 1$ Fourier mode is already unstable. This indicates that the $n = 1$ Fourier mode is the dominant mode of the instability of the perturbation of flow past oblate spheroids for the range of the Reynolds numbers that we studied.

2.4.5 Numerical results of the linear stability analysis of flow past a prolate spheroid

We discuss here the linear stability analysis results obtained for flow past a prolate spheroid with $\lambda = 1.1, ..., 1.7$ using grids of resolution of 80x80 with distortion coefficient $\alpha = 0.5$. For λ near one, the spheroid is nearly spherical; and for λ large, the spheroid is elongated along the axis of symmetry. The nondimensionalization is such that $d = a$, and the Reynolds number is defined as

$$R_a = \frac{2a\rho U}{\mu}.$$

Again, the $n = 1$ Fourier mode of the perturbation turns out to be the mode that becomes unstable.

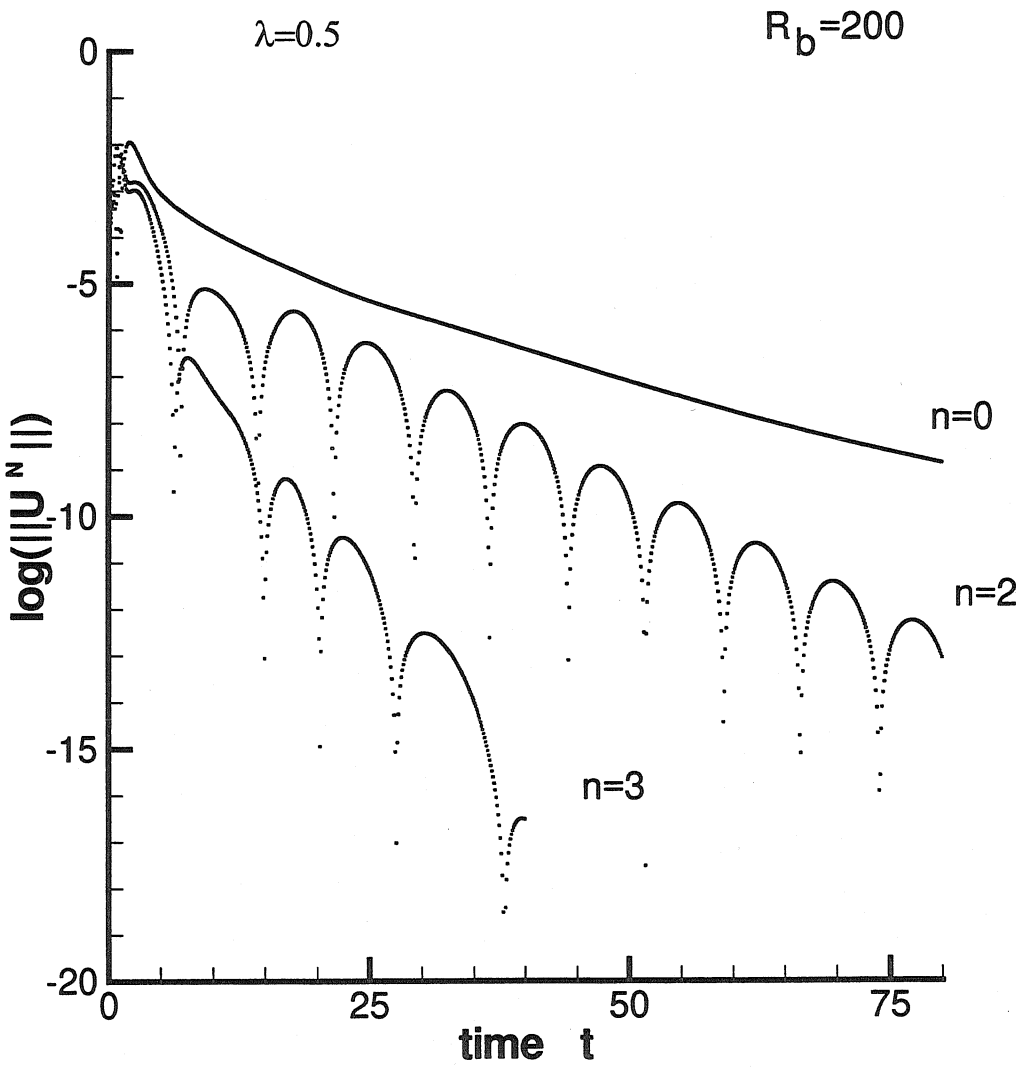

Figure 2.42: *Log* $(||\mathbf{U}^N||)$ of the $n = 0$, $n = 2$, and $n = 3$ Fourier modes of the perturbation of flow past an oblate spheroid with $\lambda = 0.5$ versus time t at $R_b = 200$.

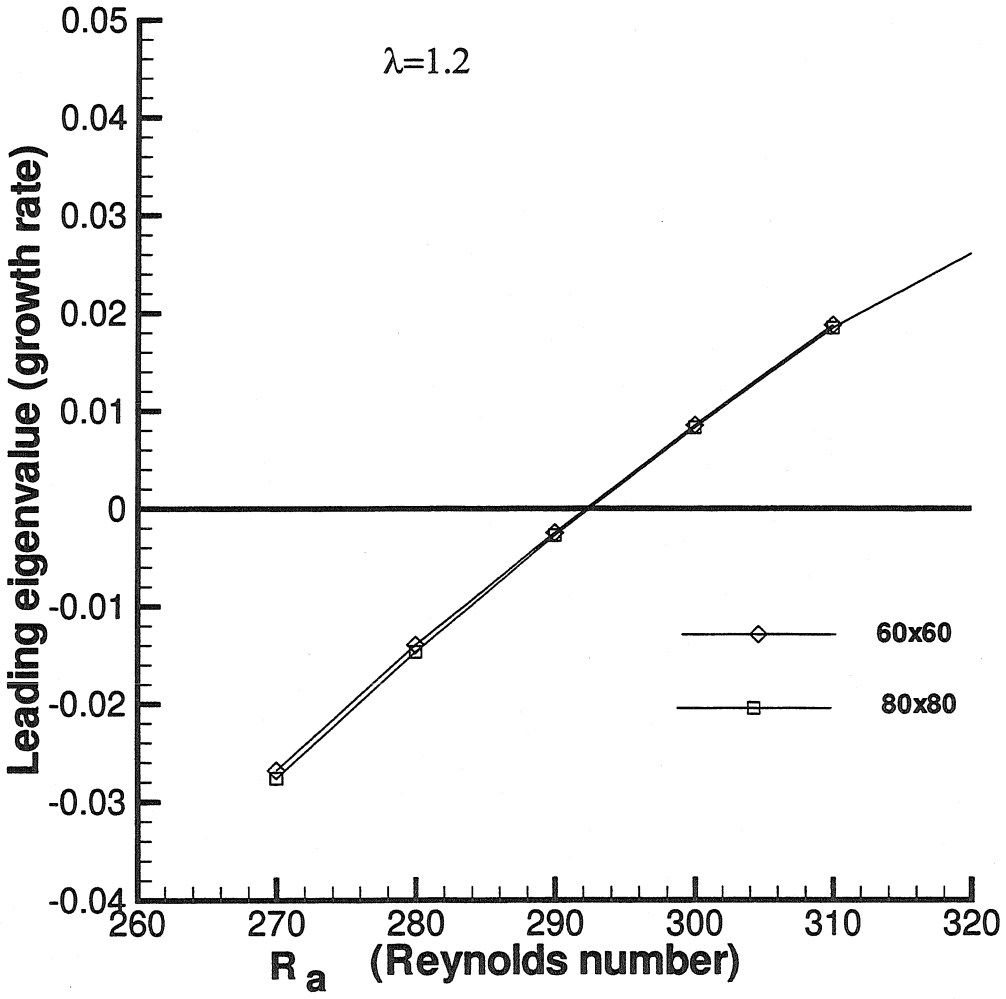

Figure 2.43: Comparison of the leading eigenvalues α_1, i.e., the growth rates, for the $n = 1$ Fourier mode of the perturbation of flow past a prolate spheroid with $\lambda = 1.2$ using 60x60 grid and 80x80 grid.

	$\lambda = 1.0$	1.1	1.2	1.3	1.4	1.5	1.6	1.7
R_a^L	212.8	250.6	292.5	338.6	389.1	444.2	504	568.3

Table 2.13: Critical Reynolds numbers at which the leading eigenvalues of the $n = 1$ Fourier mode of the perturbation of flow past a prolate spheroid are zero.

	$\lambda = 1.0$	1.1	1.2	1.3	1.4	1.5
R_a^S	281.4	343	413.5	493.4	583.6	684.2
α_2 at R_a^S	0.342ι	0.367ι	0.392ι	0.414ι	0.435ι	0.455ι

Table 2.14: Critical Reynolds numbers and the secondary eigenvalues of the $n = 1$ Fourier mode of the perturbation of flow past a prolate spheroid.

Figure 2.43 shows the leading eigenvalues of the $n = 1$ Fourier mode of the perturbation determined for $\lambda = 1.2$ under different resolutions. The two curves more or less lie on top of each other, and this indicates that the results are convergent. Figure 2.44 shows the leading eigenvalues associated with the $n = 1$ Fourier mode of the perturbation of flow past prolate spheroids for $\lambda = 1.1, ..., 1.7$. As the body becomes more prolate, the critical Reynolds numbers become larger. Similar to the case of sphere, the leading eigenvalues are purely real. Figure 2.45 shows the secondary eigenvalues obtained for $\lambda = 1.1, ..., 1.5$. Similar to the case of sphere, they are complex.

Figure 2.46 shows the critical Reynolds numbers R_a^L at which the leading eigenvalue α_1 of the $n = 1$ Fourier mode of the perturbation is zero and the critical Reynolds numbers R_a^S at which the real part of the secondary eigenvalue α_2 is zero versus the aspect ratio λ. The two curves diverge quickly as λ gets bigger. This indicates that the more prolate the body is, the higher the critical Reynolds number above which the flow may become unstable.

Figure 2.47 shows a relation between the imaginary part of the secondary eigenvalue at the critical Reynolds number R_a^S and the aspect ratio of the prolate spheroids. The curve appears to be linear and increasing as λ gets larger.

Figures 2.49 and 2.51 show the eigenfunctions corresponding to the leading eigenvalue α_1 for $\lambda = 1.2$ and 1.5. They appear to be similar to each other and are similar to the eigenfunctions corresponding to the leading eigenvalue for the sphere.

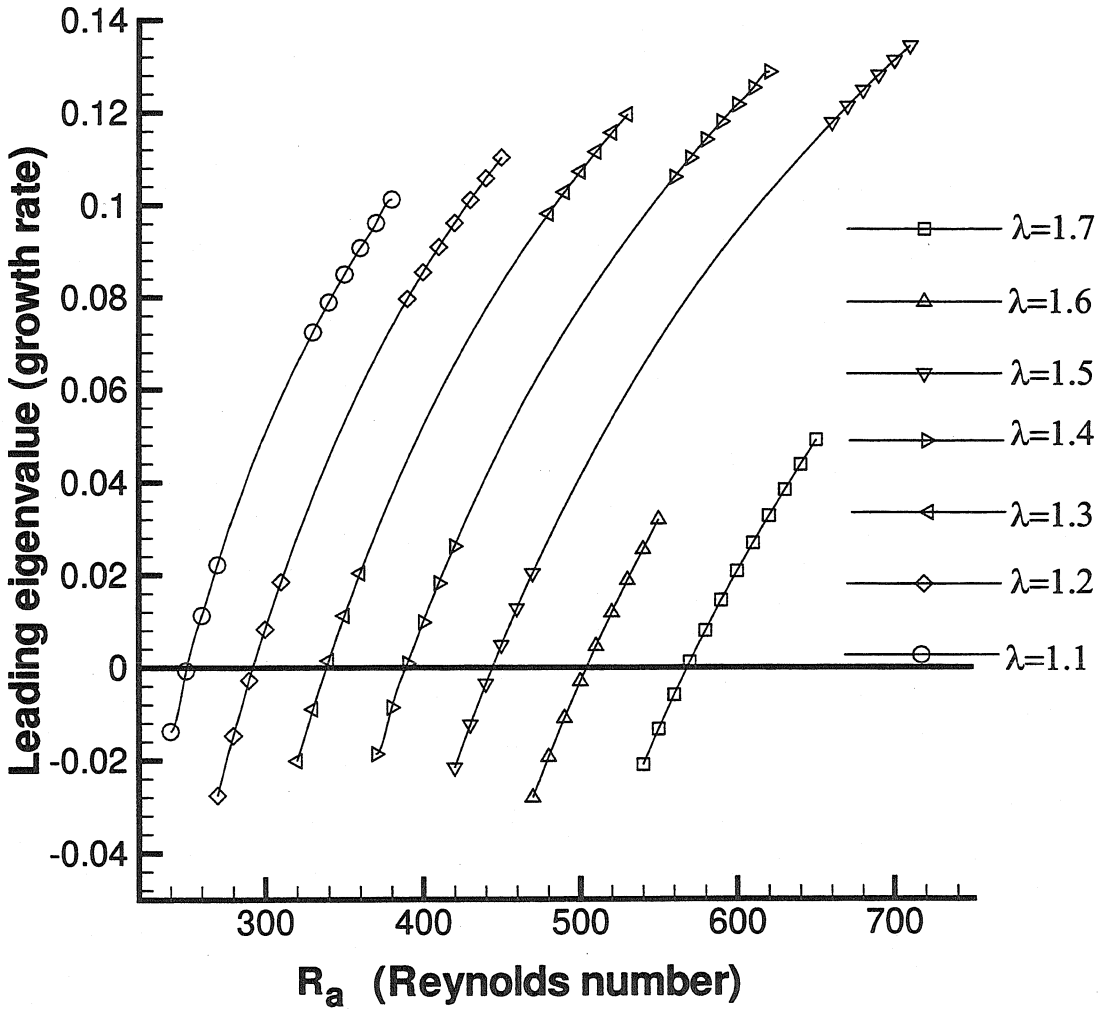

Figure 2.44: Leading eigenvalues α_1 of the $n = 1$ Fourier mode of the perturbation of flow past a prolate spheroid of various aspect ratios versus R_a.

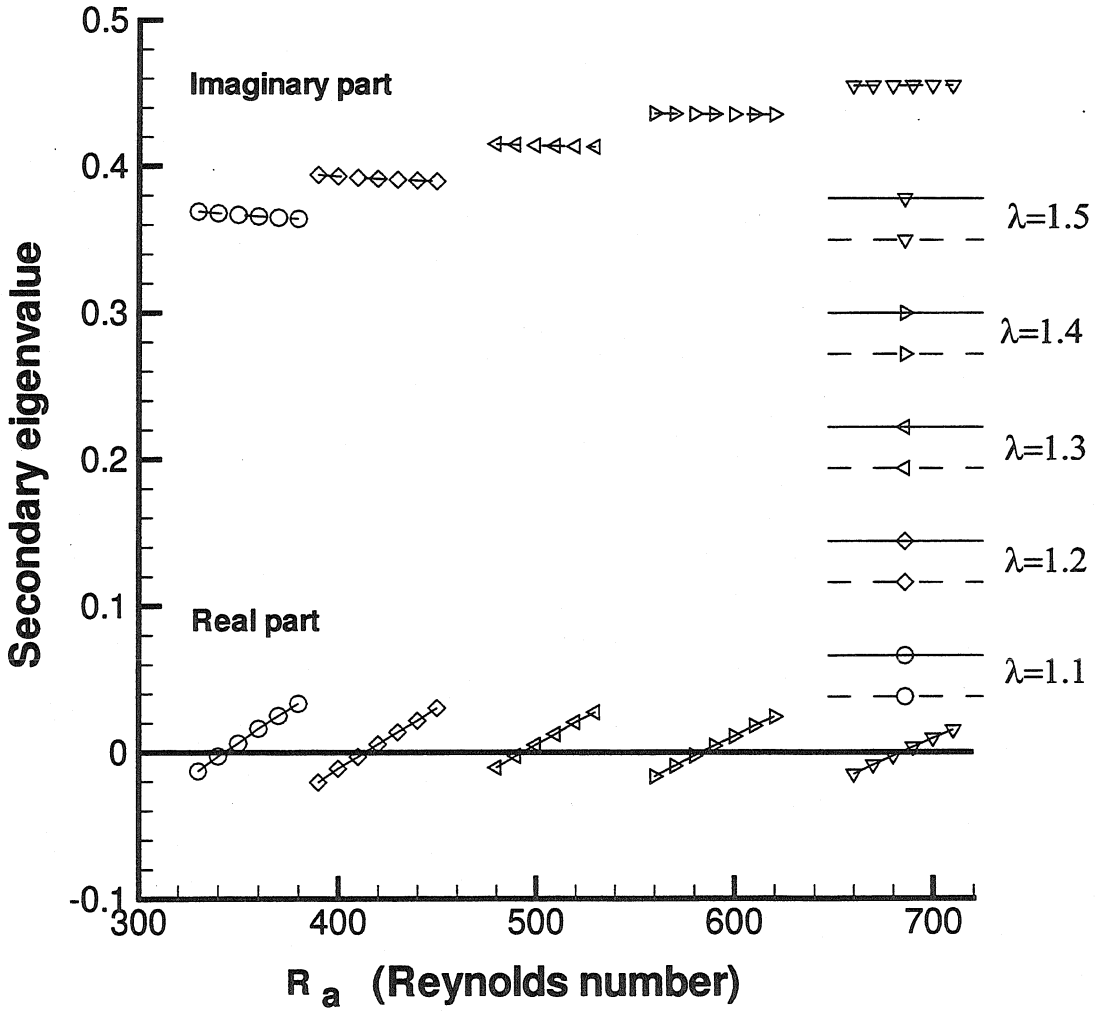

Figure 2.45: Secondary eigenvalues α_2 of the $n = 1$ Fourier mode of the perturbation of flow past a prolate spheroid of various aspect ratios versus R_a.

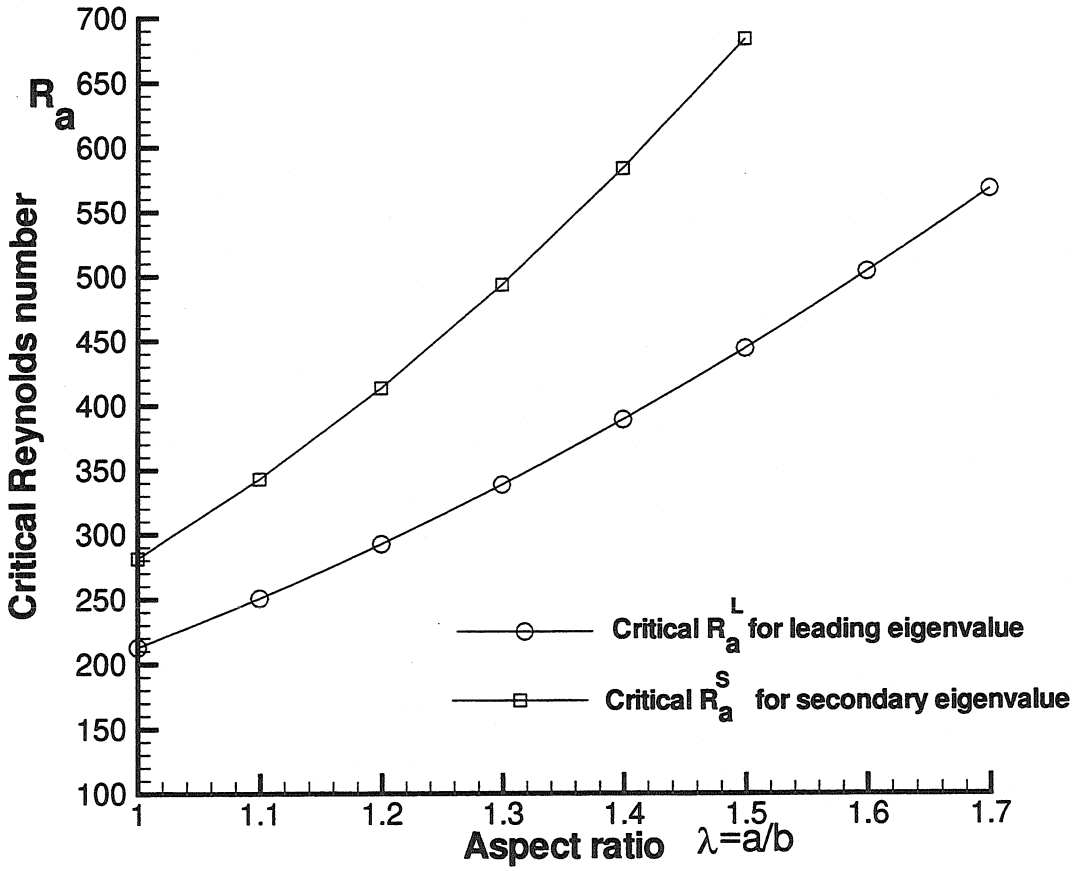

Figure 2.46: Critical Reynolds numbers R_a^L and R_a^S versus aspect ratio λ for the $n = 1$ Fourier mode of the perturbation of flow past a prolate spheroid.

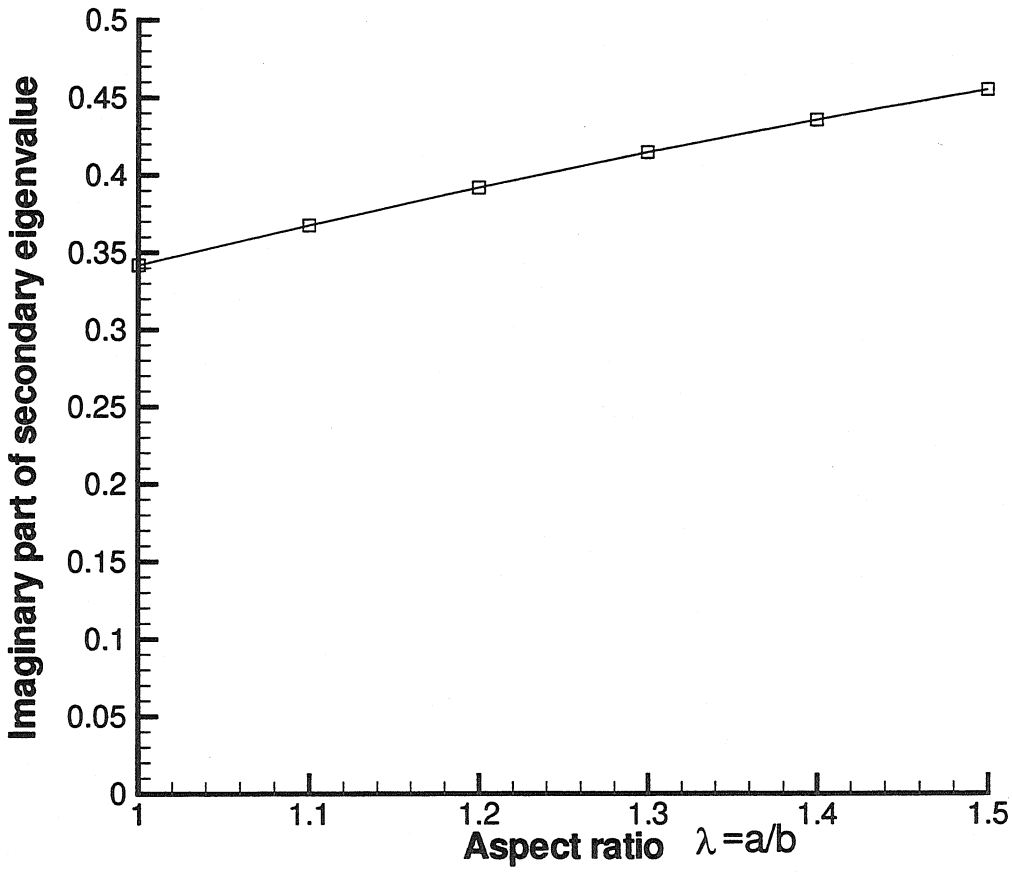

Figure 2.47: Secondary eigenvalues α_2 at the critical Reynolds numbers R_a^S versus aspect ratio λ for the $n = 1$ Fourier mode of the perturbation of flow past a prolate spheroid.

Figures 2.50 and 2.52 show the eigenfunctions corresponding to the secondary eigenvalue α_2 for $\lambda = 1.2$ and 1.5. They also appear to be similar to each other and are similar to the eigenfunctions corresponding to the secondary eigenvalue for the sphere. In addition, the figures show that the value of eigenfunctions is large near the body where the wake is located and decays to zero quickly away from the body.

Figure 2.48 shows the Fourier modes $n = 0$, $n = 2$, and $n = 3$ of the perturbations of flow past a prolate spheroid with $\lambda = 1.2$ evolving in time at $R_a = 400$. It is clear that they are all stable even when the flow is beyond the critical Reynolds number at which the $n = 1$ Fourier mode is already unstable. This indicates that the $n = 1$ Fourier mode is the dominant mode of the instability of the perturbation of flow past prolate spheroids for the range of the Reynolds numbers that we studied.

Figure 2.53 shows the results for the oblate spheroids, the sphere, and the prolate spheroids combined to form a pair of curves that show the relation between the critical Reynolds numbers R_b^L and R_b^S and the aspect ratio λ. The results for the prolate spheroids are rescaled so that the cross sectional area of the prolate spheroid is same as that of oblate spheroid by setting $R_b = R_a/\lambda$.

It turns out that both R_b^L and R_b^S seen in Figure 2.53 are fit well by a quadratic curve. This is shown by letting $R_b = c_0\lambda^2 + c_1\lambda + c_2$ and employing least squares using the given data above to obtain the coefficients c_0, c_1, and c_2. Doing so gives

$$R_b^L = 44.1\lambda^2 + 55.4\lambda + 113.5, \tag{2.38}$$

$$R_b^S = 134.8\lambda^2 + 11.8\lambda + 135.8. \tag{2.39}$$

This tells us that when $\lambda = 0$, i.e., a flat disk, the critical Reynolds numbers are 113.5 and 135.8. This agrees reasonably well with Natarajan and Acrivos's result [26] of 116.5 and 125.6. The critical Reynolds number for the secondary eigenvalue is not in as good agreement because we probably need to compute instability results for $\lambda < 0.3$ to achieve a better fit on the secondary curve (2.39). Also, we evaluate the critical Reynolds numbers from interpolating data points, and that may introduce additional uncertainties. Notice that if the spheroid is more oblate, the critical Reynolds numbers

appear to converge; and if the spheroid is more prolate, they tend to diverge rather dramatically.

In this chapter, we use a numerical grid generation method and a linear stability analysis to study the behavior of viscous flow past spheroids of various aspect ratios. Our results indicate that the mechanism for instability of flow past an axisymmetric spheroid is similar for all cases that we investigated.

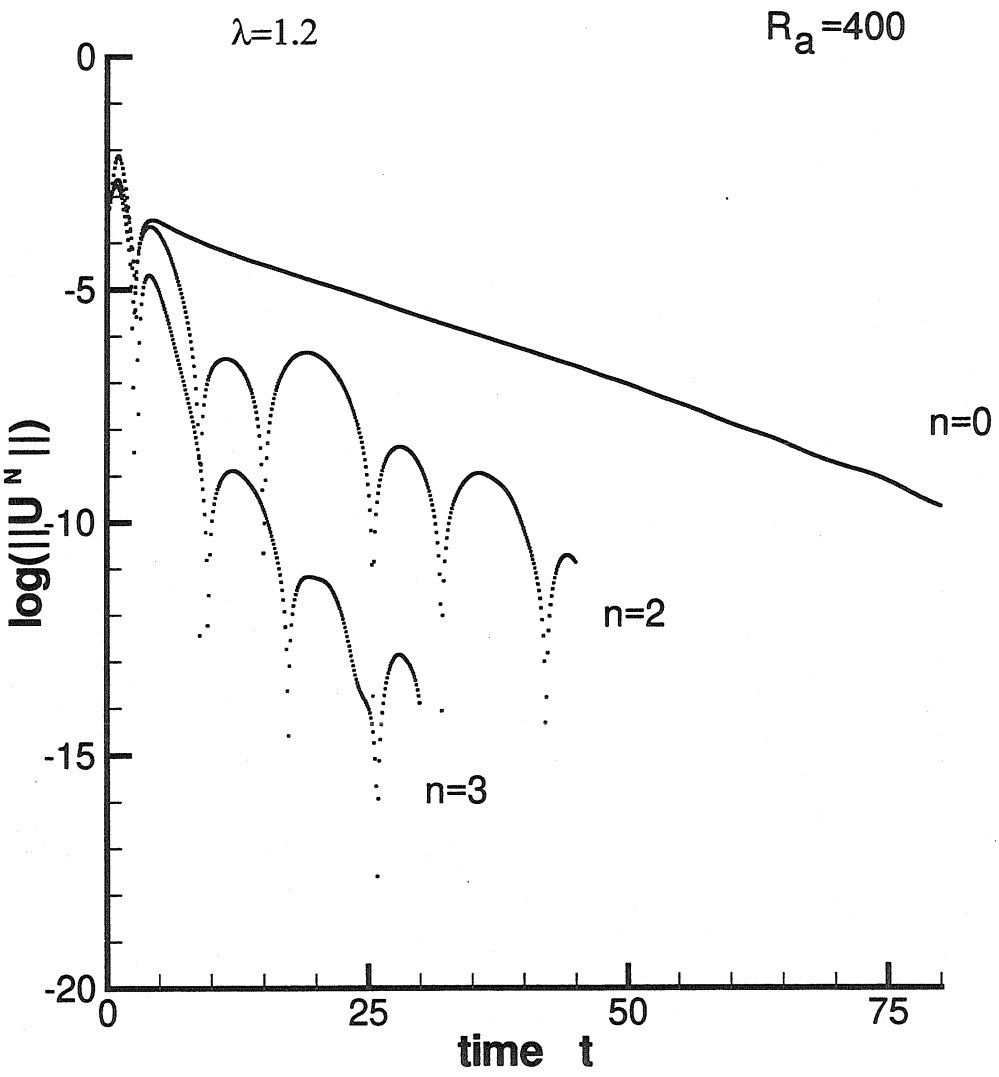

Figure 2.48: *Log* $\left(||\mathbf{U}^N||\right)$ of the $n = 0$, $n = 2$, and $n = 3$ Fourier modes of the perturbation of flow past a prolate spheroid with $\lambda = 1.2$ versus time t at $R_a = 400$.

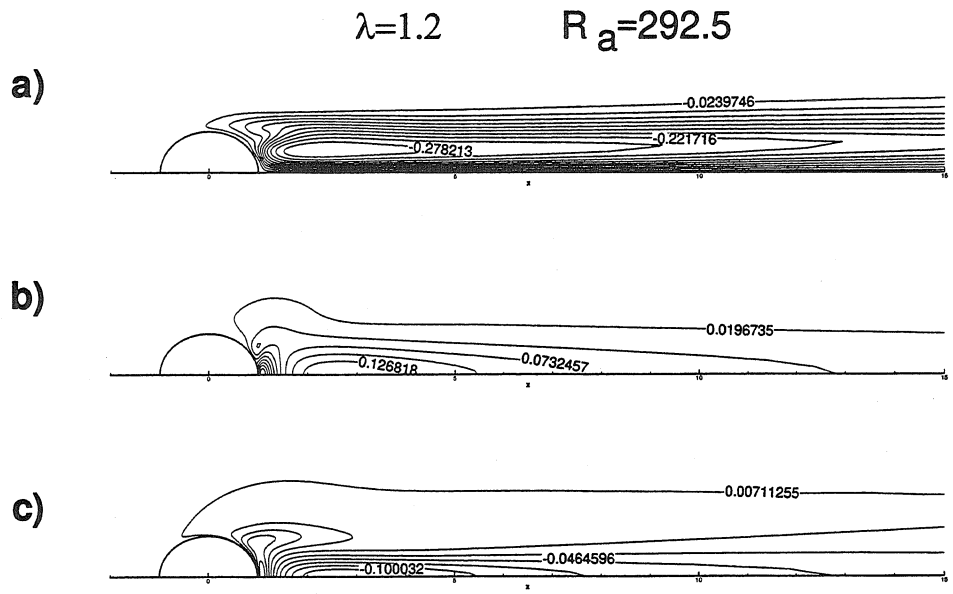

Figure 2.49: Eigenfunctions corresponding to the leading eigenvalue α_1 of the $n = 1$ Fourier mode of the perturbation of flow past a prolate spheroid with $\lambda = 1.2$ at $R_a^L = 292.5$. a) $\mathrm{Re}\,(\tilde{u}_{x_1})$, b) $\mathrm{Re}\,(\tilde{u}_{\sigma_1})$, c) $\mathrm{Im}\,(\tilde{u}_{\phi_1})$.

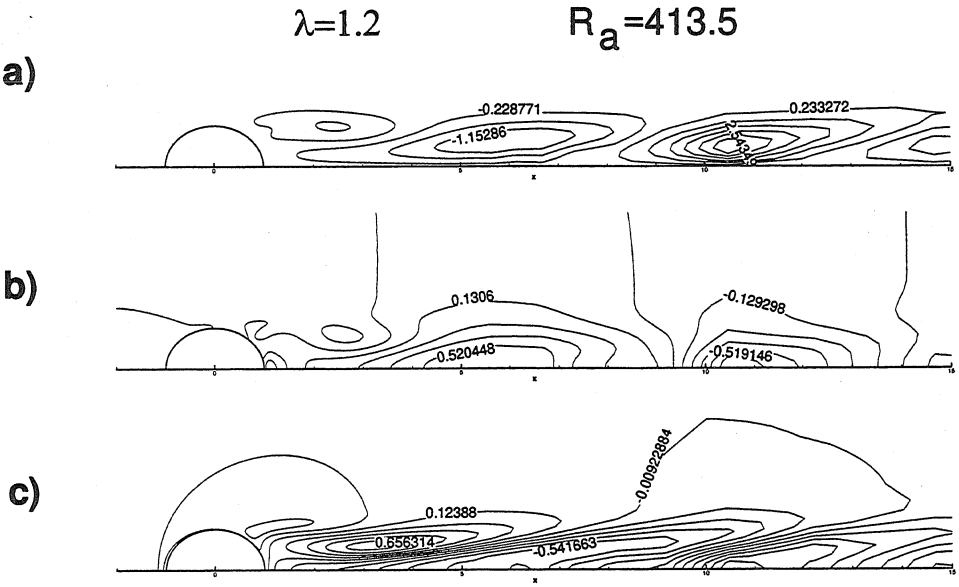

Figure 2.50: Eigenfunctions corresponding to the secondary eigenvalue α_2 of the $n = 1$ Fourier mode of the perturbation of flow past a prolate spheroid with $\lambda = 1.2$ at $R_a^S = 413.5$. a) $\mathrm{Re}\,(\tilde{u}_{x_1})$, b) $\mathrm{Re}\,(\tilde{u}_{\sigma_1})$, c) $\mathrm{Im}\,(\tilde{u}_{\phi_1})$.

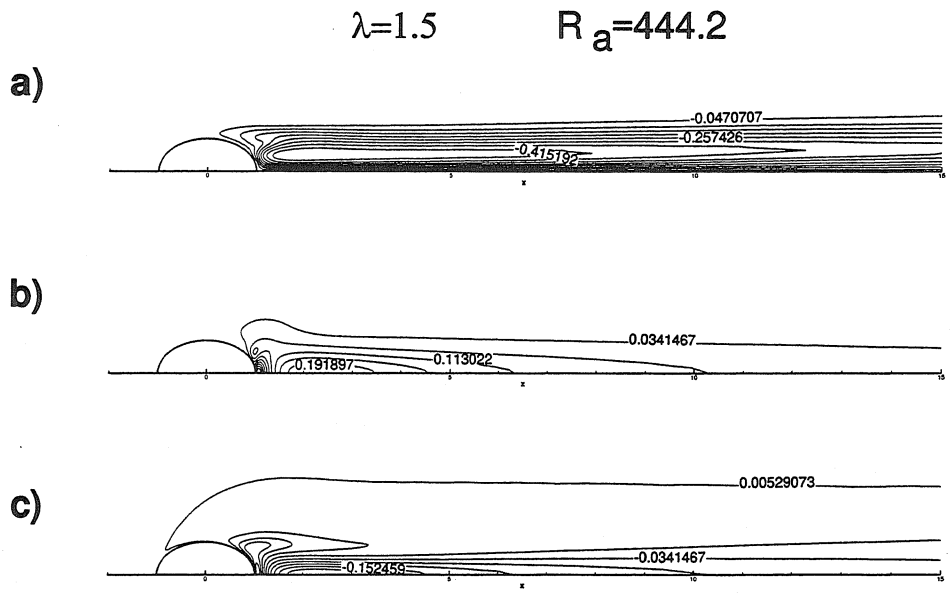

Figure 2.51: Eigenfunctions corresponding to the leading eigenvalue α_1 of the $n = 1$ Fourier mode of the perturbation of flow past a prolate spheroid with $\lambda = 1.5$ at $R_a^L = 444.2$. a) $\mathrm{Re}\,(\tilde{u}_{x_1})$, b) $\mathrm{Re}\,(\tilde{u}_{\sigma_1})$, c) $\mathrm{Im}\,(\tilde{u}_{\phi_1})$.

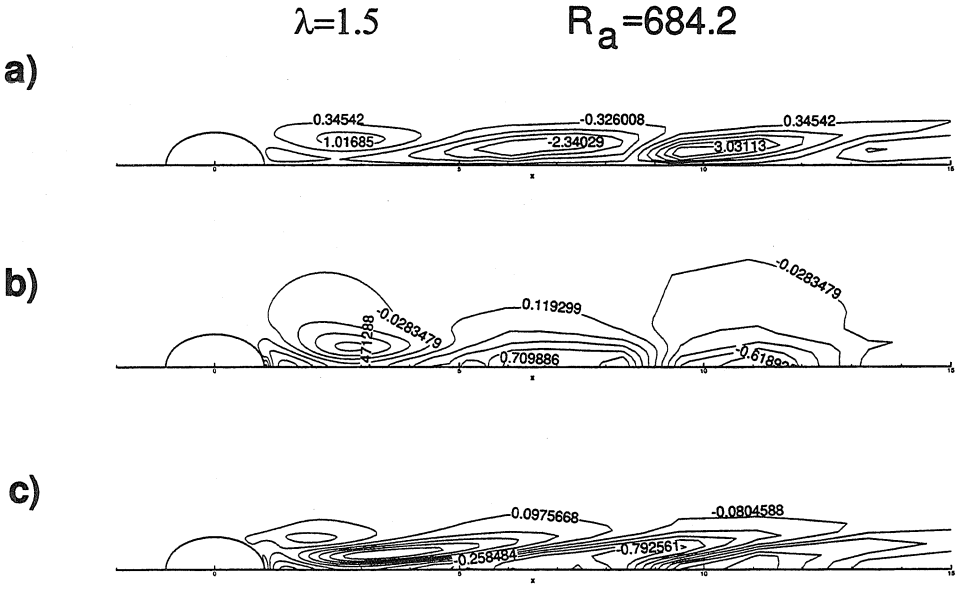

Figure 2.52: Eigenfunctions corresponding to the secondary eigenvalue α_2 of the $n = 1$ Fourier mode of the perturbation of flow past a prolate spheroid with $\lambda = 1.5$ at $R_a^s = 684.2$. a) $\mathrm{Re}\,(\tilde{u}_{x_1})$, b) $\mathrm{Re}\,(\tilde{u}_{\sigma_1})$, c) $\mathrm{Im}\,(\tilde{u}_{\phi_1})$.

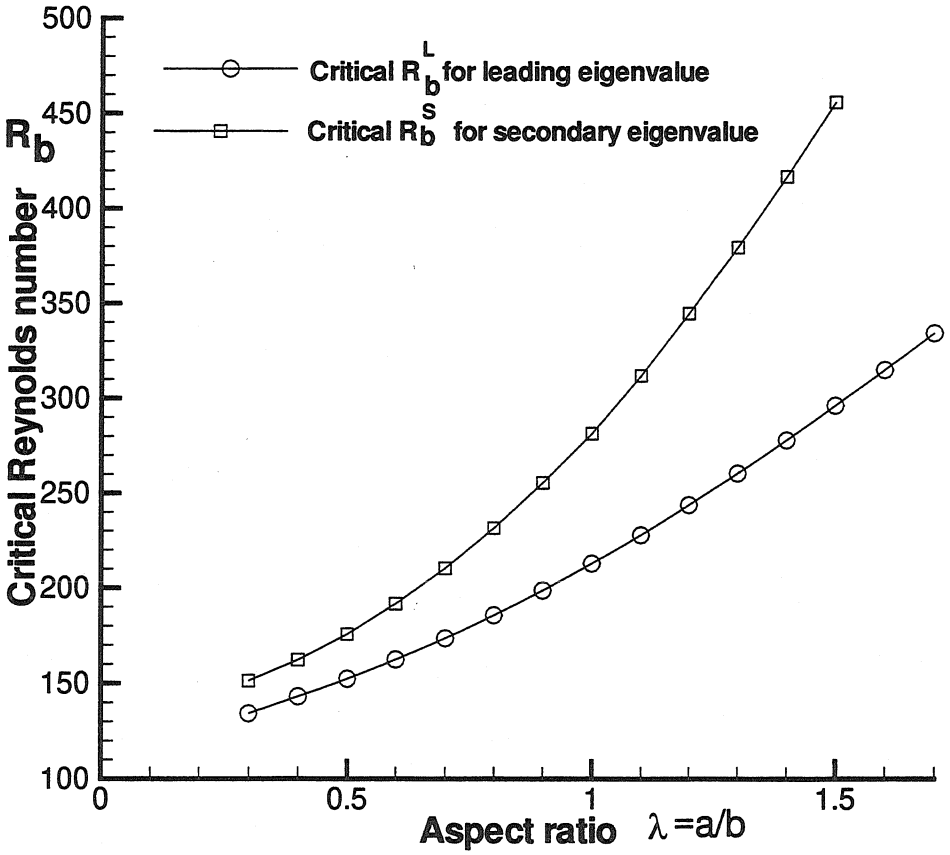

Figure 2.53: Critical Reynolds numbers R_b^L and R_b^S versus aspect ratio $\lambda = a/b$.

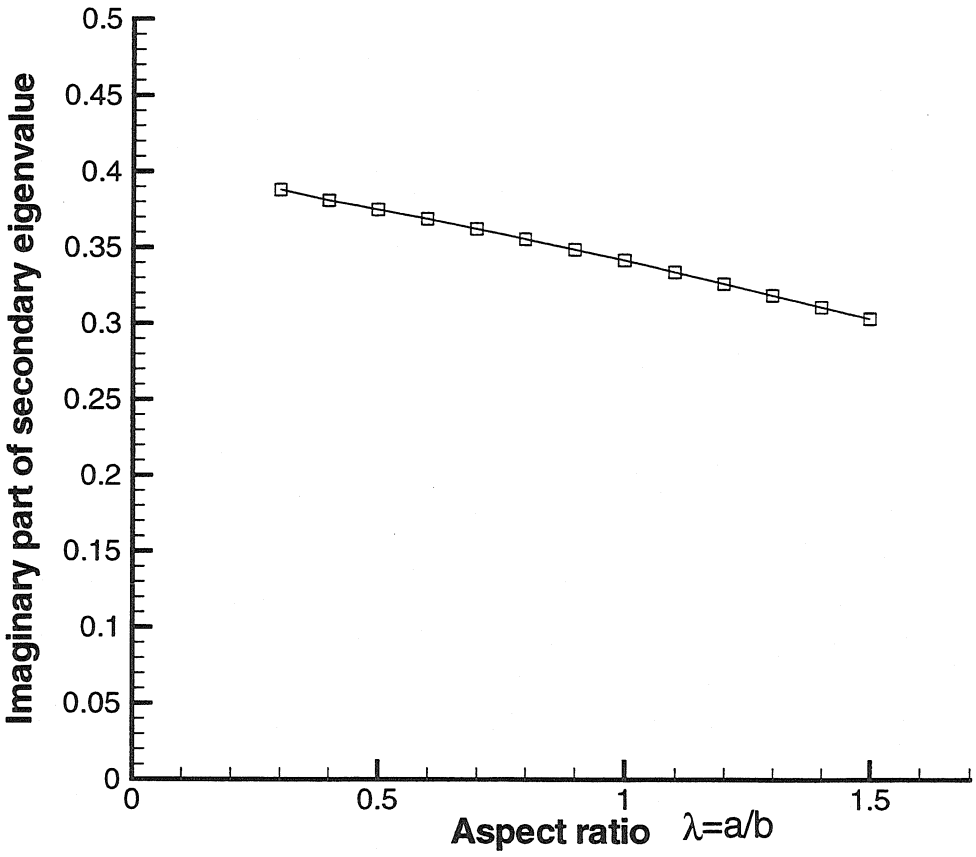

Figure 2.54: Imaginary part of secondary eigenvalues at R_b^S versus aspect ratio $\lambda = a/b$.

Chapter 3 The Behavior of Viscous Flow Past an Ellipsoidal Bubble of Fixed Shape

3.1 Introduction

In Chapter 2, we considered viscous flows past bodies while applying the no-slip boundary condition. Here, we consider flows past bodies with a free-slip boundary condition, which is characterized by zero tangential stress on the surface of the body. It is known experimentally that as a gas bubble rises in a fluid, it deforms to a shape that resembles an oblate ellipsoid [3] & [9]. Using this fact, Moore [24] used boundary layer perturbation analysis to study distorted gas bubbles rising in a fluid of small viscosity. His analysis facilitated computation of drag coefficients of flow past oblate ellipsoidal bubbles of fixed shape with free-slip boundary conditions at high Reynolds number. Moore's analysis determined the drag coefficient C_D, which is the nondimensionalized form of the drag induced on the body by the fluid flow, to be

$$C_D \sim \frac{48}{R_r} G(\mu)\,(1 + H(\mu)\, R_r^{-\frac{1}{2}}).$$

Here, R_r is the Reynolds number such that the volume of the ellipsoidal bubble is equivalent to that of a sphere of radius $r = (b^2 a)^{\frac{1}{3}}$; $G(\mu)$ and $H(\mu)$ are functions whose values are computed in Moore's paper. The variable $\mu = b/a$ is the aspect ratio of the ellipsoid. Here, b is the length of the axis of the ellipsoid orthogonal to the flow, and a is the length of the axis of the ellipsoid parallel to the flow. Figure 3.1 shows the setup of the problem.

In previous numerical work, Dandy and Leal [6] used the numerical grid generation method discussed in Chapter 2 to solve for steady, axisymmetric, viscous flow around oblate ellipsoidal bubbles of fixed shape. They showed, given an ellipsoidal bubble

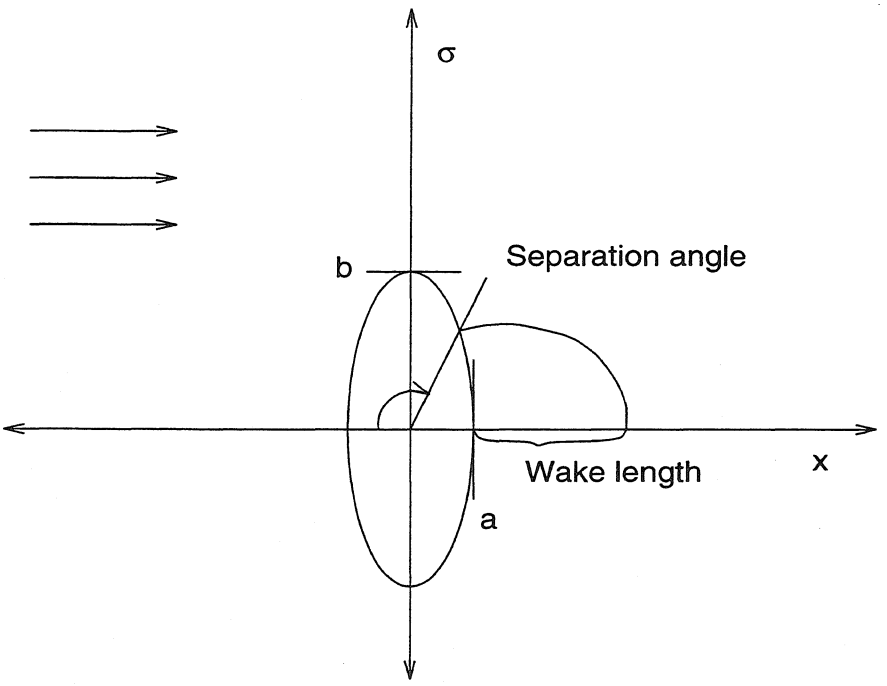

Figure 3.1: Setup of the problem.

of fixed shape with a given aspect ratio, that as the Reynolds number increases, a wake develops at the back of the ellipsoid, grows to a maximal shape, and then shrinks in size and ultimately disappears. They then concluded that even with a free-slip boundary condition, if the body is sufficiently distorted, a sufficient amount of vorticity can be generated to induce a standing wake in the flow. They also concluded that there exists a critical aspect ratio $\mu \approx 1.55$ above which a wake develops. This is achieved when the maximum value of vorticity on the surface of the body reaches a critical value of 5.25, independent of the value of μ. Later, Blanco and Magnaudet [4] revisited this problem and used their own finite-volume method to compute steady, axisymmetric, viscous flows past ellipsoidal bubbles of fixed shape. While their conclusion about wake generation was the same as Dandy and Leal [6], the specific numerical results that they obtained differed greatly. For example, Dandy and Leal [6] claimed that a standing wake exists between Reynolds number 50 and 210 when the aspect ratio of the ellipsoidal bubble is $\mu = 1.65$. Blanco and Magnaudet [4], on the other hand, did not observe a wake at any value

of the Reynolds number for all aspect ratios less than $\mu = 1.65$; according to their computations, a wake develops when the value of μ is above 1.65. Furthermore, the critical maximum vorticity required on the surface of the ellipsoidal bubble so that a wake develops is about 6.55. They attributed this discrepancy in the results to the fact that their finite-volume method somehow advects vorticity better than Dandy and Leal's method [6]. They also suggested that it would be interesting to carry out a linear stability analysis on the flows past ellipsoidal bubbles of fixed shape to see if it could provide any insight into the behavior of a rising bubble.

Dandy and Leal [6] used a grid of resolution 60x60 for their calculations, and this limited their flow computations to Reynolds numbers of around 300. In this Chapter, we revisit the problem of flow past ellipsoidal bubble of fixed shape using basically the same numerical method that Dandy and Leal [6] used with higher resolution and try to reconcile their results with Blanco and Magnaudet's [4]. In addition, a linear stability analysis is carried out using basically the same method used in Chapter 2 for rigid spheroids to see if flows past an ellipsoidal bubble of fixed shape can become unstable.

3.2 Numerical method for steady flow

The numerical method used here is basically the same method as that described in Chapter 2. Since it is extensively discussed there, the main parts of the method are only summarized here.

First, Ryskin and Leal's [33] orthogonal, curvilinear grid generation method is used to construct a numerical grid that maps the upper half of the ellipsoid of a given aspect ratio μ to a unit square. Once the grid is determined, we associate the physical coordinate (x, y, z) and the numerical, curvilinear coordinate (ξ, η, ϕ) through the relations

$$\begin{aligned} x &= x(\xi, \eta), \\ y &= \sigma(\xi, \eta)\cos(\phi), \end{aligned}$$

$$z = \sigma(\xi,\eta)\sin(\phi).$$

One feature of the Ryskin and Leal [33] grid is that the grid density in the tangential direction is controlled by using different types of distortion functions. The distortion function

$$f(\xi,\eta) = \pi\xi\left[1-\alpha\cos(\pi\eta)\right]$$

is used most often by Ryskin and Leal [34], [35]. Setting α small gives an evenly spaced grid, and setting α near one gives a grid that is denser toward the back of the ellipsoid. In practice, we use $\alpha = 0.5$ as it gives a grid that is reasonably dense toward the back of the body. This distortion function with $\alpha = 0.5$ is also used by Dandy and Leal [6] in their calculations.

Using this mesh, the Navier-Stokes equations are then solved in this new coordinate system to simulate the flow. We assume that the flow is Newtonian, incompressible, steady, and axisymmetric. This allows us to rewrite the equations in stream function-vorticity form:

$$\begin{aligned}&\frac{1}{h_\xi h_\eta}\left[\frac{\partial\psi}{\partial\xi}\frac{\partial}{\partial\eta}\left(\frac{\omega}{\sigma}\right)-\frac{\partial\psi}{\partial\eta}\frac{\partial}{\partial\xi}\left(\frac{\omega}{\sigma}\right)\right]\\ &-\frac{2}{R_b}\frac{1}{h_\xi h_\eta}\left\{\frac{\partial}{\partial\xi}\left[\frac{h_\eta}{h_\xi\sigma}\frac{\partial}{\partial\xi}(\omega\sigma)\right]+\frac{\partial}{\partial\eta}\left[\frac{h_\xi}{h_\eta\sigma}\frac{\partial}{\partial\eta}(\omega\sigma)\right]\right\}=0,\end{aligned} \tag{3.1}$$

$$\frac{-1}{h_\xi h_\eta}\left[\frac{\partial}{\partial\xi}\left(\frac{h_\eta}{h_\xi\sigma}\frac{\partial\psi}{\partial\xi}\right)+\frac{\partial}{\partial\eta}\left(\frac{h_\xi}{h_\eta\sigma}\frac{\partial\psi}{\partial\eta}\right)\right]=\omega. \tag{3.2}$$

The Reynolds number is defined by

$$R_b = \frac{2b\rho U}{\nu}.$$

As before, U is the velocity of the outer flow, ρ is the density of the fluid, and ν is the viscosity of the fluid. We wish to solve for $\psi(\xi,\eta)$ and $\omega(\xi,\eta)$ with the velocity of the flow determined by

$$u_\xi = -\frac{1}{\sigma h_\eta}\frac{\partial\psi}{\partial\eta}, \tag{3.3}$$

$$u_\eta = \frac{1}{\sigma h_\xi}\frac{\partial \psi}{\partial \xi}.$$

The functions h_ξ and h_η are scale factors and are determined by

$$h_\xi = \sqrt{\left(\frac{\partial x}{\partial \xi}\right)^2 + \left(\frac{\partial \sigma}{\partial \xi}\right)^2},$$
$$h_\eta = \sqrt{\left(\frac{\partial x}{\partial \eta}\right)^2 + \left(\frac{\partial \sigma}{\partial \eta}\right)^2}.$$

To account for the boundary condition at infinity, we write $\psi(\xi,\eta)$ as the sum of a free stream flow plus a correction:

$$\psi = \tilde{\psi} + \frac{1}{2}\sigma^2\left(1-\xi^3\right). \tag{3.4}$$

The correction $\tilde{\psi}$ then has homogeneous boundary conditions on all sides of our curvilinear grid. This also allows us to set

$$\omega(0,\eta) = 0.$$

As before, second-order, finite differencing is used to solve for $\tilde{\psi}(\xi,\eta)$ and $\omega(\xi,\eta)$ by letting $\Delta x = \frac{1}{m+1}$ and setting $\xi = i\Delta x, \eta = j\Delta x$ for $i,j = 1...m+1$ to get

$$\tilde{\psi}(\xi,\eta) = \tilde{\psi}(i\Delta x, j\Delta x) = \tilde{\psi}_{i,j},$$
$$\omega(\xi,\eta) = \omega(i\Delta x, j\Delta x) = \omega_{i,j}.$$

The equations (3.1) and (3.2) are discretized and then rearranged to give a system of difference equations and solved using Newton's method. Again, the setup of this method is extensively covered in Chapter 2.

The boundary conditions on $\tilde{\psi}_{i,j}$ and $\omega_{i,j}$ are discussed next. Along $\eta = 0$ and $\eta = 1$, we impose that the flow is axisymmetric to obtain

$$\tilde{\psi}(\xi,0) = 0,$$

$$\tilde{\psi}(\xi,1) = 0,$$

and

$$\omega(\xi,0) = 0,$$
$$\omega(\xi,1) = 0.$$

Along $\xi = 0$, we use (3.4) to obtain

$$\tilde{\psi}(0,\eta) = 0$$

and

$$\omega(0,\eta) = 0.$$

Along $\xi = 1$, however, we need to impose a free-slip condition on the surface of the ellipsoidal bubble. This obviously differs from the boundary condition in Chapter 2 where a no-slip boundary condition is imposed. A free-slip condition implies that the shear stress on the surface of the ellipsoidal bubble is zero and is expressed by

$$e_{\xi\eta} = -\frac{h_\eta}{2h_\xi}\frac{\partial}{\partial\xi}\left(\frac{u_\eta}{h_\eta}\right) - \frac{h_\xi}{2h_\eta}\frac{\partial}{\partial\eta}\left(\frac{u_\xi}{h_\xi}\right) = 0. \tag{3.5}$$

Discretizing (3.5) gives

$$H_{B_j} = D_j^0\tilde{\psi}_{m-2,j} + D_j^1\tilde{\psi}_{m-1,j} + D_j^2\tilde{\psi}_{m,j} + D_j^3$$

where

$$D_j^0 = \frac{-1}{(h_\xi\Delta x)^2\sigma},$$
$$D_j^1 = \frac{4}{(h_\xi\Delta x)^2\sigma} - \frac{1}{2(h_\xi\sigma)^2\Delta x}\frac{\partial\sigma}{\partial\xi} - \frac{1}{2h_\xi^3\sigma\Delta x}\frac{\partial h_\xi}{\partial\xi} - \frac{1}{2h_\xi^2h_\eta\sigma\Delta x}\frac{\partial h_\eta}{\partial\xi},$$
$$D_j^2 = \frac{-5}{(h_\xi\Delta x)^2\sigma} + \frac{2}{(h_\xi\sigma)^2\Delta x}\frac{\partial\sigma}{\partial\xi} + \frac{2}{h_\xi^3\sigma\Delta x}\frac{\partial h_\xi}{\partial\xi} + \frac{2}{h_\xi^2h_\eta\sigma\Delta x}\frac{\partial h_\eta}{\partial\xi},$$

	$R_b = 50$	100	200	300	400	500	600	700
60x60	1.06	0.672	0.409	0.301	0.242			
70x70	1.06	0.673	0.408	0.298	0.239	0.201	0.176	0.160
80x80	1.06	0.666	0.405	0.297	0.238	0.201	0.176	0.158

Table 3.1: Drag coefficients of flow past an ellipsoidal bubble of fixed shape with $\mu = 1.95$ using grids of resolution 60x60, 70x70, and 80x80 with distortion coefficient $\alpha = 0.5$.

$$D_j^3 = \frac{3}{2}\frac{\sigma}{h_\xi^3}\frac{\partial h_\xi}{\partial \xi} - \frac{3\sigma}{h_\xi^2} - \frac{9}{2}\frac{1}{h_\xi^2}\frac{\partial \sigma}{\partial \xi} + \frac{3}{2}\frac{\sigma}{h_\xi^2 h_\eta}\frac{\partial h_\eta}{\partial \xi}.$$

With this numerical method, steady flows past ellipsoidal bubbles are calculated for $\mu = 1.75$, 1.84, 1.95, 2.1, and 2.5 using a grid of resolution 80x80 with distortion function $\alpha = 0.5$ for Reynolds number up to 700. It takes about 15 minutes on a Sun Ultra workstation for each R_b given μ.

3.3 Results of steady flow calculation

First, we need to establish that our steady flow solver displays the requisite convergence and consistency properties. Therefore, as a test case, we compute the steady solutions for various values of R_b for flow past an ellipsoidal bubble with $\mu = 1.95$ using grids of different resolutions and with different distortion functions.

Table 3.1 and Figure 3.2 show the drag coefficients computed for steady flow past an ellipsoidal bubble of fixed shape using grids of resolutions of 60x60, 70x70, and 80x80 and with distortion function coefficient of $\alpha = 0.5$. Using a grid of resolution of 60x60 limits the steady solutions computed to about $R_b = 400$. The drag coefficients appear to agree well with one another. Figure 3.3 shows the vorticity distribution on the surface of the ellipsoidal bubble with $\mu = 1.95$ at $R_b = 300$. Again, the distributions appear to agree well under different resolutions.

Figure 3.4 a) shows the length of the wake that forms on the back of the ellipsoidal bubble as the Reynolds number R_b is increased. The wake length is computed by determining the point along $\eta = 0$ at which $u_\xi = 0$. It is clear that the three curves are in good agreement. In addition, Figure 3.4 b) shows the separation angle of the

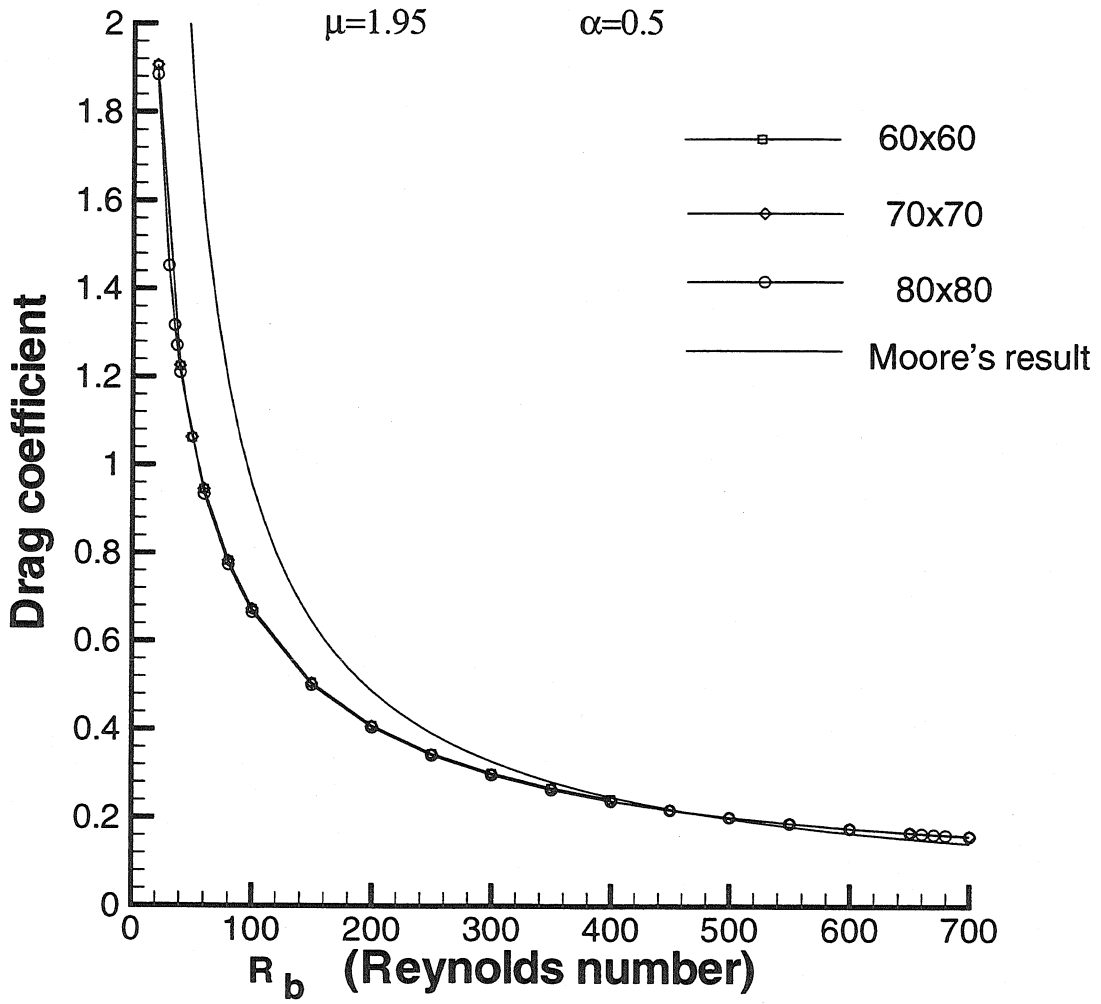

Figure 3.2: Drag coefficients of flow past an ellipsoidal bubble of fixed shape with $\mu = 1.95$ as a function of Reynolds number R_b using grids of resolution 60x60, 70x70, and 80x80 with distortion function coefficient $\alpha = 0.5$.

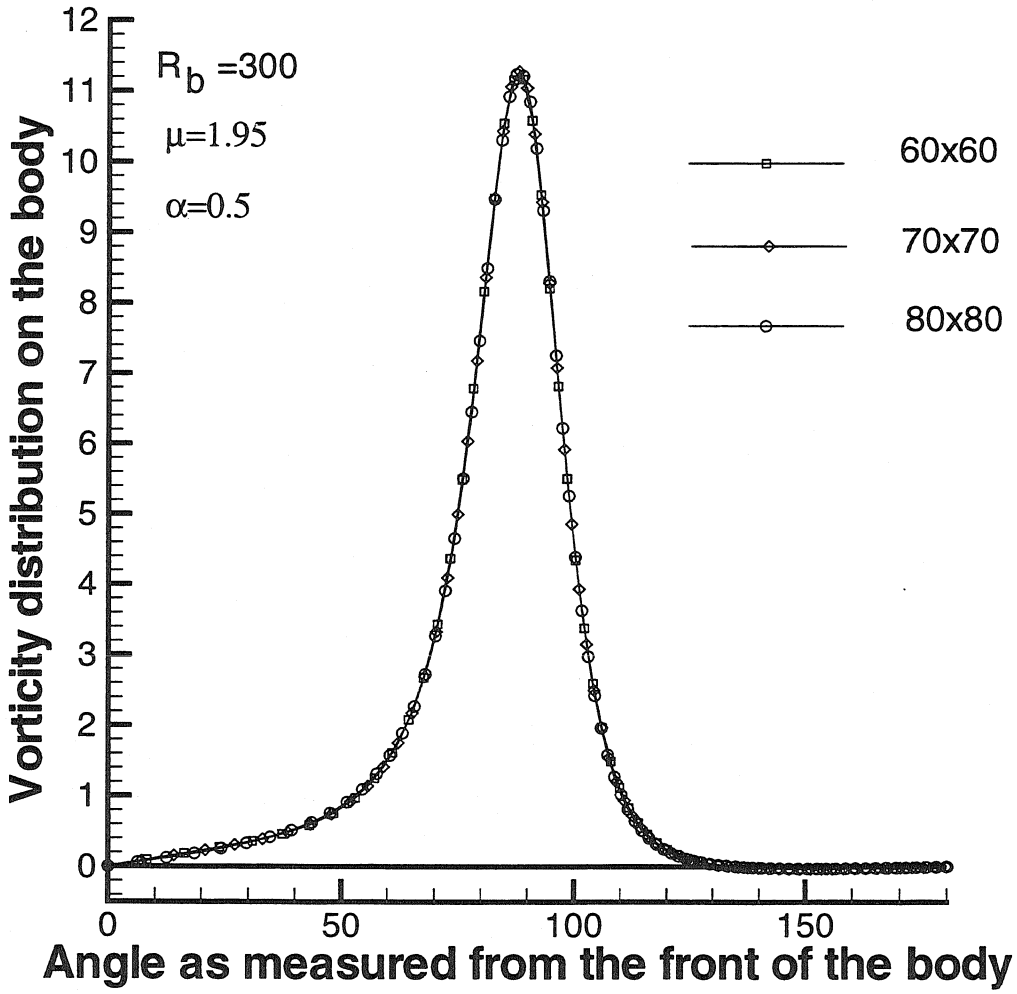

Figure 3.3: Vorticity distribution on the surface of an ellipsoidal bubble of fixed shape with $\mu = 1.95$ using grids of resolution 60x60, 70x70, and 80x80 with distortion function coefficient $\alpha = 0.5$.

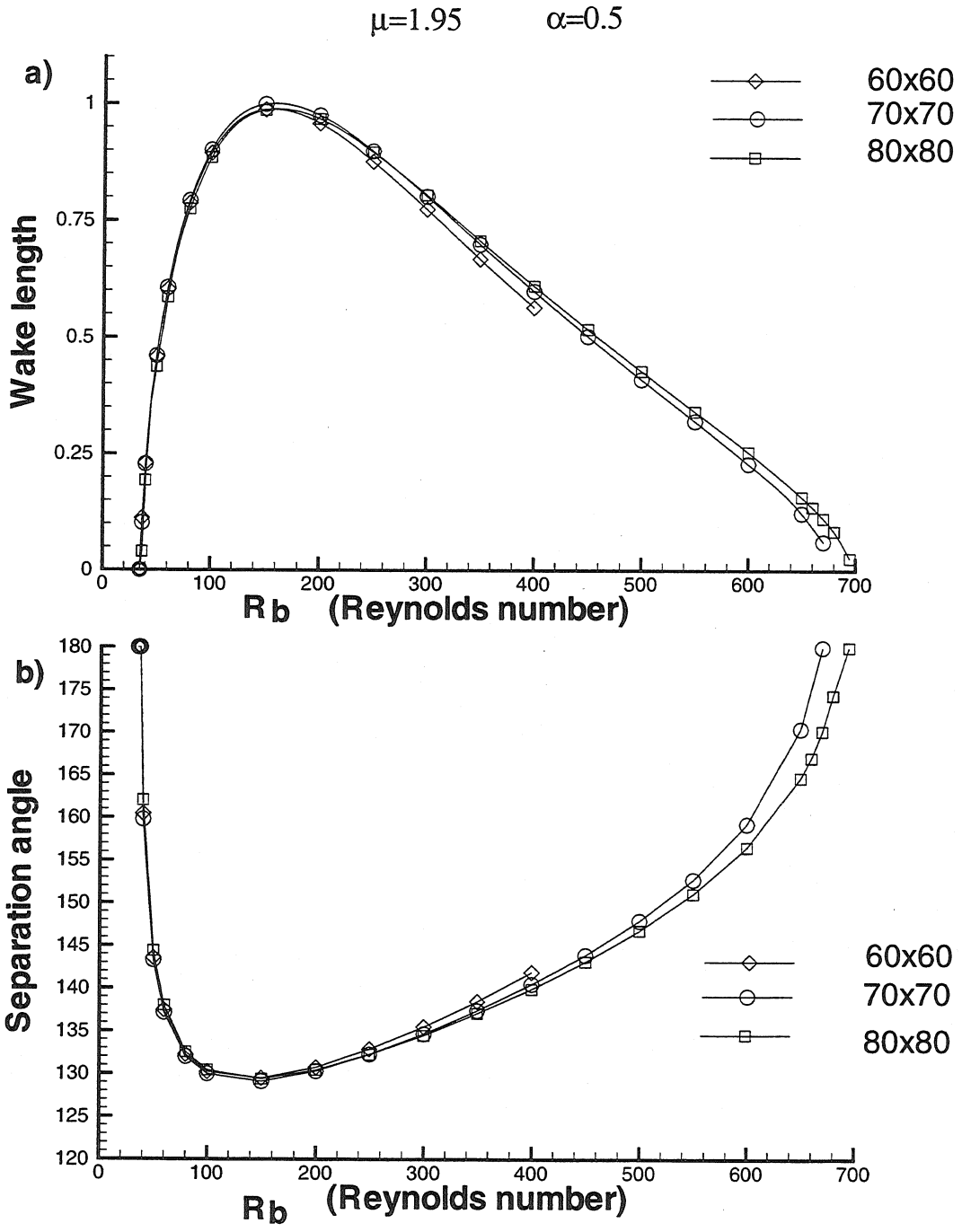

Figure 3.4: a) Length of the wake as measured from the back of an ellipsoidal bubble with $\mu = 1.95$ using grids of resolution 60x60, 70x70, and 80x80 with $\alpha = 0.5$. b) Separation angle of the wake as measured from the front of an ellipsoidal bubble with $\mu = 1.95$ using grids of resolution 60x60, 70x70, and 80x80 with $\alpha = 0.5$.

	$R_b = 50$	100	200	300	400	500	600	700
$\alpha = 0.3$	1.05	0.668	0.405	0.297	0.238			
$\alpha = 0.5$	1.06	0.666	0.405	0.297	0.233	0.201	0.176	0.158
$\alpha = 0.7$	1.06	0.663	0.404	0.297	0.238	0.201	0.177	0.159

Table 3.2: Drag coefficients of flow past an ellipsoidal bubble of fixed shape with μ= 1.95 using grids of resolution of 80x80 with distortion coefficients $\alpha = 0.3$, $\alpha = 0.5$, and $\alpha = 0.7$.

wake as measured from the front of the ellipsoidal bubble, and they also appear to be in good agreement under different resolutions. The separation angle on the surface of the ellipsoidal bubble is computed by determining the point along $\xi = 1$ at which $u_\eta = 0$. This indicates that in terms of grid resolution our results are reasonably convergent.

Next, the resolution is set to be 80x80, and the distortion function is varied. As discussed before, a distortion function with $\alpha = 0.3$ gives a grid that is more evenly spaced, while a value of $\alpha = 0.7$ gives a grid that is more dense in the back of the ellipsoidal bubble, as compared to the grid with $\alpha = 0.5$. Table 3.2 and Figure 3.5 show the drag coefficients computed for steady flow past an ellipsoidal bubble of fixed shape with resolution of the grid fixed to 80x80 and using distortion function coefficients $\alpha = 0.3$, 0.5, and 0.7. Using the distortion coefficient of $\alpha = 0.3$ produces a more evenly spaced grid, and this limits the steady solutions computed to about $R_b = 400$. This is likely due to the fact that more mesh points are needed on the back of the ellipsoidal bubble to properly resolve the wake. The drag coefficients appear to agree well with one another. Figure 3.6 shows the vorticity distribution on the surface of the ellipsoidal bubble with $\mu = 1.95$ at $R_b = 300$ using distortion coefficients $\alpha = 0.3$, $\alpha = 0.5$, and $\alpha = 0.7$. Again, the distributions appear to agree well.

Figure 3.7 a) shows the length of the wake that forms on the back of the ellipsoidal bubble as the Reynolds number R_b is increased. The figure shows that using the distortion coefficient $\alpha = 0.3$, i.e., a more evenly spaced grid, results in wakes that are slightly larger as compared to the results with $\alpha = 0.5$ and $\alpha = 0.7$. On the other hand, Figure 3.7 b) shows the separation angle of the wake, and this appears to be

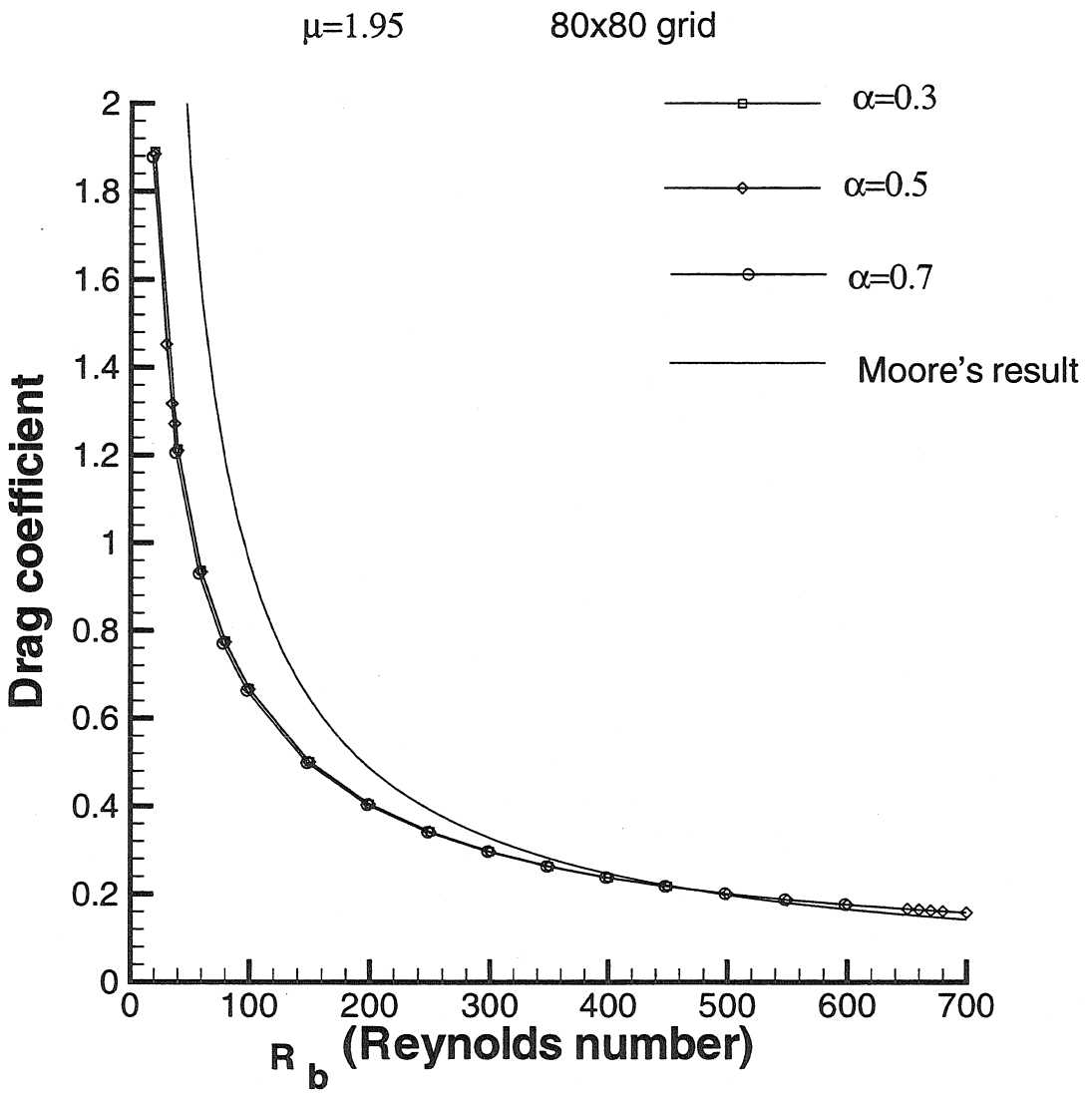

Figure 3.5: Drag coefficients of flow past an ellipsoidal bubble of fixed shape with $\mu = 1.95$ using grids of resolution 80x80 with distortion coefficients $\alpha = 0.3$, $\alpha = 0.5$, and $\alpha = 0.7$.

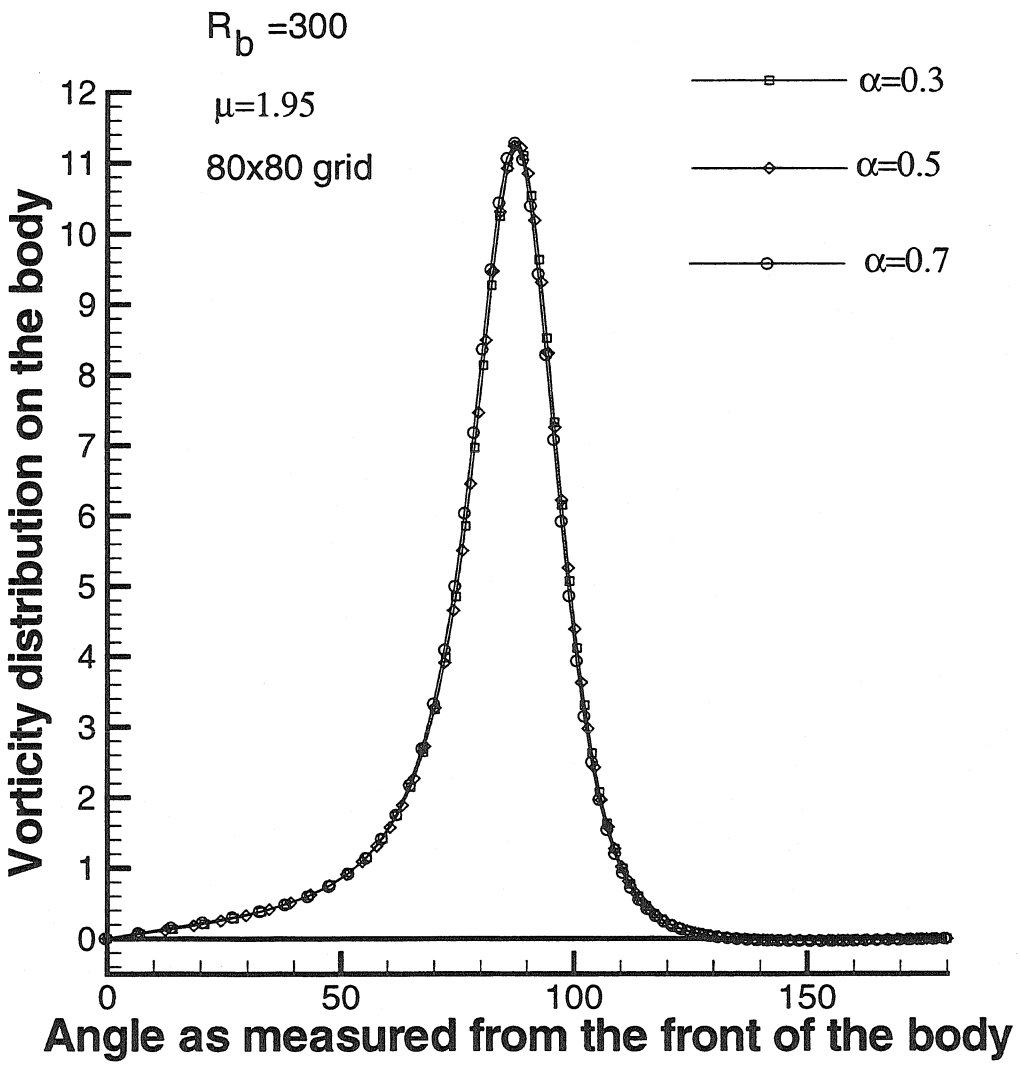

Figure 3.6: Vorticity distribution on the surface of an ellipsoidal bubble of fixed shape with $\mu = 1.95$ using grids of resolution 80x80 with distortion coefficients $\alpha = 0.3$, $\alpha = 0.5$, and $\alpha = 0.7$.

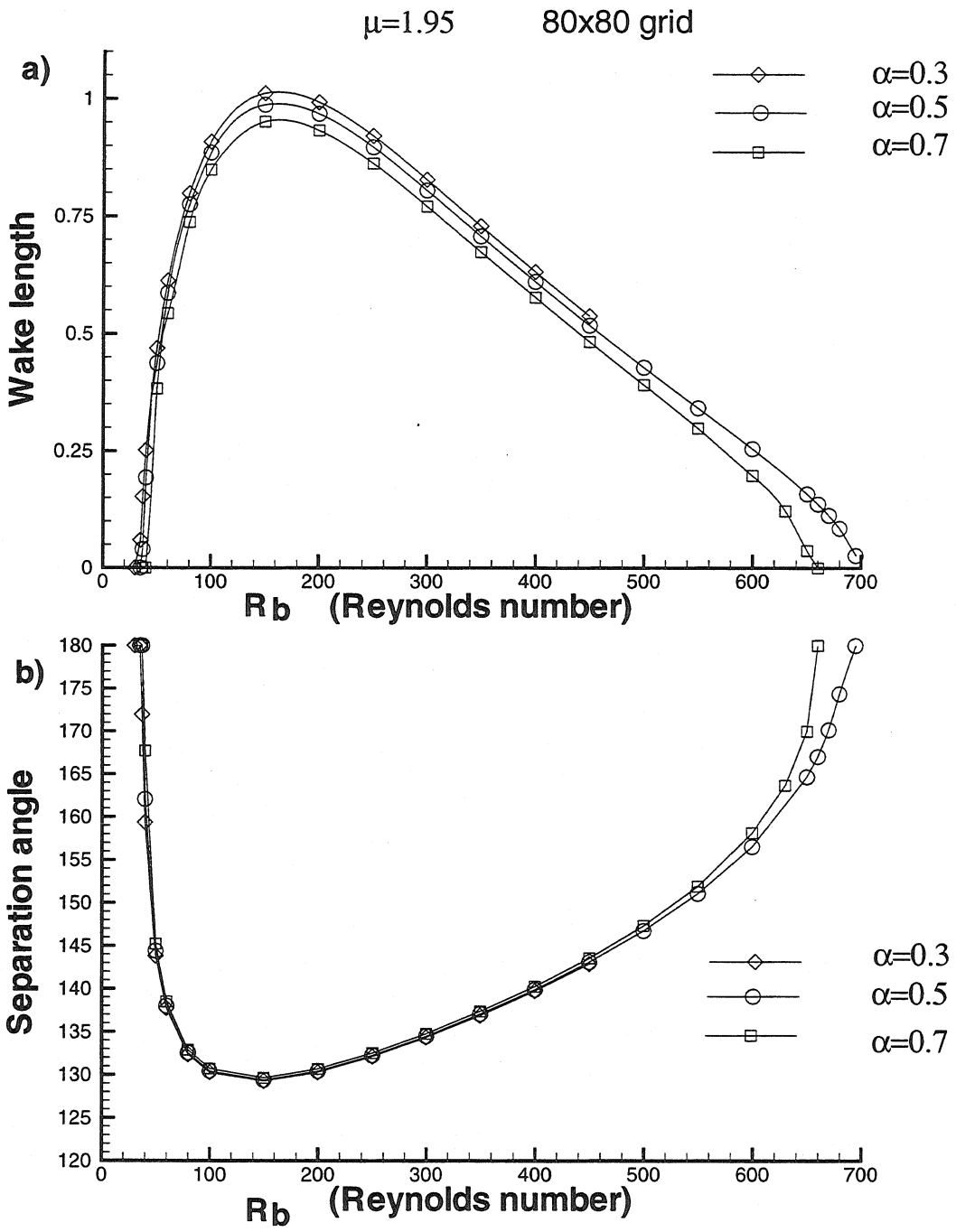

Figure 3.7: a) Length of the wake as measured from the back of an ellipsoidal bubble with $\mu = 1.95$ using grids of resolution of 80x80 with distortion coefficients $\alpha = 0.3$, $\alpha = 0.5$, and $\alpha = 0.7$. b) Separation angle of the wake as measured from the front of an ellipsoidal bubble with $\mu = 1.95$ using grids of resolution of 80x80 with distortion coefficients $\alpha = 0.3$, $\alpha = 0.5$, and $\alpha = 0.7$.

nearly identical under different distortion functions. This indicates that there is a trade-off in our numerical method in terms of using different values of α. Using grids with smaller values of α results in wakes that are slightly larger, but we are limited to lower Reynolds numbers in computing the steady solutions.

From the above results, it is clear that our flow solver gives reasonably consistent results in computing steady flow past ellipsoidal bubbles of fixed shape. There are some minor fluctuations in the size of the wake when using grids with different distortion functions. For the rest of this chapter, in our computing of steady flows for the ellipsoidal bubbles of various aspect ratios, we use grids of resolution of 80x80 with distortion coefficient of $\alpha = 0.5$.

Since our numerical method is more or less identical to Dandy and Leal's method [6], our results are compared against theirs. To begin, a flow past an ellipsoidal bubble with $\mu = 1.65$ is calculated. According to Dandy and Leal [6], a wake forms at the back of the bubble around $R_b = 40$, reaches its maximum size around $R_b = 120$, and disappears around $R_b = 240$. Figure 3.8 shows the stream function for $\mu = 1.65$ and $R_b = 60$, 120, 180, and 240. Clearly, there is no visible wake at any of the Reynolds numbers. This differs from Dandy and Leal's results as shown in Figure 3.9 and agrees with Blanco and Magnaudet's conclusion [4] that there is no wake present. The drag coefficient, which can be calculated by using the drag coefficient formula in Chapter 2, is computed to be 2.94 at $R_b = 240$; this agrees well with Moore's asymptotic result [24] of 2.93. Dandy and Leal [6] determined it to be 2.98 which is also in good agreement. So, even though we are using Dandy and Leal's method [6] & [8], the result that we obtain differs from Dandy and Leal's and appears to agree better with that of Blanco and Magnaudet.

We next compare our results with those of Blanco and Magnaudet [4] in more detail. Figure 3.10 a) shows the wake lengths, and Figure 3.10 b) shows the wake separation angles at various Reynolds numbers for flow past ellipsoidal bubbles with aspect ratios $\mu = 1.75$, 1.84, 1.95, 2.1, and 2.5. At $\mu = 1.75$, a wake develops around $R_b \approx 65$, attains its maximum size around $R_b \approx 130$, and disappears around $R_b \approx 280$. This range somewhat differs from Blanco and Magnaudet's result in that

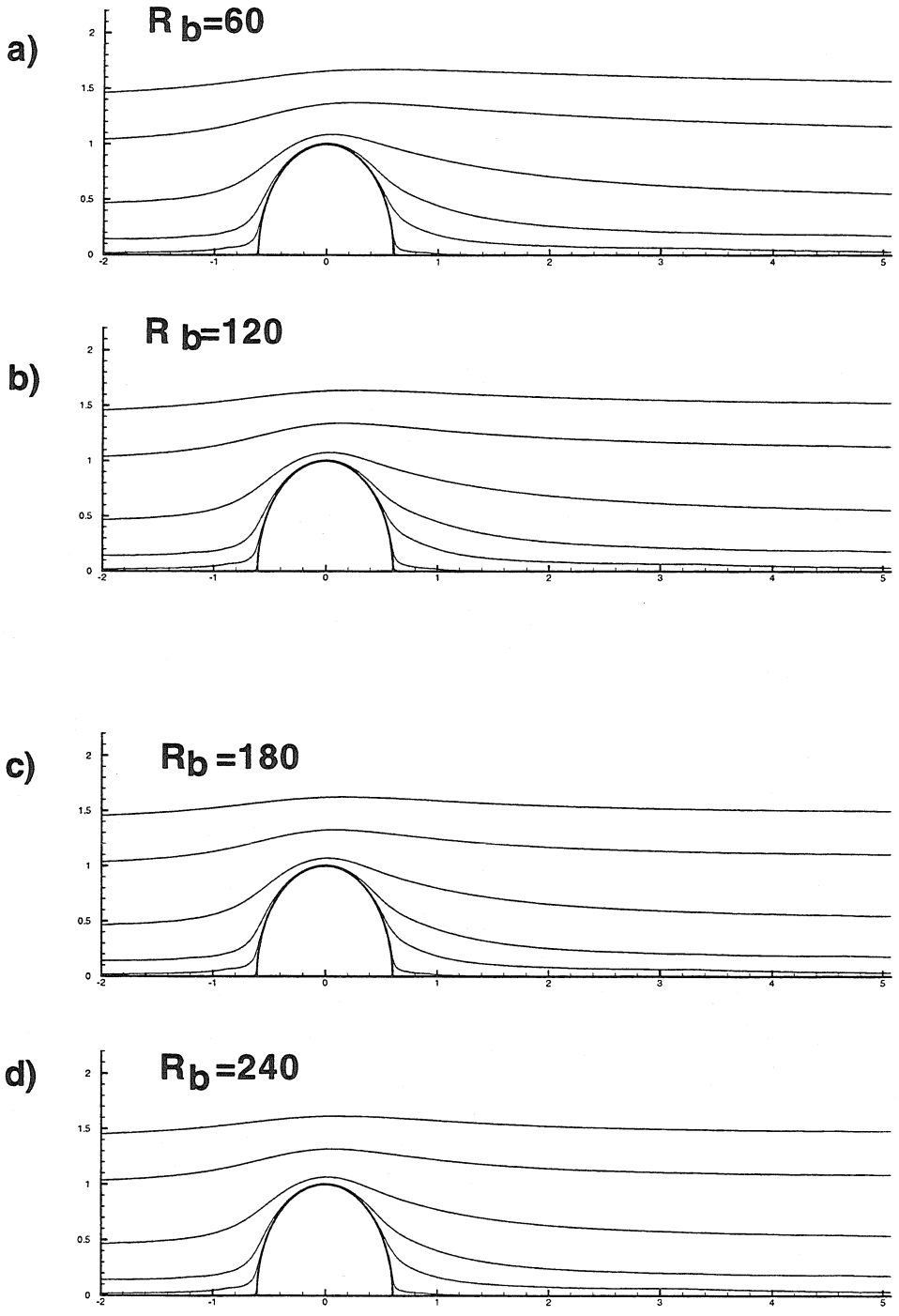

Figure 3.8: Stream lines of flow past an ellipsoidal bubble with $\mu = 1.65$ determined using our numerical method. A grid of resolution of 80x80 with distortion function coefficient $\alpha = 0.5$ is used.

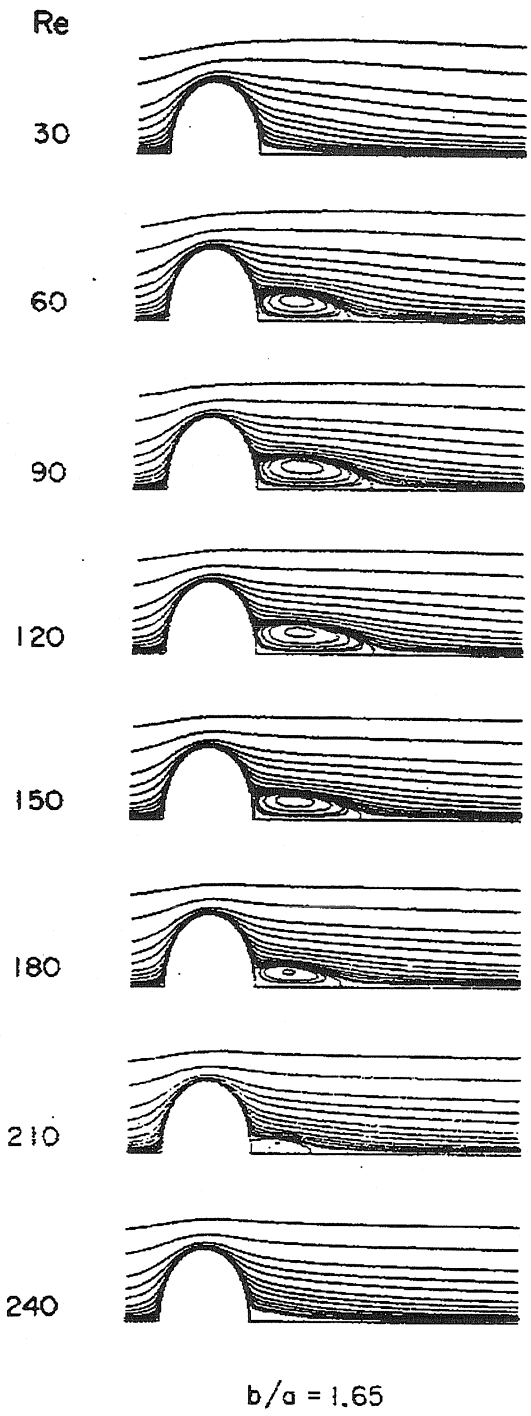

Figure 3.9: Stream lines of flow past an ellipsoidal bubble with $\mu = 1.65$ determined by Dandy and Leal [6].

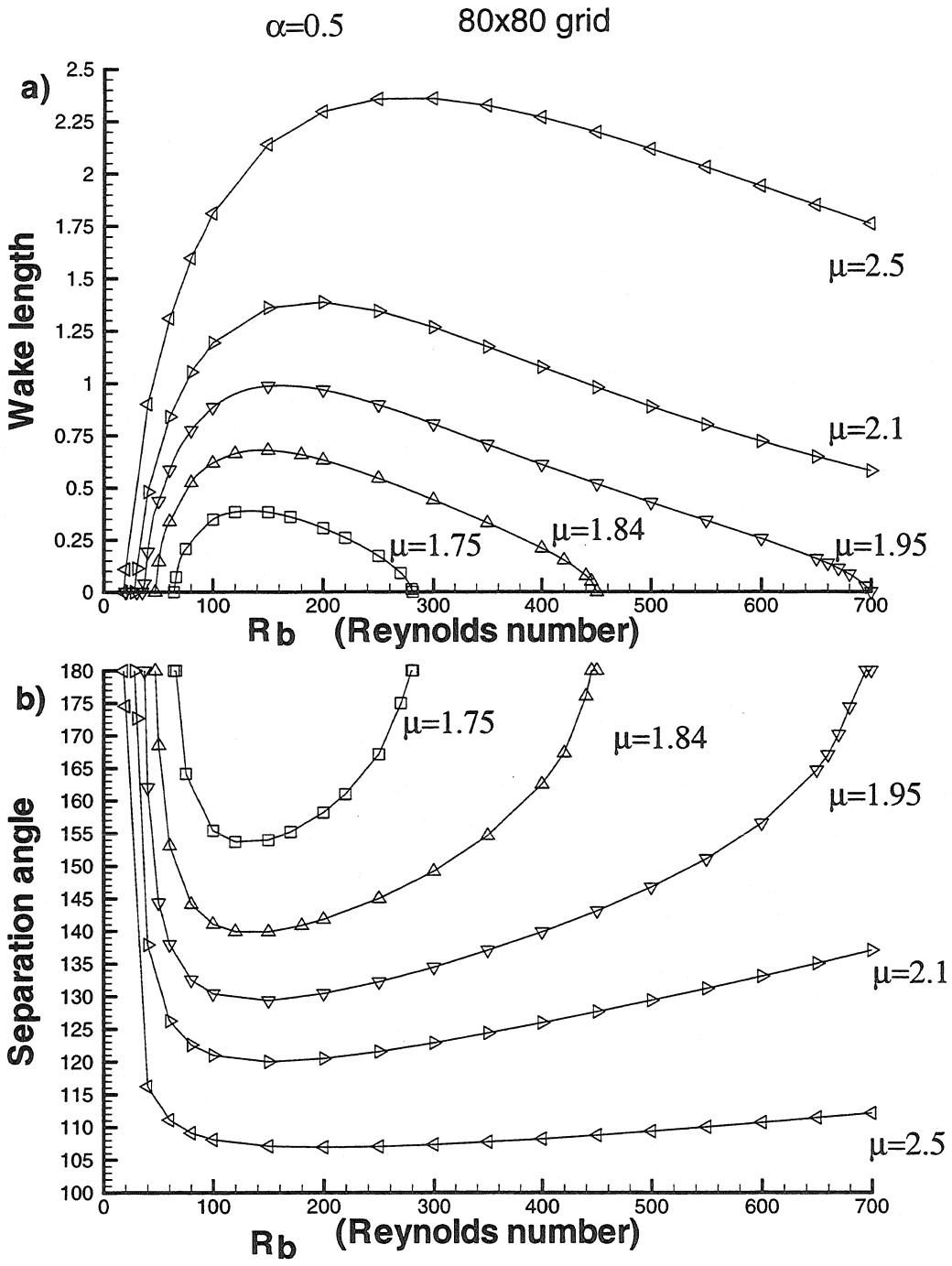

Figure 3.10: a) Length of the wake as measured from the back of the ellipsoidal bubbles with $\mu = 1.75, 1.84, 1.95, 2.1$, and 2.5. b) Separation angle of the wake as measured from the front of the ellipsoidal bubbles with $\mu = 1.75, 1.84, 1.95, 2.1$, and 2.5. 80x80 grid with distortion function coefficient $\alpha = 0.5$.

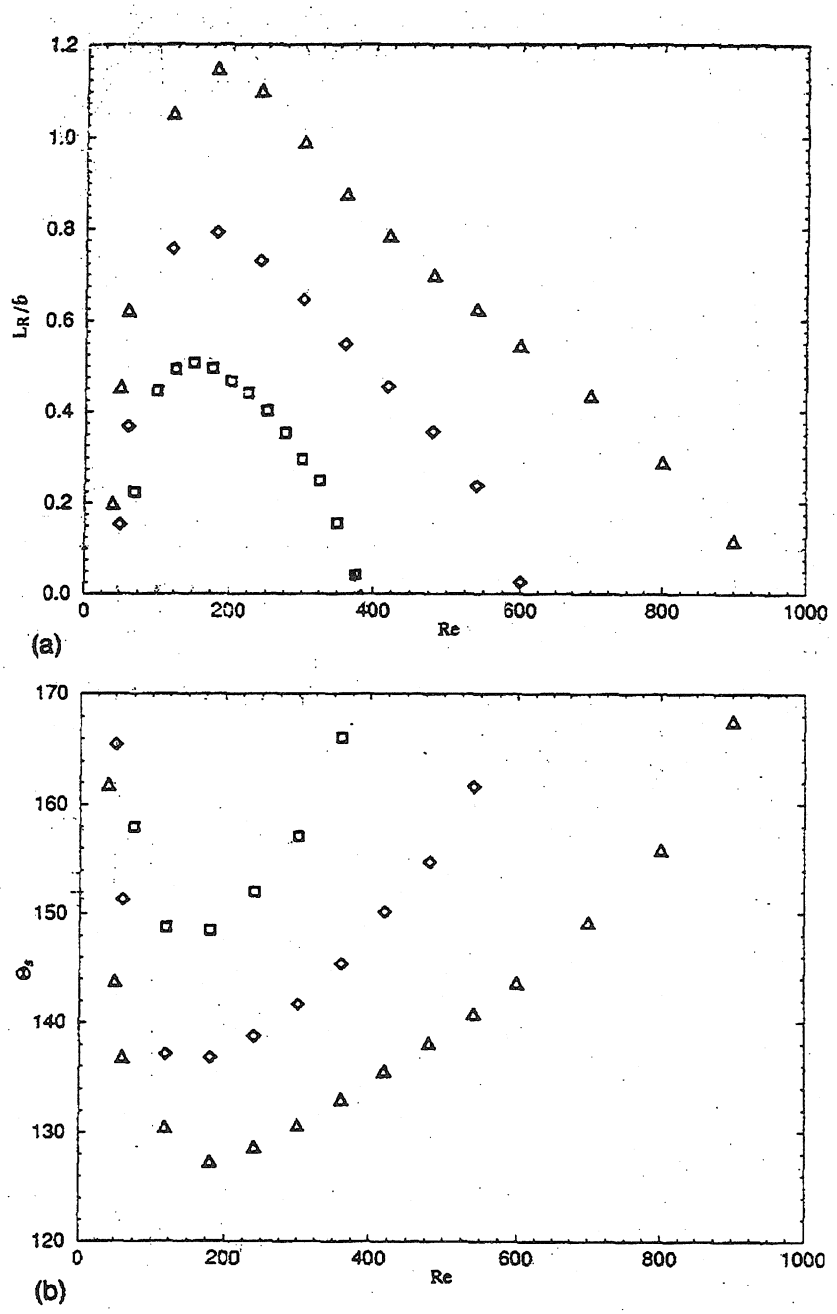

FIG. 6. Evolution of the characteristics of the standing eddy as a function of Re. (a) Reattachment length L_R/b; (b) separation angle (defined from the front stagnation point). □ χ=1.75; ◇ χ=1.84; △ χ=1.95.

Figure 3.11: Blanco and Magnaudet's result of a) wake length and b) separation angle.

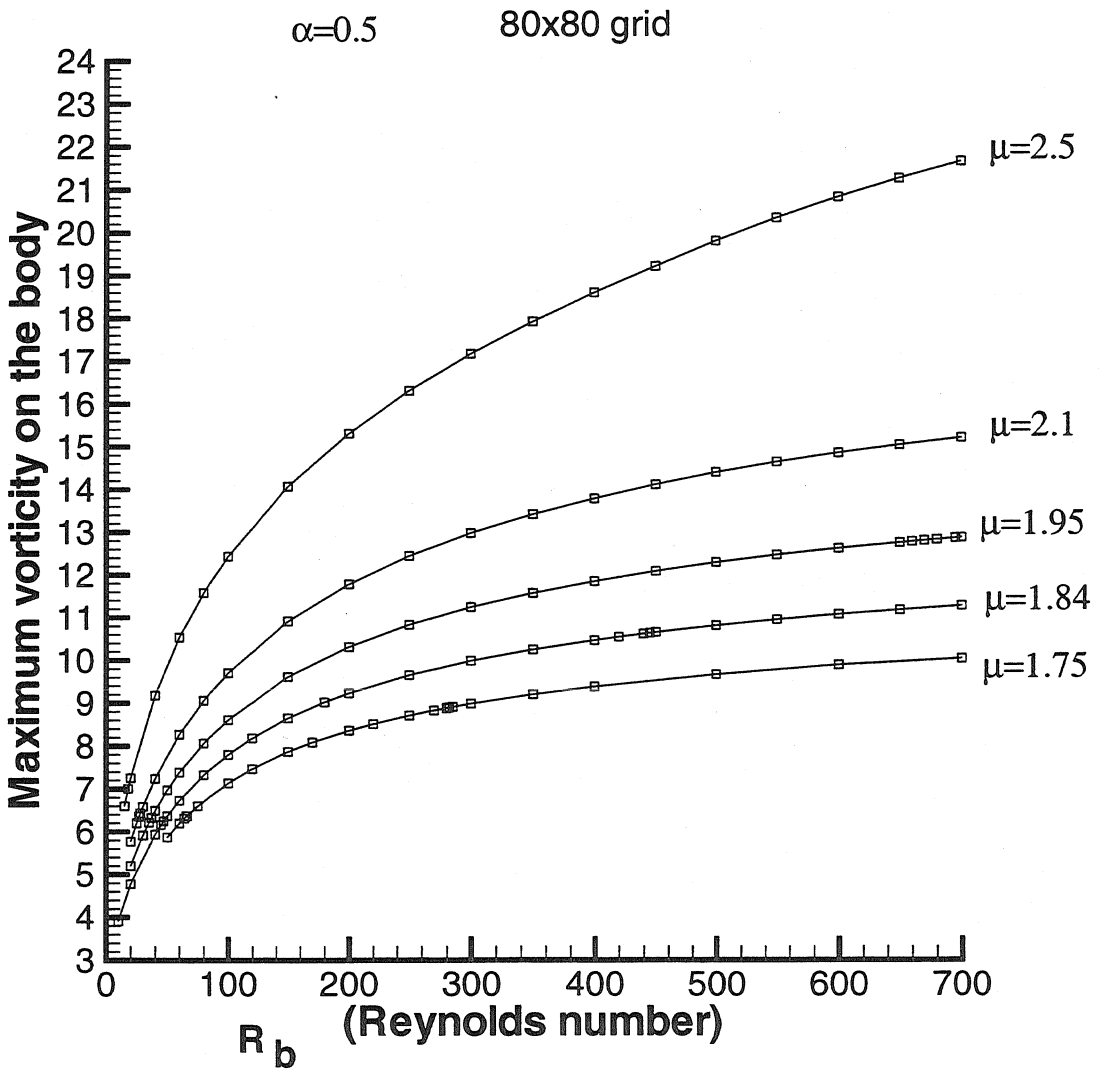

Figure 3.12: Maximum vorticity on the surface of the ellipsoidal bubbles as a function of the Reynolds number R_b.

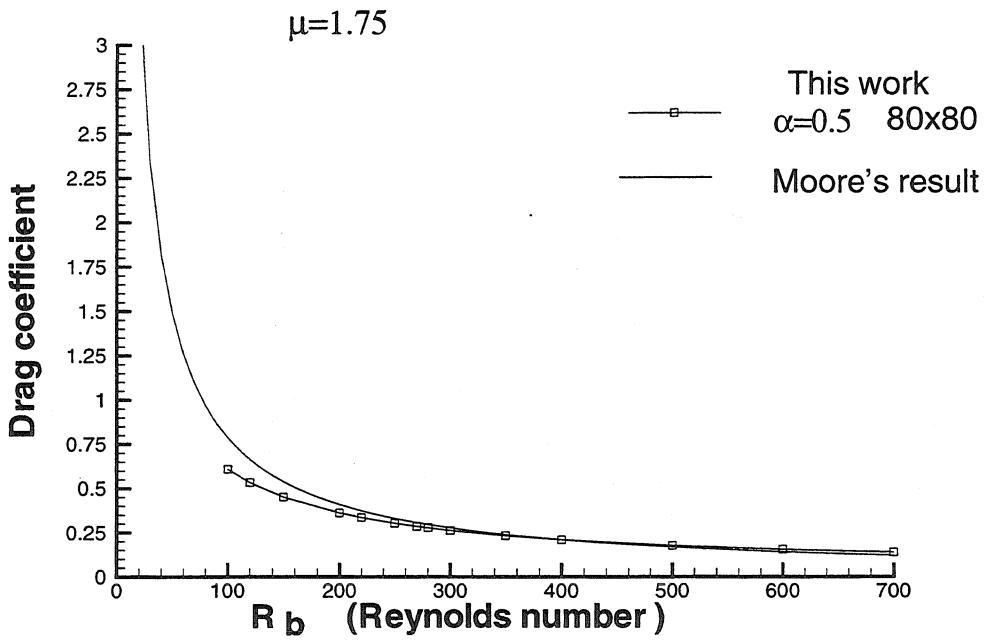

Figure 3.13: Drag coefficient as a function of Reynolds number for $\mu = 1.75$.

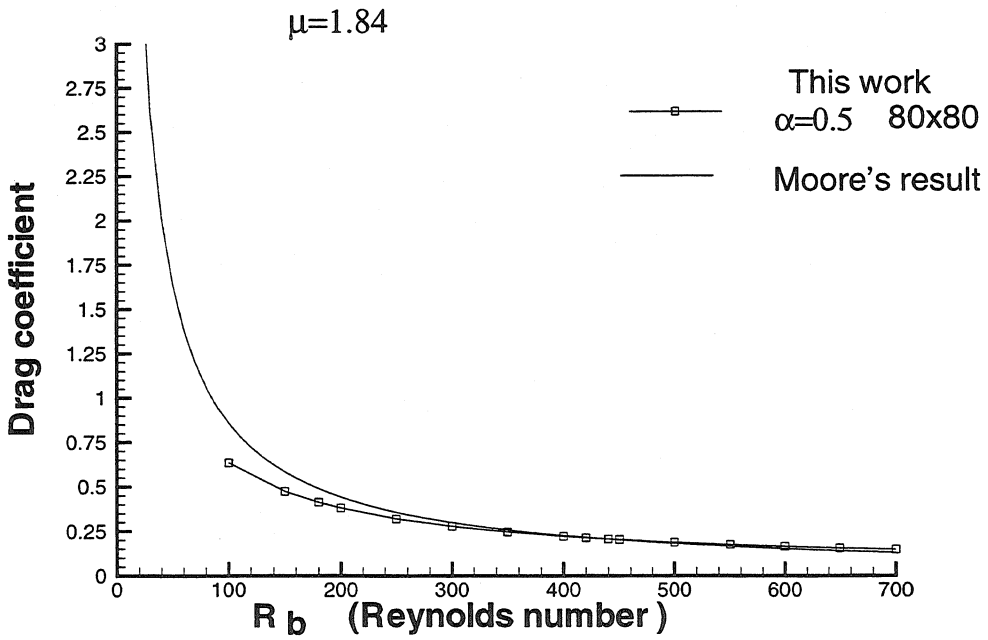

Figure 3.14: Drag coefficient as a function of Reynolds number for $\mu = 1.84$.

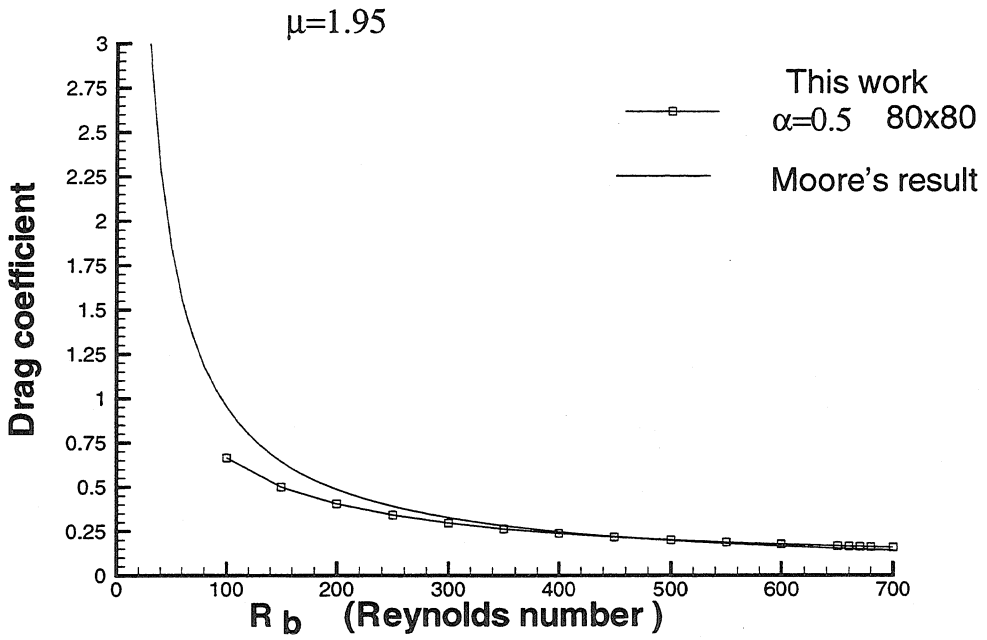

Figure 3.15: Drag coefficient as a function of Reynolds number for $\mu = 1.95$.

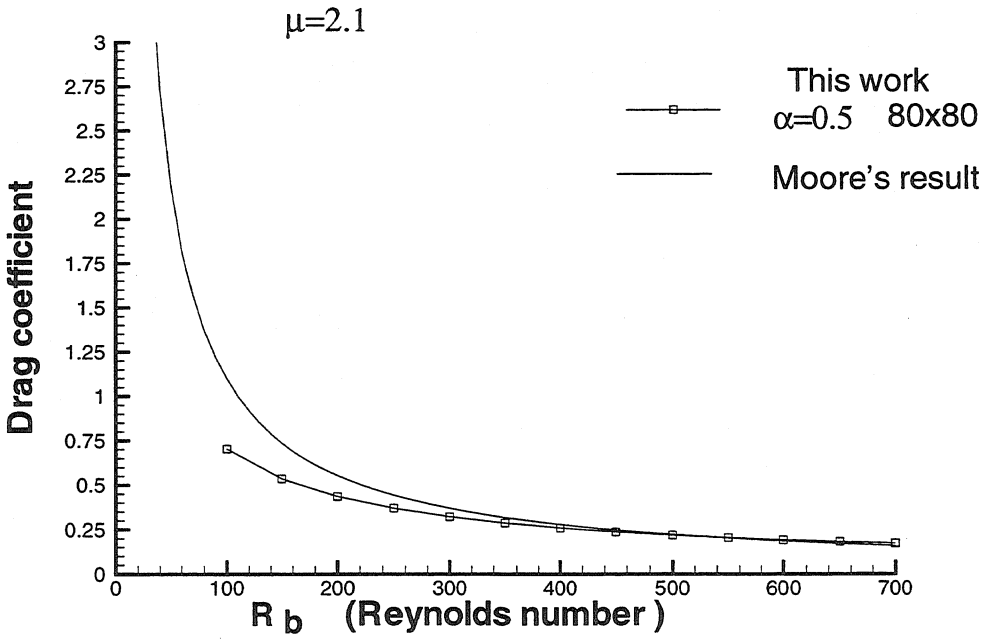

Figure 3.16: Drag coefficient as function of Reynolds number for $\mu = 2.1$.

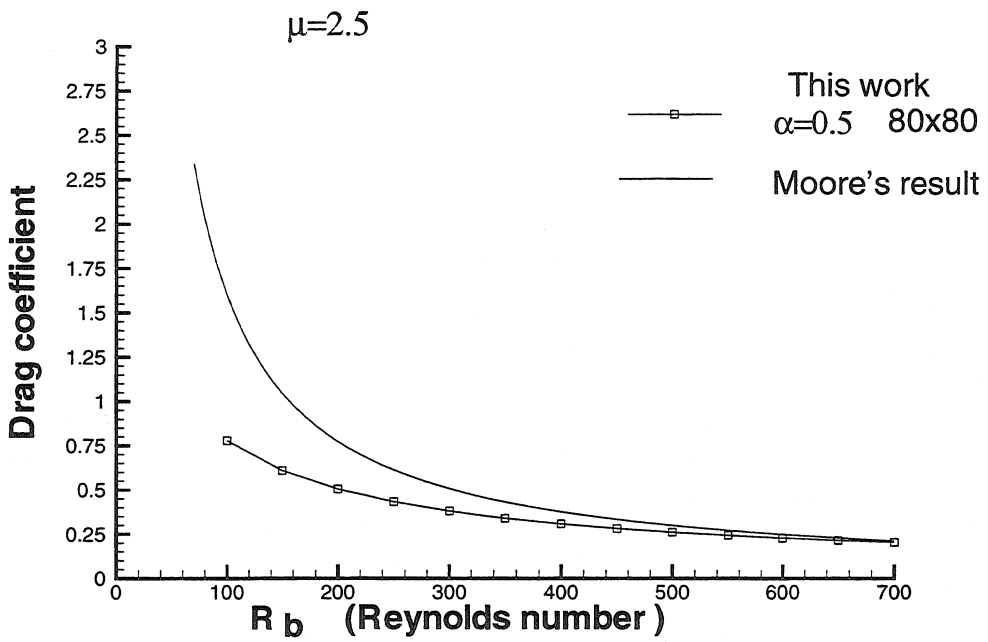

Figure 3.17: Drag coefficient as function of Reynolds number for $\mu = 2.5$.

they found the range to be from $R_b \approx 62$ to $R_b \approx 360$. For $\mu = 1.84$, our results are such that the wake persists from $R_b \approx 48$ to $R_b \approx 445$, while Blanco and Magnaudet found the range to be from $R_b \approx 40$ to $R_b \approx 600$. For $\mu = 1.95$, the range comes out to be $R_b \approx 36$ to $R_b \approx 696$, while Blanco and Magnaudet determined them to be from $R_b \approx 36$ to $R_b \approx 960$. Furthermore, carefully comparing Figures 3.12 and 3.10 b) shows that the critical maximum value of vorticity on the surface of the ellipsoidal bubble associated with the development of the wake is about 6.3 for $\mu = 1.75$, 1.84, and 1.95. This agrees well with Blanco and Magnaudet's value of 6.55 and differs from Dandy and Leal's value of 5.25. Basically, it appears that the onset of the wake is similar in both of the numerical methods. On the other hand, our calculations show the range of Reynolds number in which the wake exists to be smaller than Blanco and Magnaudet's calculations. Also, Figures 3.13, 3.14, 3.15, 3.16, and 3.17 show that in terms of drag coefficients our calculations agree well with Moore's asymptotic results. Blanco and Magnaudet's results also agree well with Moore's results.

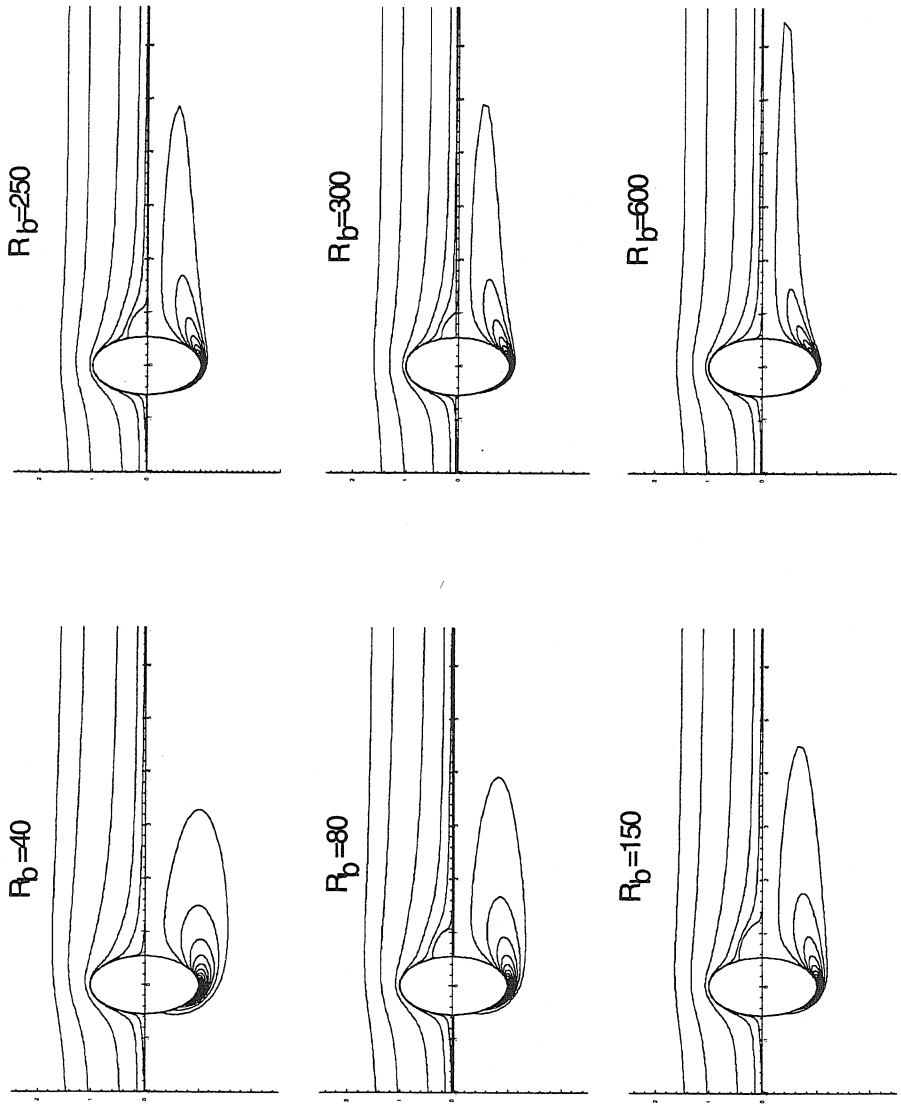

Figure 3.18: Steady flow past an ellipsoidal bubble with $\mu = 1.84$. In each case the left side is the stream function, and the right side is the vorticity.

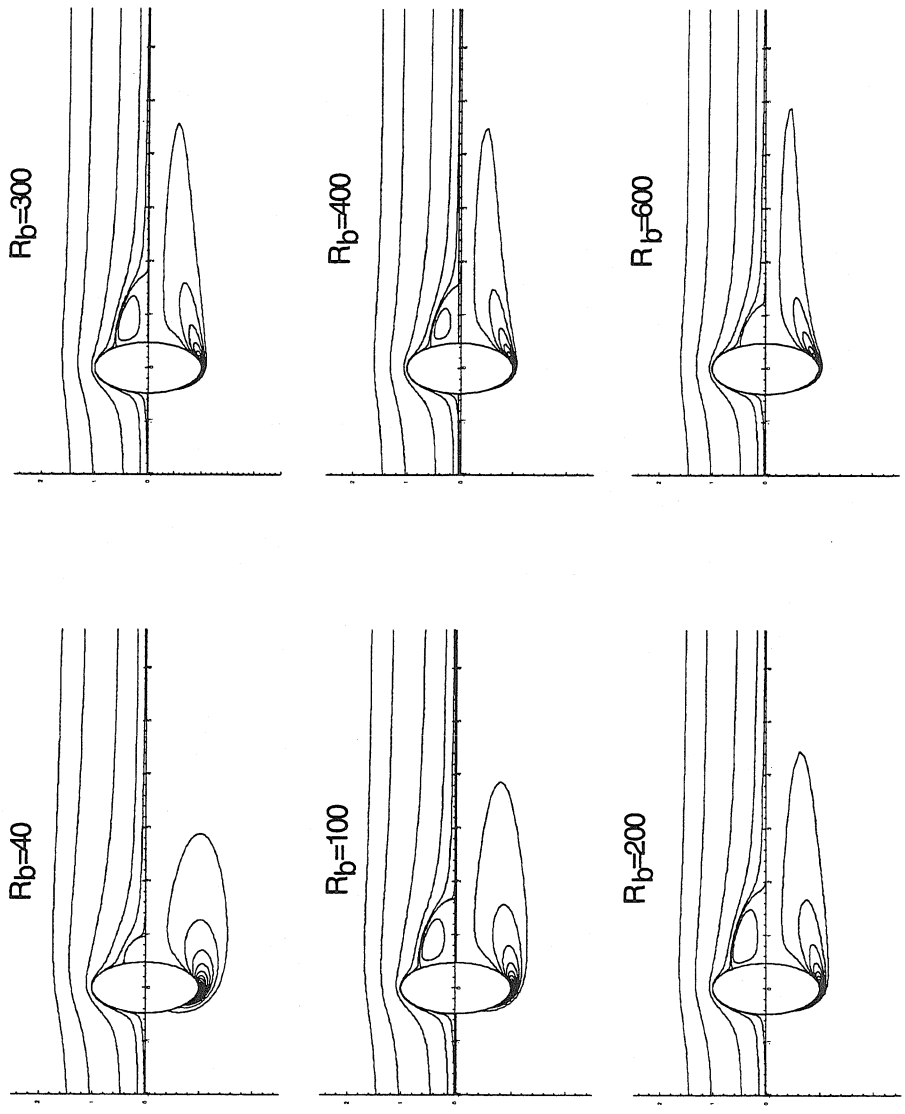

Figure 3.19: Steady flow past an ellipsoidal bubble with $\mu = 2.1$. In each case the left side is the stream function, and the right side is the vorticity.

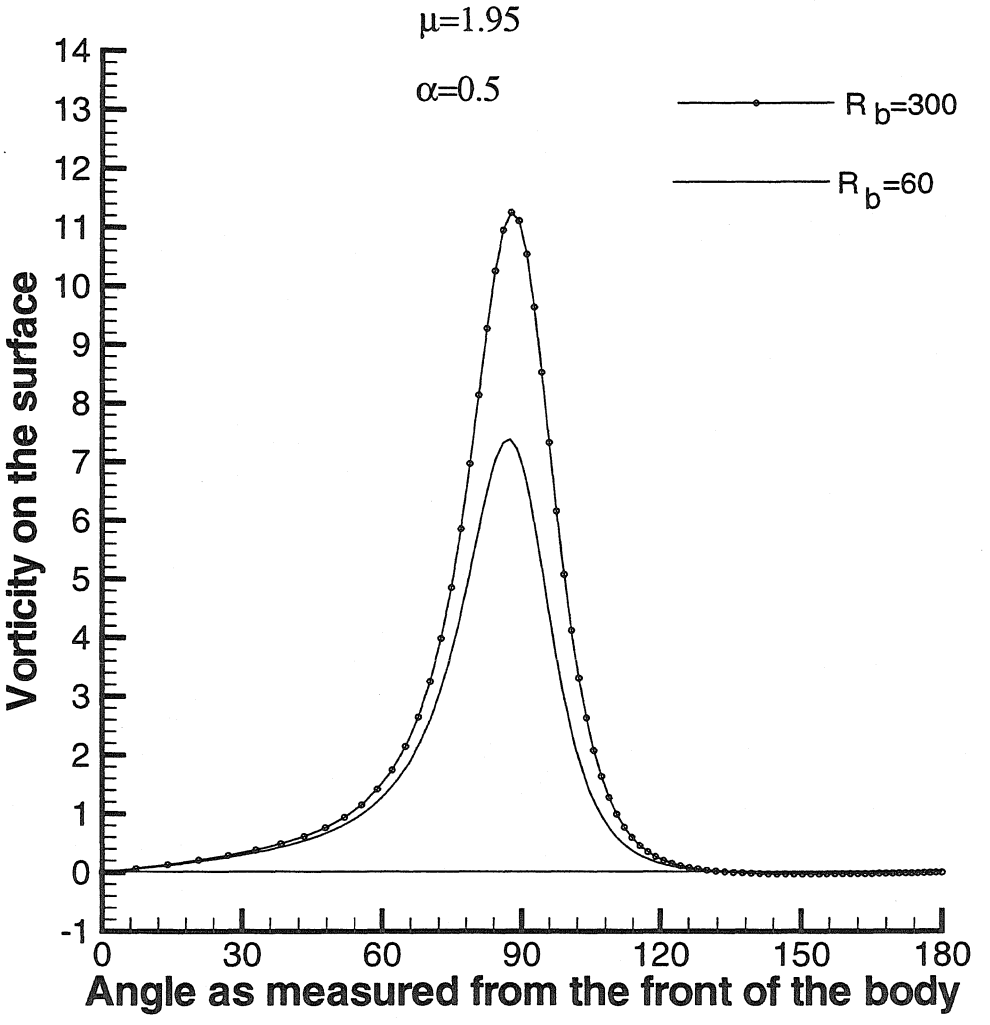

Figure 3.20: Surface vorticity distribution for an ellipsoidal bubble of fixed shape with $\mu = 1.95$ at $R_b = 60$ and $R_b = 300$.

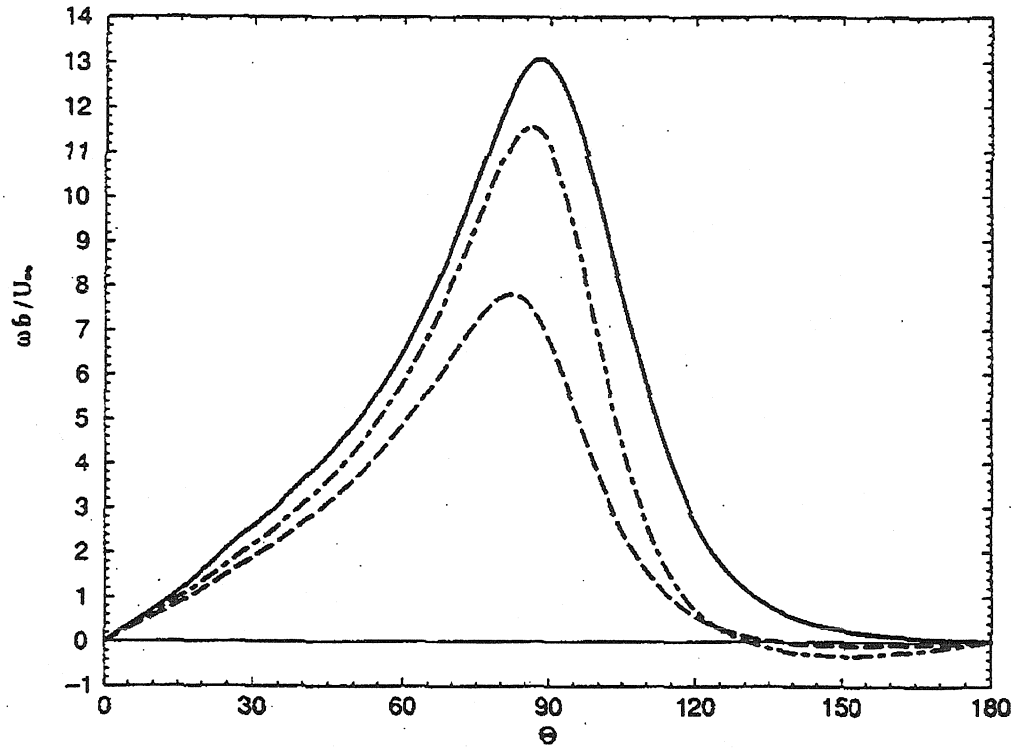

FIG. 10. Surface vorticity distribution (χ=1.95). — Re=60; ---- Re=300; — Re=1000.

Figure 3.21: Blanco and Magnaudet's result [4] for vorticity distribution on the surface of an ellipsoidal bubble with $\mu = 1.95$, $R_b = 60$, 300, 1000.

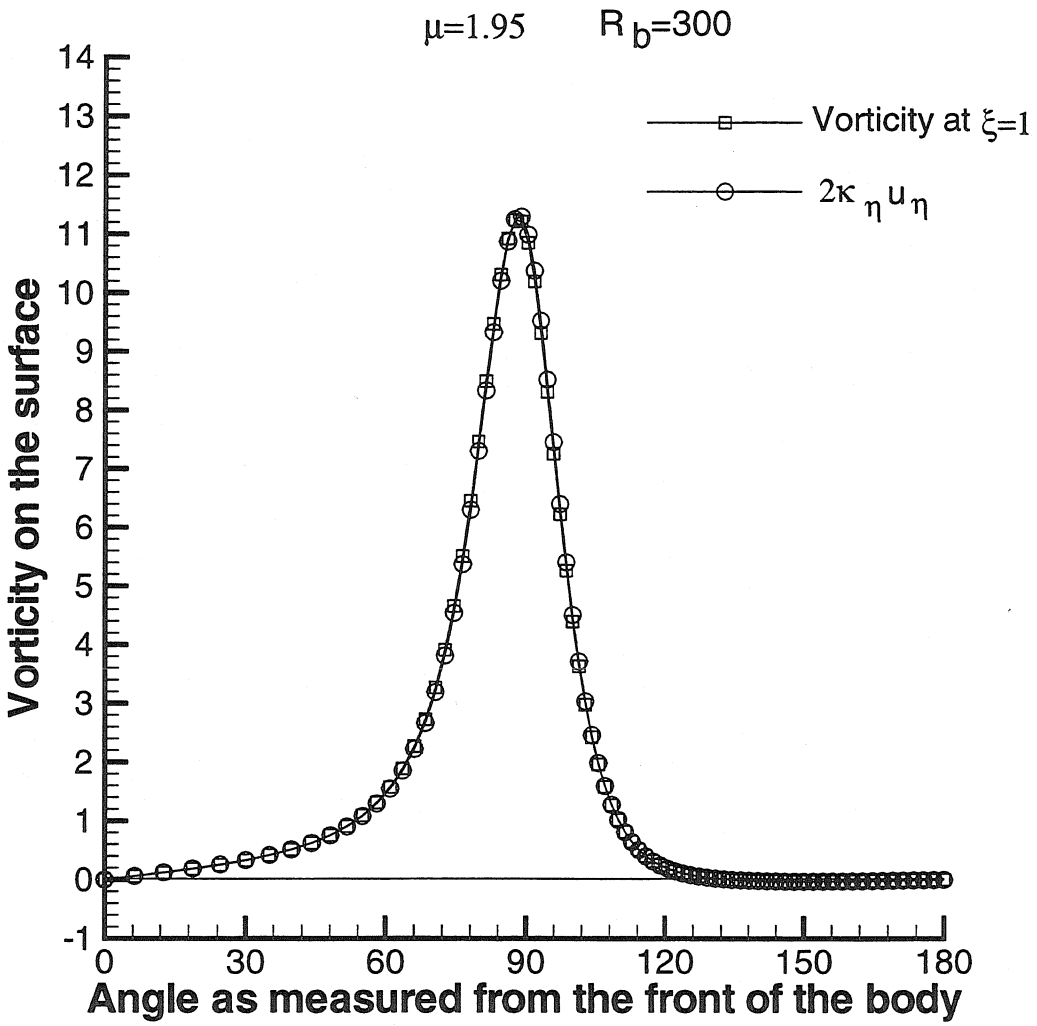

Figure 3.22: Comparison of vorticity and $2\kappa_\eta u_\eta$ on the surface of an ellipsoidal bubble of fixed shape with $\mu = 1.95$ and $R_b = 300$ as a check for consistency.

μ	R	100	200	300	400	500	600	700
1.75	Moore	0.787	0.409	0.277	0.210	0.169	0.142	0.122
	Blanco&Magnaudet	0.609	0.357	0.251	0.195		0.132	
	Our result	0.610	0.361	0.263	0.209	0.177	0.155	0.139
1.84	Moore	0.859	0.443	0.299	0.226	0.182	0.152	0.131
	Blanco&Magnaudet	0.594	0.359	0.259	0.202		0.141	
	Our result	0.635	0.381	0.278	0.222	0.188	0.164	0.147
1.95	Moore	0.954	0.487	0.327	0.247	0.198	0.166	0.142
	Blanco&Magnaudet	0.627	0.386	0.277	0.220		0.152	
	Our result	0.666	0.405	0.297	0.238	0.201	0.176	0.158
2.1	Moore	1.10	0.554	0.370	0.278	0.225	0.186	0.159
	Our result	0.704	0.436	0.322	0.259	0.219	0.192	0.172
2.5	Moore	1.60	0.773	0.508	0.377	0.3	0.250	0.212
	Our result	0.780	0.505	0.381	0.308	0.261	0.228	0.205

Table 3.3: Drag coefficients of flow past ellipsoidal bubbles of fixed shape.

Figure 3.20 shows the vorticity distribution on the surface of the ellipsoidal bubble with $\mu = 1.95$ at $R_b = 60$ and 300. Figure 3.21 shows the result obtained by Blanco and Magnaudet using the same values for μ and R_b. Comparing the two figures may give some hint as to why our results differ from Blanco and Magnaudet's results. According to our calculations, the maximum vorticity values on the surface of the ellipsoidal bubble at $R_b = 60$ and $R_b = 300$ are about 7.4 and 11.3, respectively. These values agree well with Blanco and Magnaudet's value of 7.8 and 11.6. However, the width of the peak in our case is narrower compared to Blanco and Magnaudet's. For example, at $R_b = 60$, Blanco and Magnaudet determine the vorticity at 30° to be about 1.9, while according to our calculations it is about 0.3. So, it appears that the discrepancy in the results between Blanco and Magnaudet's and our approach may come from differences in imposing the free-slip boundary condition along the surface of the ellipsoidal bubble.

The free-slip condition can be rewritten as

$$\omega(1,\eta) - 2\kappa_\eta u_\eta \mid_{\xi=1} = 0,$$

where κ_η is the normal curvature of the ellipsoidal bubble. The curvature κ_η is defined by

$$\kappa_\eta = -\frac{1}{h_\xi h_\eta}\frac{\partial h_\eta}{\partial \xi}.$$

To double check our results, we compare $\omega(1,\eta)$ and $2\kappa_\eta u_\eta$ in Figure 3.22 for $\mu = 1.95$ and $R_b = 300$. They appear to be in good agreement. This indicates that the free-slip condition is well satisfied on the surface.

Another reason for the differences in the results may be the differences in the numerical methods used. Blanco and Magnaudet solved the flow equations in primitive variables on a truncated rectangular grid. For the boundary conditions far away from the body, different types of conditions were imposed on the velocity and the pressure for the upstream and the downstream of the flow. It is possible that the differences in types of the grids and the boundary conditions used for flow far away from the body may contribute to the differences in the results as well.

Somehow, the finite-volume method used by Blanco and Magnaudet generates somewhat more vorticity on the surface of the body compared to our second-order finite differencing method. This then explains why their results indicate a somewhat larger wake for a wider range of Reynolds numbers compared to our results for the flow past the same ellipsoidal bubble. Of course, it is still not clear why both of our results differ so much from Dandy and Leal's results, especially since our approach is basically the same as Dandy and Leal's.

3.4 Numerical method for the linear stability analysis

Blanco and Magnaudet [4] suggest at the end of their paper that, given these steady, axisymmetric solutions, it would be interesting to carry out a linear stability analysis similar to Kim and Pearlstein [17] and Natarajan and Acrivos [26] to study the dynamics of bubbles, even though the fixed shape of the bubble makes the problem very simplified compared to the actual bubble problem. Since we are successful in

replicating and expanding on Natarajan and Acrivos's result as shown in Chapter 2, we attempt to follow up on Blanco and Magnaudet's suggestion to carry out this linear stability analysis.

Again, the details of the numerical linear stability analysis are in Chapter 2. We summarize the main points of the method. The method of linear stability analysis is used to investigate perturbations that may deviate from the steady, axisymmetric base flow past an ellipsoidal bubble of fixed shape. The main focus of this method is to determine the critical Reynolds numbers at which the flow may become unstable.

The Navier-Stokes equation in primitive variable form is

$$\begin{aligned} \mathbf{u}_t + (\mathbf{u}\cdot\nabla)\mathbf{u} &= -\frac{1}{2}\nabla p + \frac{bg}{U^2}\hat{\mathbf{x}} + \frac{2}{R_b}\nabla^2\mathbf{u}, \\ \nabla\cdot\mathbf{u} &= 0. \end{aligned} \tag{3.6}$$

The perturbations to the pressure p and the three velocity components u_ξ, u_η, and u_ϕ are expanded in Fourier series in the azimuthal ϕ direction:

$$\begin{aligned} u_\xi &= U_{\xi_S}(\xi,\eta) + \varepsilon \sum_{n=-\infty}^{+\infty} e^{\iota n\phi}\tilde{u}_{\xi n}(\xi,\eta,t), \\ u_\eta &= U_{\eta_S}(\xi,\eta) + \varepsilon \sum_{n=-\infty}^{+\infty} e^{\iota n\phi}\tilde{u}_{\eta n}(\xi,\eta,t), \\ u_\phi &= \varepsilon \sum_{n=-\infty}^{+\infty} e^{\iota n\phi}\tilde{u}_{\phi n}(\xi,\eta,t), \\ p &= P_S(\xi,\eta) + \varepsilon \sum_{n=-\infty}^{+\infty} e^{\iota n\phi}\tilde{p}_n(\xi,\eta,t). \end{aligned} \tag{3.7}$$

The terms U_{ξ_S} and U_{η_S} are the radial and polar components of the steady, axisymmetric base flow velocity field and are calculated using (3.3). The variable ε is a small parameter of perturbation, and ι is the imaginary number $\sqrt{-1}$. The perturbed variables are physical quantities and are expected to be real. So, $\tilde{u}_n = \tilde{u}^*_{-n}$. Expanding the perturbation in the azimuthal direction as a Fourier series reduces the problem to our original, two-dimensional grid. The expressions (3.7) are substituted into the

Navier-Stokes equations (3.6), and a set of $O(\varepsilon)$ perturbation equations is derived.

We next address the boundary conditions. First, we account for $\tilde{p}_n$ along $\xi = 1$ by imposing the divergence free condition. The variables $\tilde{u}_{\eta n}$, $\tilde{u}_{\phi n}$ are also unknown along $\xi = 1$. This gives

$$\frac{1}{h_\xi}\frac{\partial}{\partial \xi}\tilde{u}_{\xi n}(1,\eta) + \frac{1}{h_\eta}\frac{\partial}{\partial \eta}\tilde{u}_{\eta n}(1,\eta) + \left(\frac{1}{h_\xi h_\eta}\frac{\partial h_\xi}{\partial \eta} + \frac{1}{\sigma h_\eta}\frac{\partial \sigma}{\partial \eta}\right)\tilde{u}_{\eta n}(1,\eta) + \iota\frac{n}{\sigma}\tilde{u}_{\phi n}(1,\eta) = 0.$$

Also, the free-slip condition is imposed on the perturbations:

$$\begin{aligned} h_\eta \frac{\partial}{\partial \xi}\tilde{u}_{\eta n}(1,\eta) - \frac{\partial h_\eta}{\partial \xi}\tilde{u}_{\eta n}(1,\eta) &= 0, \\ \sigma \frac{\partial}{\partial \xi}\tilde{u}_{\phi n}(1,\eta) - \frac{\partial \sigma}{\partial \xi}\tilde{u}_{\phi n}(1,\eta) &= 0. \end{aligned}$$

This accounts for all the unknowns $\tilde{p}_n, \tilde{u}_{\eta n}$, and $\tilde{u}_{\phi n}$ on the surface of the ellipsoidal bubble. Since the surface of the ellipsoidal bubble is fixed, $\tilde{u}_{\xi n} = 0$ at $\xi = 1$. Along $\xi = 0, \eta = 0$, and $\eta = 1$, the same boundary conditions used in Chapter 2 are applied.

The equations are then processed the same way as described in Chapter 2, discretized using second-order, finite differencing, and then rearranged in proper order with the appropriate boundary conditions to form a large linear system of discretized equations. The linear system is then solved using the sparse matrix LU decomposition solver used in Chapter 2, and this allows us to evolve the perturbations $\tilde{p}_n$,$\tilde{u}_{\xi n}$, $\tilde{u}_{\eta n}$, and $\tilde{u}_{\phi n}$ in time. Since the system is linear, the perturbations can be represented by

$$\begin{aligned} \tilde{u} &\sim c_1 e^{\beta_1 t}\tilde{v}_1 + c_2 e^{\beta_2 t}\tilde{v}_2 + c_3 e^{\beta_3 t}\tilde{v}_3 + ..., \\ \mathrm{Re}(\beta_1) &\geq \mathrm{Re}(\beta_2) \geq \mathrm{Re}(\beta_3) \geq ... \end{aligned}$$

The terms $\beta_1, \beta_2, ...$ are the eigenvalues associated with the linear system, and $\tilde{v}_1, \tilde{v}_2, ...$ are their corresponding eigenfunctions. Clearly when β_1 is positive, $\tilde{u}$ becomes unstable. When t is large, $c_1 e^{\beta_1 t}\tilde{v}_1$ dominates $\tilde{u}$, and taking the logarithm of $\tilde{u}$ gives a linear curve in time whose slope gives the value of β_1. The value of β_2 can be determined applying the Gram-Schmidt orthogonalization method. Again, this is covered

μ	2.4	2.5	2.6	2.7	2.8	2.9	3.0
R_b^L	271.3	235.4	215.2	201.9	193.2	186.9	182.6

Table 3.4: Critical Reynolds numbers at which the leading eigenvalue of the $n = 1$ Fourier mode of the perturbation is zero.

in more detail in Chapter 2.

3.5 Linear stability analysis results

If the body is spherical, the free-slip condition is such that no wake forms on the back of the bubble for any Reynolds number. So, it is expected that the instability in the flow would occur if the aspect ratio $\mu = b/a$ of the ellipsoidal bubble is large enough to generate enough vorticity that can cause instability in the flow. The linear stability analysis is carried out for $\mu = 2.4, ..., 3.0$. A grid of resolution 70x70 with distortion function $\alpha = 0.5$ is used in solving the perturbation equations. For the sake of convenience, we let R_b^L be the critical Reynolds number at which the growth rate, i.e., the leading eigenvalue β_1, of the perturbation is zero. We then let R_b^S be the critical Reynolds number at which the secondary eigenvalue β_2, or at least its real part, is zero.

Similar to the results of Chapter 2, it is the Fourier mode $n = 1$ of the perturbation that becomes unstable. Figure 3.23 shows the leading eigenvalues, i.e., the growth rates, of the $n = 1$ Fourier mode of the perturbations at various Reynolds numbers R_b for $\mu = 2.4, ..., 3.0$. It is clear that as μ becomes larger, the curves of leading eigenvalues become more steep. It also turns out that, similar to the case of rigid spheroids, the leading eigenvalues are purely real.

Figure 3.24 shows the secondary eigenvalues of the perturbations at various Reynolds numbers R_b for $\mu = 2.6, ..., 3.0$. They turn out to be complex, and once again this is similar to the results obtained in the case of rigid spheroids.

Figure 3.25, Table 3.4, and Table 3.5 show the critical Reynolds numbers R_b^L and R_b^S at which the leading eigenvalue β_1 and the real part of the secondary eigenvalue β_2 of the $n = 1$ Fourier mode of the perturbation are zero with respect to the various

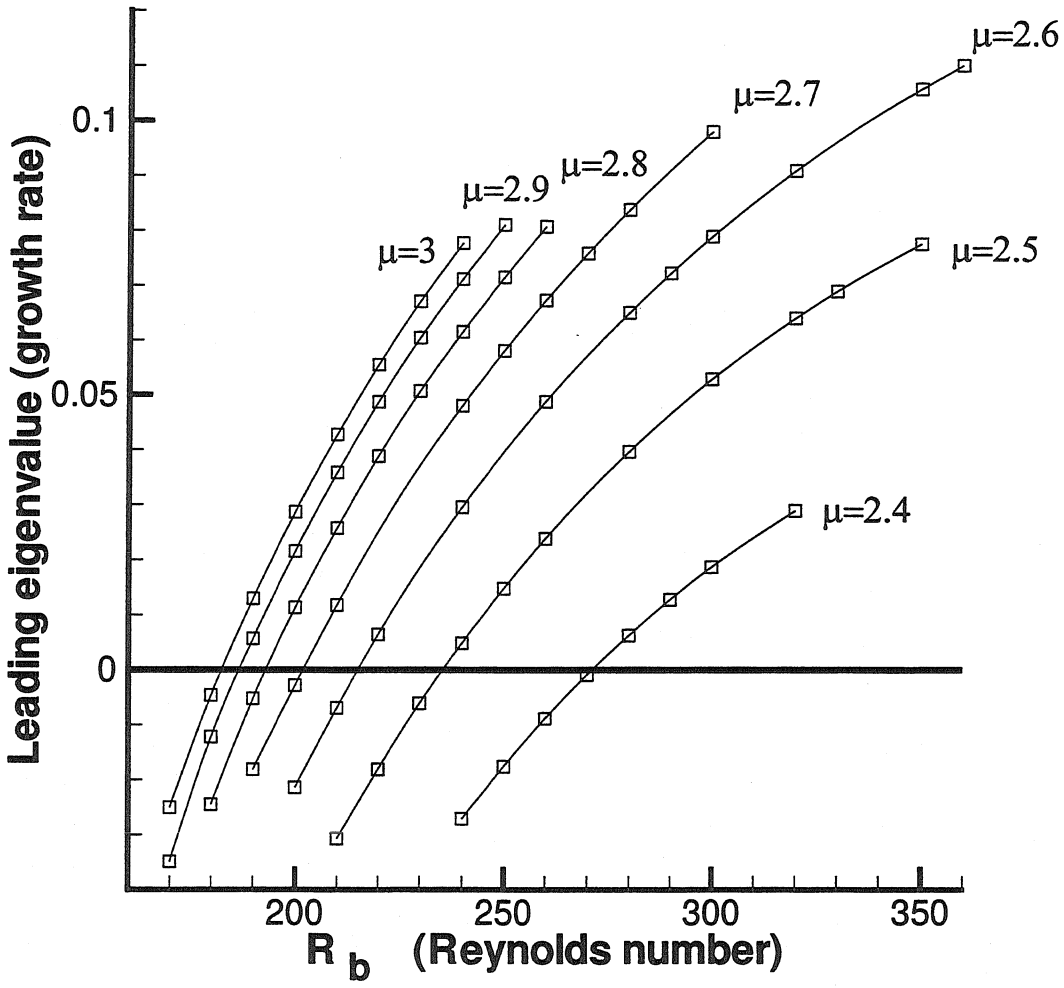

Figure 3.23: Leading eigenvalues, i.e., the growth rates, of the $n = 1$ Fourier mode of the perturbation of flow past an ellipsoidal bubble of fixed shape versus Reynolds number R_b for $\mu = 2.4$, 2.5, 2.6, 2.7, 2.8, 2.9, and 3.0.

μ	2.6	2.7	2.8	2.9	3.0
R_b^S	298	257.1	235.7	222.7	214.7
β_2 at R_b^S	0.471ι	0.471ι	0.469ι	0.469ι	0.469ι

Table 3.5: Critical Reynolds numbers at which the real part of secondary eigenvalue of the $n = 1$ Fourier mode of the perturbation is zero and the imaginary part of the secondary eigenvalues at the critical Reynolds numbers are shown.

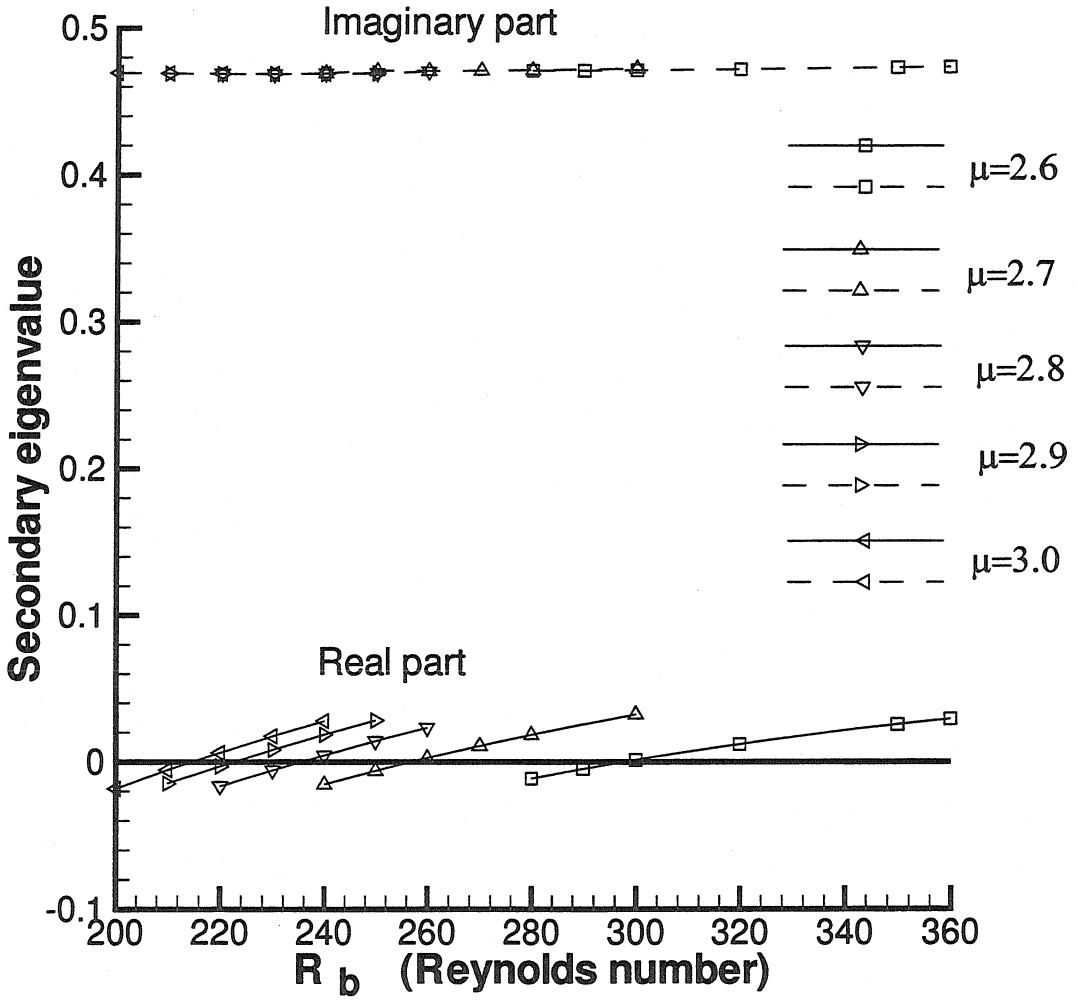

Figure 3.24: Secondary eigenvalues of the $n = 1$ Fourier mode of the perturbation of flow past an ellipsoidal bubble of fixed shape versus Reynolds number R_b.

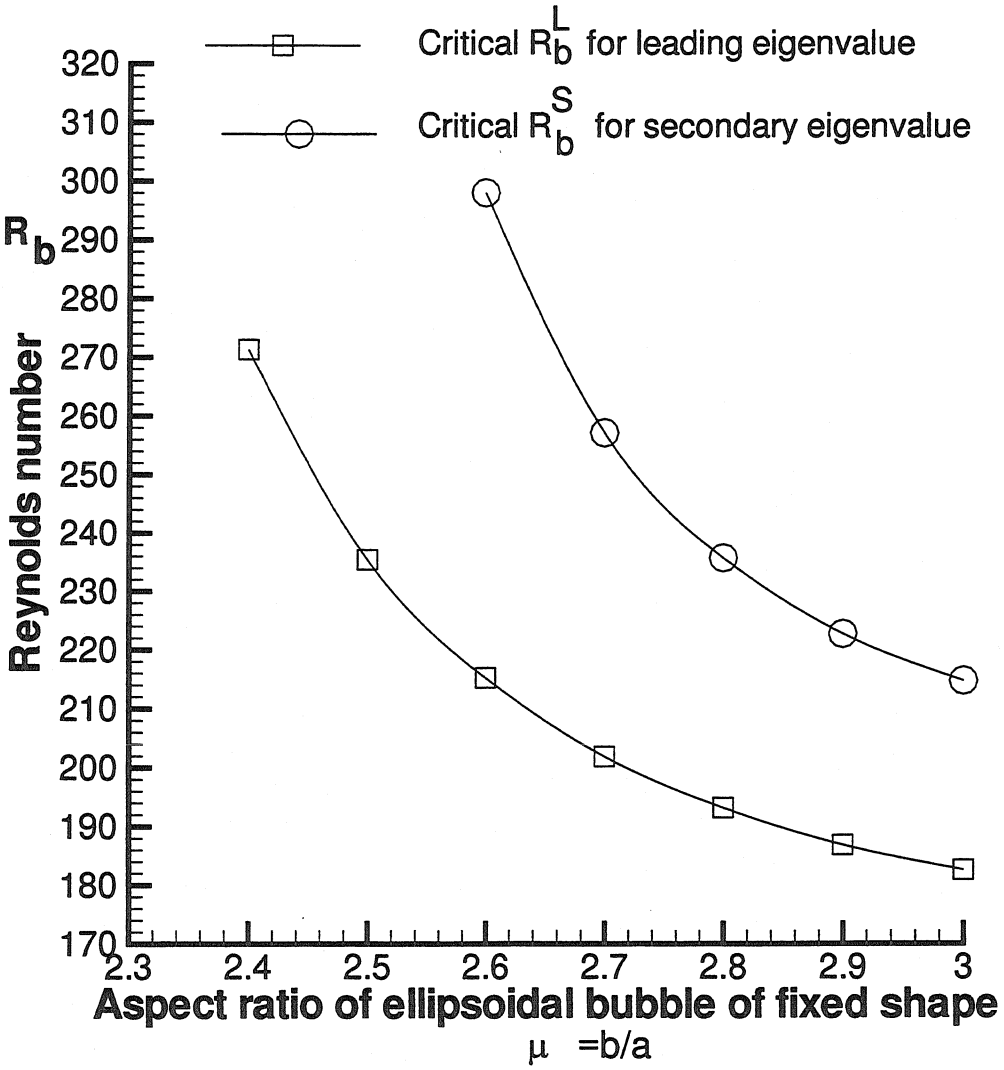

Figure 3.25: Critical Reynolds numbers R_b^L at which the leading eigenvalue is zero and R_b^S at which the real part of the secondary eigenvalue of the $n = 1$ Fourier mode of the perturbation of flow past an ellipsoidal bubble of fixed shape is zero versus aspect ratios $\mu = b/a$.

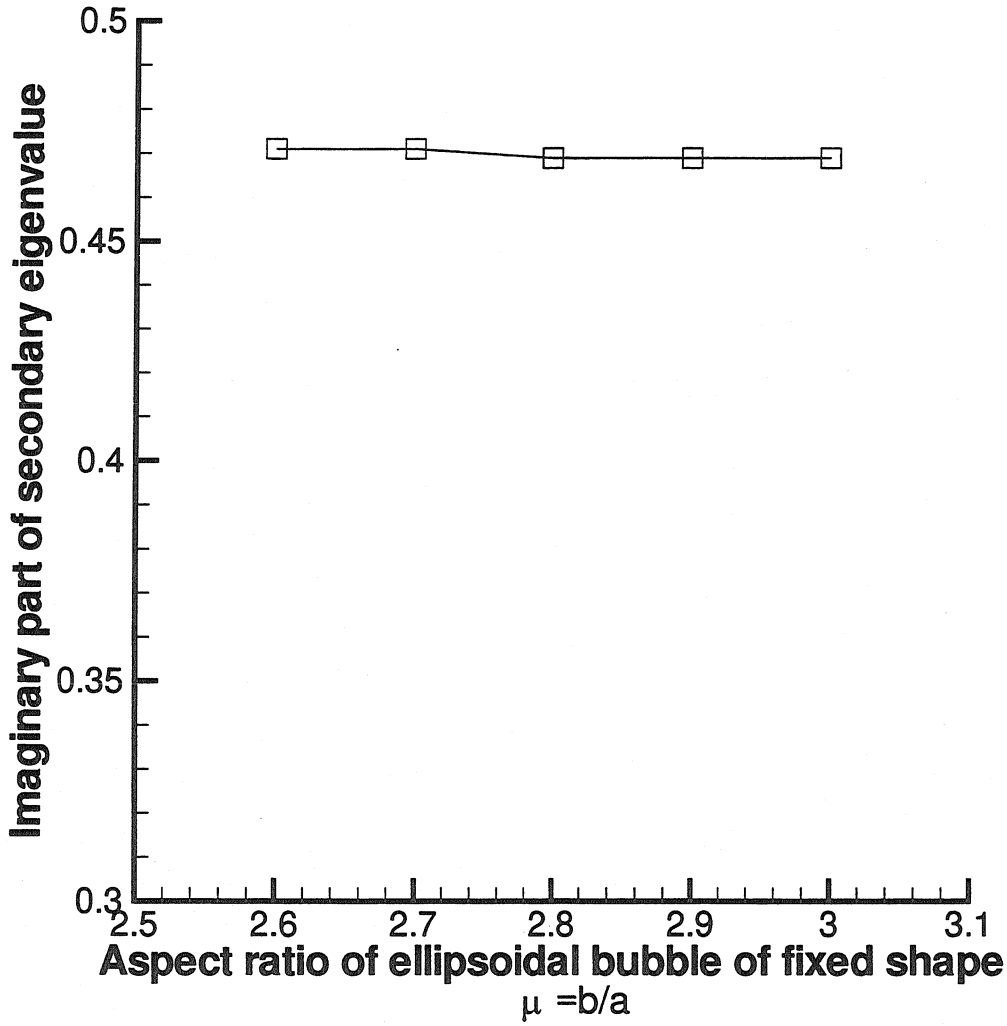

Figure 3.26: Imaginary part of the secondary eigenvalue of the $n = 1$ Fourier mode of the perturbation of flow past an ellipsoidal bubble of fixed shape at R_b^S versus the aspect ratio $\mu = b/a$.

values of μ. As μ becomes larger, the critical Reynolds numbers become smaller. Figure 3.28 shows the eigenfunctions associated with the leading eigenvalue of the perturbation at $R_b^L = 193.2$ for the ellipsoidal bubble with $\mu = 2.8$, and Figure 3.29 shows the eigenfunctions associated with the secondary eigenvalue of the perturbation at $R_b^S = 235.7$ for the ellipsoidal bubble with $\mu = 2.8$. The eigenfunctions appear to be very similar qualitatively when compared to the eigenfunctions determined for the rigid, oblate spheroids as shown in Chapter 2.

Figure 3.27 shows the Fourier modes $n = 2$, and $n = 3$ of the perturbations of flow past an ellipsoidal bubble of fixed shape with $\mu = 2.8$ evolving in time at $R_b = 250$. It is clear that they are all stable even when the flow is beyond the critical Reynolds number at which the $n = 1$ Fourier mode is already unstable. This indicates that the $n = 1$ Fourier mode is the dominant nonaxisymmetric mode of the instability of the perturbation of flow past an ellipsoidal bubble of fixed shape for the range of the Reynolds numbers that we studied.

So, according to our results, the instability of the perturbations of flow past ellipsoidal bubbles of fixed shape is very similar to the case of rigid, no-slip, oblate spheroids. It is the $n = 1$ Fourier mode of the perturbation that becomes unstable, and the leading eigenvalue of the perturbation is purely real. Since it is observed experimentally that gas bubbles become unstable via oscillatory motion, our results do not give much insight into such behavior.

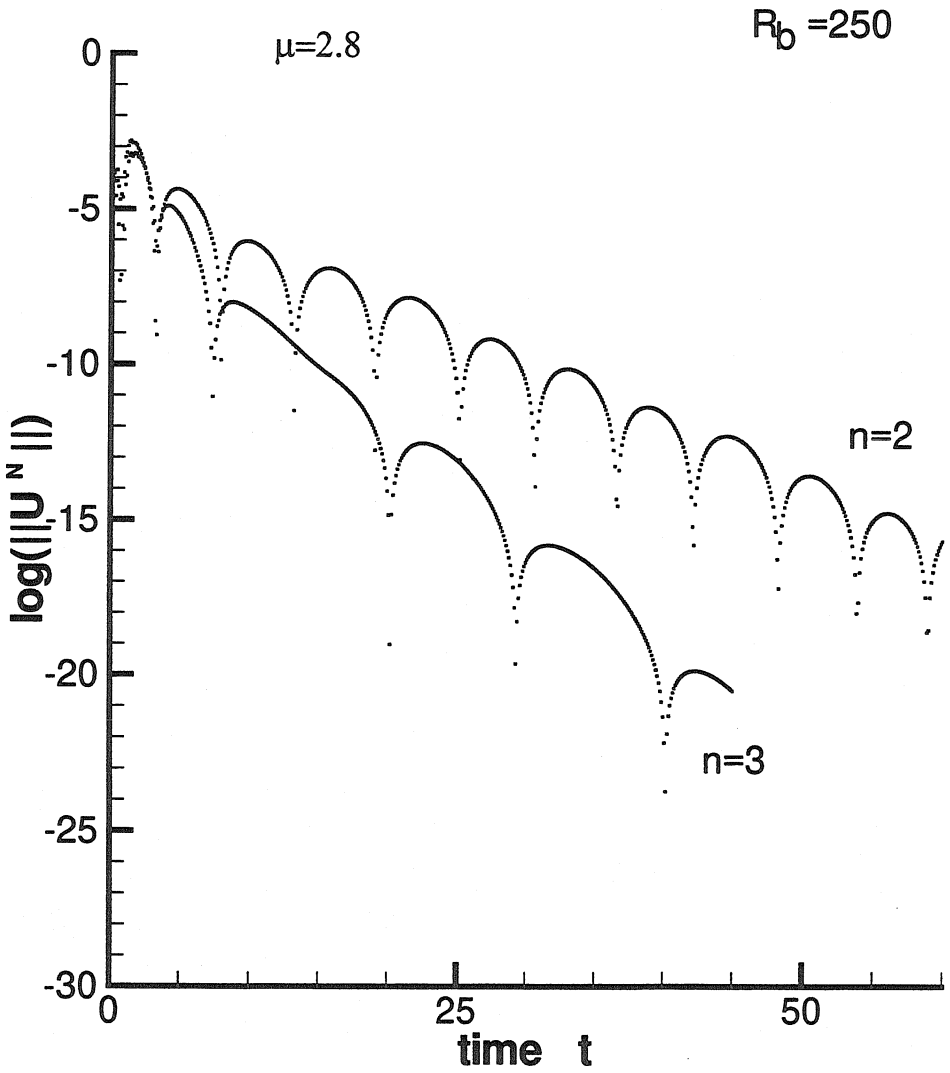

Figure 3.27: *Log* $\left(||\mathbf{U}^N||\right)$ of the $n = 2$ and $n = 3$ Fourier modes of the perturbation of flow past an ellipsoidal bubble of fixed shape with $\mu = 2.8$ versus time t at $R_b = 250$.

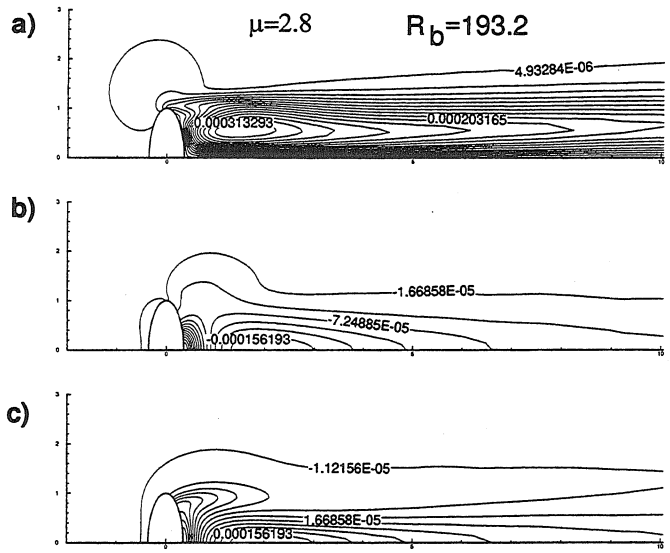

Figure 3.28: Eigenfunctions of the leading eigenvalue of the $n = 1$ Fourier mode of the perturbation at $R_b^L = 193.2$ for flow past an ellipsoidal bubble of fixed shape with $\mu = 2.8$. a) Re $(\tilde{u}_{x_1})$, b) Re $(\tilde{u}_{\sigma_1})$, c) Im $(\tilde{u}_{\phi_1})$.

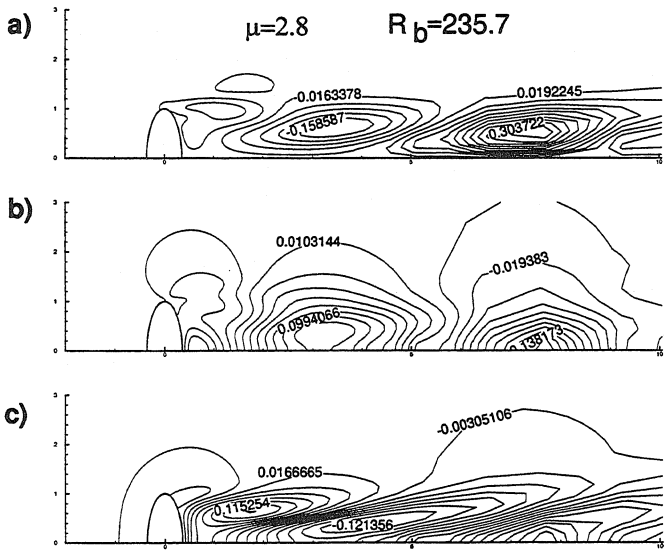

Figure 3.29: Eigenfunctions of the secondary eigenvalue of the $n = 1$ Fourier mode of the perturbation at $R_b^S = 235.7$ for flow past an ellipsoidal bubble of fixed shape with $\mu = 2.8$. a) Re $(\tilde{u}_{x_1})$, b) Re $(\tilde{u}_{\sigma_1})$, c) Im $(\tilde{u}_{\phi_1})$.

Chapter 4 Steady Flow Past an Axisymmetric Bubble

4.1 Introduction

Chapter 2 deals with flows past a solid, rigid body whose surface does not move in relation to the surrounding flow. In this chapter we consider flows past a body with a deformable free surface. Such problems are characterized by an interface between two or more fluids whose motion is governed by pressure, surface tension, and viscous forces along the interface. This movement of the interface makes computation difficult, especially when multiple fluids are involved. One of the simpler cases that are studied is the case of a rising gas bubble in a quiescent fluid.

There are many papers that deal with rising bubbles experimentally. One of the earliest is the results by P. G. Saffman [36]. He studied rising air bubbles in distilled water and noticed that, under certain conditions, the bubbles oscillate and sometimes spiral as they rise. He concluded that the interaction of the wake and the free surface may cause such behavior. Other researchers include Tsuge and Hibino [46], Bhaga and Weber [3], and Haberman and Morton [14] who observed path instabilities of bubbles rising in various types of fluids.

Numerical calculations have been attempted by a number of authors. Ryskin and Leal [34] used a numerical, orthogonal grid generation method to solve for the steady flow past a rising axisymmetric bubble for various values of fluid viscosity and surface tension. Unverdi and Tryggvason [47] used an interface tracking method to compute three-dimensional, rising bubbles. More recently, Takagi, Matsumoto, and Huang [40] used their own orthogonal grid generation method to study axisymmetric bubbles. They assumed the flow to be axisymmetric and evolved the velocity field and pressure of the flow around the bubble in time and showed that at certain Reynolds

numbers and Weber numbers, a dimensionless measure of surface tension, the surface of the bubble oscillates in an axisymmetric manner as the bubble rises. Though this does not indicate path instability of a rising bubble, they noted that comparing their results with experiments showed that the occurrence of axisymmetric oscillation of the bubble coincides with path instabilities observed in experiments.

In this chapter, we revisit Ryskin and Leal's approach [34] and duplicate and thus verify some of their results in computing steady, axisymmetric flow past a rising bubble. We have developed an alternative method of grid generation which in contrast to that developed by Ryskin and Leal [34] does not involve iterations in solving for the numerical grids. While they computed solutions up to a Reynolds number of 200 and a Weber number of 10, in our case, we have been able to obtain results up to a Reynolds number of 400 and a Weber number of 5.

4.2 Numerical grid generation

In this section, we describe the use of Symm's conformal mapping method to construct a boundary fitted grid to compute the flow about the deformable bubble. In his paper, Symm [39] uses conformal mapping to map the exterior of a two-dimensional region as shown in Figure 4.1 to the exterior of a unit circle as shown in Figure 4.2. The region D is mapped to D_c, and the curve L is mapped to the unit circle L_c. Symm's method is such that this mapping is computed directly without any iteration as occurs for example in Chapter 2.

We present a brief description of this method. Let

$$z = x + \iota\sigma = re^{\iota\theta}$$

be a point in physical z space as shown in Figure 4.1, and let

$$w = x_c + \iota\sigma_c = r_c e^{\iota\theta_c}$$

be its corresponding point in conformal w space as shown in Figure 4.2. We want the

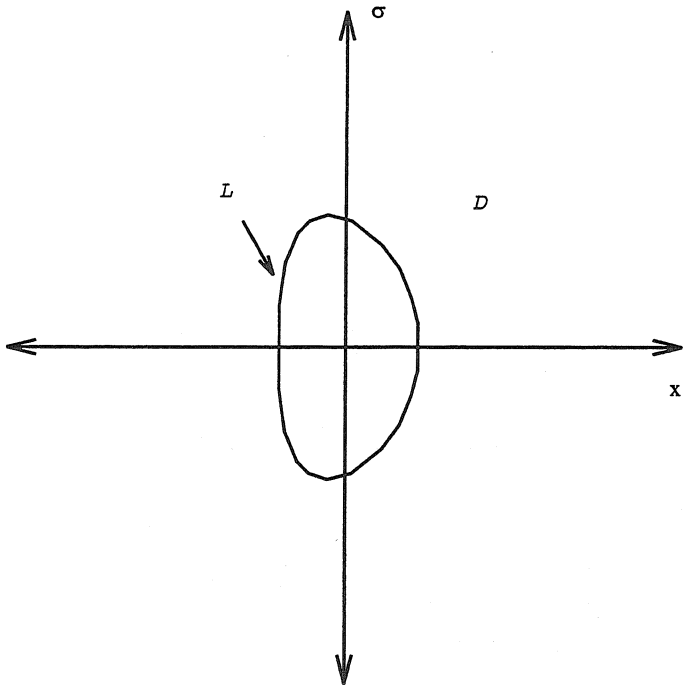

Figure 4.1: Physical z space (x, σ).

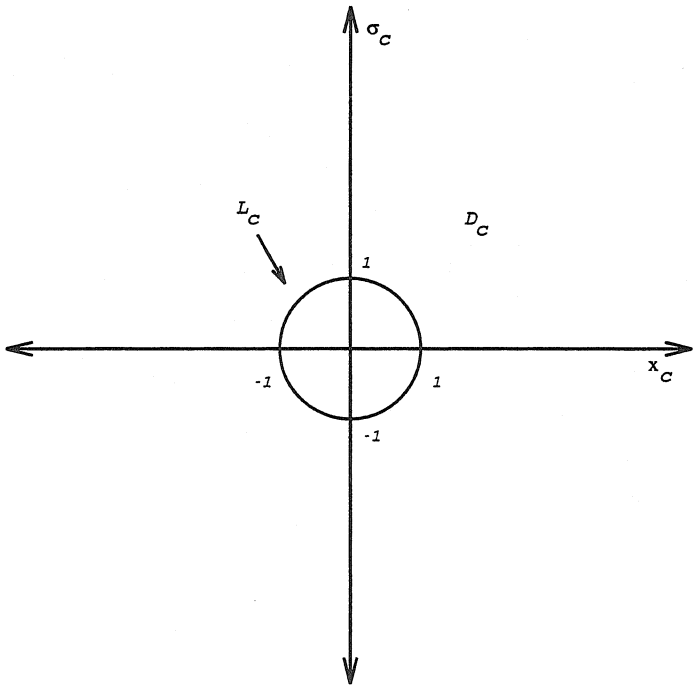

Figure 4.2: Conformal w space (x_c, σ_c).

conformal map $w(z)$ to be such that

$$|w(z)|_{z\in L} = 1$$

and

$$w(z) = \infty \text{ for } z = \infty.$$

It is known that

$$\lim_{z\to\infty} \frac{1}{|w'(z)|} = c$$

where c is called the transfinite diameter of the interior region of the curve L [27]. This allows us to impose

$$w'(z) \to \frac{1}{c} \text{ as } z \to \infty \tag{4.1}$$

on $w(z)$. Now, let

$$\alpha(z) = \log\left(\frac{w(z)}{z}\right).$$

Solving for $w(z)$ gives

$$w(z) = e^{\log z + \alpha(z)}.$$

As $z \to \infty$, from (4.1),

$$\alpha(z) \to \log\left(\frac{1}{c}\right) = -\log c.$$

Now, let

$$\alpha(z) = \phi(z) + \gamma$$

where

$$\gamma = -\log c.$$

The function $\phi(z)$ then is analytic in D and

$$\phi(z) \to 0 \text{ as } z \to \infty. \tag{4.2}$$

This allows us to represent $\phi(z)$ as

$$\phi(z) = g(z) + \iota h(z)$$

where $g(z)$ and $h(z)$ are conjugate harmonic functions in D. The function $g(z)$ can therefore be presented as single-layer logarithmic potential

$$g(z) = \int_L \log|z-\zeta|\, s(\zeta)\, |d\zeta|\,, \tag{4.3}$$

where $s(\zeta)$ is a source density on L. Also,

$$h(z) = \int_L Arg\,(z-\zeta)\, s(\zeta)\, |d\zeta|\,.$$

This reduces the problem to determining the source function $s(z)$ and γ.

Applying

$$|w(z)|_{z\in L} = 1$$

gives

$$\int_L \log|z-\zeta|\, s(\zeta)\, |d\zeta| + \gamma = -\frac{1}{2}\log\left(x^2+y^2\right) \tag{4.4}$$

where

$$z = x + \iota y \in L.$$

Also, using (4.2) gives

$$\int_L s(\zeta)\, |d\zeta| = 0. \tag{4.5}$$

Let $z_j = x_j + \iota\sigma_j$, $j = 0, .., 2m+1$ be the discretized nodal points of the curve L, and let I_j denote the intervals $z_j \le z \le z_{j+1}$. To simplify the integral (4.4) further, the function $s(z)$ is approximated to be constant at each interval I_j. So,

$$s(z) = s_j,\ z \in I_j.$$

This allows the integral equations (4.4) and (4.5) to be approximated as

$$\sum_{j=0}^{2m+1} s_j \int_{I_j} \log|z-\zeta|\,|d\zeta| + \gamma = -\frac{1}{2}\log\left(x^2+\sigma^2\right) \tag{4.6}$$

and

$$\sum_{j=0}^{2m+1} s_j \int_{I_j} |d\zeta| = 0 \tag{4.7}$$

for $z \in L$. The equation (4.6) is then evaluated at

$$z_{h_i} = x_{h_i} + \iota\sigma_{h_i}$$

where

$$\begin{aligned} x_{h_i} &= \frac{1}{2}\left(x_i + x_{i+1}\right), \\ \sigma_{h_i} &= \frac{1}{2}\left(\sigma_i + \sigma_{i+1}\right), \end{aligned}$$

to obtain

$$\sum_{j=0}^{2m+1} s_j \int_{I_j} \log|z_{h_i}-\zeta|\,|d\zeta| + \gamma = -\frac{1}{2}\log\left(x_{h_i}^2+\sigma_{h_i}^2\right).$$

Let $\zeta = z_{j+1}t + (1-t)\,z_j$ to give

$$\begin{aligned} \int_{I_j} \log|z_{h_i}-\zeta|\,|d\zeta| &= \int_{z_j}^{z_{j+1}} \log|z_{h_i} - (z_{j+1}t + (1-t)\,z_j)|\,d\,|z_{j+1}t + (1-t)\,z_j| \\ &= |z_{j+1}-z_j| \int_0^1 \log|(z_{h_i} - z_j - t\,(z_{j+1}-z_j))|\,dt \\ &= \frac{1}{2} se_j \left(1 - \frac{b_{ij}}{cij}\right) \log\left(a_{ij} + c_{ij} - 2b_{ij}\right) \\ &\quad + \frac{1}{2} se_j \left[2\frac{sq}{c_{ij}} \arctan\left(\frac{c_{ij}-b_{ij}}{sq}\right) - 2\right] \\ &\quad + \frac{1}{2} se_j \left[\frac{b_{ij}}{c_{ij}} \log a_{ij} + 2\frac{sq}{c_{ij}} \arctan\left(\frac{b_{ij}}{sq}\right)\right] \end{aligned}$$

where

$$\begin{aligned} a_{ij} &= (x_{h_i} - x_j)^2 + (\sigma_{h_i} - \sigma_j)^2, \\ b_{ij} &= (x_{h_i} - x_j)(x_{j+1} - x_j) + (\sigma_{h_i} - \sigma_j)(\sigma_{j+1} - \sigma_j), \\ c_{ij} &= (x_{j+1} - x_j)^2 + (\sigma_{j+1} - \sigma_j)^2, \\ se_j &= \sqrt{c_{ij}}, \\ sq &= \sqrt{a_{ij}c_{ij} - b_{ij}^2}. \end{aligned}$$

If $i = j$,

$$\begin{aligned} \int_{I_j} \log|z_{h_j} - \zeta|\,|d\zeta| &= \int_{z_j}^{z_{h_j}} \log|z_{h_j} - \zeta|\,|d\zeta| + \int_{z_{h_j}}^{z_{j+1}} \log|z_{h_j} - \zeta|\,|d\zeta| \\ &= \int_0^1 \log|z_{h_j} - (z_{h_j}t + (1-t)z_j)|\,d\,|z_{h_j}t + (1-t)z_j| \\ &\quad + \int_0^1 \log|z_{h_j} - (z_{j+1}t + (1-t)z_{h_j})|\,d\,|z_{j+1}t + (1-t)z_{h_j}| \\ &= \frac{1}{2} se_j (\log a_{ij} - 2). \end{aligned}$$

The discretized equations (4.6) and (4.7) are solved easily as a linear system to determine s_j, $j = 0, ..., 2m+1$ and γ. With these values determined, given a point $z = x + i\sigma$, its corresponding (x_c, σ_c) can now be determined using

$$\begin{aligned} x_c &= |z|\, e^{g+\gamma} \cos(Arg(z) + h), \\ \sigma_c &= |z|\, e^{g+\gamma} \sin(Arg(z) + h) \end{aligned}$$

where

$$\begin{aligned} g &= \sum_{j=0}^{2m+1} s_j \int_{I_j} \log|z - \zeta|\,|d\zeta|, \\ h &= \sum_{j=0}^{2m+1} s_j \int_{I_j} Arg(z - \zeta)\,|d\zeta|. \end{aligned}$$

Furthermore, for each of the node points

$$z = x_j + \iota\sigma_j = r_j e^{\iota\theta_j}$$

for $j = 0, ..., 2m+1$ on the curve L in physical space, a corresponding conformal point

$$w = x_{c_j} + \iota\sigma_{c_j} = e^{\iota\theta_{c_j}}$$

on the curve of unit circle L_c can be found using the above equations.

For our purposes though, we need to determine the mapping that associates the point z in physical space as shown in Figure 4.1 as a function of the point w in conformal space as shown in Figure 4.2. To determine this mapping, z is set to be

$$\begin{aligned} z &= x + \iota\sigma \\ &= e^{\log w + \beta} \end{aligned} \tag{4.8}$$

where

$$\begin{aligned} \beta &= \sum_{k=0}^{\infty} c_k w^{-k} \\ &= \sum_{k=0}^{\infty} \left(c_{R_k} + \iota c_{I_k}\right) r_c^{-k} e^{-\iota k\theta_c}. \end{aligned}$$

This expression comes from the fact that the inverse of a conformal map is also conformal and that an analytic function over an annulus can be written as a Laurent series. To get the coefficients $c_k = c_{R_k} + \iota c_{I_k}$, the equation (4.8) is evaluated at $z = re^{\iota\theta} \in L$ and $w = e^{\iota\theta_c} \in L_c$ to get

$$\begin{aligned} \log r &= c_{R_o} + \sum_{k=1}^{\infty} \left[c_{R_k} \cos\left(k\theta_c\right) + c_{I_k} \sin\left(k\theta_c\right)\right], \\ \theta - \theta_c &= c_{I_o} + \sum_{k=1}^{\infty} \left[c_{I_k} \cos\left(k\theta_c\right) - c_{R_k} \sin\left(k\theta_c\right)\right]. \end{aligned}$$

Applying the appropriate orthogonality conditions give

$$\begin{aligned} c_{R_o} &= \frac{1}{2\pi}\int_0^{2\pi} \log r d\theta_c, \\ c_{R_k} &= \frac{1}{2\pi}\int_0^{2\pi} \left[\log r \cos\left(k\theta_c\right) - \left(\theta - \theta_c\right)\sin\left(k\theta_c\right)\right] d\theta_c, \end{aligned}$$

and

$$\begin{aligned} c_{I_o} &= \frac{1}{2\pi}\int_0^{2\pi} \left(\theta - \theta_c\right) d\theta_c, \\ c_{I_k} &= \frac{1}{2\pi}\int_0^{2\pi} \left[\log r \sin\left(k\theta_c\right) + \left(\theta - \theta_c\right)\cos\left(k\theta_c\right)\right] d\theta_c. \end{aligned}$$

For numerical purposes, the Laurent series β is truncated at some finite M, and the trapezoidal rule is used to evaluate the integrals. Given a point $w = x_c + \iota\sigma_c = r_c e^{\iota\theta_c}$ in conformal w space, we can find a point $z = x + \iota\sigma$ in physical z space using:

$$\begin{aligned} x &= r_c e^{\alpha_1}\cos(\theta_c + \alpha_2), \\ \sigma &= r_c e^{\alpha_1}\sin(\theta_c + \alpha_2), \end{aligned} \tag{4.9}$$

where

$$\begin{aligned} \alpha_1 &= c_{R_o} + \sum_{k=1}^{M} \frac{1}{r_c^k}\left[c_{R_k}\cos\left(k\theta_c\right) + c_{I_k}\sin\left(k\theta_c\right)\right], \\ \alpha_2 &= c_{I_o} + \sum_{k=1}^{M} \frac{1}{r_c^k}\left[c_{I_k}\cos\left(k\theta_c\right) - c_{R_k}\sin\left(k\theta_c\right)\right]. \end{aligned} \tag{4.10}$$

Since we intend to solve for steady, axisymmetric flow past a bubble, the physical domain of the problem can be restricted to the upper half plane. In addition, we need to truncate the physical domain sufficiently far away from the bubble so that the velocity field of the flow can be approximated by the free stream flow. Figure 4.3 shows the truncated physical domain of the problem, and Figure 4.4 shows the corresponding truncated conformal domain of the problem. The outer limit curve L_o is determined by using the equations (4.9) to map a semicircle of radius Γ_c to L_o.

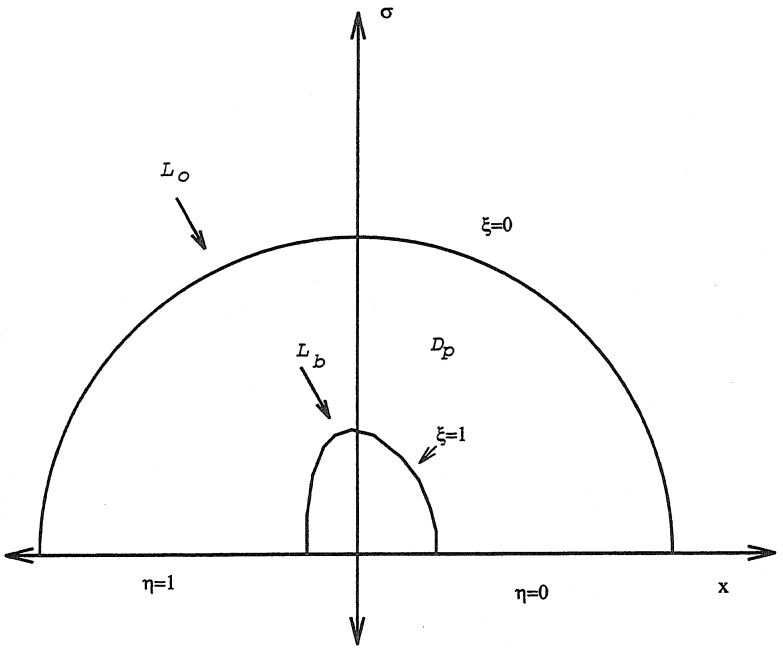

Figure 4.3: Truncated physical domain of z space.

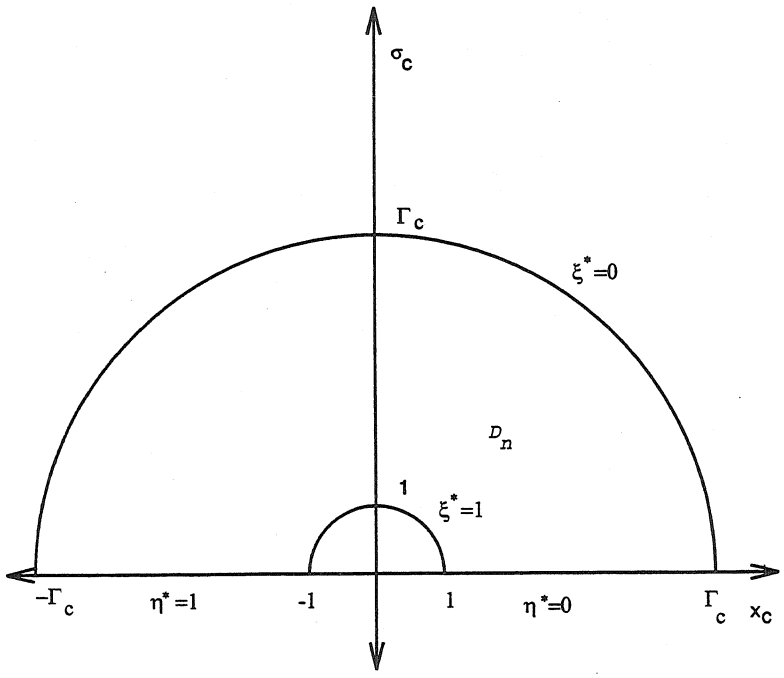

Figure 4.4: Truncated conformal w space.

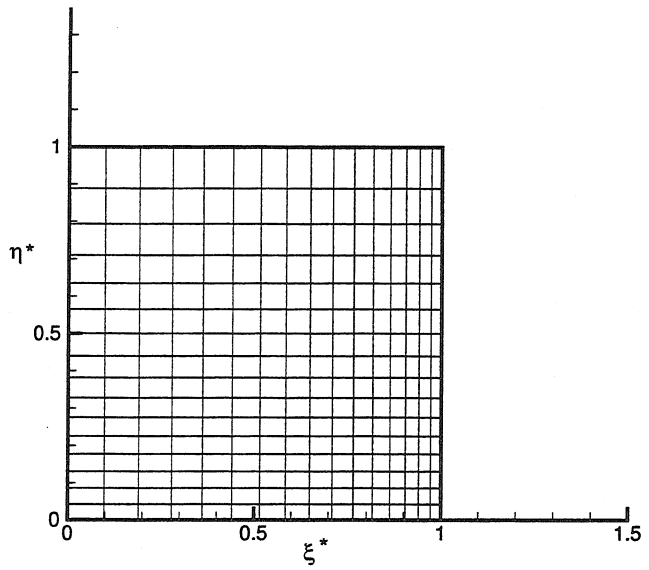

Figure 4.5: Auxiliary curvilinear space (ξ^*, η^*).

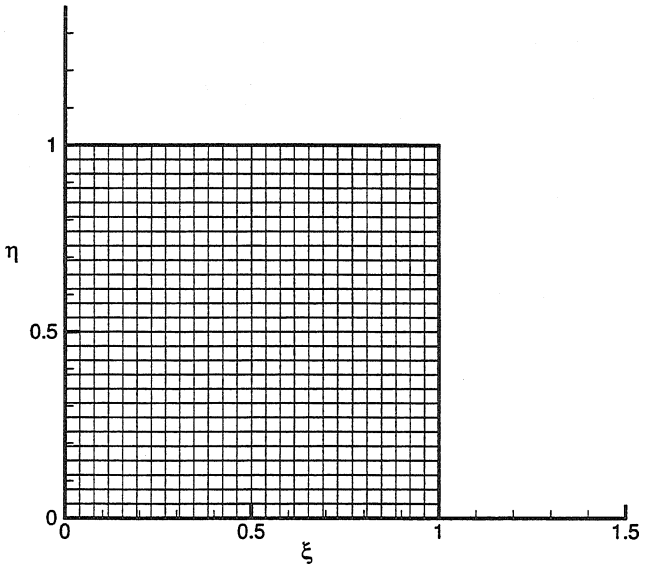

Figure 4.6: Curvilinear space (ξ, η).

Typically, we use $\Gamma_c \approx 70$. Under the mapping of (4.9), the curve L_o is a nearly semicircular curve far away from the curve L_b, which corresponds the surface of the bubble. The equations (4.9) also map the semicircle of radius one in w space to curve L_b in z space and maps the region D_n to D_p.

To further simplify the solution of the flow equations, the region D_n in conformal w space is mapped to the unit square shown in Figure 4.5 by

$$\begin{aligned} x_c &= \Gamma_c^{(1-\xi^*)} \cos(\pi\eta^*), \\ \sigma_c &= \Gamma_c^{(1-\xi^*)} \sin(\pi\eta^*). \end{aligned} \tag{4.11}$$

These relations map the unit square shown in Figure 4.5 defined by $0 < \xi^*, \eta^* < 1$ to the region D_n shown in Figure 4.4 . The upper half of the annulus $1 \leq |w| \leq \Gamma_c$ is mapped to the unit square such that $\eta^* = 0$ and $\eta^* = 1$ correspond to segments $1 \leq w \leq \Gamma_c$ and $-\Gamma_c \leq w \leq -1$. The segment $\xi^* = 0$ corresponds to the semicircle of radius Γ_c, and $\xi^* = 1$ corresponds to the unit semicircle. The functions (4.11) are not conformal since they are obtained by scaling the coordinates r_c and θ_c by $\log(\Gamma_c)$ and π so that the resulting auxiliary curvilinear domain shown in Figure 4.5 is a unit square.

It is desirable to control the grid density so that more of the mesh points are placed near and to the right of the body. To accomplish this, one more mapping is carried out:

$$\begin{aligned} \xi^* &= A_1\xi^2 + A_2\xi, \\ \eta^* &= B_1 - \sqrt{B_2 + B_3\eta}. \end{aligned} \tag{4.12}$$

The coefficients A_1, A_2, B_1, B_2, and B_3 are chosen so that

$$\begin{aligned} \xi^*(0) &= 0, \\ \xi^*(1) &= 1, \\ \eta^*(0) &= 0, \end{aligned}$$

and

$$\eta^*(1) = 1.$$

After some trial and error, we use

$$\begin{aligned} A_1 &= -\frac{3}{5}, \\ A_2 &= \frac{8}{5}, \end{aligned}$$

and

$$\begin{aligned} B_1 &= \frac{3}{2}, \\ B_2 &= \frac{9}{4}, \\ B_3 &= -2. \end{aligned}$$

These two monotonic functions allow evenly spaced grid points in the unit square (ξ, η) as shown in Figure 4.6 to be allocated nearer to $\xi^* = 1$ and $\eta^* = 0$. This can be seen by comparing Figure 4.5 and Figure 4.6.

By combining the equations (4.9), (4.11), and (4.12), we have an effective way to map the upper half of the exterior of an arbitrary closed curve shown in Figure 4.3 to the unit square shown in Figure 4.6. Figures 4.7 a) and b) show some of the grids generated by this method. They show that the grids are indeed dense nearer and to the right of the body. Because it involves no iteration and only one LU decomposition of a matrix whose size is the number of nodes on the curve L, grid generation takes very little computation time. It also cuts down on the number of degrees of freedom. It is especially useful in our case in trying to find a grid that fits around a body whose shape is determined as part of the flow solution.

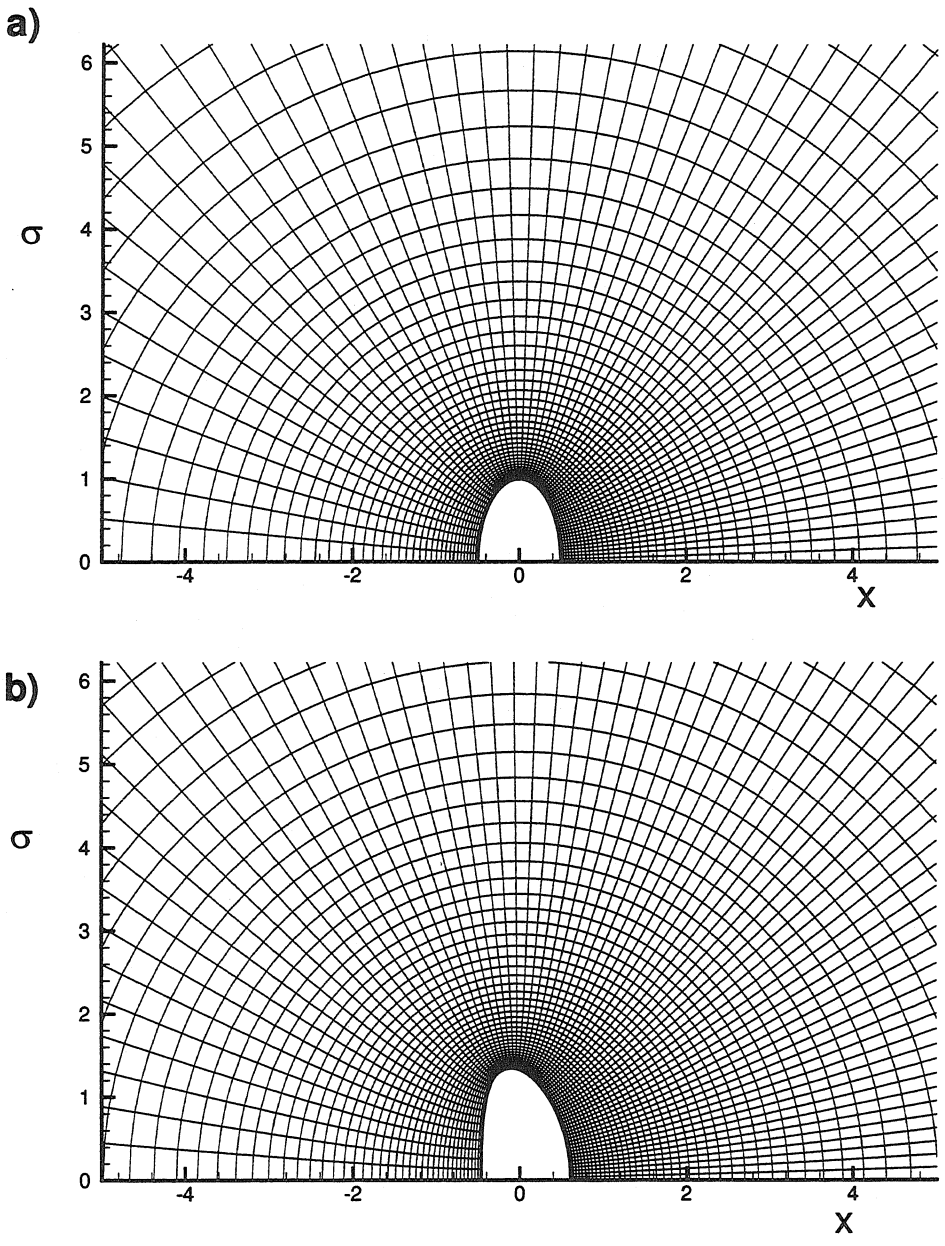

Figure 4.7: a) Grid fitted around an ellipsoid. b) Grid fitted around a bubble.

4.3 Flow equations

We next formulate the flow problem as a solution to the Navier-Stokes equations. The flow is assumed to be incompressible, Newtonian, steady, and axisymmetric. Also, the bubble is assumed to be such that pressure inside the bubble is constant and that the surface tension coefficient is constant. Writing the equations in stream function-vorticity form in (ξ, η) coordinates gives

$$\begin{aligned} &\frac{1}{h_\xi h_\eta}\left[\frac{\partial\psi}{\partial\xi}\frac{\partial}{\partial\eta}\left(\frac{\omega}{\sigma}\right)-\frac{\partial\psi}{\partial\eta}\frac{\partial}{\partial\xi}\left(\frac{\omega}{\sigma}\right)\right] \\ &-\frac{2}{R}\frac{1}{h_\xi h_\eta}\left\{\frac{\partial}{\partial\xi}\left[\frac{h_\eta}{h_\xi\sigma}\frac{\partial}{\partial\xi}(\omega\sigma)\right]+\frac{\partial}{\partial\eta}\left[\frac{h_\xi}{h_\eta\sigma}\frac{\partial}{\partial\eta}(\omega\sigma)\right]\right\}=0, \end{aligned} \tag{4.13}$$

$$\frac{-1}{h_\xi h_\eta}\left[\frac{\partial}{\partial\xi}\left(\frac{h_\eta}{h_\xi\sigma}\frac{\partial\psi}{\partial\xi}\right)+\frac{\partial}{\partial\eta}\left(\frac{h_\xi}{h_\eta\sigma}\frac{\partial\psi}{\partial\eta}\right)\right]=\omega \tag{4.14}$$

with the velocity vector $\mathbf{u} = u_\xi\hat{\boldsymbol{\xi}} + u_\eta\hat{\boldsymbol{\eta}}$ defined by

$$\begin{aligned} u_\xi &= -\frac{1}{h_\eta\sigma}\frac{\partial\psi}{\partial\eta}, \\ u_\eta &= \frac{1}{h_\xi\sigma}\frac{\partial\psi}{\partial\xi}. \end{aligned} \tag{4.15}$$

Here

$$R = \frac{2r_e\rho U}{\mu}$$

is the Reynolds number derived from nondimensionalization. ρ is the density of the outer fluid, and U is the velocity of the free stream flow. μ is the viscosity, and r_e is the effective radius of the bubble such that the volume of the bubble is $\frac{4}{3}\pi r_e^3$.

We next address the boundary conditions. At $\xi = 0$, the flow along the curve L_o as shown in Figure 4.3 is far away from the bubble and can be approximated as a free stream flow by imposing

$$u_x|_{\xi=0} = (\hat{\mathbf{x}}\cdot\mathbf{u})_{\xi=0} = 1.$$

Using the definition of the velocity components (4.15), we can see that this is equiv-

alent to imposing $\psi = \frac{1}{2}\sigma^2$ at $\xi = 0$. So, we set ψ as

$$\psi = \tilde{\psi} + \frac{1}{2}\sigma^2(1 - \xi^3)$$

so that $\psi = \frac{1}{2}\sigma^2$ at $\xi = 0$, and $\psi = 0$ at $\xi = 1$. This then allows us to impose homogeneous boundary conditions on $\tilde{\psi}$ for all sides of our curvilinear computational grid. It also allows us to set

$$\omega(0, \eta) = 0.$$

Along $\eta = 0$ and $\eta = 1$, we impose the flow to be axisymmetric to get

$$\begin{aligned} \tilde{\psi}(\xi, 0) &= 0, \\ \tilde{\psi}(\xi, 1) &= 0, \\ \omega(\xi, 0) &= 0, \\ \omega(\xi, 1) &= 0. \end{aligned}$$

Along $\xi = 1$ which corresponds to the interface of the bubble, since the flow is steady,

$$\tilde{\psi}(1, \eta) = 0.$$

In addition, the condition of continuity of stress is imposed [7]. This boundary condition is

$$\hat{\mathbf{n}} \cdot \mathbf{T} = \frac{4}{W} (\nabla \cdot \hat{\mathbf{n}}) \hat{\mathbf{n}} \tag{4.16}$$

where $\hat{\mathbf{n}}$ is a unit vector normal to the surface of the bubble, $\mathbf{T}$ is the stress tensor associated with the flow, and W is the Weber number defined by

$$W = \frac{2\rho U^2 r_e}{\tau}.$$

Here, τ is the surface tension coefficient. Rewriting (4.16) in (ξ, η) coordinates gives two boundary conditions that need to be satisfied, assuming steady and axisymmetric flow.

The first of these is the free-slip, or zero shear stress condition, which is imposed along $\xi = 1$:

$$e_{\xi\eta}\,|_{\xi=1} = \left[-\frac{h_\eta}{2h_\xi}\frac{\partial}{\partial\xi}\left(\frac{u_\eta}{h_\eta}\right) - \frac{h_\xi}{2h_\eta}\frac{\partial}{\partial\eta}\left(\frac{u_\xi}{h_\xi}\right)\right]_{\xi=1} = 0. \tag{4.17}$$

The second is the normal stress condition which accounts for the balancing of pressure and viscous forces of the outer flow with the surface tension coupled to the curvature of the bubble. In our curvilinear coordinates, this condition takes the form

$$\left(-p + \frac{8}{R}e_{\xi\xi} + K\right)_{\xi=1} = \frac{4}{W}\left(-\frac{1}{h_\xi h_\eta}\frac{\partial h_\eta}{\partial\xi} - \frac{1}{h_\xi\sigma}\frac{\partial\sigma}{\partial\xi}\right)_{\xi=1} \tag{4.18}$$

where

$$\begin{aligned}
p &= \frac{3}{4}C_D x - u_\eta^2 - \frac{4}{R}\int_0^\eta \frac{h_\eta}{h_\xi\sigma}\frac{\partial}{\partial\xi}(\sigma\omega)d\eta', \\
e_{\xi\xi} &= \frac{1}{h_\xi}\frac{\partial u_\xi}{\partial\xi} + \frac{u_\eta}{h_\xi h_\eta}\frac{\partial h_\xi}{\partial\eta}, \\
C_D &= 2\int_0^1 \left[u_\eta^2\sigma\frac{\partial\sigma}{\partial\eta} - \frac{2}{R}\frac{h_\eta}{h_\xi}\left(\sigma^2\frac{\partial\omega}{\partial\xi} + \omega\sigma\frac{\partial\sigma}{\partial\xi}\right) + \frac{8}{R}e_{\xi\xi}\sigma\frac{\partial\sigma}{\partial\eta}\right]_{\xi=1} d\eta.
\end{aligned}$$

The term K is a constant of integration associated with the pressure and is determined by enforcing the volume of the bubble to remain $\frac{4}{3}\pi$. In (ξ,η) coordinates, the volume of the bubble is given by

$$Vol = -\pi\int_0^1 \left(\sigma^2\frac{\partial x}{\partial\eta}\right)_{\xi=1} d\eta. \tag{4.19}$$

4.4 Numerical method

Now that all the equations for the flow are given, we formulate the method to solve them numerically. The flow equations (4.13) and (4.14) have to be solved subject to the constraint of (4.17), (4.18), and (4.19). We next describe the general steps that are taken to solve them.

1. We want to compute the stream function ψ and vorticity ω for a given R and W. We use a previously computed solution, for example a flow past a spherical bubble, as the initial condition.

2. Given ψ and ω, a new boundary shape is determined in order to satisfy the normal stress condition (4.18). This is done by using a linear perturbation and minimization technique and is covered in detail in a later section.

3. Given the new boundary shape, a new grid that fits around the new shape has to be computed. This new grid is determined using the grid generation method developed in the previous section.

4. Over the new grid, the flow equations (4.13) and (4.14) are solved along with the free-slip boundary condition (4.17). This is done using Newton's method and is similar in approach to the computation of the steady solutions for flow past an ellipsoidal bubble of fixed shape described in Chapter 2.

5. With the new ψ and ω, steps (2)-(4) are repeated until they all converge to some steady state. In practice, the normal stress condition (4.18) ends up minimized to be around $O(10^{-2})$ for grid of 70x70 resolution. In a later section, we show that this can be improved with higher resolution.

4.4.1 Prediction of new boundary shape

Here the method of predicting a new boundary shape is discussed. First, the current iteration values of ψ and ω do not satisfy the normal stress condition (4.18). So, the shape of the bubble has to deform in such a way that the normal stress deviation from zero can be minimized. In other words, the boundary condition (4.18) has to be satisfied at some curve $\xi = 1 + \delta(\eta)$ such that

$$\left(-p + \frac{8}{R} e_{\xi\xi}\right)_{\xi=1+\delta(\eta)} + K - \frac{4}{W}\left(-\frac{1}{h_\xi h_\eta}\frac{\partial h_\eta}{\partial \xi} - \frac{1}{h_\xi \sigma}\frac{\partial \sigma}{\partial \xi}\right)_{\xi=1+\delta(\eta)} = 0.$$

It is assumed that $|\delta(\eta)| << 1$ which implies that the new shape of the bubble is a small perturbation away from the current bubble shape. Linearizing the equations gives, at $\xi = 1$,

$$T_0 + T_1 \frac{\partial^2}{\partial \eta^2}\delta(\eta) + T_2 \frac{\partial}{\partial \eta}\delta(\eta) + T_3 \delta(\eta) + K = 0 \tag{4.20}$$

where

$$\begin{aligned}
T_0 &= \left(-p + \frac{8}{R}e_{\xi\xi}\right)_{\xi=1} - \frac{4}{W}\left(-\frac{1}{h_\xi h_\eta}\frac{\partial h_\eta}{\partial \xi} - \frac{1}{h_\xi \sigma}\frac{\partial \sigma}{\partial \xi}\right)_{\xi=1}, \\
T_1 &= -\frac{4}{W}\left(\frac{h_\xi}{h_\eta^2}\right), \\
T_2 &= \frac{4}{W}\left(\frac{-2}{h_\eta^2}\frac{\partial h_\xi}{\partial \eta} - \frac{h_\xi}{h_\eta^2 \sigma}\frac{\partial \sigma}{\partial \eta} + \frac{h_\xi}{h_\eta^3}\frac{\partial h_\eta}{\partial \eta}\right), \\
T_3 &= -\frac{\partial p}{\partial \xi} + \frac{8}{R}\left[u_\eta\left(\frac{-1}{h_\eta h_\xi^2}\frac{\partial h_\xi}{\partial \eta}\frac{\partial h_\xi}{\partial \xi} - \frac{1}{h_\xi h_\eta^2}\frac{\partial h_\xi}{\partial \eta}\frac{\partial h_\eta}{\partial \xi} + \frac{1}{h_\xi h_\eta}\frac{\partial^2 h_\xi}{\partial \xi \partial \eta}\right)\right] \\
&\quad + \frac{8}{R}\left(\frac{-1}{h_\xi^2}\frac{\partial u_\xi}{\partial \xi}\frac{\partial h_\xi}{\partial \xi} + \frac{1}{h_\xi h_\eta}\frac{\partial u_\eta}{\partial \xi}\frac{\partial h_\xi}{\partial \eta} + \frac{1}{h_\xi}\frac{\partial^2 u_\xi}{\partial \xi^2}\right) \\
&\quad + \frac{4}{W}\left[\frac{1}{h_\xi h_\eta}\frac{\partial^2 h_\eta}{\partial \xi^2} + \frac{1}{h_\xi \sigma}\frac{\partial^2 \sigma}{\partial \xi^2} - \frac{1}{h_\xi^2 h_\eta}\frac{\partial h_\eta}{\partial \xi}\frac{\partial h_\xi}{\partial \xi}\right] \\
&\quad + \frac{4}{W}\left[-\frac{1}{h_\xi^2 \sigma}\frac{\partial h_\xi}{\partial \xi}\frac{\partial \sigma}{\partial \xi} - \frac{1}{h_\xi}\left(\frac{1}{\sigma}\frac{\partial \sigma}{\partial \xi}\right)^2 - \frac{1}{h_\xi}\left(\frac{1}{h_\eta^2}\frac{\partial h_\eta}{\partial \xi}\right)^2\right].
\end{aligned}$$

The volume equation (4.19) is also linearized to give

$$\int_0^1 \left(\sigma^2 \frac{\partial x}{\partial \eta}\right)_{\xi=1} d\eta + \frac{4}{3} + \int_0^1 \delta(\eta)\left(\sigma^2 \frac{\partial^2 x}{\partial \xi \partial \eta} + 2\sigma \frac{\partial \sigma}{\partial \xi}\frac{\partial x}{\partial \eta}\right)_{\xi=1} d\eta = 0. \tag{4.21}$$

In addition, the new shape of the bubble has to be constrained so that it stays fixed relative to the origin. To accomplish this, the centroid condition is imposed to give

$$\int_0^1 \left(x\sigma^2 \frac{\partial x}{\partial \eta}\right)_{\xi=1} d\eta + \int_0^1 \delta(\eta)\left[x\sigma^2 \frac{\partial^2 x}{\partial \xi \partial \eta} + \left(2x\sigma \frac{\partial \sigma}{\partial \xi} + \frac{\partial x}{\partial \xi}\sigma^2\right)\frac{\partial x}{\partial \eta}\right]_{\xi=1} d\eta = 0. \tag{4.22}$$

Second-order, centered, finite differencing is applied to approximate the derivatives

of $\delta(\eta)$. Let $\eta = j\Delta x, j = 0, .., m+1$ with $\Delta x = \frac{1}{m+1}$ to get $\delta(\eta) = \delta(j\Delta x) = \delta_j$. This gives

$$H_{N_j} = T_0 + T_{c_1}\delta_{j-1} + T_{c_2}\delta_j + T_{c_3}\delta_{j+1} \tag{4.23}$$

where

$$\begin{aligned} T_{c_1} &= \frac{T_1}{\Delta x^2} - \frac{T_2}{2\Delta x}, \\ T_{c_2} &= \frac{-2T_1}{\Delta x^2} + T_3, \\ T_{c_3} &= \frac{T_1}{\Delta x^2} + \frac{T_2}{2\Delta x}. \end{aligned}$$

We then use the trapezoidal integration rule on the equations (4.21) and (4.22) to obtain

$$V_p = v_0 + \sum_{j=1}^{m} \delta_j v_j$$

where

$$\begin{aligned} v_0 &= \int_0^1 \left(\sigma^2 \frac{\partial x}{\partial \eta}\right)_{\xi=1} d\eta + \frac{4}{3}, \\ v_j &= \Delta x \left(\sigma^2 \frac{\partial^2 x}{\partial \xi \partial \eta} + 2\sigma \frac{\partial \sigma}{\partial \xi}\frac{\partial x}{\partial \eta}\right)_{\xi=1,\eta=j\Delta x}; \end{aligned}$$

and

$$C_p = c_0 + \sum_{j=1}^{m} \delta_j c_j$$

where

$$\begin{aligned} c_0 &= \int_0^1 \left(x\sigma^2 \frac{\partial x}{\partial \eta}\right)_{\xi=1} d\eta, \\ c_j &= \Delta x \left[x\sigma^2 \frac{\partial^2 x}{\partial \xi \partial \eta} + \left(2x\sigma \frac{\partial \sigma}{\partial \xi} + \frac{\partial x}{\partial \xi}\sigma^2\right)\frac{\partial x}{\partial \eta}\right]_{\xi=1,\eta=j\Delta x}. \end{aligned}$$

We also define the term Ω by

$$\Omega = \sum_{j=0}^{m+1} \left(H_{N_j}\right)^2.$$

The unknowns are δ_j, $j = 0, ..., m+1$ and K, and we want to minimize Ω subject to the constraints of $V_p = 0$ and $C_p = 0$. To do this, we apply the method of Lagrange multipliers. Let

$$\Pi = \Omega + \lambda_0 V_p + \lambda_1 C_p.$$

Then, define a system of equations $\mathbf{G}$ composed of

$$\mathbf{G} = \begin{bmatrix} \frac{\partial}{\partial \delta_j}\Pi, j = 0, ..., m+1 \\ \frac{\partial}{\partial K}\Pi \\ \frac{\partial}{\partial \lambda_0}\Pi \\ \frac{\partial}{\partial \lambda_1}\Pi. \end{bmatrix}.$$

This system is then solved using Newton's method. In practice, it usually takes just one iteration to obtain a converged solution. With δ_j determined, the new, predicted boundary shape is determined by

$$\begin{aligned} x^{new}(1,\eta) &= x^{old}(1,\eta) + \delta_j \frac{\partial}{\partial \xi} x^{old}(1,\eta), \\ \sigma^{new}(1,\eta) &= \sigma^{old}(1,\eta) + \delta_j \frac{\partial}{\partial \xi} \sigma^{old}(1,\eta). \end{aligned}$$

4.4.2 Outer flow solver

Given a grid system fitted around an axisymmetric body, the Navier-Stokes equations need to be solved along with the free-slip boundary condition (4.17). The numerical approach taken is the same as that used to solve for the steady solutions for flow past an ellipsoidal bubble of fixed shape in Chapter 3. That is, the unknowns, $\omega(\xi,\eta) = \omega(i\Delta x, j\Delta x) = \omega_{i,j}$ and $\tilde{\psi}(\xi,\eta) = \tilde{\psi}(i\Delta x, j\Delta x) = \tilde{\psi}_{i,j}$ with $\Delta x = \frac{1}{m+1}$, are discretized using second-order, centered, finite differencing; and the discretized equations are solved as a system of equations using Newton's method. One major change in the discretized equations is the boundary condition imposed on $\xi = 1$.

C_D	$R = 50\ W = 1$	$R = 50\ W = 2$	$R = 100\ W = 1$	$R = 100\ W = 2$
40x40	0.787	0.910	0.468	0.564
60x60	0.776	0.900	0.453	0.545
70x70	0.773	0.893	0.449	0.539
80x80	0.772	0.891	0.446	0.535

Table 4.1: Comparison of the drag coefficients of steady flow past an axisymmetric bubble with grids of different resolution.

Discretizing (4.17) gives

$$H_{B_j} = D_j^0 \tilde{\psi}_{m-2,j} + D_j^1 \tilde{\psi}_{m-1,j} + D_j^2 \tilde{\psi}_{m,j} + D_j^3$$

where

$$\begin{aligned}
D_j^0 &= \frac{-1}{(h_\xi \Delta x)^2 \sigma}, \\
D_j^1 &= \frac{4}{(h_\xi \Delta x)^2 \sigma} - \frac{1}{2(h_\xi \sigma)^2 \Delta x} \frac{\partial \sigma}{\partial \xi} - \frac{1}{2 h_\xi^3 \sigma \Delta x} \frac{\partial h_\xi}{\partial \xi} - \frac{1}{2 h_\xi^2 h_\eta \sigma \Delta x} \frac{\partial h_\eta}{\partial \xi}, \\
D_j^2 &= \frac{-5}{(h_\xi \Delta x)^2 \sigma} + \frac{2}{(h_\xi \sigma)^2 \Delta x} \frac{\partial \sigma}{\partial \xi} + \frac{2}{h_\xi^3 \sigma \Delta x} \frac{\partial h_\xi}{\partial \xi} + \frac{2}{h_\xi^2 h_\eta \sigma \Delta x} \frac{\partial h_\eta}{\partial \xi}, \\
D_j^3 &= \frac{3}{2} \frac{\sigma}{h_\xi^3} \frac{\partial h_\xi}{\partial \xi} - \frac{3\sigma}{h_\xi^2} - \frac{9}{2} \frac{1}{h_\xi^2} \frac{\partial \sigma}{\partial \xi} + \frac{3}{2} \frac{\sigma}{h_\xi^2 h_\eta} \frac{\partial h_\eta}{\partial \xi}.
\end{aligned}$$

Once again, the outer flow solver takes up most of the computation time as it involves finding an LU decomposition of a large sparse matrix. In practice, this LU decomposition only has to be done once in the beginning of the whole computational loop as long as the initial ω and ψ are such that the deformation of the bubble shape is not too large.

4.5 Numerical results

First, we compute steady solutions using the above method for $R = 50$, 100 and $W = 1$, 2 using grids of different resolutions to check the convergence of our method. Table 4.1 compares the drag coefficient of the flows under grids of different resolution, and they appear to be in good agreement.

C_D	Ryskin and Leal [34]	This work
$R = 20\ W = 2$	1.74	1.74
$R = 20\ W = 4$	2.16	2.15
$R = 20\ W = 6$	2.56	2.57
$R = 100\ W = 2$	0.54	0.54
$R = 100\ W = 4$	0.81	0.82
$R = 100\ W = 6$	1.23	1.20
$R = 200\ W = 2$	0.33	0.33
$R = 200\ W = 4$	0.59	0.59
$R = 200\ W = 6$	0.95	0.90

Table 4.2: Comparison of the drag coefficients of steady flow past an axisymmetric bubble computed by our method and Ryskin and Leal's method.

Because our method uses minimization of the normal stress condition (4.18) in determining the shape of the bubble, our computed solutions are such that the normal stress condition is not quite fully zeroed out.

Figure 4.8 shows how well our computed steady solutions satisfy the normal stress condition (4.18), as the resolution of the grid used is increased. Let

$$R_{avN} = \frac{1}{m+2} \sum_{j=0}^{m+1} \left| R_{st}(\eta) \right|,$$

where

$$R_{st}(\eta) = \left[-p + \frac{8}{R} e_{\xi\xi} + K - \frac{4}{W} \left(-\frac{1}{h_\xi h_\eta} \frac{\partial h_\eta}{\partial \xi} - \frac{1}{h_\xi \sigma} \frac{\partial \sigma}{\partial \xi} \right) \right]_{\xi=1}.$$

Figure 4.8 compares R_{avN},which is basically the average of the absolute value of the residual normal stress condition, with respect to the resolution of the grids used in computing the steady solutions for the cases of $R = 50$, 100 and $W = 1$, 2. It is clear that the value of R_{avN} gets smaller in all four cases as the resolution is increased. This implies that the results will get better if we can increase the resolution of the grid. Of course, increasing the resolution also increases the computation time. Therefore, for the rest this chapter, we use the grid with 70x70 resolution to compute our steady flows past a deforming bubble.

Next, we compare our results with the results of Ryskin and Leal [34]. Our approach to solving this problem is similar, but there are a couple of differences. One

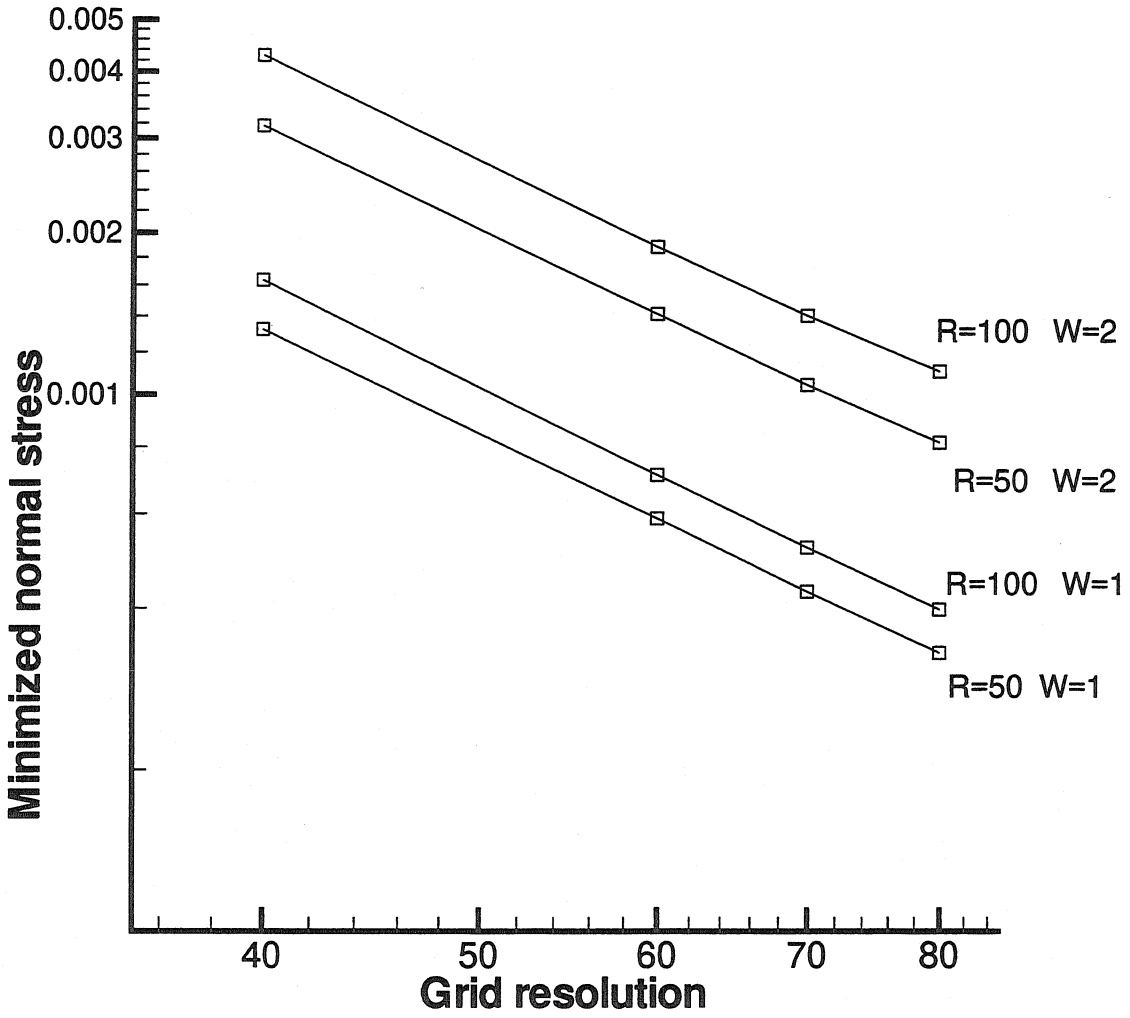

Figure 4.8: Comparison of how well our computed steady solutions satisfy the normal stress condition on the surface of the bubble under different resolutions.

C_D	$W=1$	2	3	4	5	6	7	8
$R=20$	1.56	1.74	1.94	2.15		2.57	2.75	2.90
100	0.45	0.54	0.66	0.82	1.01	1.20		
200	0.26	0.33	0.44	0.59	0.76	0.90		
300	0.20	0.25	0.36	0.51	0.68	0.80		
400	0.16	0.22	0.32	0.49	0.67			

Table 4.3: Drag coefficients of flow past an axisymmetric bubble at various Reynolds numbers and Weber numbers.

major difference is that our numerical grid generation does not involve iteration. In addition, the boundary shape prediction step differs from their approach. Table 4.2 compares the drag coefficients of the numerical solutions computed by our method and Ryskin and Leal's method. They appear to agree well with one another. Figures 4.10, 4.12, and 4.14 show the stream lines of flow past a bubble computed by Ryskin and Leal [34], and Figures 4.11, 4.13, and 4.15 show the stream lines of flow past a bubble computed using our method. Again, they all appear to agree with one another well.

Still, our method is not necessarily better than Ryskin and Leal's. They were able to compute steady solutions for W up to 10, while our method does not seem to work well for W larger than 5 for R large. In addition, our bubble shape prediction step only manages to minimize rather than zero out the normal stress condition. It is not clear how well Ryskin and Leal's method satisfies the normal stress condition, since their paper does not discuss convergence.

Solutions are computed for R up to 400 and W up to about 5. It takes about 50 minutes on a Sun Ultra workstation to compute each solution. Table 4.3 and Figure 4.9 show the drag coefficients computed for various Reynolds numbers and Weber numbers. It is clear that increasing the Weber number increases the drag coefficient. As the Weber number increases, the corresponding curvilinear grid becomes more distorted, making the computation of the outer flow more difficult. So, our method does not work well for W larger than 5 if R is large.

Figures 4.16-4.20 show the steady solutions computed by our method. For low Reynolds number, the bubble leans toward the back as the Weber number increases.

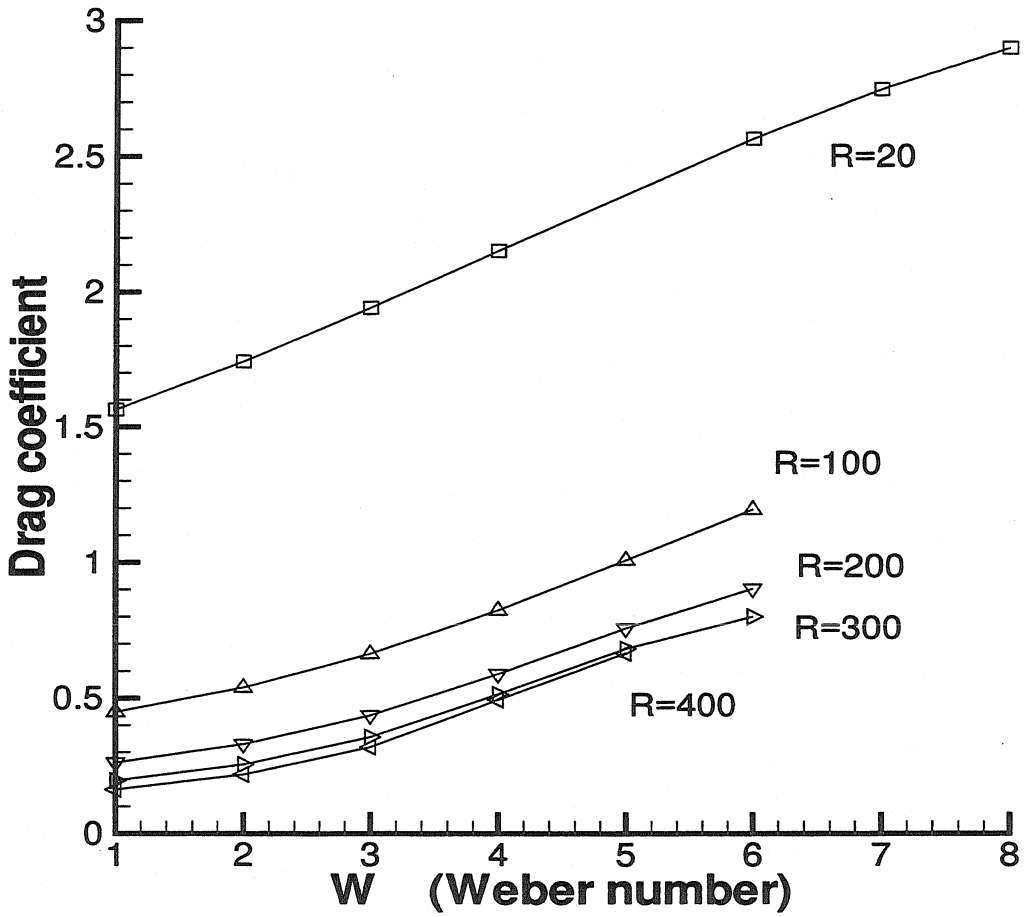

Figure 4.9: Drag coefficients of flow past an axisymmetric bubble for various R and W.

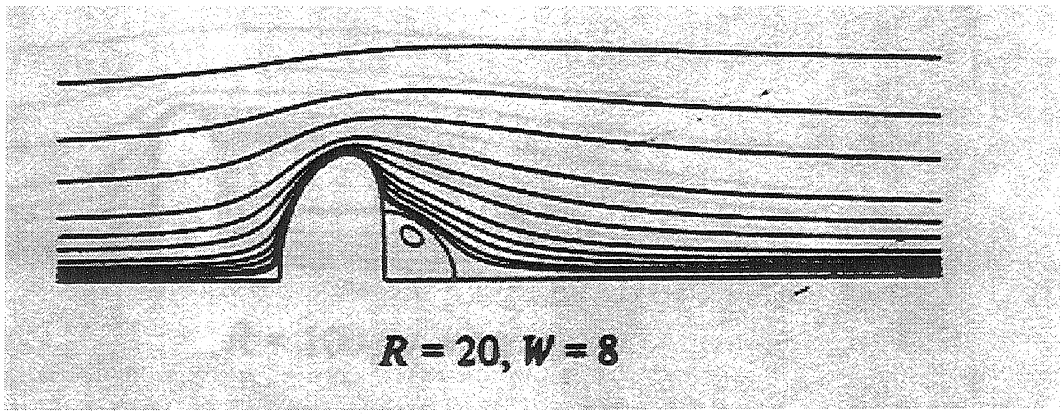

Figure 4.10: Stream lines of flow past an axisymmetric bubble at $R = 20, W = 8$ as determined by Ryskin and Leal.

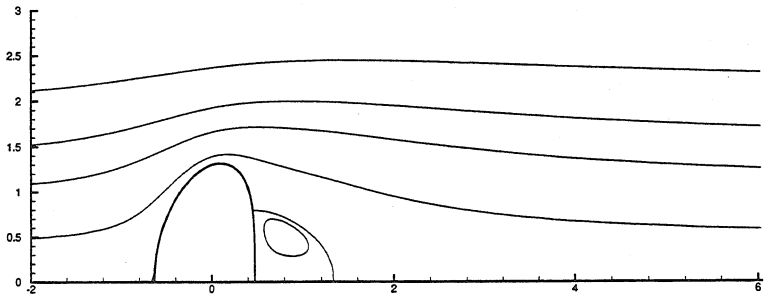

Figure 4.11: Stream lines of flow past an axisymmetric bubble at $R = 20$, $W = 8$ determined using our method.

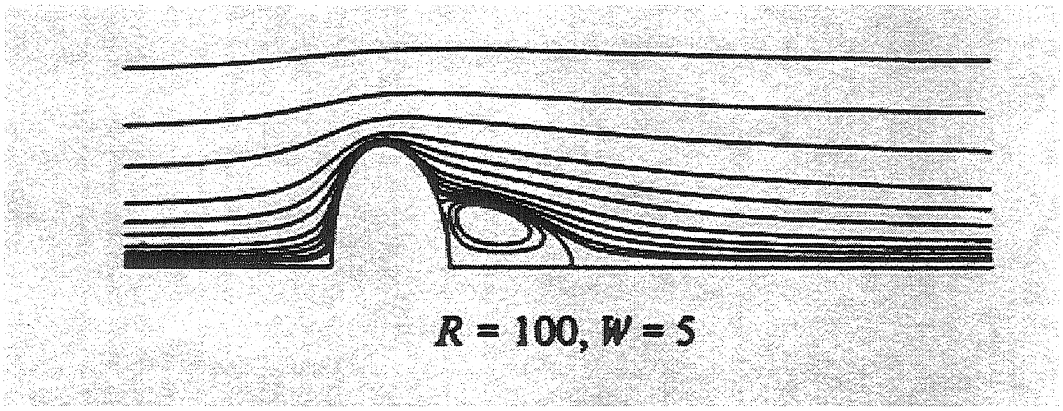

Figure 4.12: Stream lines of flow past an axisymmetric bubble at $R = 100$, $W = 5$ determined by Ryskin and Leal.

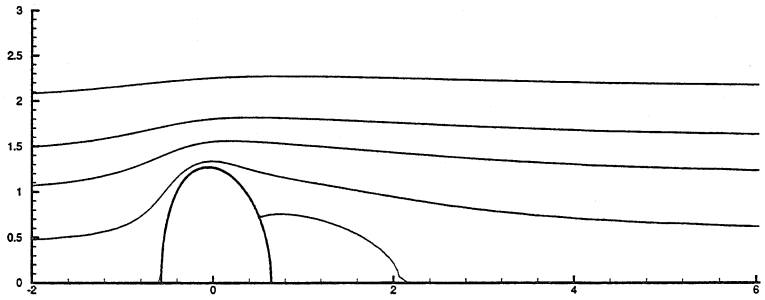

Figure 4.13: Stream lines of flow past an axisymmetric bubble at $R = 100$, $W = 5$ determined using our method.

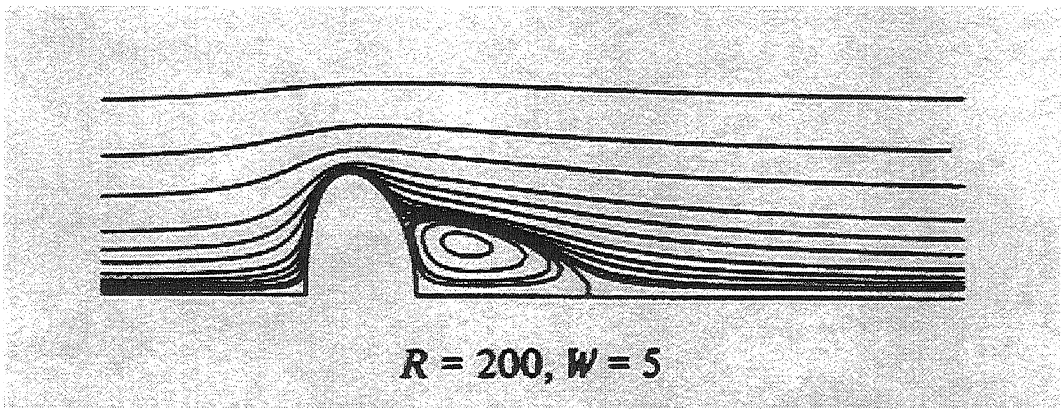

Figure 4.14: Stream lines of flow past an axisymmetric bubble at $R = 200$, $W = 5$ determined by Ryskin and Leal.

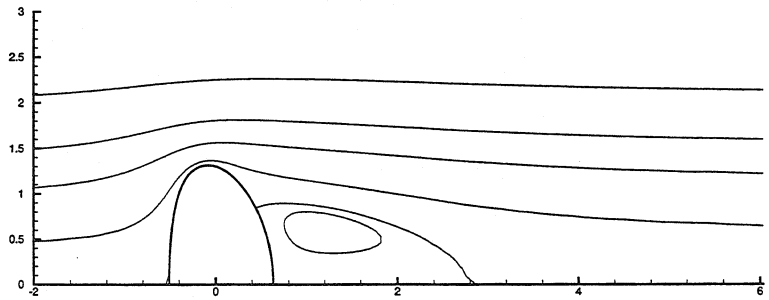

Figure 4.15: Stream lines of flow past an axisymmetric bubble at $R = 200$, $W = 5$ determined using our method.

For Reynolds number large, the bubble leans forward as the Weber number increases.

In conclusion, we have developed an alternative method in computing steady flow past an axisymmetric bubble. A resolution study and comparison with Ryskin and Leal's results indicate that our method is reasonably successful in computing the flow fields.

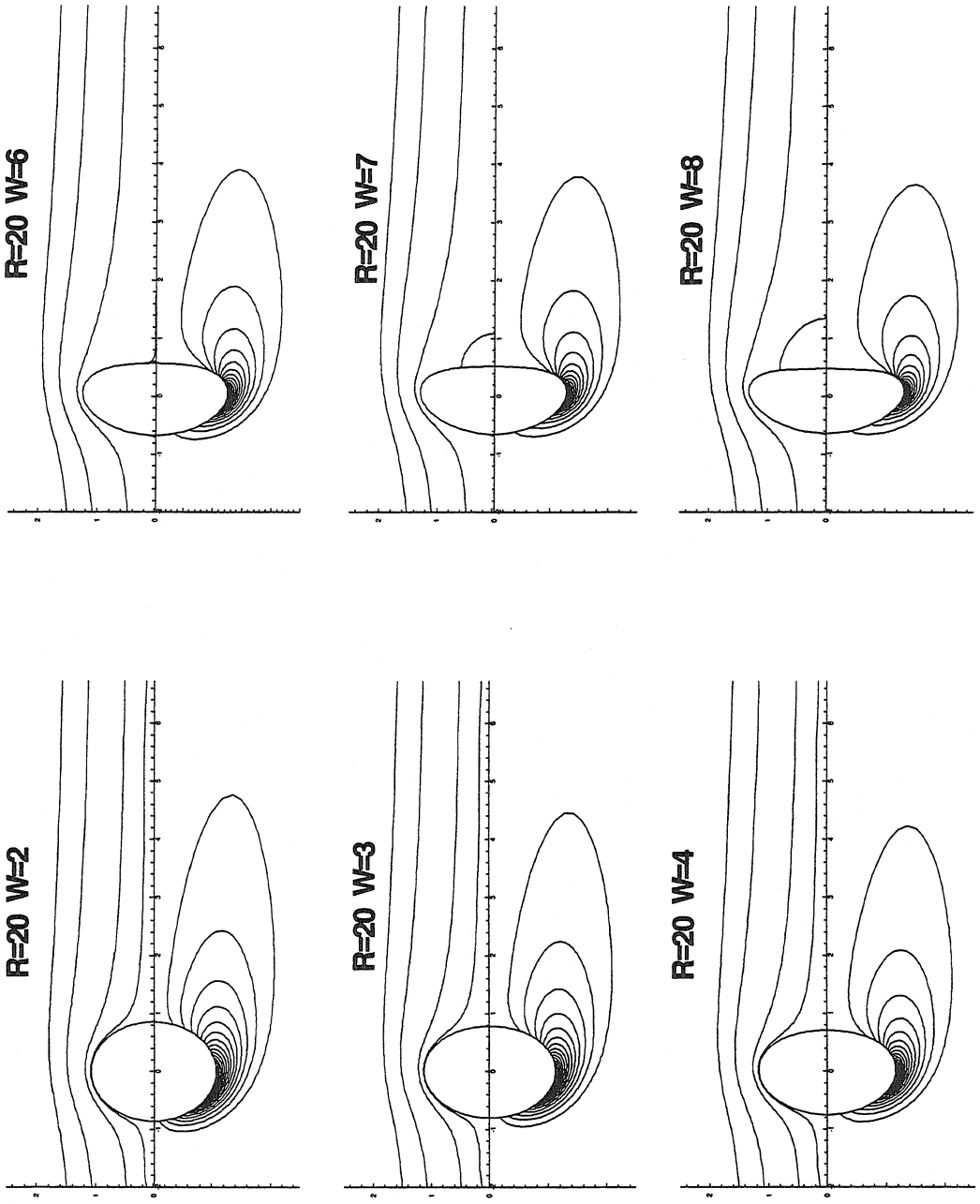

Figure 4.16: Steady flow past an axisymmetric bubble at $R = 20$, $W = 2, ..., 8$. In each case the left side is the stream function, and the right side is the vorticity.

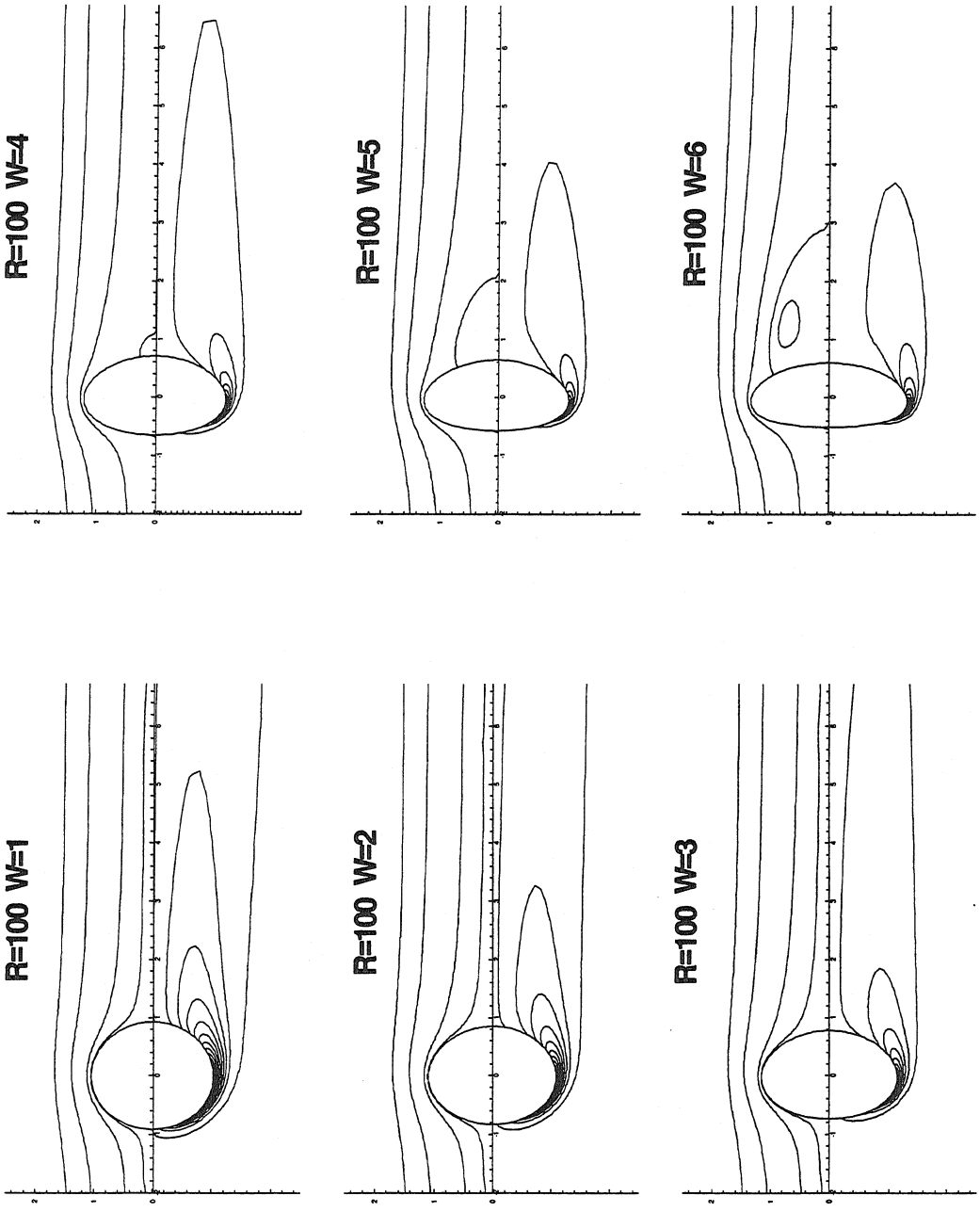

Figure 4.17: Steady flow past an axisymmetric bubble at $R = 100$, $W = 1, ..., 6$. In each case the left side is the stream function, and the right side is the vorticity.

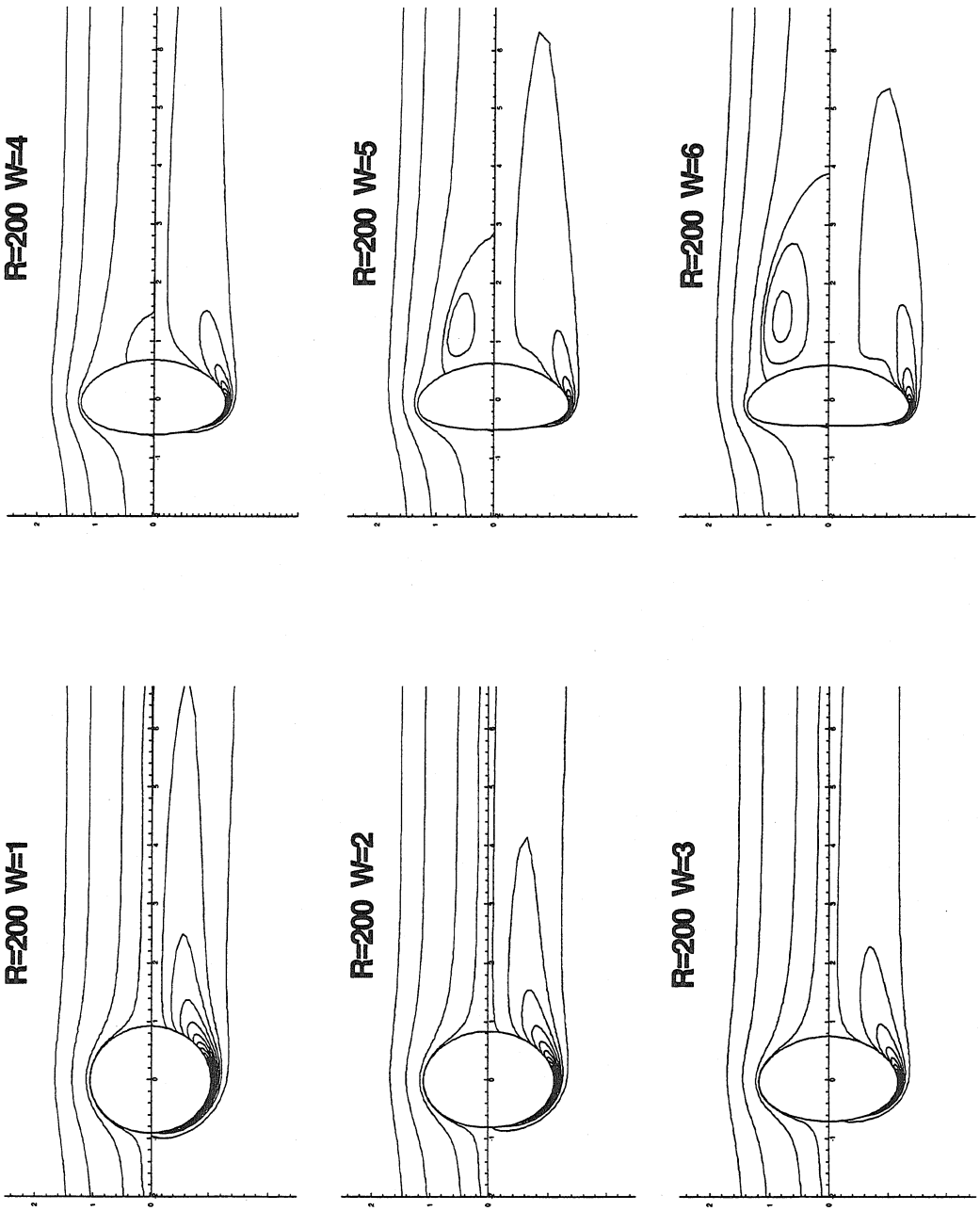

Figure 4.18: Steady flow past an axisymmetric bubble at $R = 200$, $W = 1, ..., 6$. In each case the left side is the stream function, and the right side is the vorticity.

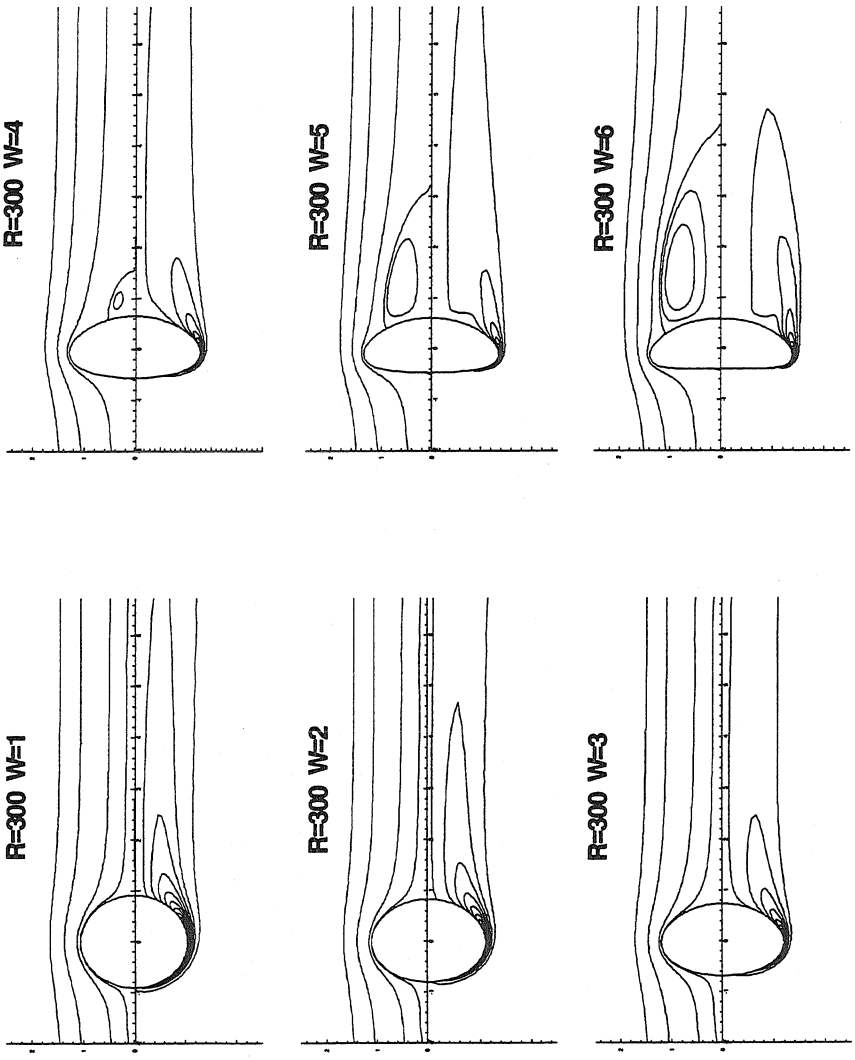

Figure 4.19: Steady flow past an axisymmetric bubble at $R = 300$, $W = 1, ..., 6$. In each case the left side is the stream function, and the right side is the vorticity.

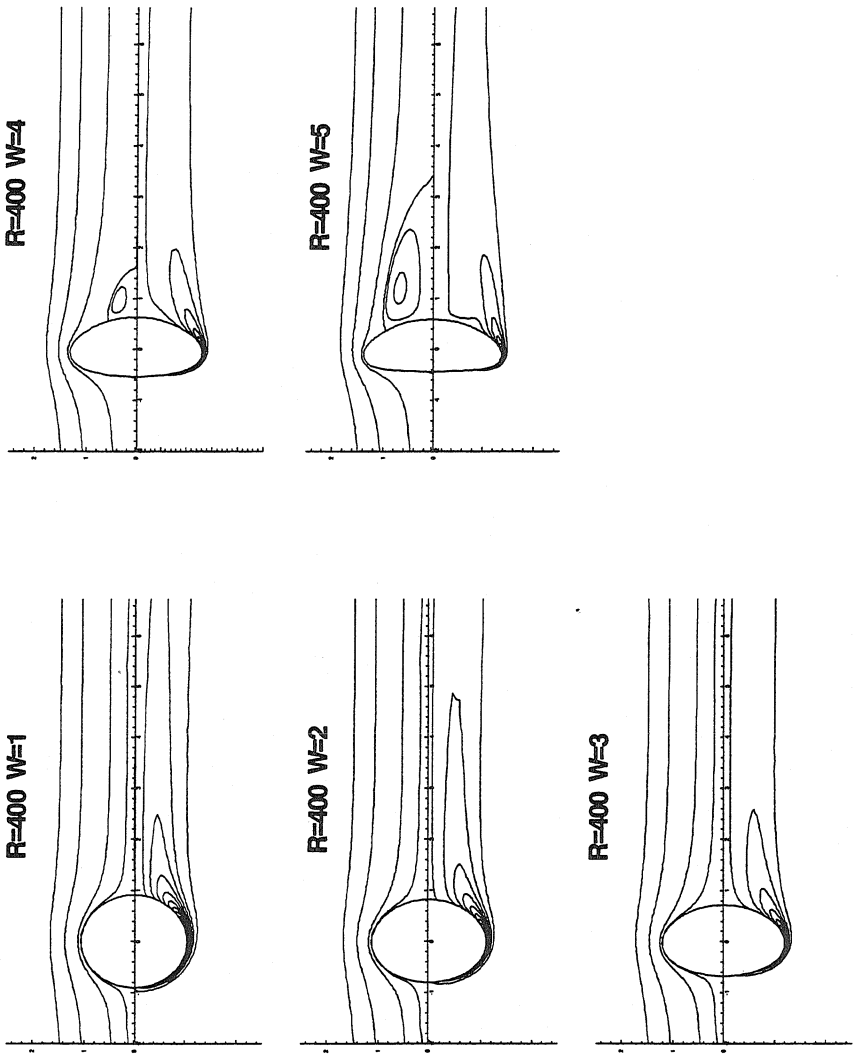

Figure 4.20: Steady flow past an axisymmetric bubble at $R = 400$, $W = 1, ..., 5$. In each case the left side is the stream function, and the right side is the vorticity.

Chapter 5 Steady Flow Past a Symmetric, Two-dimensional Bubble

5.1 Introduction

The previous chapters have dealt with flows past an axisymmetric, three-dimensional body. In this chapter we consider flows past a symmetric, two-dimensional body with a free surface. Such flows are studied experimentally by placing a gas bubble between a pair of plates filled with a thin layer of fluid. This is the so called Hele-Shaw cell set up. Many authors including Walter and Davidson [48], Rowe and Partridge [32], and Maxworthy [21] performed such experiments and observed flattened bubbles steadily rising in various deformed shapes. More recently, Kelley and Wu [16] performed experiments with a similar setup and observed nearly circular bubbles zigzagging as they moved upward. They also observed wakes at the back of the bubbles as well.

In terms of analytical results, Saffman [37] gives a good summary in the study of viscous fingering in Hele-Shaw cells. Shankar [38] solved the fluid equations around a symmetric, two-dimensional bubble assuming an inviscid flow and showed that it deforms to an oblate, elliptical shape. Expanding on Shankar's results, Nie and Tanveer [28] used similar methods to study instability of a two-dimensional bubble rising through an inviscid flow and showed, via a linear stability analysis, that it is stable.

In this chapter, we apply the techniques developed in Chapter 4 in which flows past an axisymmetric bubble are calculated to that of viscous incompressible flows past a symmetric, two-dimensional bubble. We are able to obtain steady flows for Reynolds number R up to 120 and the Weber number W up to 4.5. It is shown that a rising two-dimensional bubble deforms to an elliptical shape, and a standing wake develops behind the bubble. The size of the wake increases dramatically as the Weber

number is increased.

5.2 Flow equations

To determine the flow past a two-dimensional body, the Navier-Stokes equations are again solved. The flow is assumed to be incompressible, Newtonian, steady, symmetric, and two-dimensional. Figure 5.1 shows the setup of the problem to be solved, and Figure 5.2 shows the curvilinear coordinate system in which the Navier-Stokes equations are solved. To rewrite the flow equations in our curvilinear coordinate system, the velocity vector $\mathbf{u}$ is set as

$$\mathbf{u} = u_\xi \hat{\boldsymbol{\xi}} + u_\eta \hat{\boldsymbol{\eta}} + u_z \hat{\mathbf{z}},$$

with components

$$\begin{aligned} u_\xi &= -\frac{1}{h_\eta}\frac{\partial \psi}{\partial \eta}, \\ u_\eta &= \frac{1}{h_\xi}\frac{\partial \psi}{\partial \xi}, \\ u_z &= 0, \end{aligned} \tag{5.1}$$

where ψ is the stream function. Writing the equations in stream function-vorticity form in curvilinear (ξ, η) coordinates gives

$$\begin{aligned} &\frac{1}{h_\xi h_\eta}\left(\frac{\partial \psi}{\partial \xi}\frac{\partial \omega}{\partial \eta} - \frac{\partial \psi}{\partial \eta}\frac{\partial \omega}{\partial \xi}\right) \\ &-\frac{2}{R}\frac{1}{h_\xi h_\eta}\left[\frac{\partial}{\partial \xi}\left(\frac{h_\eta}{h_\xi}\frac{\partial \omega}{\partial \xi}\right) + \frac{\partial}{\partial \eta}\left(\frac{h_\xi}{h_\eta}\frac{\partial \omega}{\partial \eta}\right)\right] = 0, \end{aligned} \tag{5.2}$$

$$\frac{-1}{h_\xi h_\eta}\left[\frac{\partial}{\partial \xi}\left(\frac{h_\eta}{h_\xi}\frac{\partial \psi}{\partial \xi}\right) + \frac{\partial}{\partial \eta}\left(\frac{h_\xi}{h_\eta}\frac{\partial \psi}{\partial \eta}\right)\right] = \omega. \tag{5.3}$$

The term

$$R = \frac{2 r_e \rho U}{\mu}$$

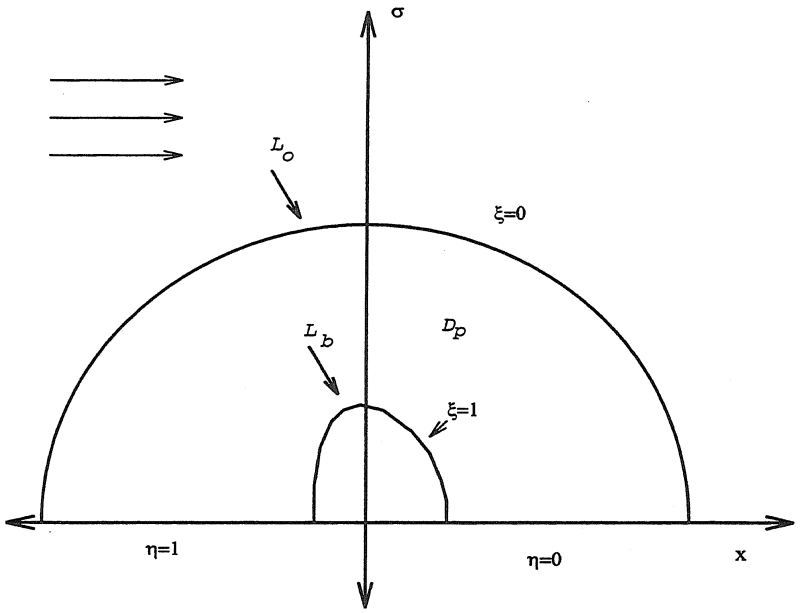

Figure 5.1: Set up of the two-dimensional bubble problem.

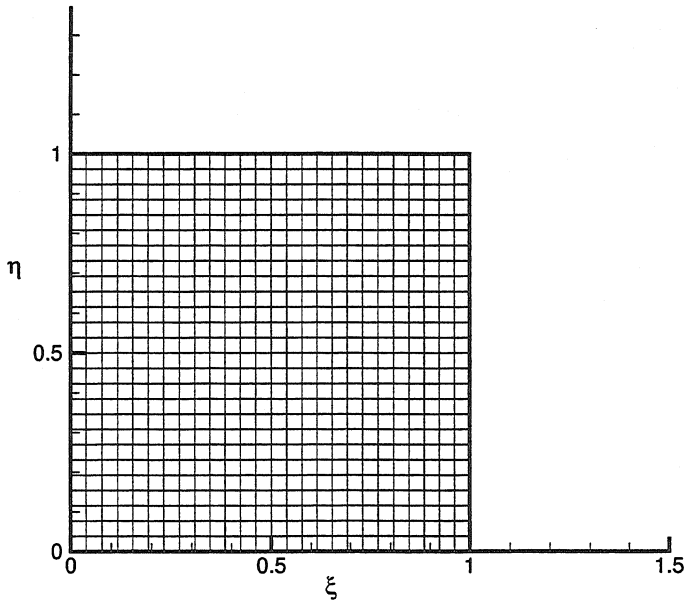

Figure 5.2: Curvilinear space (ξ, η).

is the Reynolds number derived from nondimensionalization. ρ is the density of the outer fluid, U is the velocity of the free stream, μ is the viscosity, and r_e is the effective radius of the bubble so that the area of the bubble is equal to πr_e^2. The scale factors h_ξ and h_η associated with our curvilinear coordinate system are

$$\begin{aligned} h_\xi &= \sqrt{\left(\frac{\partial x}{\partial \xi}\right)^2 + \left(\frac{\partial \sigma}{\partial \xi}\right)^2}, \\ h_\eta &= \sqrt{\left(\frac{\partial x}{\partial \eta}\right)^2 + \left(\frac{\partial \sigma}{\partial \eta}\right)^2}. \end{aligned}$$

We next address the boundary conditions. At $\xi = 0$, the flow along the outer boundary L_o as shown in Figure 5.1 is far away from the bubble and can, therefore, be approximated by the free-stream flow. This is done by imposing

$$u_x|_{\xi=0} = (\hat{\mathbf{x}} \cdot \mathbf{u})_{\xi=0} = 1.$$

Using the definition of the velocity components (5.1), we can see that this is equivalent to imposing

$$\psi = \sigma$$

at $\xi = 0$. So, we let

$$\psi = \tilde{\psi} + \sigma(1 - \xi^2)$$

so that $\psi = \sigma$ at $\xi = 0$ and $\psi = 0$ at $\xi = 1$. This also allows us to set

$$\omega(0, \eta) = 0.$$

We also require that the flow is symmetric about the $x-$axis. Therefore, along $\eta = 0$ and $\eta = 1$,

$$\begin{aligned} \tilde{\psi}(\xi, 0) &= 0, \\ \tilde{\psi}(\xi, 1) &= 0, \\ \omega(\xi, 0) &= 0, \end{aligned}$$

$$\omega(\xi,1) \;=\; 0.$$

Along $\xi = 1$ which corresponds to the interface of the bubble, since the flow is steady,

$$\tilde{\psi}(1,\eta) = 0.$$

In addition, the continuity of stress condition is imposed [7]. This boundary condition is expressed by

$$\hat{\mathbf{n}} \cdot \mathbf{T} = \frac{4}{W} (\nabla \cdot \hat{\mathbf{n}})\, \hat{\mathbf{n}} \tag{5.4}$$

where $\hat{\mathbf{n}}$ is a unit vector normal to the surface of the bubble, $\mathbf{T}$ is the stress tensor associated with the flow, and W is the Weber number defined by

$$W = \frac{\rho U^2 2 r_e}{\tau}$$

where τ is the surface tension coefficient. Rewriting (5.4) in (ξ,η) coordinates gives two boundary conditions that must to be satisfied, assuming steady and symmetric flow.

The first is the free-slip, or zero shear stress, condition which is imposed along $\xi = 1$ via the expression

$$e_{\xi\eta}|_{\xi=1} = \left[-\frac{h_\eta}{2h_\xi} \frac{\partial}{\partial \xi} \left(\frac{u_\eta}{h_\eta} \right) - \frac{h_\xi}{2h_\eta} \frac{\partial}{\partial \eta} \left(\frac{u_\xi}{h_\xi} \right) \right]_{\xi=1} = 0. \tag{5.5}$$

The second boundary condition is the normal stress condition which accounts for the balance of the pressure and viscous forces of the outer flow with the surface tension forces along the interface of the bubble. In our curvilinear coordinates, the condition takes the form

$$\left(-p + K + \frac{8}{R} e_{\xi\xi} \right)_{\xi=1} = \frac{4}{W} \left(-\frac{1}{h_\xi h_\eta} \frac{\partial h_\eta}{\partial \xi} \right)_{\xi=1} \tag{5.6}$$

where

$$p \;=\; \frac{2}{\pi} C_D x - u_\eta^2 - \frac{4}{R} \int_0^\eta \frac{h_\eta}{h_\xi} \frac{\partial \omega}{\partial \xi} d\eta',$$

$$e_{\xi\xi} = \frac{1}{h_\xi}\frac{\partial u_\xi}{\partial \xi} + \frac{u_\eta}{h_\xi h_\eta}\frac{\partial h_\xi}{\partial \eta},$$
$$C_D = \int_0^1 \left(u_\eta^2 \frac{\partial \sigma}{\partial \eta} - \frac{4}{R}\frac{\sigma h_\eta}{h_\xi}\frac{\partial \omega}{\partial \xi} + \frac{8}{R} e_{\xi\xi}\frac{\partial \sigma}{\partial \eta} \right)_{\xi=1} d\eta.$$

Here, K is a constant of integration associated with the pressure and is determined by enforcing the volume of the bubble to remain π. In (ξ, η) coordinates, the volume of the bubble is determined by

$$Vol = -2\int_0^1 \left(\sigma \frac{\partial x}{\partial \eta} \right)_{\xi=1} d\eta. \tag{5.7}$$

5.3 Numerical method

Given the problem as defined above, we next discuss our approach to numerically solving the equations (5.2) and (5.3) with the boundary conditions (5.5), (5.6), and (5.7). We list below the algorithm applied here.

1. We want to compute the stream function ψ and vorticity ω for a given R and W. We use a previously computed solution, for example a flow past a circular bubble, as the initial condition.

2. Given ψ and ω, a new boundary shape is determined in order to satisfy the normal stress condition (5.6). This is done by using linear perturbation and the minimization technique covered in detail below.

3. Given the new boundary shape, a new grid that fits around the new shape is then determined. This new grid is determined using the grid generation method developed in Chapter 4.

4. Over the new grid, the flow equations (5.2) and (5.3) are solved along with the free-slip boundary condition (5.5). This is done using Newton's method in a way similar to that used to compute steady solutions in previous chapters.

5. With the new ψ and ω, steps (2)-(4) are repeated until they all converge to some steady state. In practice, the normal stress condition (5.6) ends up minimized

to be around $O(10^{-2})$ for a grid of 70x70 resolution. In a later section, we show that this can be improved with higher resolution.

5.3.1 Prediction of new boundary shape

Here the method of predicting a new boundary shape is discussed. First, the current iteration values of ψ and ω do not satisfy the normal stress condition (5.6). The shape of the bubble must be deformed in such a way so that the deviation of the normal stress from zero can be minimized. In other words, (5.6) has to be satisfied on some curve $\xi = 1 + \delta(\eta)$ such that

$$\left(-p + K + \frac{8}{R}e_{\xi\xi}\right)_{\xi=1+\delta(\eta)} - \frac{4}{W}\left(-\frac{1}{h_\xi h_\eta}\frac{\partial}{\partial\xi}h_\eta\right)_{\xi=1+\delta(\eta)} = 0. \tag{5.8}$$

It is assumed here that $|\delta(\eta)| << 1$ which implies that the new shape of the bubble is a small perturbation away from the current bubble shape. Linearizing the equation (5.8) gives, at $\xi = 1$,

$$T_0 + T_1\frac{\partial^2}{\partial\eta^2}\delta(\eta) + T_2\frac{\partial}{\partial\eta}\delta(\eta) + T_3\delta(\eta) + K = 0 \tag{5.9}$$

where

$$\begin{aligned}
T_0 &= \left(-p + \frac{8}{R}e_{\xi\xi}\right)_{\xi=1} - \frac{4}{W}\left(-\frac{1}{h_\xi h_\eta}\frac{\partial h_\eta}{\partial\xi}\right)_{\xi=1}, \\
T_1 &= \frac{-4}{W}\left(\frac{h_\xi}{h_\eta^2}\right), \\
T_2 &= \frac{4}{W}\left(\frac{-2}{h_\eta^2}\frac{\partial h_\xi}{\partial\eta} + \frac{h_\xi}{h_\eta^3}\frac{\partial h_\eta}{\partial\eta}\right), \\
T_3 &= -\frac{\partial p}{\partial\xi} + \frac{8}{R}\left[u_\eta\left(\frac{-1}{h_\eta h_\xi^2}\frac{\partial h_\xi}{\partial\eta}\frac{\partial h_\xi}{\partial\xi} - \frac{1}{h_\xi h_\eta^2}\frac{\partial h_\xi}{\partial\eta}\frac{\partial h_\eta}{\partial\xi} + \frac{1}{h_\xi h_\eta}\frac{\partial^2 h_\xi}{\partial\xi\partial\eta}\right)\right] \\
&\quad + \frac{8}{R}\left(\frac{-1}{h_\xi^2}\frac{\partial u_\xi}{\partial\xi}\frac{\partial h_\xi}{\partial\xi} + \frac{1}{h_\xi h_\eta}\frac{\partial u_\eta}{\partial\xi}\frac{\partial h_\xi}{\partial\eta} + \frac{1}{h_\xi}\frac{\partial^2 u_\xi}{\partial\xi^2}\right) \\
&\quad + \frac{4}{W}\left[\frac{-1}{h_\xi^2 h_\eta}\frac{\partial h_\eta}{\partial\xi}\frac{\partial h_\xi}{\partial\xi} - \frac{1}{h_\xi}\left(\frac{1}{h_\eta^2}\frac{\partial h_\eta}{\partial\xi}\right)^2 + \frac{1}{h_\xi h_\eta}\frac{\partial^2 h_\eta}{\partial\xi^2}\right].
\end{aligned}$$

The volume equation (5.7) is also linearized to give

$$\int_0^1 2\left(\sigma\frac{\partial x}{\partial \eta}\right)_{\xi=1} d\eta + \pi + \int_0^1 \delta(\eta)\left(2\sigma\frac{\partial^2 x}{\partial\xi\partial\eta} + 2\frac{\partial\sigma}{\partial\xi}\frac{\partial x}{\partial\eta}\right)_{\xi=1} d\eta = 0. \tag{5.10}$$

In addition, the new shape of the bubble has to be constrained so that it stays fixed relative to the origin. To accomplish this, the centroid condition is imposed to give

$$\int_0^1 2\left(x\sigma\frac{\partial x}{\partial \eta}\right)_{\xi=1} d\eta + \int_0^1 \delta(\eta)\left[2x\sigma\frac{\partial^2 x}{\partial\xi\partial\eta} + 2\left(x\frac{\partial\sigma}{\partial\xi} + \frac{\partial x}{\partial\xi}\sigma\right)\frac{\partial x}{\partial\eta}\right]_{\xi=1} d\eta = 0. \tag{5.11}$$

Second-order, centered, finite differences are applied to approximate the derivatives of $\delta(\eta)$. Let $\eta = j\Delta x, j = 0, ..., m+1$ with $\Delta x = \frac{1}{m+1}$ and $\delta(\eta) = \delta(j\Delta x) = \delta_j$. This gives

$$H_{N_j} = T_0 + T_{C_1}\delta_{j-1} + T_{C_2}\delta_j + T_{C_3}\delta_{j+1} + K \tag{5.12}$$

where

$$\begin{aligned} T_{C_1} &= \frac{T_1}{\Delta x^2} - \frac{T_2}{2\Delta x}, \\ T_{C_2} &= \frac{-2T_1}{\Delta x^2} + T_3, \\ T_{C_3} &= \frac{T_1}{\Delta x^2} + \frac{T_2}{2\Delta x}. \end{aligned}$$

We then use the trapezoidal integration rule on the equations (5.10) and (5.11) to obtain

$$V_p = v_0 + \sum_{j=1}^{m} \delta_j v_j$$

where

$$\begin{aligned} v_0 &= \int_0^1 2\left(\sigma\frac{\partial x}{\partial \eta}\right)_{\xi=1} d\eta + \pi, \\ v_j &= \left(2\sigma\frac{\partial^2 x}{\partial\xi\partial\eta} + 2\frac{\partial\sigma}{\partial\xi}\frac{\partial x}{\partial\eta}\right)_{\xi=1,\eta=j\Delta x}; \end{aligned}$$

and

$$C_p = c_0 + \sum_{j=1}^{m} \delta_j c_j$$

where

$$\begin{aligned} c_0 &= \int_0^1 2\left(x\sigma\frac{\partial x}{\partial \eta}\right)_{\xi=1} d\eta, \\ c_j &= \left[2x\sigma\frac{\partial^2 x}{\partial\xi\partial\eta} + 2\left(x\frac{\partial\sigma}{\partial\xi} + \sigma\frac{\partial x}{\partial\xi}\right)\frac{\partial x}{\partial\eta}\right]_{\xi=1,\eta=j\Delta x}. \end{aligned}$$

We also define the term Ω by

$$\Omega = \sum_{j=0}^{m+1} \left(H_{N_j}\right)^2.$$

The unknowns are δ_j, $j = 0, ..., m+1$ and K. We want to minimize Ω subject to the constraints $V_p = 0$ and $C_p = 0$. To do this, we apply the method of Lagrange multipliers. Let

$$\Pi = \Omega + \lambda_0 V_p + \lambda_1 C_p.$$

Then, define a system of equations $\mathbf{G}$ composed of

$$\mathbf{G} = \begin{bmatrix} \frac{\partial}{\partial\delta_j}\Pi, j = 0, ..., m+1 \\ \frac{\partial}{\partial K}\Pi \\ \frac{\partial}{\partial\lambda_0}\Pi \\ \frac{\partial}{\partial\lambda_1}\Pi. \end{bmatrix}.$$

This system is then solved using Newton's method. In practice it usually takes just one iteration to obtain a converged solution. With δ_j determined, the new, predicted boundary shape of the bubble becomes

$$\begin{aligned} x^{new}(1, j\Delta x) &= x_j^{old}(1, j\Delta x) + \delta_j \frac{\partial}{\partial\xi} x^{old}(1, j\Delta x), \\ \sigma^{new}(1, j\Delta x) &= \sigma_j^{old}(1, j\Delta x) + \delta_j \frac{\partial}{\partial\xi} \sigma^{old}(1, j\Delta x). \end{aligned}$$

5.3.2 Outer flow solver

Given a grid system fitted around the upper half of a symmetric body, the Navier-Stokes equations (5.2) and (5.3) have to be solved along with the free-slip boundary condition (5.5). First, we rewrite the flow equations (5.2) and (5.3) in a more manageable form to get

$$q_{\omega 1}\frac{\partial^2\omega}{\partial\xi^2}+q_{\omega 2}\frac{\partial^2\omega}{\partial\eta^2}+q_{\omega 3}\frac{\partial\omega}{\partial\xi}+q_{\omega 4}\frac{\partial\omega}{\partial\eta}=0 \tag{5.13}$$

where

$$\begin{aligned}
q_{\omega 1} &= -\frac{2}{R}\frac{1}{h_\xi},\\
q_{\omega 2} &= -\frac{2}{R}\frac{1}{h_\eta},\\
q_{\omega 3} &= \frac{2}{R}\left(\frac{1}{h_\xi^3}\frac{\partial h_\xi}{\partial\xi}-\frac{1}{h_\eta h_\xi^2}\frac{\partial h_\eta}{\partial\xi}\right)-(1-\xi^2)\frac{1}{h_\eta h_\xi}\frac{\partial\sigma}{\partial\eta}-\frac{1}{h_\eta h_\xi}\frac{\partial\tilde{\psi}}{\partial\eta},\\
q_{\omega 4} &= \frac{2}{R}\left(\frac{1}{h_\eta^3}\frac{\partial h_\eta}{\partial\eta}-\frac{1}{h_\xi h_\eta^2}\frac{\partial h_\xi}{\partial\eta}\right)+(1-\xi^2)\frac{1}{h_\eta h_\xi}\frac{\partial\sigma}{\partial\xi}\\
&\quad+\frac{1}{h_\eta h_\xi}\frac{\partial\tilde{\psi}}{\partial\xi}-\frac{2\xi\sigma}{h_\eta h_\xi};
\end{aligned}$$

and

$$q_{\psi 1}\frac{\partial^2\tilde{\psi}}{\partial\xi^2}+q_{\psi 2}\frac{\partial^2\tilde{\psi}}{\partial\eta^2}+q_{\psi 3}\frac{\partial\tilde{\psi}}{\partial\xi}+q_{\psi 4}\frac{\partial\tilde{\psi}}{\partial\eta}+\omega+q_{\psi 5}=0 \tag{5.14}$$

where

$$\begin{aligned}
q_{\psi 1} &= \frac{1}{h_\xi^2},\\
q_{\psi 2} &= \frac{1}{h_\eta^2},\\
q_{\psi 3} &= \frac{1}{h_\xi^2 h_\eta}\frac{\partial h_\eta}{\partial\xi}-\frac{1}{h_\xi^3}\frac{\partial h_\xi}{\partial\xi},\\
q_{\psi 4} &= \frac{1}{h_\xi h_\eta^2}\frac{\partial h_\xi}{\partial\eta}-\frac{1}{h_\eta^3}\frac{\partial h_\eta}{\partial\eta},\\
q_{\psi 5} &= \sigma\left(\frac{-2\xi}{h_\xi^2 h_\eta}\frac{\partial h_\eta}{\partial\xi}+\frac{2\xi}{h_\xi^3}\frac{\partial h_\xi}{\partial\xi}-\frac{2}{h_\xi^2}\right)-\frac{4\xi}{h_\xi^2}\frac{\partial\sigma}{\partial\xi}.
\end{aligned}$$

The numerical approach taken is the same as the one used to solve for the steady solutions for flow past an ellipsoidal bubble of fixed shape in Chapter 3. That is, the unknowns $\omega(\xi,\eta) = \omega(i\Delta x, j\Delta x) = \omega_{i,j}$ and $\tilde{\psi} = \tilde{\psi}(i\Delta x, j\Delta x) = \tilde{\psi}_{i,j}$ with $\Delta x = \frac{1}{m+1}$ are discretized using second-order, centered, finite differences, and the discretized equations are solved as a system of equations using Newton's method. Discretizing the equation (5.13) gives

$$H_{0_{i,j}} = A^0_{i,j}\omega_{i-1,j} + A^1_{i,j}\omega_{i,j-1} + A^2_{i,j}\omega_{i,j} + A^3_{i,j}\omega_{i,j+1} + A^4_{i,j}\omega_{i+1,j}, \tag{5.15}$$

where

$$\begin{aligned}
A^0_{i,j} &= \frac{-1}{2}\frac{q_{\omega 3}}{\Delta x} + \frac{q_{\omega 1}}{(\Delta x)^2}, \\
A^1_{i,j} &= \frac{q_{\omega 2}}{(\Delta x)^2} - \frac{1}{2}\frac{q_{\omega 4}}{\Delta x}, \\
A^2_{i,j} &= -2\frac{q_{\omega 2}}{(\Delta x)^2} - 2\frac{q_{\omega 1}}{(\Delta x)^2}, \\
A^3_{i,j} &= \frac{q_{\omega 2}}{(\Delta x)^2} + \frac{1}{2}\frac{q_{\omega 4}}{\Delta x}, \\
A^4_{i,j} &= \frac{1}{2}\frac{q_{\omega 3}}{\Delta x} + \frac{q_{\omega 1}}{(\Delta x)^2};
\end{aligned}$$

and discretizing the equation (5.14) gives

$$\begin{aligned}
H_{1_{i,j}} &= B^0_{i,j}\tilde{\psi}_{i-1,j} + B^1_{i,j}\tilde{\psi}_{i,j-1} + B^2_{i,j}\tilde{\psi}_{i,j} + B^3_{i,j}\tilde{\psi}_{i,j+1} \\
&\quad + B^4_{i,j}\tilde{\psi}_{i+1,j} + B^5_{i,j}\omega_{i,j} + B^6_{i,j},
\end{aligned} \tag{5.16}$$

where

$$\begin{aligned}
B^0_{i,j} &= \frac{-1}{2}\frac{q_{\psi 3}}{\Delta x} + \frac{q_{\psi 1}}{(\Delta x)^2}, \\
B^1_{i,j} &= \frac{q_{\psi 2}}{(\Delta x)^2} - \frac{1}{2}\frac{q_{\psi 4}}{\Delta x}, \\
B^2_{i,j} &= -2\frac{q_{\psi 2}}{(\Delta x)^2} - 2\frac{q_{\psi 1}}{(\Delta x)^2},
\end{aligned}$$

$$
\begin{aligned}
B^3_{i,j} &= \frac{q_{\psi 2}}{(\Delta x)^2} + \frac{1}{2}\frac{q_{\psi 4}}{\Delta x}, \\
B^4_{i,j} &= \frac{1}{2}\frac{q_{\psi 3}}{\Delta x} + \frac{q_{\psi 1}}{(\Delta x)^2}, \\
B^5_{i,j} &= 1, \\
B^6_{i,j} &= q_{\psi 5}.
\end{aligned}
$$

Discretizing the free-slip boundary condition (5.5) gives

$$H_{B_j} = D^0_j \tilde{\psi}_{m-2,j} + D^1_j \tilde{\psi}_{m-1,j} + D^2_j \tilde{\psi}_{m,j} + D^3_j \tag{5.17}$$

where

$$
\begin{aligned}
D^0_j &= \frac{-1}{(h_\xi \Delta x)^2}, \\
D^1_j &= \frac{4}{(h_\xi \Delta x)^2} - \frac{1}{2h^3_\xi \Delta x}\frac{\partial h_\xi}{\partial \xi} - \frac{1}{2h^2_\xi h_\eta \Delta x}\frac{\partial h_\eta}{\partial \xi}, \\
D^2_j &= \frac{-5}{(h_\xi \Delta x)^2} + \frac{2}{h^3_\xi \Delta x}\frac{\partial h_\xi}{\partial \xi} + \frac{2}{h^2_\xi h_\eta \Delta x}\frac{\partial h_\eta}{\partial \xi}, \\
D^3_j &= -\frac{2\sigma}{h^2_\xi} - \frac{4}{h^2_\xi}\frac{\partial \sigma}{\partial \xi} + 2\frac{\sigma}{h^3_\xi}\frac{\partial h_\xi}{\partial \xi} + 2\frac{\sigma}{h^2_\xi h_\eta}\frac{\partial h_\eta}{\partial \xi}.
\end{aligned}
$$

The equations (5.15), (5.16), and (5.17) are rearranged to form a system of discretized equations, and Newton's method is used on the system to solve for $\omega_{i,j}$ and $\tilde{\psi}_{i,j}$.

To check that the outer flow solver works properly in the case of a two-dimensional flow, the outer flow solver is used to compute steady flows past a rigid cylinder. To do this, the no-slip boundary condition is imposed at $\xi = 1$, which is expressed by

$$H_{B_j} = D^0_j \tilde{\psi}_{m-1,j} + D^1_j \tilde{\psi}_{m,j} + D^2_j$$

where

$$
\begin{aligned}
D^0_j &= \frac{1}{2\Delta x}, \\
D^1_j &= -\frac{2}{\Delta x},
\end{aligned}
$$

C_D	This work (70x70)	Fornberg [11]	Takami & Keller [41]
$R = 10$	2.82		
20	2.04	2.0001	2.0027
40	1.52	1.4980	1.5359
60	1.30		1.3246
80	1.16		
100	1.07	1.058	

Table 5.1: Drag coefficients for a range of Reynolds numbers for flow past a rigid cylinder.

C_D	$R = 40\ W = 1$	$R = 40\ W = 2$	$R = 80\ W = 1$	$R = 80\ W = 2$
40x40	1.03	1.27	0.70	
60x60	1.02	1.27	0.68	0.93
70x70	1.02	1.27	0.68	0.92
80x80	1.02	1.27	0.67	0.92

Table 5.2: Comparison of the drag coefficients of steady flow past a symmetric, two-dimensional bubble with grids of different resolutions.

$$D_j^2 \;=\; -2\sigma.$$

Table 5.1 shows the drag coefficients of flows past a rigid cylinder at various Reynolds numbers computed using our method and also compares them with previous results. They appear to agree well with one another. Figure 5.3 shows the computed steady solutions, and they appear to agree well with the results of Fornberg [11]. This gives us the confidence that the outer flow solver works properly for two-dimensional flow calculations.

5.4 Numerical results

First, we compute the steady solutions of flow past a symmetric, two-dimensional bubble for $R = 40$, 80 and $W = 1, 2$ using grids of different resolutions to check the convergence of our method. Table 5.2 compares the drag coefficient of the flows computed using grids of different resolutions, and they appear to be in good agreement. In addition, Figure 5.4 shows the stream lines of the flow past a symmetric, two-dimensional bubble for $R = 40$, $W = 2$ computed using our method with grids

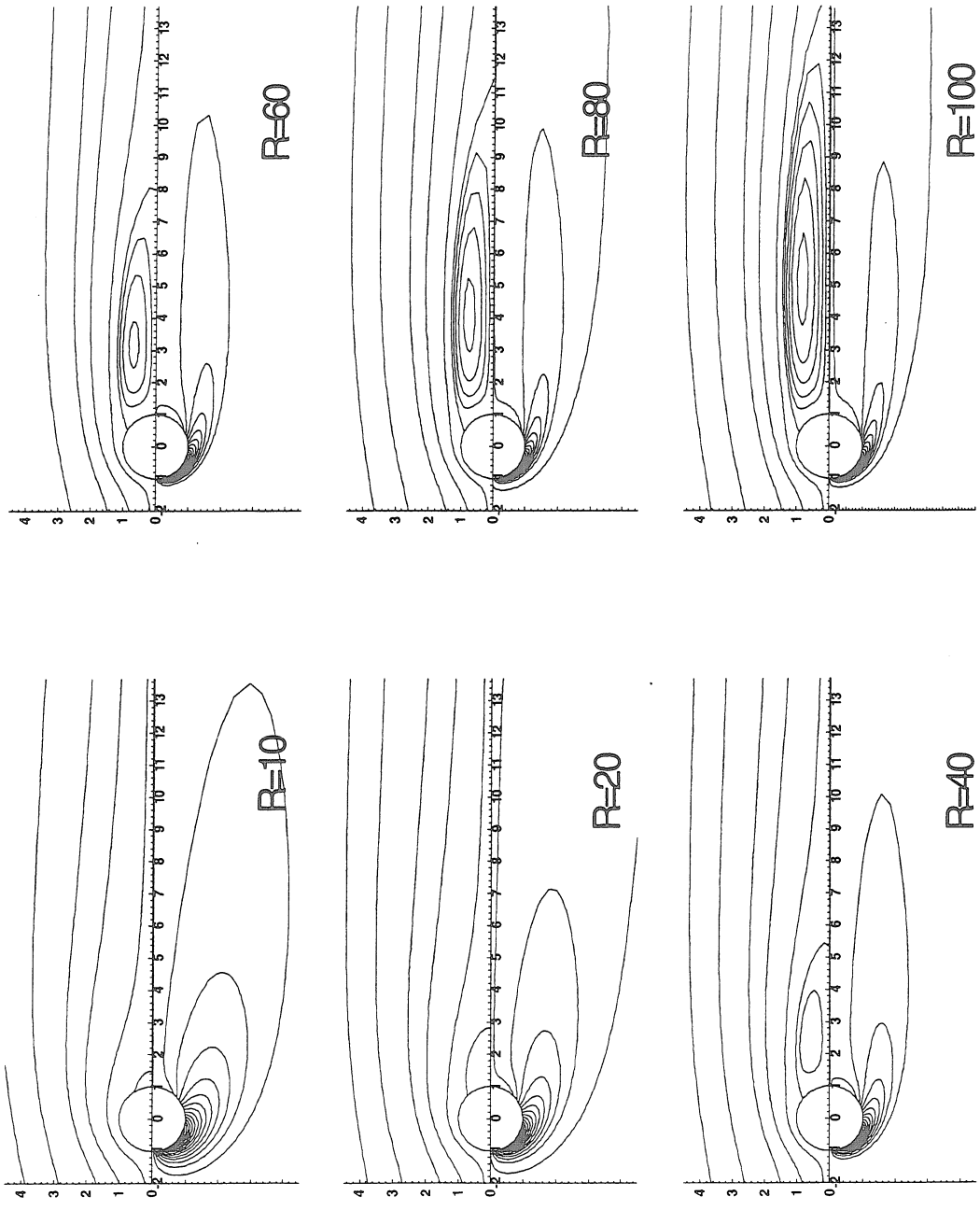

Figure 5.3: Steady flows past a rigid cylinder at $R = 10$, 20, 40, 60, 80, 100. In each case the left side is the stream function, and the right side is the vorticity.

of different resolution. They appear to be in good agreement. This also appears to hold true for $R = 80$, $W = 2$ as shown in Figure 5.5.

Because our method uses minimization of the normal stress condition (5.6) in determining the shape of the bubble, the solutions that are computed using our method are such that the normal stress condition is not fully zeroed out. Figure 5.6 shows how well our computed steady solutions satisfy the normal stress condition (5.6) as the resolution is increased. Let

$$R_{avN} = \frac{1}{m+2} \sum_{j=0}^{m+1} |R_{st}(\eta)|,$$

where

$$R_{st}(\eta) = \left[-p + K + \frac{8}{R} e_{\xi\xi} - \frac{4}{W} \left(-\frac{1}{h_\xi h_\eta} \frac{\partial h_\eta}{\partial \xi} \right) \right]_{\xi=1}.$$

Figure 5.6 compares R_{avN}, which is basically the average of the absolute value of the residual normal stress condition, with respect to the resolution of the grids used in computing the steady solutions for $R = 40$, 80 and $W = 1$, 2. It is clear that in all cases the value of R_{avN} gets smaller as the resolution is increased. This indicates that increasing the grid resolution will give better results. Of course, increasing the resolution also increases the computation time. Therefore, as done in the previous chapter, we use the grid with 70x70 resolution to compute the steady flows past a symmetric, two-dimensional deforming bubble.

Solutions are computed for R up to 120 and W up to 4.5. It takes about 50 minutes on a Sun Ultra workstation to compute each solution. Because the outer flow solver involves solving a large sparse matrix, constructing its LU decomposition takes up most of the computing time. However, the LU decomposition only has to be done once in the beginning of the whole computational loop.

Table 5.3 and Figure 5.7 show the drag coefficients of the flows past a symmetric, two-dimensional bubble computed using our method. It is clear that increasing the Weber number W increases the drag coefficient. This is expected since vorticity on the bubble is dependent on the curvature of the bubble, and increasing W deforms

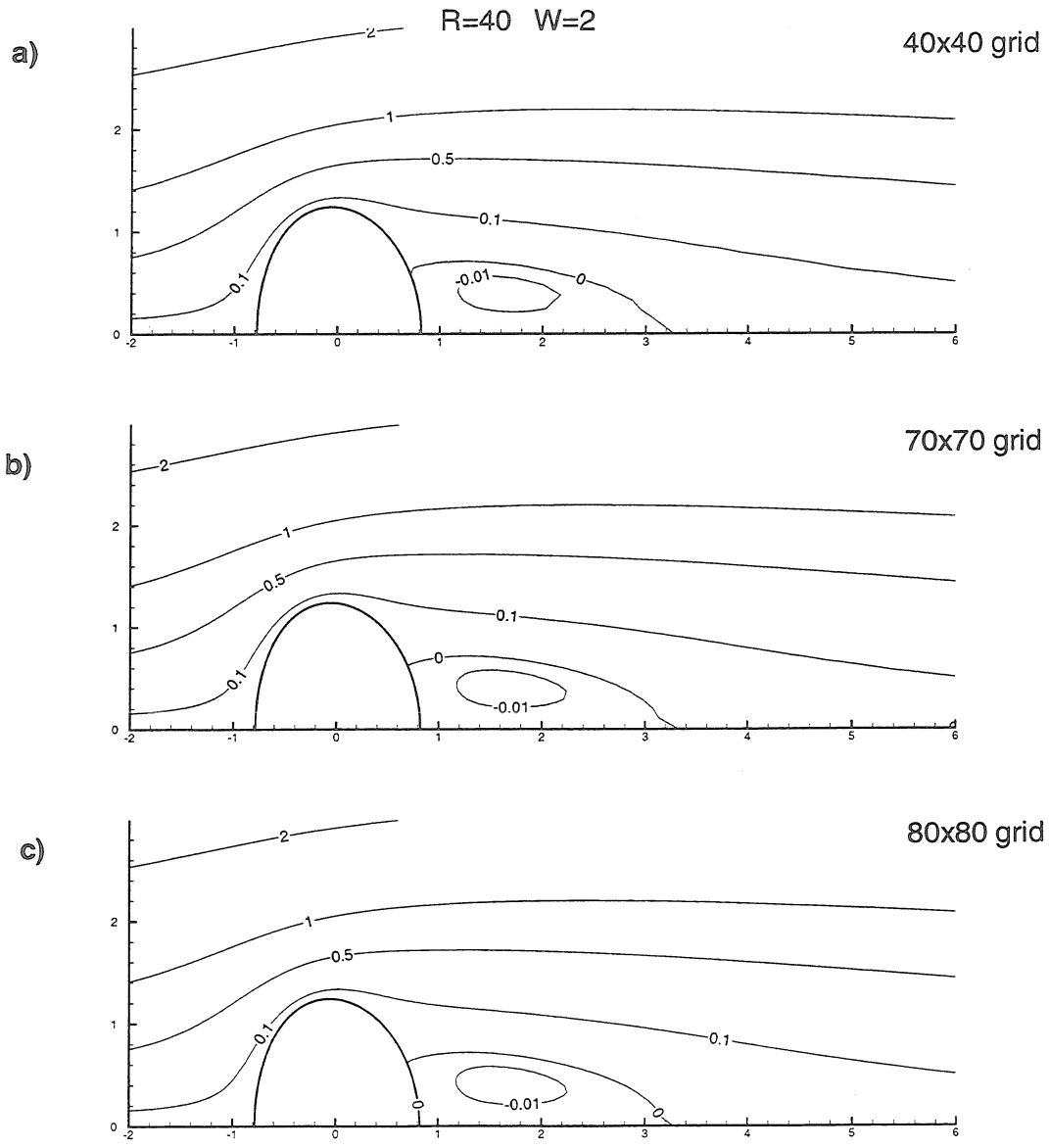

Figure 5.4: Stream lines of flow past a symmetric, two-dimensional bubble at $R = 40$, $W = 2$ computed using grids of resolution a) 40x40, b) 70x70, and c) 80x80.

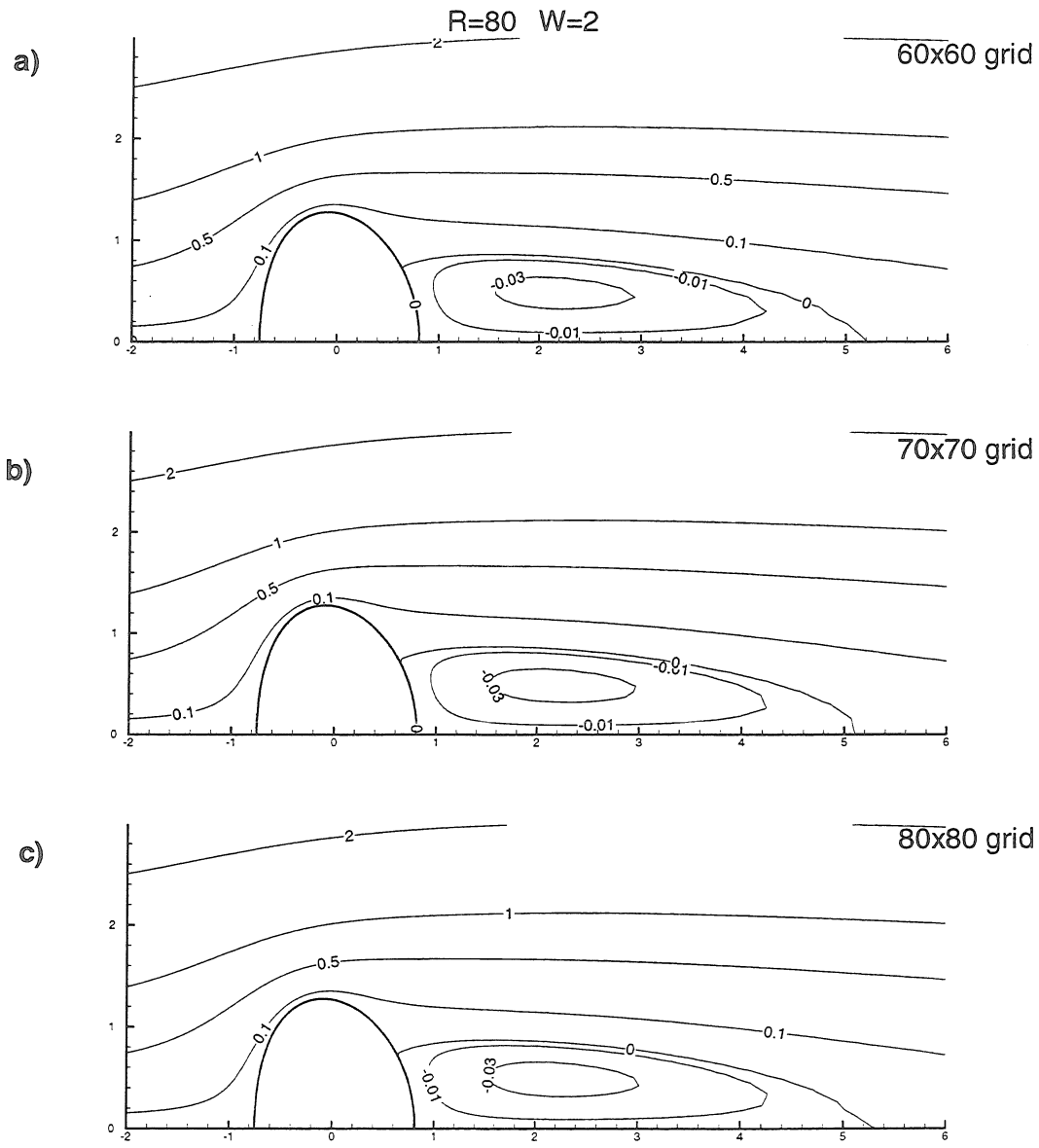

Figure 5.5: Stream lines of flow past a symmetric, two-dimensional bubble at $R = 80$, $W = 2$ computed using grids of resolution a) 60x60, b) 70x70, and c) 80x80.

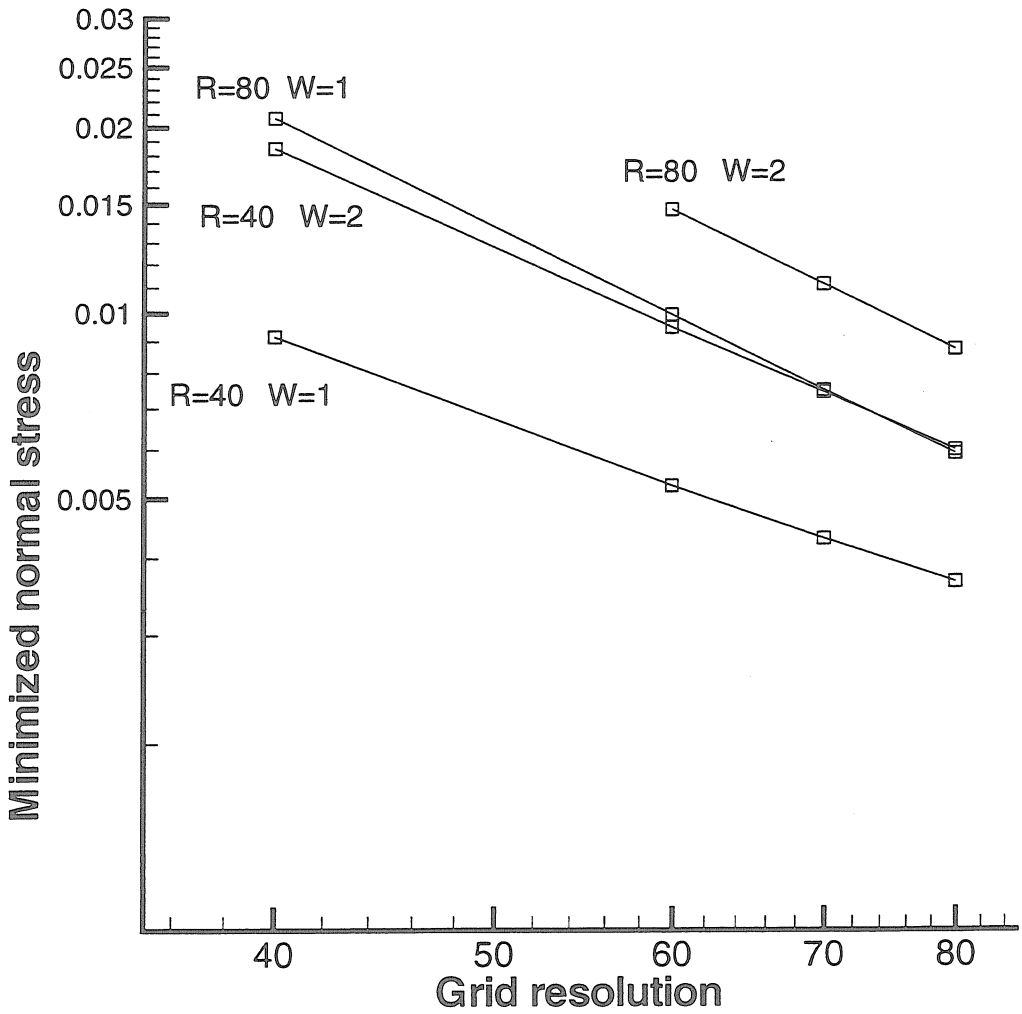

Figure 5.6: Comparison of how well our computed steady solutions satisfy the normal stress condition on the surface of the bubble under different resolutions.

C_D	$W=1$	2	3	3.5	4	4.5
$R=5$	3.35	3.64	3.88	3.98	4.05	4.09
10	2.24	2.50	2.77	2.90	3.03	3.14
20	1.52	1.77	2.04	2.18	2.31	2.45
40	1.02	1.27	1.52	1.65	1.77	1.90
60	0.80	1.05	1.29	1.40	1.51	1.62
80	0.68	0.92	1.15	1.25	1.35	1.46
100	0.59	0.83	1.05	1.15		
120	0.53	0.77	0.98			

Table 5.3: Drag coefficients of flow past a symmetric, two-dimensional bubble.

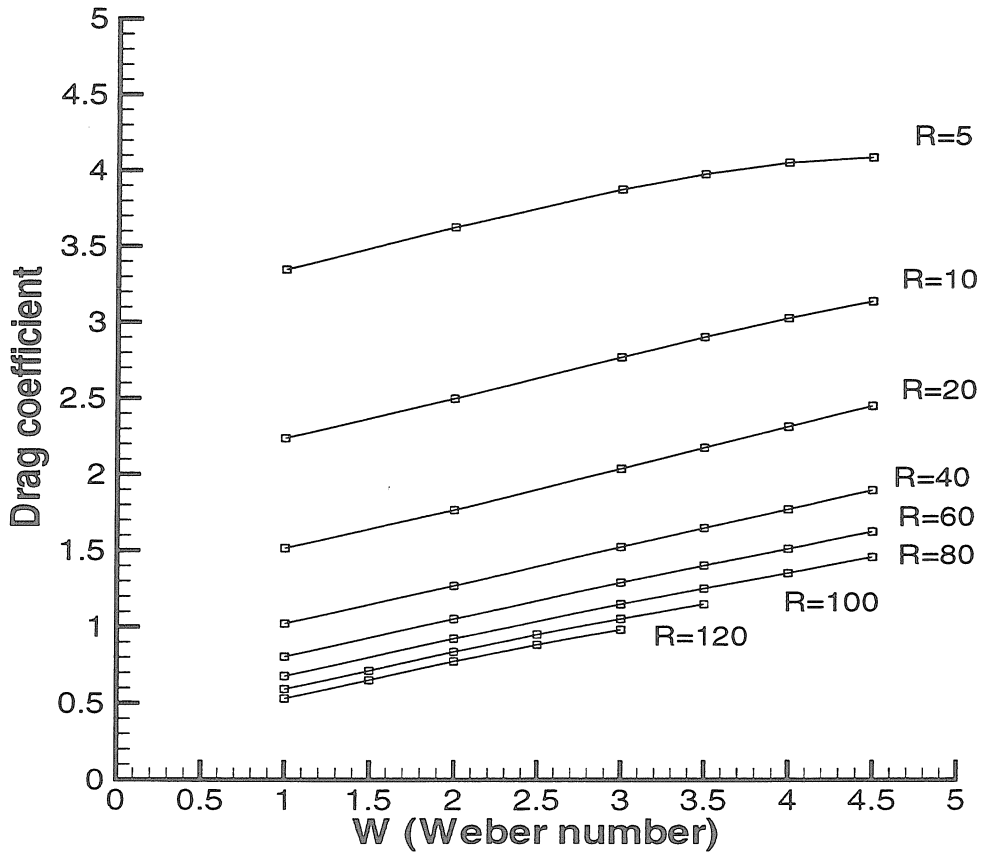

Figure 5.7: Drag coefficients of flow past a symmetric, two-dimensional bubble for various R and W.

the bubble more. As W increases, the corresponding curvilinear grid becomes more distorted, making the computation of outer flow more difficult. So, our steady solutions are limited to $R = 120$ and $W = 4.5$. Still, numerical solutions are obtained for a reasonable range of Reynolds numbers and Weber numbers using our method.

Figures 5.8-5.15 show the steady solutions computed by our method. For low Reynolds numbers, the bubble leans toward the back as the Weber number increases. Figure 5.10 indicates that the bubble deforms to an elliptical shape at $R = 20$. For higher Reynolds numbers, the bubble leans forward as the Weber number increases.

In conclusion, we have developed a numerical method to compute steady, symmetric flows past a deforming, two-dimensional bubble using numerical grid generation. Resolution study indicates that our method is reasonably successful in computing the flow fields.

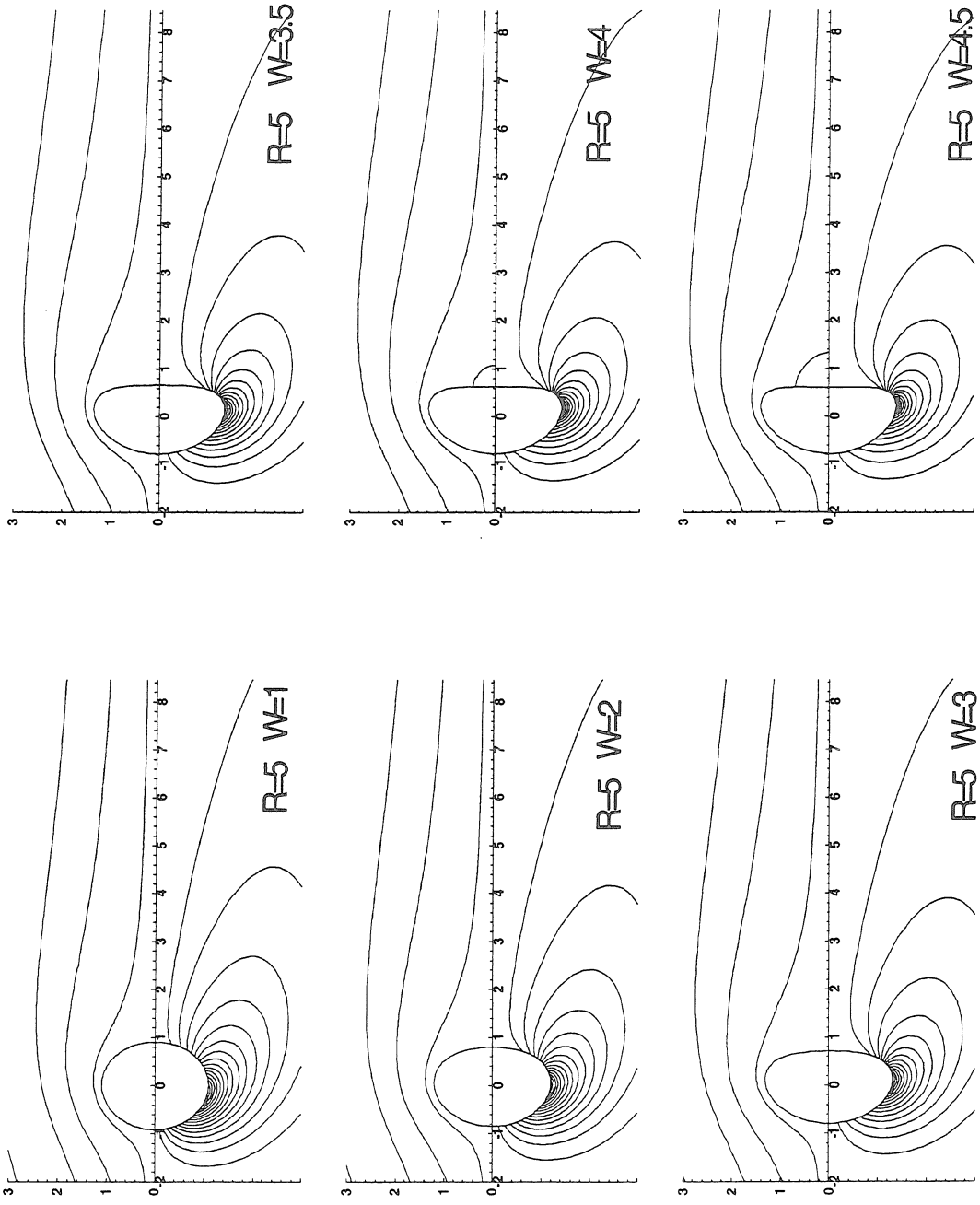

Figure 5.8: Steady flow past a symmetric, two-dimensional bubble at $R = 5$ and $W = 1$, 2, 3, 3.5, 4, 4.5. In each case the left side is the stream function, and the right side is the vorticity.

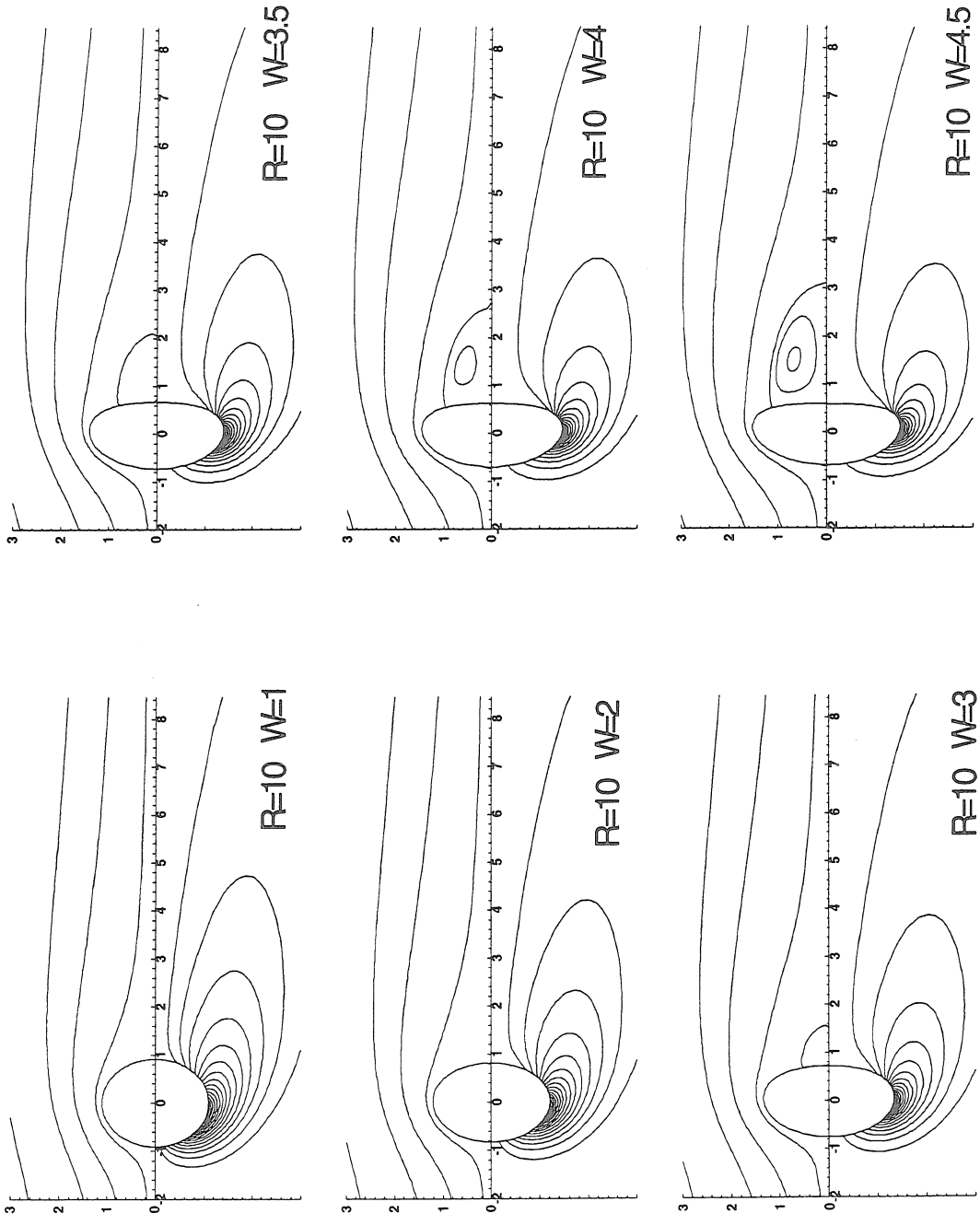

Figure 5.9: Steady flow past a symmetric, two-dimensional bubble at $R = 10$ and $W = 1$, 2, 3, 3.5, 4, 4.5. In each case the left side is the stream function, and the right side is the vorticity.

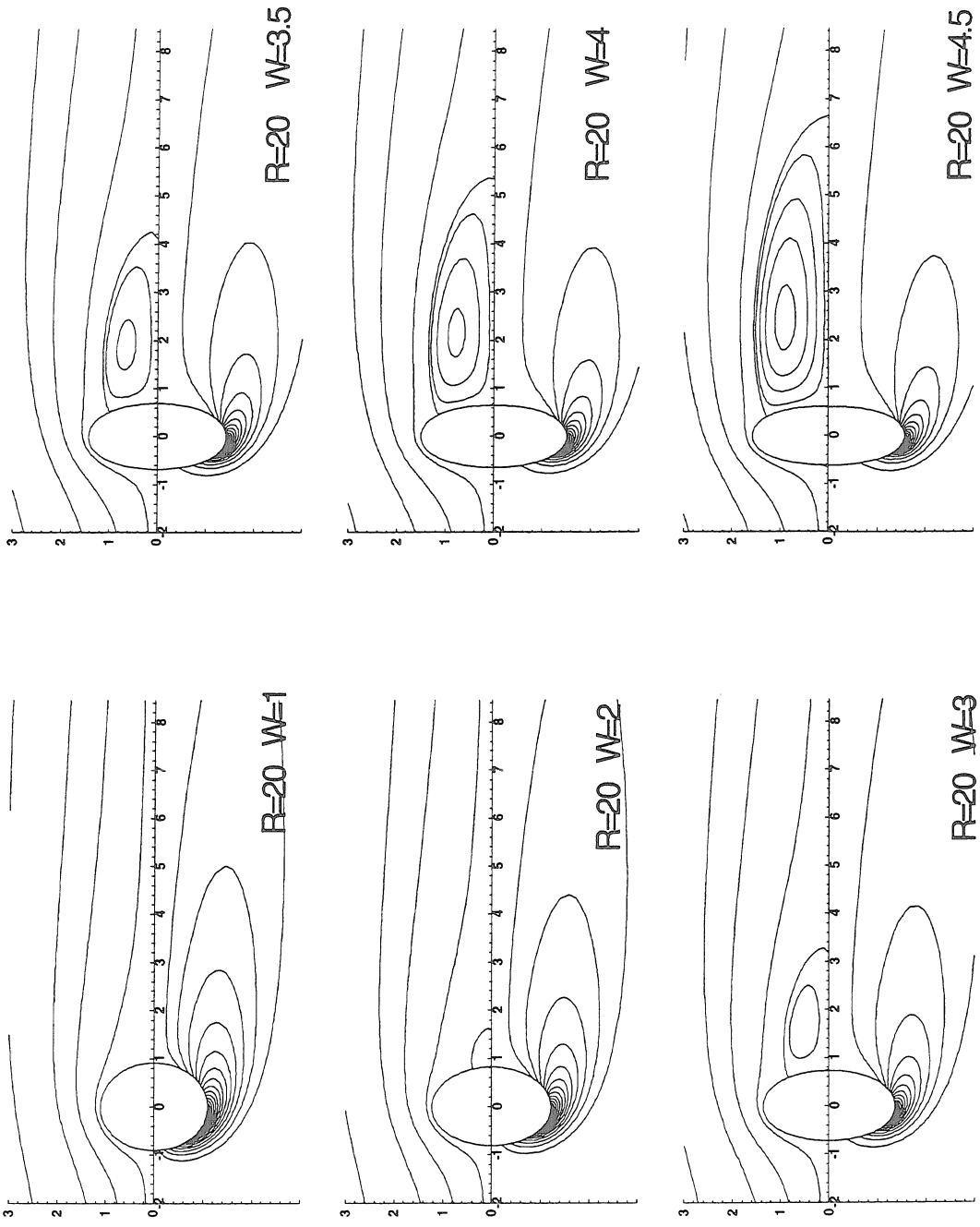

Figure 5.10: Steady flow past a symmetric, two-dimensional bubble at $R = 20$ and $W = 1$, 2, 3, 3.5, 4, 4.5. In each case the left side is the stream function, and the right side is the vorticity.

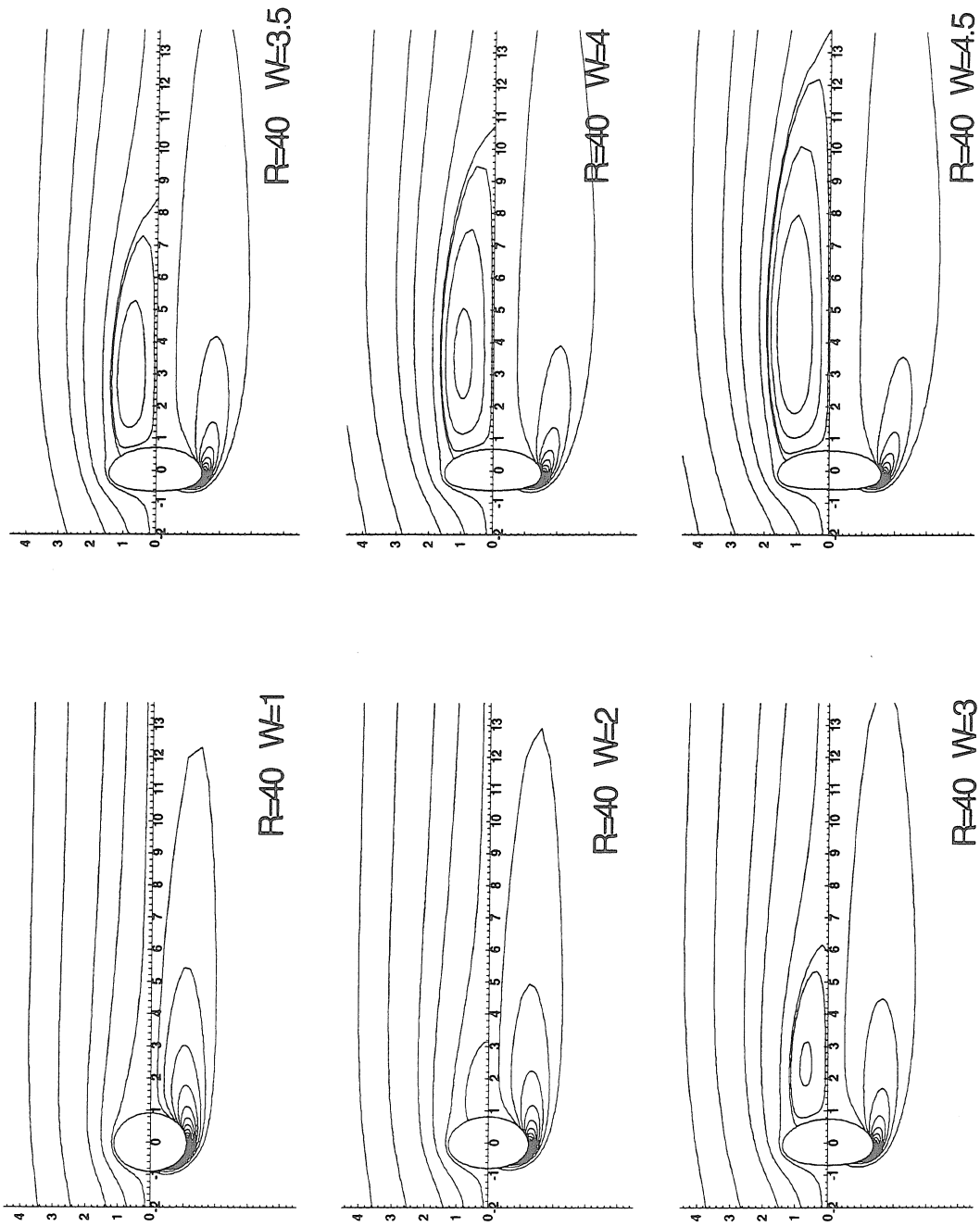

Figure 5.11: Steady flow past a symmetric, two-dimensional bubble at $R = 40$ and $W = 1$, 2, 3, 3.5, 4, 4.5. In each case the left side is the stream function, and the right side is the vorticity.

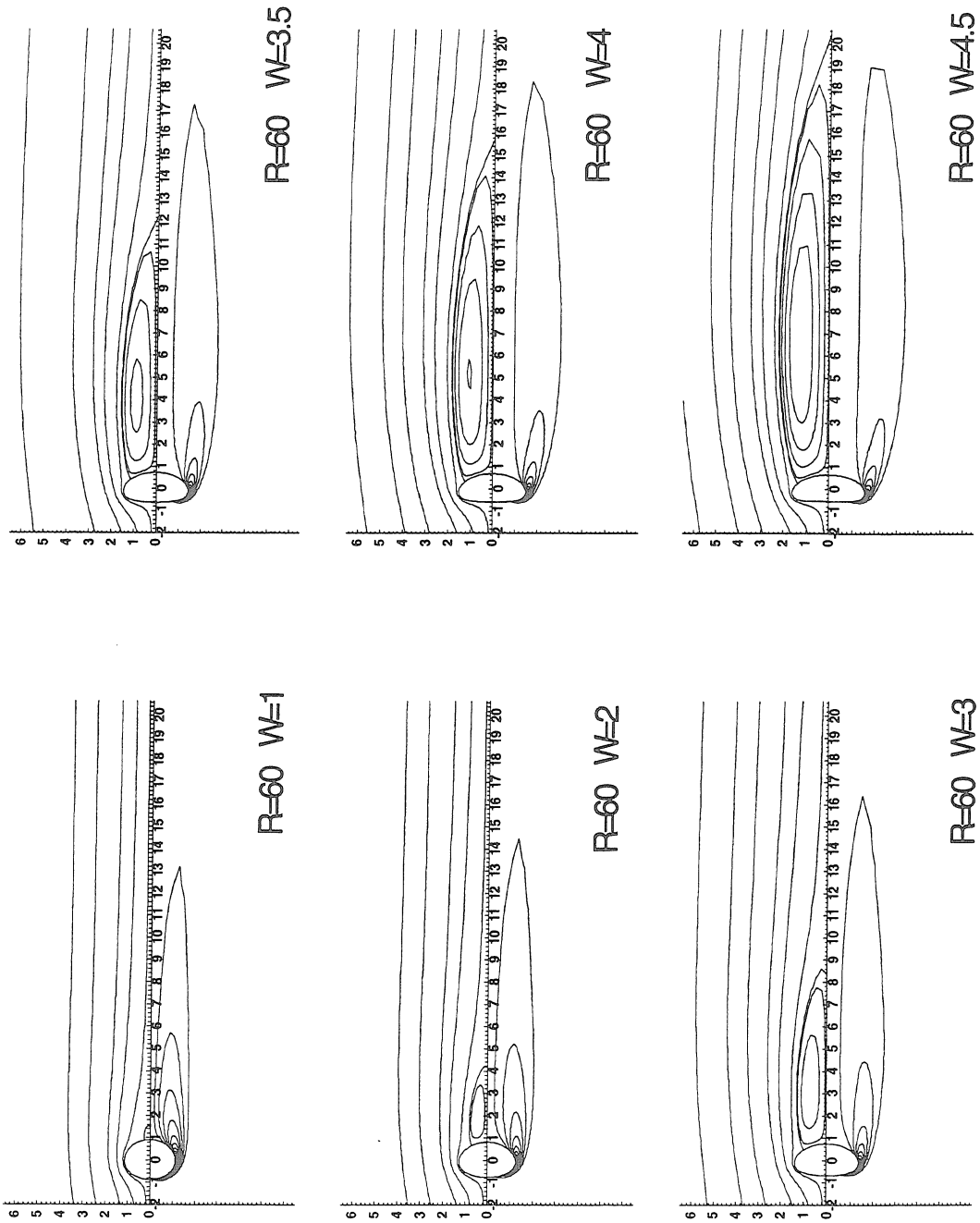

Figure 5.12: Steady flow past a symmetric, two-dimensional bubble at $R = 60$ and $W = 1$, 2, 3, 3.5, 4, 4.5. In each case the left side is the stream function, and the right side is the vorticity.

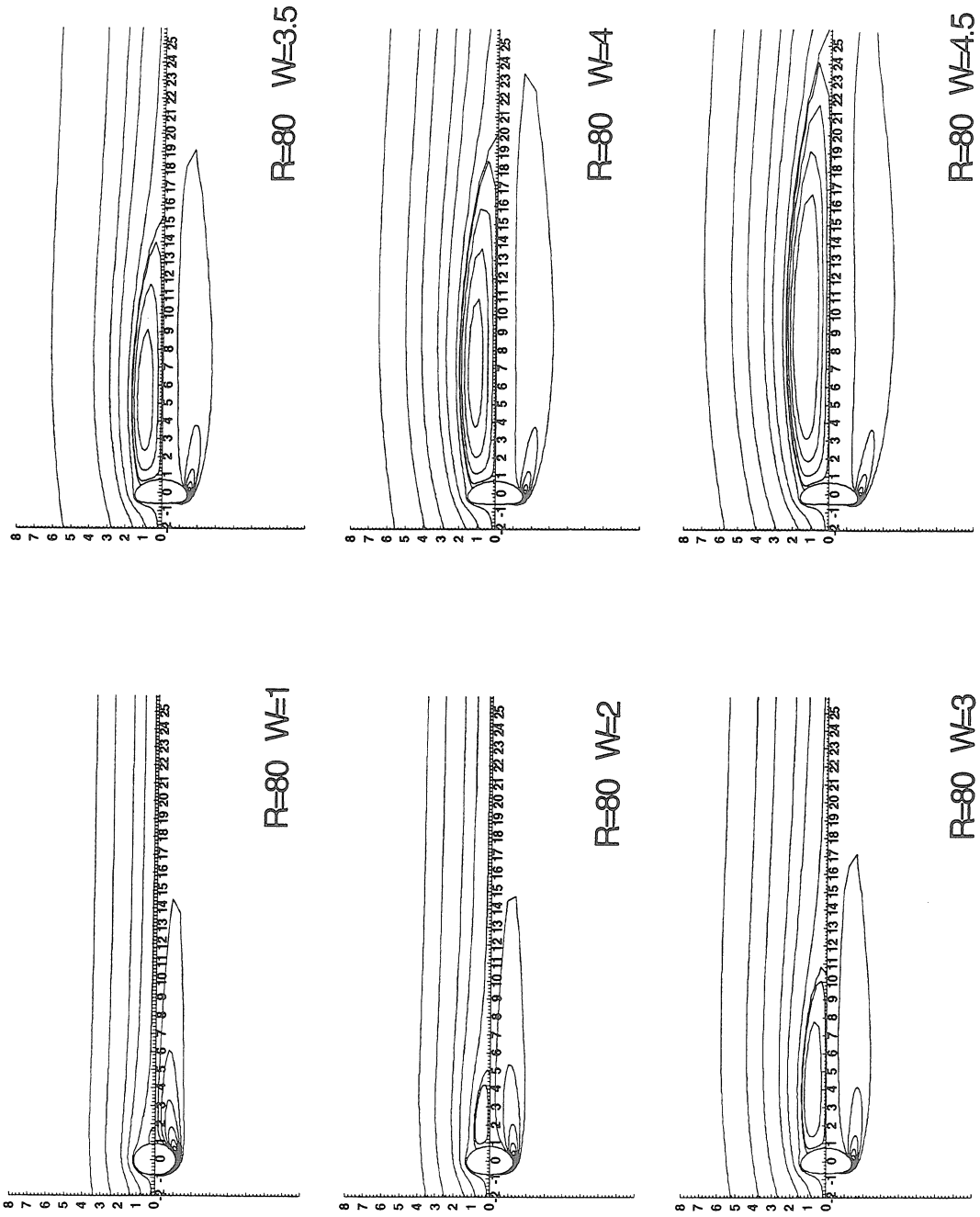

Figure 5.13: Steady flow past a symmetric, two-dimensional bubble at $R = 80$ and $W = 1$, 2, 3, 3.5, 4, 4.5. In each case the left side is the stream function, and the right side is the vorticity.

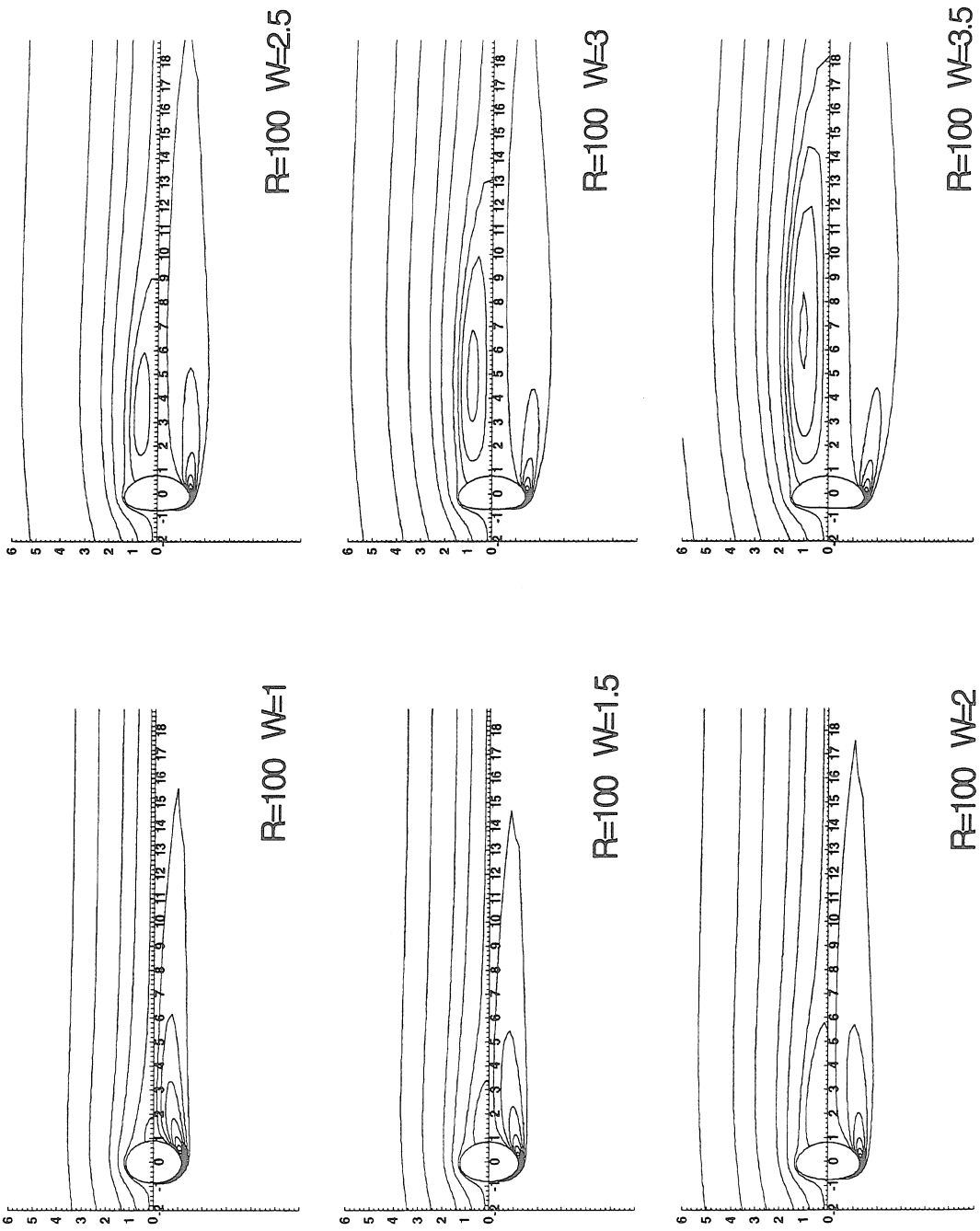

Figure 5.14: Steady flow past a symmetric, two-dimensional bubble at $R = 100$ and $W = 1$, 1.5, 2, 2.5, 3, 3.5. In each case the left side is the stream function, and the right side is the vorticity.

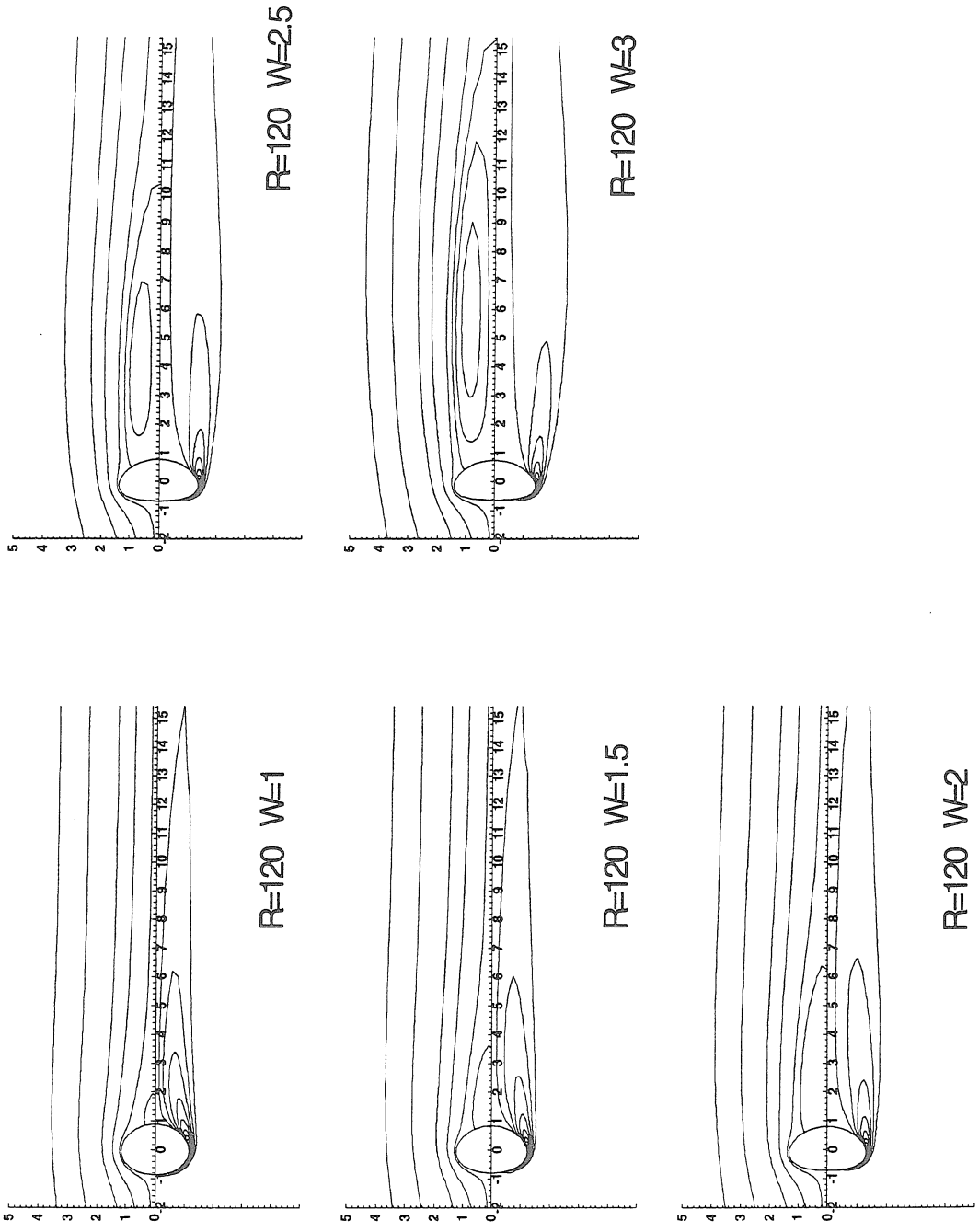

Figure 5.15: Steady flow past a symmetric, two-dimensional bubble at $R = 120$ and $W = 1$, 1.5, 2, 2.5, 3. In each case the left side is the stream function, and the right side is the vorticity.

Chapter 6 Conclusion

In this thesis, we investigated viscous flow past bodies with a no-slip boundary condition and a free-slip boundary condition. We used the numerical grid generation method developed by Ryskin and Leal [33] to compute steady flows past oblate and prolate spheroids and determined the critical Reynolds numbers above which the axisymmetric, steady flow past spheroids become unstable using a linear stability analysis. We then computed the steady flows past ellipsoidal bubbles of fixed shape and applied the linear stability analysis to study their instability as well. We also developed an alternative method in computing viscous, steady flow past axisymmetric, deforming bubbles and symmetric, two-dimensional bubbles.

One of the more interesting extensions that can be performed based on our work is the investigation of the path instability of a rising bubble. It is possible to adapt the linear stability analysis method used in Chapters 2 and 3 with the steady flow computed for deforming bubble in Chapter 4 to investigate such instability. However, in addition to perturbing the flow field, the interface of the bubble has to be perturbed as well. The continuity of stress condition

$$\hat{\mathbf{n}} \cdot \mathbf{T} = \frac{4}{W} (\nabla \cdot \hat{\mathbf{n}}) \hat{\mathbf{n}}$$

needs to be satisfied at some perturbed surface

$$\xi = 1 + \varepsilon \sum_{n=0}^{\infty} \Lambda_n (\eta, t) e^{\imath n \phi}.$$

Let

$$F = \xi - \left(1 + \varepsilon \sum_{n=0}^{\infty} \Lambda_n (\eta, t) e^{\imath n \phi} \right).$$

The normal vector is then

$$\begin{aligned}\hat{\mathbf{n}} &= \frac{\nabla F}{\|\nabla F\|} \\ &= \hat{\boldsymbol{\xi}} + \left[\varepsilon \sum_{n=0}^{\infty} e^{\iota n\phi}\left(-\frac{h_\xi}{h_\eta}\frac{\partial}{\partial\eta}\Lambda_n(\eta,t)\right)\right]\hat{\boldsymbol{\eta}} + \left[\varepsilon \sum_{n=0}^{\infty} e^{\iota n\phi}\left(-\iota n\frac{h_\xi}{\sigma}\Lambda_n(\eta,t)\right)\right]\hat{\boldsymbol{\phi}}.\end{aligned}$$

We also need the two tangent vectors

$$\mathbf{t}_\eta = \left[\varepsilon \sum_{n=0}^{\infty} e^{\iota n\phi}\left(\frac{h_\xi}{h_\eta}\frac{\partial}{\partial\eta}\Lambda_n(\eta,t)\right)\right]\hat{\boldsymbol{\xi}} + \hat{\boldsymbol{\eta}}$$

and

$$\mathbf{t}_\phi = \left[\varepsilon \sum_{n=0}^{\infty} e^{\iota n\phi}\left(\iota n\frac{h_\xi}{\sigma}\Lambda_n(\eta,t)\right)\right]\hat{\boldsymbol{\xi}} + \hat{\boldsymbol{\phi}}.$$

In addition, the velocity and the pressure of the stress tensor $\mathbb{T}$ are also perturbed and evaluated at $\xi = 1 + \varepsilon\sum_{n=0}^{\infty}\Lambda_n(\eta)\,e^{\iota n\phi}$ and expanded about $\varepsilon = 0$ to give

$$\begin{aligned}u\left(1+\varepsilon\sum_{n=0}^{\infty}\Lambda_n(\eta,t)\,e^{\iota n\phi},\eta,\phi,t\right) &= U_s(1,\eta) \\ &\quad +\varepsilon\sum_{n=0}^{\infty} e^{\iota n\phi}\left[\Lambda_n(\eta,t)\frac{\partial}{\partial\xi}U_s(1,\eta)+\tilde{u}_n(1,\eta,t)\right].\end{aligned}$$

Putting them altogether gives three boundary conditions. First of these is the perturbed normal stress condition:

$$q_0^1\tilde{p}_n + q_1^1\frac{\partial}{\partial\xi}\tilde{u}_{\xi n} + q_2^1\tilde{u}_{\eta n} + q_3^1\frac{\partial^2}{\partial\eta^2}\Lambda_n + q_4^1\frac{\partial}{\partial\eta}\Lambda_n + q_5^1\Lambda_n = 0$$

where

$$\begin{aligned}q_0^1 &= -1, \\ q_1^1 &= \frac{8}{R}\frac{1}{h_\xi}, \\ q_2^1 &= \frac{8}{R}\frac{1}{h_\xi h_\eta}\frac{\partial h_\xi}{\partial\eta},\end{aligned}$$

$$
\begin{aligned}
q_3^1 &= -\frac{4}{W}\frac{h_\xi}{h_\eta^2}, \\
q_4^1 &= \frac{4}{W}\left(-\frac{2}{h_\eta^2}\frac{\partial h_\xi}{\partial \eta}+\frac{h_\xi}{h_\eta^3}\frac{\partial h_\eta}{\partial \eta}-\frac{h_\xi}{h_\eta^2\sigma}\frac{\partial \sigma}{\partial \eta}\right), \\
q_5^1 &= -\frac{\partial P_s}{\partial \xi}+\frac{8}{R}\left[U_{\eta s}\left(-\frac{1}{h_\xi^2 h_\eta}\frac{\partial h_\xi}{\partial \eta}\frac{\partial h_\xi}{\partial \xi}+\frac{1}{h_\xi h_\eta}\frac{\partial^2 h_\xi}{\partial \xi \partial \eta}-\frac{1}{h_\xi h_\eta^2}\frac{\partial h_\xi}{\partial \eta}\frac{\partial h_\eta}{\partial \xi}\right)\right] \\
&\quad +\frac{8}{R}\left(\frac{1}{h_\xi h_\eta}\frac{\partial h_\xi}{\partial \eta}\frac{\partial}{\partial \xi}U_{\eta s}-\frac{1}{h_\xi^2}\frac{\partial h_\xi}{\partial \xi}\frac{\partial}{\partial \xi}U_{\xi s}+\frac{1}{h_\xi}\frac{\partial^2}{\partial \xi^2}U_{\xi s}\right) \\
&\quad +\frac{4}{W}\left[-\frac{1}{h_\xi^2 h_\eta}\frac{\partial h_\eta}{\partial \xi}\frac{\partial h_\xi}{\partial \xi}-\frac{1}{h_\xi \sigma^2}\left(\frac{\partial \sigma}{\partial \xi}\right)^2-\frac{1}{h_\eta^2 h_\xi}\left(\frac{\partial h_\eta}{\partial \xi}\right)^2\right] \\
&\quad +\frac{4}{W}\left(\frac{h_\xi}{\sigma^2}n^2+\frac{1}{h_\xi h_\eta}\frac{\partial^2 h_\eta}{\partial \xi^2}+\frac{1}{h_\xi \sigma}\frac{\partial^2 \sigma}{\partial \xi^2}-\frac{1}{h_\xi^2 \sigma}\frac{\partial \sigma}{\partial \xi}\frac{\partial h_\xi}{\partial \xi}\right).
\end{aligned}
$$

The second is the perturbed shear stress condition in the η direction:

$$
q_0^2\frac{\partial}{\partial \eta}\tilde{u}_{\xi n}+q_1^2\frac{\partial}{\partial \xi}\tilde{u}_{\eta n}+q_2^2\tilde{u}_{\xi n}+q_3^2\tilde{u}_{\eta n}+q_4^2\frac{\partial}{\partial \eta}\Lambda_n+q_5^2\Lambda_n=0
$$

where

$$
\begin{aligned}
q_0^2 &= \frac{1}{2}, \\
q_1^2 &= \frac{h_\eta}{2h_\xi}, \\
q_2^2 &= -\frac{1}{2h_\xi}\frac{\partial h_\xi}{\partial \eta}, \\
q_3^2 &= -\frac{1}{2h_\xi}\frac{\partial h_\eta}{\partial \xi}, \\
q_4^2 &= \frac{U_{\eta s}}{h_\eta}\frac{\partial h_\xi}{\partial \eta}-\frac{h_\xi}{h_\eta}\frac{\partial}{\partial \eta}U_{\eta s}+\frac{\partial}{\partial \xi}U_{\xi s}, \\
q_5^2 &= -\frac{U_{\eta s}}{2h_\xi}\frac{\partial^2 h_\eta}{\partial \xi^2}+\frac{h_\eta}{2h_\xi}\frac{\partial^2}{\partial \xi^2}U_{\eta s}-\frac{1}{2h_\xi}\frac{\partial h_\xi}{\partial \eta}\frac{\partial}{\partial \xi}U_{\xi s}+\frac{1}{2}\frac{\partial^2}{\partial \xi \partial \eta}U_{\xi s}+\frac{1}{2h_\xi}\frac{\partial h_\xi}{\partial \xi}\frac{\partial}{\partial \eta}U_{\xi s}.
\end{aligned}
$$

The third is the perturbed shear stress condition in the ϕ direction:

$$
\iota q_0^3\tilde{u}_{\xi n}+q_1^3\frac{\partial}{\partial \xi}\tilde{u}_{\phi n}+q_2^3\tilde{u}_{\phi n}+\iota q_3^3\Lambda_n=0
$$

where

$$\begin{aligned} q_0^3 &= \frac{n}{2}, \\ q_1^3 &= \frac{\sigma}{2h_\xi}, \\ q_2^3 &= -\frac{1}{2h_\xi}\frac{\partial \sigma}{\partial \xi}, \\ q_3^3 &= \left[\left(\frac{1}{h_\eta}\frac{\partial h_\xi}{\partial \eta} - \frac{h_\xi}{h_\eta \sigma}\frac{\partial \sigma}{\partial \eta}\right) U_{\eta s} + \frac{\partial}{\partial \xi} U_{\xi s}\right] n. \end{aligned}$$

We also have the kinematic condition:

$$\frac{\partial}{\partial t}\Lambda_n + q_0^4 \tilde{u}_{\xi n} + q_1^4 \frac{\partial}{\partial \eta}\Lambda_n + q_2^4 \Lambda_n = 0$$

where

$$\begin{aligned} q_0^4 &= -\frac{1}{h_\xi}, \\ q_1^4 &= \frac{U_{\eta s}}{h_\eta}, \\ q_2^4 &= -\frac{1}{h_\xi}\frac{\partial}{\partial \xi} U_{\xi s}. \end{aligned}$$

We can also impose the boundary conditions along $\eta = 0$ and $\eta = 1$ on Λ_n using symmetry to get

$$\frac{\partial}{\partial \eta}\Lambda_0|_{\eta=0,1} = 0$$

for $n = 0$, and

$$\Lambda_n|_{\eta=0,1} = 0$$

for $n \geq 1$.

The above boundary conditions along with the perturbation equations in Chapter 2 can be all put together in a manner described in Chapter 2 and solved using Newton's method to determine the eigenvalues associated with the linear system of the perturbations in time.

We have attempted to do this. However, we were not able to obtain a converged

solution. Our method of computing the steady flow uses minimization to determine the shape of the bubble and gives results that agrees well with previous results, but it may not be accurate enough to be used as the base flow in a linear stability analysis. It is likely that a very accurate base flow past an axisymmetric deforming bubble is needed to perform the linear stability analysis well. Using a grid of very high resolution gives more accurate steady flows as shown in Chapter 4; however, that requires much more memory and computation time. Perhaps a spectral method may be necessary in computing the steady base flow past a bubble instead of our current method of second order finite differences. Still, it would be very interesting to expand on our work and use the linear stability analysis to investigate path instability of a rising bubble.

Bibliography

[1] E. Achenbach, Vortex shedding from spheres, *Journal of Fluid Mechanics*, 62:209–221, 1974.

[2] G. K. Batchelor, *Introduction to Fluid Dynamics*, Cambridge University Press, 1967.

[3] D. Bhaga and M. E. Weber, Bubbles in viscous liquids: shapes, wakes, and velocities, *Journal of Fluid Mechanics*, 105:61–85, 1981.

[4] A. Blanco and J. Magnaudet, The structure of the axisymmetric high-Reynolds number flow around an ellipsoidal bubble of fixed shape, *Physics of Fluids*, 7(6):1265–1274, June 1995.

[5] R. Clift, J. R. Grace, and M. E. Weber, *Bubbles, Drops, and Particles*, Academic Press, 1978.

[6] D. S. Dandy and L. G. Leal, Boundary-layer separation from a smooth slip surface, *Physics of Fluids*, 29(5):1360–1366, May 1986.

[7] D. S. Dandy and L. G. Leal, Buoyancy-driven motion of a deformable drop through a quiescent liquid at intermediate Reynolds numbers, *Journal of Fluid Mechanics*, 208:161–192, 1989.

[8] D. S. Dandy and L. G. Leal, A Newton method for solving free-surface flow problems, *International Journal for Numerical Methods in Fluids*, 9(12):1469–1486, December 1989.

[9] P. C. Duineveld, The rise velocity and shape of bubbles in pure water at high Reynolds number, *Journal of Fluid Mechanics*, 292:325–332, 1995.

[10] R. Duraiswami and A. Prosperetti, Orthogonal mapping in two dimensions, *Journal of Computational Physics*, 98:254–268, 1992.

[11] B. Fornberg, A numerical study of steady flow past a circular cylinder, *Journal of Fluid Mechanics*, 98:819–855, 1980.

[12] B. Fornberg, Steady viscous flow past a sphere at high Reynolds numbers, *Journal of Fluid Mechanics*, 190:471–489, 1988.

[13] A. Goldburg and B. H. Florsheim, Transition and Strouhal number for the incompressible wake of various bodies, *Physics of Fluids*, 9:45–50, 1966.

[14] W. L. Haberman and R. K. Morton, An experimental investigation of the drag and shape of air bubbles rising in various liquids, *David Taylor Model Basin Report no. 802*, 1953.

[15] J. Happel and H. Brenner, *Low Reynolds Number Hydrodynamics*, Prentice-Hall, 1965.

[16] E. Kelley and M. Wu, Path instabilities of rising bubbles in a Hele-Shaw cell, *Physical Review Letters*, pages 1265–1268, 1997.

[17] I. Kim and A. Pearlstein, Stability of the flow past a sphere, *Journal of Fluid Mechanics*, 211:73–93, 1990.

[18] K. S. Kundert and A. Sangiovanni-Vincentelli, *Sparse 1.3*, University of California at Berkeley.

[19] J. Magnaudet, M. Rivero, and J. Fabre, Accelerated flows past a rigid sphere or a spherical bubble. Part 1. Steady straining flow, *Journal of Fluid Mechanics*, 284:97–135, 1995.

[20] J.H. Masliyah and N. Epstein, Numerical study of steady flow past spheroids, *Journal of Fluid Mechanics*, 44:493–512, 1970.

[21] T. Maxworthy, Bubble formation, motion, and interaction in a Hele-Shaw cell, *Journal of Fluid Mechanics*, 173:95–114, 1986.

[22] D.I. Meiron, On the stability of gas bubbles rising in an inviscid fluid, *Journal of Fluid Mechanics*, 198:101–114, 1989.

[23] W. Moller, Experimentelle Untersuchengen zur Hydrodynamik der Kugel, *Phys. Z.*, 39:57–80, 1938.

[24] D. W. Moore, The velocity of rise of distorted gas bubbles in a liquid of small viscosity, *Journal of Fluid Mechanics*, 23:749–766, 1965.

[25] P. M. Morse and H. Feshbach, *Methods of Theoretical Physics*, McGraw-Hill, 1953.

[26] R. Natarajan and A. Acrivos, The instability of the steady flow past spheres and disks, *Journal of Fluid Mechanics*, 254:323–344, 1993.

[27] Zeev Nehari, *Conformal Mapping*, McGraw-Hill Book Company Inc., 1952.

[28] Q. Nie and S. Tanveer, The stability of a two-dimensional rising bubble, *Physics of Fluids*, 7(6):1292–1306, June 1995.

[29] L. Quarterpelle and M. Verri, On the spectral solution of the three-dimensional Navier-Stokes equations in spherical and cylindrical regions, *Computer Physics Communications Communications*, 90:1–43, 1995.

[30] R. D. Richtmeyer and K. W. Morton, *Difference Methods for Initial-Value Problems*, Interscience, 1967.

[31] F. W. Roos and W. W. Willmarth, Some experimental results on sphere and disk drag, *AIAA Journal*, 9:285–291, 1971.

[32] P. N. Rowe and B. A. Partridge, A note on the initial motion and break-up of a two-dimensional air bubble in water, *Chemical Engineering Science*, 19:81–82, 1964.

[33] G. Ryskin and L. G. Leal, Orthogonal mapping, *Journal of Computational Physics*, 50:71–100, 1983.

[34] G. Ryskin and L. G. Leal, Numerical solution of free-boundary problems in fluid mechanics. Part 1. The finite-difference technique, *Journal of Fluid Mechanics*, 148:1–17, 1984.

[35] G. Ryskin and L. G. Leal, Numerical solution of free-boundary problems in fluid mechanics. Part 2. Buoyancy-driven motion of a gas bubble through a quiescent liquid, *Journal of Fluid Mechanics*, 148:19–35, 1984.

[36] P. G. Saffman, On the rise of small air bubbles in water, *Journal of Fluid Mechanics*, 1:249–275, September 1956.

[37] P. G. Saffman, Viscous fingering in Hele-Shaw cells, *Journal of Fluid Mechanics*, 173:73–94, 1986.

[38] P. N. Shankar, On the shape of a two-dimensional bubble in uniform motion, *Journal of Fluid Mechanics*, 244:187–200, 1992.

[39] G. T. Symm, Numerical mapping of exterior domains, *Numerische Mathematik*, 10:437–445, 1967.

[40] S. Takagi, Y. Matsumoto, and H. Huang, Numerical analysis of a single rising bubble using boundary-fitted coordinate system, *JSME International Journal Series B*, 40(1):42–50, 1997.

[41] H. Takami and H. B. Keller, Steady two-dimensional viscous flow of an incompressible fluid past a circular cylinder, *Phys. Fluids Supple. II51*, 1969.

[42] S. Taneda, Studies on wake vortices(III). Experimental investigation of the wake behind a sphere at low Reynolds numbers, *Rep. Res. Inst. Appl. Mech. Kyushu University*, 4:99–105, 1956.

[43] S. J. Tavener, Stability of the O(2)-symmetric flow past a sphere in a pipe, *Physics of Fluids*, 6:3884–3892, December 1994.

[44] A.G. Tomboulides, S.A. Orszag, and G.E. Karniadakis, Direct and large-eddy simulation of axisymmetric wakes, *AIAA-93-0546*, 1993.

[45] J. Toulcova and J. Podzimek, Contribution to the question of the catching of aerosol particles in the wake of falling water droplets, *J. Rech. Atmos.*, 3:89–95, 1968.

[46] H. Tsuge and S. Hibino, The onset conditions of oscillatory motion of single gas bubbles rising in various liquids, *Journal of Chemical Engineering of Japan*, 10(1):66–68, 1977.

[47] S.O. Unverdi and G. Tryggvason, A front-tracking method for viscous, incompressible, multi-fluid flows, *Journal of Computational Physics*, 100(1):25–37, May 1992.

[48] J. K. Walters and J. F. Davidson, The initial motion of a gas bubble formed in an inviscid liquid. Part 1. The two-dimensional bubble, *Journal of Fluid Mechanics*, 12:408–416, 1962.

[49] J. S. Wu and G. M. Faeth, Sphere wakes in still surroundings at intermediate Reynolds numbers, *AIAA Journal*, 31(8):1448–1455, August 1993.

[50] J. Zikmundova, Experimental investigation of the wake behind a sphere and a spheroid for Reynolds numbers from 44 to 495, *J. Rech. Atmos.*, 4:7–18, 1970.